Wide Field Aperture Synthesis Radio Astronomy

Douglas Carl-Johan Bock

A thesis
submitted for the degree of
Doctor of Philosophy
at the
University of Sydney

September, 1997

Abstract

This thesis is focussed on the Molonglo Observatory Synthesis Telescope (MOST), reporting on two primary areas of investigation. Firstly, it describes the recent upgrade of the MOST to perform an imaging survey of the southern sky. Secondly, it presents a MOST survey of the Vela supernova remnant and follow-up multiwavelength studies.

The MOST Wide Field upgrade is the most significant instrumental upgrade of the telescope since observations began in 1981. It has made possible the nightly observation of fields with area ~ 5 square degrees, while retaining the operating frequency of 843 MHz and the pre-existing sensitivity to point sources and extended structure. The MOST will now be used to make a sensitive (rms ≈ 1 mJy beam^{-1}) imaging survey of the sky south of declination $-30°$. This survey consists of two components: an extragalactic survey, which will begin in the south polar region, and a Galactic survey of latitudes $|b| < 10°$. These are expected to take about ten years. The upgrade has necessitated the installation of 352 new preamplifiers and phasing circuits which are controlled by 88 distributed microcontrollers, networked using optic fibre. The thesis documents the upgrade and describes the new systems, including associated testing, installation and commissioning.

The thesis continues by presenting a new high-resolution radio continuum survey of the Vela supernova remnant (SNR), made with the MOST before the completion of the Wide Field upgrade. This remnant is the closest and one of the brightest SNRs. The contrast between the structures in the central pulsar-powered nebula and the synchrotron radiation shell allows the remnant to be identified *morphologically* as a member of the composite class. The data are the first of a composite remnant at spatial scales comparable with those available for the Cygnus Loop and the Crab Nebula, and make possible a comparison of radio, optical and soft X-ray emission from the resolved shell filaments. The survey covers an area of 50 square degrees at a resolution of $43'' \times 60''$, while imaging structures on scales up to $30'$. It has been used for comparison with Wide Field observations to evaluate the performance of the upgraded MOST.

The central plerion of the Vela SNR (Vela X) contains a network of complex filamentary structures. The validity of the imaging of these filaments has been confirmed with Very Large Array (VLA) observations at 1.4 GHz. Unlike the situation in the Crab Nebula, the filaments are not well correlated with Hα emission. Within a few parsec of the Vela pulsar the emission is much more complex than previously seen: both very sharp edges and more diffuse emission are present. It has been postulated that one of the brightest filaments in Vela X is associated with the X-ray feature (called a 'jet') which appears to be emanating from the region of the pulsar. However, an analysis of the MOST and VLA data shows that this radio filament has a flat spectral index similar to another more distant filament within the plerion, indicating that it is probably unrelated to the X-ray feature.

Preface

It has been MOST enjoyable and satisfying to be part of the major upgrade of the Molonglo Observatory Synthesis Telescope. This project has involved all the staff of the Astrophysics Department in the School of Physics, and much of the material in the early chapters is an account of the collective effort.

I must especially thank my supervisor and co-supervisors. Michael Large has been instrumental not only to my contribution to the project, but also conceived of the Wide Field upgrade, identifying the existing features of the MOST that made it possible. Tony Turtle planned the initial observations and provided continued advice for the MOST Vela SNR survey. Anne Green helped me expand my horizons into multiwavelength studies and gave me extra encouragement while I was writing this thesis. Dale Frail introduced me to observing at the VLA and was a wealth of information on SNRs. All made helpful comments on drafts of this thesis.

The Wide Field upgrade could not have taken place without the extraordinary dedication of the staff at Molonglo: Duncan Campbell-Wilson, Jeff Webb, Mick White and Boyd Smithers, who worked in trying conditions to install the new hardware and keep the telescope in good order. In Sydney, Ralph Davison, Fred Peterson, Barbara Piestrzynski and the workshop staff kept up supplies of vital components for the project. Ralph particularly helped me with electronics. The foresight of one of the great radio astronomers, Bernard Mills, has made the MOST an instrument which continues to be productive today.

I thank also many people with whom I had helpful discussions or who read and commented upon drafts of parts of this thesis, including Lewis Ball, Lawrence Cram, David Crawford, John Dickel, Bryan Gaensler, Richard Hunstead, Tom Landecker, Phil Lukins, Bruce McAdam, Vince McIntyre, Doug Milne, Gordon Robertson, Elaine Sadler, Bob Sault, Ian Skillen and many others at the School of Physics, ATNF and NRAO.

I am grateful to be able to include data obtained by several others in this thesis. Mike Bessell and Andrew Walker made and reduced the Hα observations of the Vela shell and Vela X. Vince McIntyre and Tanya Hill helped with additional reduction. Doug Milne, Berndt Aschenbach and Craig Markwardt kindly provided electronic versions of their data. I acknowledge the support provided by software authors both within and outside the School of Physics, including Lawrence Cram, David Crawford, Richard Gooch, Neil Killeen, Bob Sault and Taisheng Ye. Dick Manchester, Matthew Bailes and Peter McCulloch provided Vela pulsar timing data.

Thanks are due also to Miller Goss at NRAO and Tom Landecker at DRAO for their hospitality while I was visiting their institutions. I acknowledge financial support in the form of an Australian Postgraduate Award while a student, and also travel support from the Department of Industry Science and Technology (Access to Major Research Facilities Program), the Science Foundation for Physics, the James Kently Memorial Scholarship, the R. and M. Bentwich Scholarship, the Astronomical Society of Australia and the Science Faculty (Conference Travel Grants Scheme) .

My family and close friends have always been supportive of my study. My brother Timothy helped me with statistics. I particularly thank my mother who, apart from proofreading this thesis, made many sacrifices to ensure that my brothers and I received an excellent education.

This thesis was typeset by the author using the LaTeX document preparation system (Lamport 1994).

Statement of originality

The work contained in this thesis is the result of the sole and original endeavours of myself, Douglas Carl-Johan Bock, except where noted otherwise. The latter exclusions include some of the work contained in chapters 2, 3 and 8, which was undertaken in collaboration with others. In each case a statement explaining the extent to which the work was my own is incorporated within the chapter.

Douglas Carl-Johan Bock
The University of Sydney
Sydney, Australia
September 1997

Next to our own sun, Vela X was probably the most important star in the history of humanity.

George Michanowsky, 1977, The Once and Future Star: Exploring the Mysterious Link Between the Great Southern Supernova (Vela X) and the Origins of Civilization, (New York: Hawthorn).

Contents

List of Tables

List of Figures

Acronyms, Abbreviations and Conventions

A list of acronyms and abbreviations used frequently in this thesis is given below. A reference to the section where they are introduced is given in parentheses, where usage of the terms is peculiar to the MOST.

A700	The HP-A700 observing computer (3.2.2)
`AIPS`	Astronomical Image Processing System
ADC	Analogue-to-Digital Converter
ARC	Arc (zenithal equidistant) projection
ATCA	Australia Telescope Compact Array
BC	Bay Controller (2.5.2)
BL	Bay Linker (2.5.4)
BP	Bay Phaser (2.4.2)
Dec., δ	Declination
EPROM	Erasable Programmable Read Only Memory
FITS	Flexible Image Transport System
FWHM	Full Width at Half Maximum
HA	Hour Angle
HPBW	Half-Power Beam Width
ISM	Interstellar Medium
IF	Intermediate Frequency (2.4.3)
Jy	Jansky, a unit of flux density; $1\,\mathrm{Jy} = 10^{-26}\,\mathrm{W\,m^{-2}\,Hz^{-1}}$
LED	Light Emitting Diode
LNA	Low Noise Amplifier (2.4.1)
LO	Local Oscillator
MC	Master Controller (2.5.1)
MD	Meridian Distance (2.1)
`MIRIAD`	Multichannel Image Reconstruction Image Analysis and Display
MOST	Molonglo Observatory Synthesis Telescope
MVS	MOST Vela Supernova Remnant Survey
NCP	North Celestial Pole (slant orthographic) projection
NRAO	National Radio Astromomy Observatory[1]
RA	Right Ascension
RF	Radio Frequency

SN(e)	Supernova(e)
SNR	Supernova Remnant
TCC	Telescope Control Computer (3.2.2)
VLA	Very Large Array
WF	Wide Field (2.3)

Typography notes When referring to computer software, I have used the `typewriter` style, capitalised or not as indicated by common usage, for example `AIPS HGEOM` but `MIRIAD regrid`. Algorithms such as CLEAN are given in Roman type. I introduce new terms in *italics.*

Epoch usage I have tried, as far as possible, to use J2000 coordinates throughout this thesis. However, the MOST uses exclusively B1950 coordinates for observing and data archiving. To avoid confusion I have retained B1950 coordinates in discussions of MOST observing parameters.

Spectral indices All radio spectral indices, α, in this thesis are quoted assuming the relationship $S_\nu \propto \nu^\alpha$.

Chapter 1

Introduction

1.1 Radio astronomy of the southern sky

Australia has been at the forefront of radio astronomy since it began in the 1940s with experience gained during the Second World War and following the recent pioneering experiments of Jansky and Reber. The localisation of radio emission from the extragalactic source Cygnus A and the identification of radio emission from the Crab Nebula cemented the place of radio astronomy as a key observational discipline.

Observations made of the southern sky have a unique advantage. The bulk of our Galaxy, including the Galactic Centre, as well as the next two closest galaxies, the Large and Small Magellanic Clouds, are best visible from the south. Very productive radio telescopes in the Southern Hemisphere—including the Parkes Telescope, the Australia Telescope Compact Array, the Molonglo Cross and the Molonglo Observatory Synthesis Telescope—have supported active and internationally recognised research programmes.

This thesis is about how one of these telescopes, the Molonglo Observatory Synthesis Telescope (MOST), has been upgraded to be capable of fast, high resolution and high sensitivity surveys of the southern sky, keeping its work at the forefront of modern astronomy. It is also about one MOST survey in particular: the MOST Vela supernova remnant survey, which was undertaken during the upgrade of the MOST, and which has provided a base for extending our understanding of the nature of supernova remnants.

1.2 The Molonglo Observatory Synthesis Telescope: An historical perspective

The origin of the MOST is in the 408 MHz Molonglo (Mills) Cross, construction of which began in 1962, with the first observations in 1965 using only the east-west arm of the Cross (Mills 1991). In 1967 the Cross was completed, with an instantaneous pencil beam of $3'$. The next ten years saw observations for the southern sky survey

which made the Cross most well-known, leading to publication of the Molonglo Reference Catalogue (Large et al. 1981; Large et al. 1991). Other surveys included a catalogue of sources in the Magellanic Clouds (MC4: Clark & Caswell 1976) and Galactic surveys of extended emission (Green 1974) and small-diameter sources (Clark & Crawford 1974). One particularly famous early discovery was of the Vela pulsar (Large et al. 1968), which provided the first association between a pulsar and a supernova remnant (the Vela supernova remnant—studied in this thesis). The short period of the pulsar (89 ms) indicated that pulsars were probably rotating neutron stars, rather than white dwarfs.

By the mid 1970s, the entire sky available to the Molonglo Cross had been surveyed. A more effective use of the reflector could be made by using it in a fundamentally different instrument. In 1978, the Cross ceased operation. The Molonglo Observatory Synthesis Telescope was then formed from the east-west arm of the Cross.[1] Figure 1.1 shows the MOST as it is today.

Although early plans (Mills 1991; Mills & Little 1972) had envisaged a conversion to an instrument operating at 1420 MHz, funding constraints dictated a technically more feasible conversion to 843 MHz. The result is a telescope which is complementary to other telescopes such as the ATCA and the (now-defunct) Fleurs Synthesis Telescope, rather than in competition with them. A comprehensive retrospective of the Molonglo Cross and its transformation to the MOST is given by Mills (1991).

1.3 The MOST Wide Field upgrade and surveys of the southern sky

Since beginning operation as a synthesis telescope in 1981, the MOST has been able to image elliptical fields of size up to $70' \times 70'\mathrm{cosec}\,|\delta|$. This capability has been used from the start for surveys, of the Galactic Plane (Whiteoak et al. 1989; Green 1994, 1997), supernova remnants (Mills 1985; Whiteoak & Green 1996), pulsars (Large et al. 1984; Manchester 1985), the Small Magellanic Cloud (Ye & Turtle 1993) and extragalactic objects (Jones & McAdam 1992; Burgess & Hunstead 1994).

Along the way, the surveys made with the MOST have benefited from hardware and software improvements. The installation of new radio-frequency phase shifters (Amy & Large 1990) substantially reduced the incidence in images of grating rings—elliptical artefacts of off-field sources. Improvements to image processing, such as the introduction of a form of self-calibration (Cram & Ye 1995), and to image display (Gray 1994, pp230–234), have increased the utility of the data collected with the telescope.

Soon after the installation of the phase shifters, it was realised (Large et al. 1994) that the principle could be extended to allow a factor of five increase in the area of the sky covered in a single observation. A serendipitous feature of the design of

[1] To avoid confusion later, I should remark here that the two halves of the east-west arm of the Molonglo Cross have become known as the east and west *arms* of the MOST.

Figure 1.1 The Molonglo Observatory Synthesis Telescope (following page). A view of the western end of the west arm supporting the author, and showing the waveguide and feed elements (protected by black polypropylene flower pots) illuminating the parabolic mesh. The east and west arms of the MOST formed part of the Molonglo Cross. The disused north and south arms of the Molonglo Cross are visible in the background.

the MOST, dating from the origin of the Molonglo Cross, is that the receiver for each of the 88 *bays* of the telescope is fed by four independent colinear waveguides. This allows the application of a stepwise phase gradient to the signals from the four waveguides to offset the pointing of the bay. This feature has made possible the implementation on the MOST of the Wide Field observing mode, which is described in subsequent chapters.

Large area sky surveys are intrinsically valuable as ways of discovering new objects and studying large scale structure and source statistics. They are normally expensive and time-consuming. The realisation that the Wide Field mode would be effective in making large southern sky surveys with the MOST has become the natural driving force behind the Wide Field upgrade. The new observing mode makes possible a survey of the southern sky south of declination $-30°$ within the projected lifetime of the MOST antenna structure. The main science goals which motivate the survey are to:

- investigate the large-scale properties of faint radio sources, in particular the star-forming galaxies which begin to dominate the radio source population at levels of a few mJy;
- study the clustering of faint radio sources over a large area of sky;
- gain a statistically complete picture of the largest bound structures in the universe, the rich clusters of galaxies;
- search for very distant quasars and hyperluminous starburst galaxies;[2]
- search for Galactic variables and supernova remnants, and investigate the large scale thermal and non-thermal emission in the Galaxy.

A further discussion of the scientific aims of the surveys may be found in Bock et al. (1997).

Two main regions of the southern sky will be surveyed, with slightly different observing parameters. The extragalactic survey will cover the region south of declination $-30°$ which lies at high Galactic latitude ($|b| > 30°$); while the Galactic Plane survey will cover the southern Galactic Plane ($l = 240$–$365°$, $|b| < 10°$). Both surveys will overlap the NRAO VLA Sky Survey (NVSS; Condon et al. 1997) in the declination zone $-30°$ to $-40°$. This will provide a spectral index measurement for sources detected in both surveys, since the Wide Field surveys are at 843 MHz and the NVSS is at 1400 MHz. As well, it will allow an independent check of our position measurements. The Galactic Plane survey will include a re-survey of the area of the first epoch MOST Galactic Plane survey (Whiteoak et al. 1989; Green 1994), which was restricted to $|b| < 1\overset{\circ}{.}5$.

Radio telescopes world-wide are experiencing increasing levels of radio-frequency interference, largely as a result of the communications revolution in the last 5–10 years. The southern sky surveys made possible by the Wide Field upgrade are timely.

[2]Such extreme objects are rare but particularly important in setting limits for the earliest epoch of galaxy formation on the one hand, and starburst models for active galactic nuclei on the other.

1.4 Overview of this thesis

This thesis begins with a presentation of the MOST Wide Field upgrade, the most significant instrumental upgrade of the telescope since observations began in 1981. When I joined the project, in January 1994, the concept was well-developed and prototypes of some of the hardware components had been produced. My role was to take part in the realisation of the Wide Field upgrade of the telescope. This included planning and resource allocation, commissioning, testing, sub-system development, and prototype evaluation and modification. Chapter 2 explains the concept of the Wide Field upgrade, and outlines the major components developed for it. A discussion of the Wide Field communications system, for which I was solely responsible, has been placed in appendix A—not because it is subsidiary, but because it is an in-depth description of one sub-system and might otherwise interrupt the flow of the thesis. Chapter 3 covers the process of upgrading the telescope, including hardware installation, commissioning and preliminary astronomical testing.

In chapter 4, the Vela supernova remnant (SNR) is introduced. This object, one of the closest supernova remnants and a member of the composite class, is one of only a few remnants conclusively associated with a pulsar (the Vela pulsar). It offers the opportunity to study a supernova remnant in great detail. Chapter 4 provides the astronomical motivation for its study, preceded by the survey of the remnant using the MOST in pre-Wide Field mode presented in chapter 5. However, the survey is also important in the context of the Wide Field upgrade—it is used for assessment of Wide Field images in chapter 6, which continues the theme of astronomically testing the Wide Field system. Once again, some important material is presented in appendices. These are appendix B, which summarises observations used to test the Wide Field system; appendix C, which describes the method used for removing the effect of the the Vela pulsar from the MOST Vela supernova remnant survey images; and appendix D, which provides further information on the reduction and mosaicing of the survey observations.

Chapters 7 and 8 lead on from the astronomical results of the MOST Vela supernova remnant survey. In chapter 7, the interaction of the the expanding Vela SNR shell with the interstellar medium is investigated in a multi-wavelength study. Chapter 8 focuses on the central region of the Vela SNR, known as Vela X, where additional observations using the Very Large Array are presented with the aim of increasing our understanding of the remnant. A final discussion is presented in chapter 9. References are placed after the appendices.

Chapter 2

The MOST Wide Field System

Section 1.3 outlined the motivation for the Wide Field upgrade of the Molonglo Observatory Synthesis Telescope. This chapter describes the concept of the field widening and the hardware required. The upgrade of the MOST was a major project involving a substantial fraction of the Astrophysics Department's effort over several years. The material in this chapter reports on the group's work, and shares material with Bock et al. (1997) and Large et al. (1994). The technical project for which I was solely responsible is documented in appendix A: The MOST Wide Field Communications System.

2.1 The Molonglo Observatory Synthesis Telescope

The MOST is a multi-element interferometer operating at 843 MHz (wavelength, $\lambda = 0.356$ m), receiving right hand circular polarisation (IEEE) in a 3 MHz bandwidth. The reflectors of the MOST are two colinear cylindrical paraboloids aligned almost east-west, each 11.6 m wide and 778 m long. These two *arms* are separated by a 15 m gap and have a total aperture area of more than 18 000 m^2. Figure 2.1 illustrates the natural coordinates for steering the MOST. The *tilt* is the rotation angle about an E-W axis. Tilt is zero at the zenith and positive to the north. The term *meridian distance* is used to describe the angle a point in the sky (or a MOST phased beam) makes with the meridian plane. As a point at declination δ moves across the sky, its meridian distance MD is related to its instantaneous hour angle HA approximately[1] by

$$\sin MD = \sin HA \operatorname{cosec} |\delta|.$$

Points west of the meridian have a positive meridian distance.

The elements of the interferometer are the 44 contiguous 50λ (17.6 m) lengths of each arm called *bays*. The feed of each bay is an array of 88 circularly polarised

[1]The exact relation is more complicated because the arms, though colinear, are not quite horizontal or east-west.

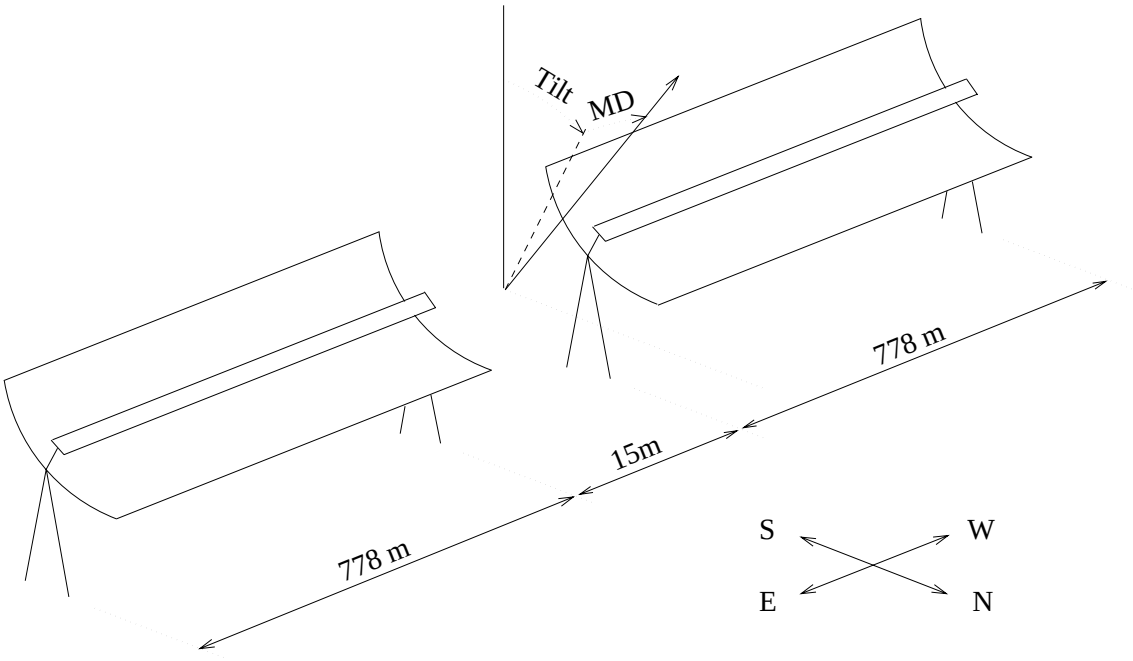

Figure 2.1 Schematic of the Molonglo Observatory Synthesis Telescope. As shown in this sketch, the MOST uses 'alt-alt' coordinates for steering the beams. A drive shaft and distributed gear boxes enable the reflectors to be rotated about their east-west axis at rates up to 5 degrees per minute: the *tilt* is measured from the zenith with limits of $+55°$ (to the north) and $-55°$ (to the south). Continuously variable linear phase gradients set up in the line feed of the MOST move the beams relative to the reflector in a direction orthogonal to the tilt at a similar rate: the *meridian distance* is measured from the plane of the meridian, with limits of $+67°$ (to the west) and $-67°$ (to the east). As explained in the text, installation of electronic hardware to effect small but rapid offsets of the beams in meridian distance has enabled the area of the MOST's field to be quintupled by time-sharing.

resonant ring antennae (Mills & Little 1972). To steer the beam of a bay in meridian distance, the appropriate linear phase gradient is set up by differential rotation of the ring antennae. During a synthesis observation, the meridian distance and tilt pointing are continuously adjusted so that the primary beam of each bay tracks the field centre. The radio frequency signals from each bay are amplified, down-converted to an intermediate frequency (11 MHz) and returned, via 900 m lengths of coaxial cable, to the central laboratory for signal processing.

The features of MOST described up to this point have been essentially unchanged since its inauguration in 1981, and the principle of operation is similar to that of more conventional interferometers which use discrete dishes as elements instead of contiguous bays. In the following paragraphs I outline the unusual fan-beam image

forming process used by the MOST and describe how hardware developments have allowed the image diameter to be doubled.

2.2 Image forming with the MOST

The IF signals from the 44 bays of the east arm of the telescope are combined at the central laboratory with equal weight to form a fan beam. Similarly, the west arm signals are combined to form a west-arm fan beam. During an observation, the phase and delay introduced into the signal from each bay are continuously updated so that the beams track the chosen field centre. An interferometer fan beam, with spatial frequency weighting appropriate for Earth-rotation synthesis, is generated by multiplying the east-arm signal by the corresponding west-arm signal (using an analogue multiplying circuit).

By combining the contributions from the bays with slightly different phase gradients a comb of 64 simultaneous interferometer fan beams is generated. The angular size of each beam (Durdin et al. 1984) is $40'' \sec|MD|$ (at first zeros) in meridian distance and about 2° (FWHM) in the tilt coordinate.[2] The beams are equally spaced at near the Nyquist interval of $22'' \sec|MD|$. Together they cover a strip of sky $23' \sec|MD|$ wide. The beams are interlaced with an $11''$ offset to simplify interpolation during data processing. This set of beams is known as a *block*.[3] The technique for synthesising a $23'$ field using a single block of beams is illustrated in figure 2.2.

The position angle of the comb of beams on the sky depends on the hour angle. The position angle of the beams at the start of an observation ($HA = -6^{\rm h}$) is shown in figure 2.2 (a). The figure also shows the elliptical half-power isophote of the bay beam. Figures 2.2 (b) & (c) show how the bay beams and fan beams rotate relative to the sky during the first six hours of a synthesis observation (which would continue to $HA = +6^{\rm h}$). See Perley (1979) and Crawford (1984) for further details of the fan beam synthesis technique. The small circle in (c) represents the fully synthesised area (i.e. the area with continuous u-v coverage in the image) which has dimensions $23' \times 23'\mathrm{cosec}\,|\delta|$.

2.2.1 Calibration

The drive time overhead of the MOST and the desire for complete or nearly complete u-v coverage limits the observation of calibrators to times outside the 12 hr used for a synthesis observation. The method of calibration initially used for Wide Field

[2] An approximate formula for the tilt beamwidth, which varies with meridian distance, is given by Reynolds (1986, p20).

[3] It should be noted here that the beams on the sky are strictly arcs of *small circles* on the celestial sphere. They become straight lines in the back-projection (NCP) plane, i.e. in figures 2.2 and 2.3.

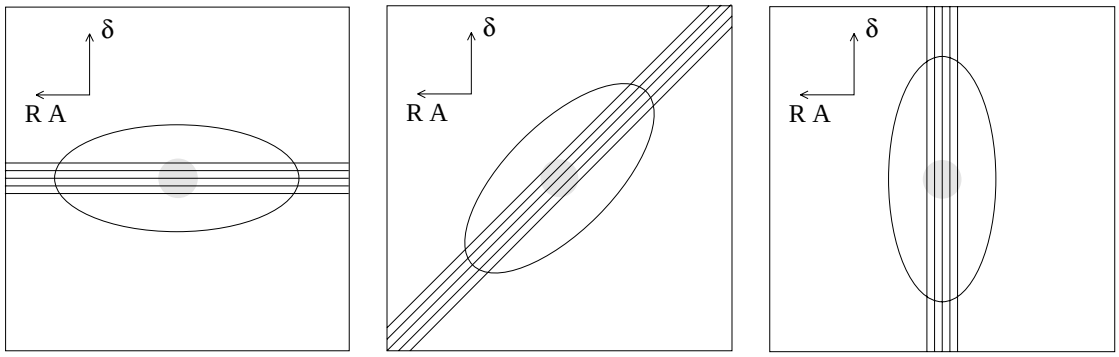

(a) $HA = -6^{\mathrm{h}}$ (b) $HA = -3^{\mathrm{h}}$ (c) $HA = 0^{\mathrm{h}}$

Figure 2.2 Single-block MOST fan beam synthesis. During MOST synthesis observations, the block of 64 fan beams (represented here by 5 parallel lines) rotates about the chosen field centre. The diagrams show the position angle of the beams, back projected on to the equatorial plane, at three hour angles. After a full synthesis ($-6^{\mathrm{h}} \leq HA < 6^{\mathrm{h}}$) the data are combined to form a $23'$ image, represented by the shaded circle. The ellipse in the diagrams represents the primary beam of the bays, whose exact shape depends on hour angle and declination.

observations is unchanged from the method used with earlier observations. For completeness I will briefly outline it here.

Before and after each observation, several (typically five) strong non-varying unresolved sources are each observed for five 24 s integrations (*SCANS*). Each SCAN comprises four 6 s groups of measurements. These four groups are made using in turn interlaced and non-interlaced beamset positions with each sense of the slow phase switch (see footnote to page 12). The calibration sources used are listed by Campbell-Wilson & Hunstead (1994).

The measured data are fitted for several telescope parameters, including those appropriate to the calibration of synthesis observations: *gain*, *offset* and *phase*.[4] A goodness-of-fit measurement is provided to facilitate rejection of calibration observations affected by confusion. While 'gain' is used in the sense usual for interferometric calibration, the terms 'offset' and 'phase' deserve a little elaboration. These terms define a two-parameter model of the error in the phase gradient applied along the telescope. The 'phase' (in degrees) measures the discontinuity of phase between the two arms of the telescope, whereas the 'offset' is a measure of source displacement (in arcseconds) attributed to a uniform error in phase gradient on each arm. A precise definition may be found in Hogan (1992, p13).

[4]Presently only the fitted parameters are recorded. It is planned to change the mode of observing calibration sources to short synthesis observations as this more accurately reproduces the telescope operation during a full 12 hour synthesis.

Naturally this three parameter calibration is only an approximate model: the gain and phase in the signal path from each of the 88 bays are actually independently time-varying. A novel method of self-calibration, adaptive deconvolution (Cram & Ye 1995), is applied where possible to estimate time-dependent values for the three parameters.

2.3 Widening the field of view

In the basic mode of synthesis described in the previous paragraphs, the fully synthesised area is much less than the available field defined by the primary beam of the bays. For example any point outside the shaded area in figure 2.2 is recorded by the fan beams only for a limited range of hour-angle. While useful images can often be formed by suitable CLEANing of partially synthesised fields, a strength of the MOST lies in the quality of its fully synthesised images. The most straightforward technique to increase the fully synthesised area would be to increase the number of real time fan beams to cover the width of the field defined by the bay beam. An alternative solution, adopted for the MOST, is to time-share, covering the field by cyclically offsetting the comb of fan beams through a range of meridian distance. Some of the issues involved are illustrated in figure 2.3.

Figure 2.3 (a) shows the beams at meridian transit (as in figure 2.2 (c)) superimposed on the field (shaded circle) to be imaged by time-sharing. The grating lobes which inevitably arise from the periodic bay structure of the MOST are also shown. As can be seen in the profile, the fan beams are centred on the peak of the bay beam, while the first order grating responses due to the bay periodicity are small as they lie at the nulls of the bay beam. Figure 2.3 (b) illustrates two problems which arise with the time-sharing technique when the comb of beams is offset:

- the gain of the principal fan beams is reduced;
- the grating responses are increased as they are shifted from the nulls of the bay beam.

Both these problems would be solved if the bay beam could be offset synchronously with the fan beams, as shown in figure 2.3 (c). The implementation of this facility to offset the bay beams rapidly and simultaneously with the fan beams is the essence of the *MOST Wide Field upgrade*, allowing images of size $163' \times 163' \operatorname{cosec} |\delta|$ to be fully synthesised using the central and six offset positions.

Wide Field observations using such a seven-position switching pattern are called *7–block* observations. The observations made using the maximum field size available before 1996 ($70'$) are known as *3–block* observations and use what are now the three inner of the 7 switching positions used in a Wide Field observation. From 1989, 3–block observations used a somewhat simplified bay beam switching method to suppress the bay grating rings (Amy & Large 1990). This method provided a two-step phase gradient to offset a bay beam by introducing an additional 60° phase

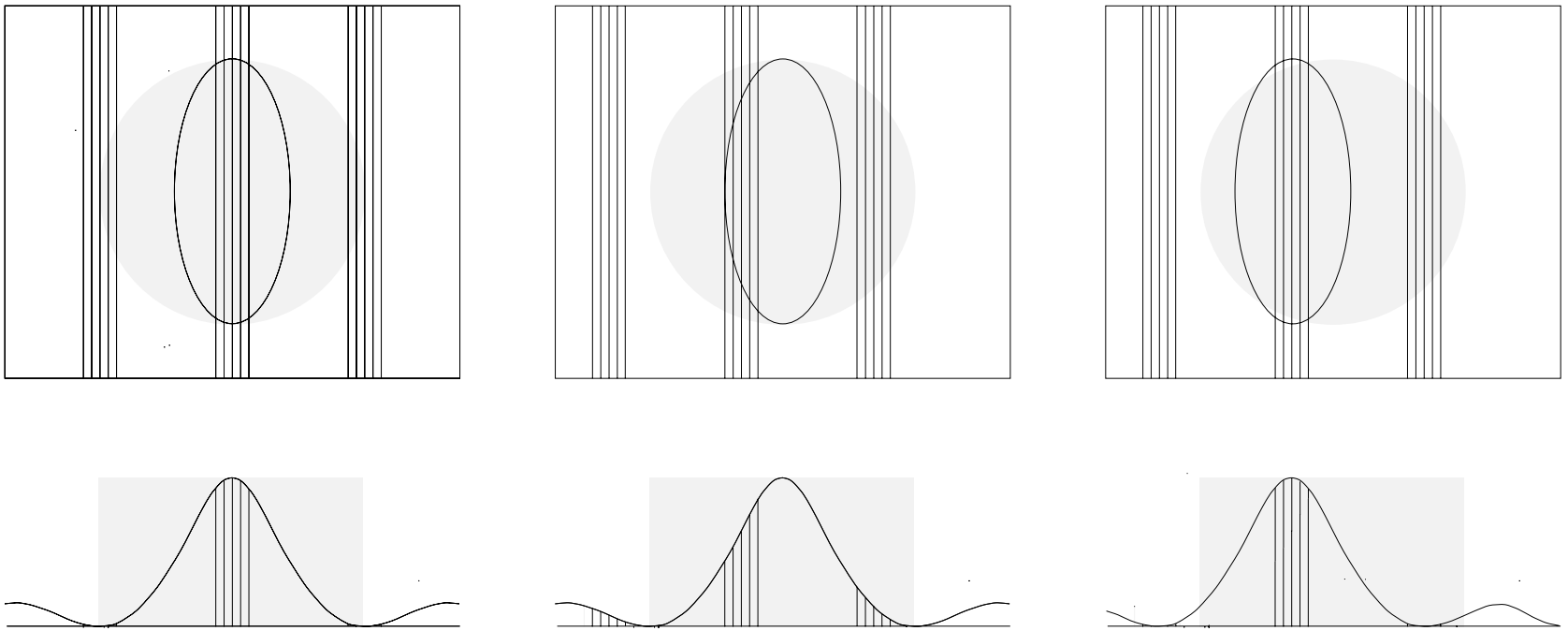

Figure 2.3 Widening the field of view of the MOST by time sharing. A representation of the MOST beams at the mid point of a 12 hour synthesis with the field to be synthesised shown as a shaded circle. In (a) the fan beams and the bay primary beam are located centrally on the field. The first order grating lobes due to the bay periodicity (see text) are largely suppressed as they lie about the nulls of the bay primary beam, as seen in the profile. Figure (b) shows the two problems that arise if the time-sharing is attempted by simply offsetting the fan beams: the fan beam gains are reduced and the grating responses are enhanced as they no longer lie on primary beam nulls. These problems are overcome if the primary beams are offset with the fan beams. Figure (c) shows one of the 7 offsets used to synthesise a wide field. Note that, for clarity, the amplitude of the bay sidelobes has been exaggerated.

shift into the signals derived from each *half* of the bay in turn. A comprehensive description of the MOST as it was before Wide Field conversion is given by Robertson (1991).

It takes 28 s to acquire one set of responses recorded as a single sample. Table 2.1 gives the parameters of the 28 s data acquisition cycle for a Wide Field observation. Data from each of the 64 hard-wired beams for each switching position and each

Cycle count	Block number	Interlacing offset	Phase switch
1	1 (W)	0	+
2	2	0	+
3	3	0	+
4	4	0	+
5	5	0	+
6	6	0	+
7	7 (E)	0	+
8	7	1	+
9	6	1	+
10	5	1	+
11	4	1	+
12	3	1	+
13	2	1	+
14	1	1	+
15	1	1	−
16	2	1	−
17	3	1	−
18	4	1	−
19	5	1	−
20	6	1	−
21	7	1	−
22	7	0	−
23	6	0	−
24	5	0	−
25	4	0	−
26	3	0	−
27	2	0	−
28	1	0	−

Table 2.1 Parameters of the 28 s cycle in a MOST Wide Field 7–block observation

interlacing offset are integrated for 1 s in the 28 s cycle with each sense of the slow phase switch.[5] The pairs of measurements made with each sense of the slow phase

[5]In the MOST two phase switches together provide a high level of immunity from DC offsets and spurious correlations arising from crosstalk between the east- and west-arm signals. This is done by reversing the phase of the response from one arm with respect to the other before multiplication of the two signals. The *fast* phase switch operates at 400 Hz and has its effect removed within the hardware. The *slow* phase switch operates twice during each data acquisition cycle, as shown in

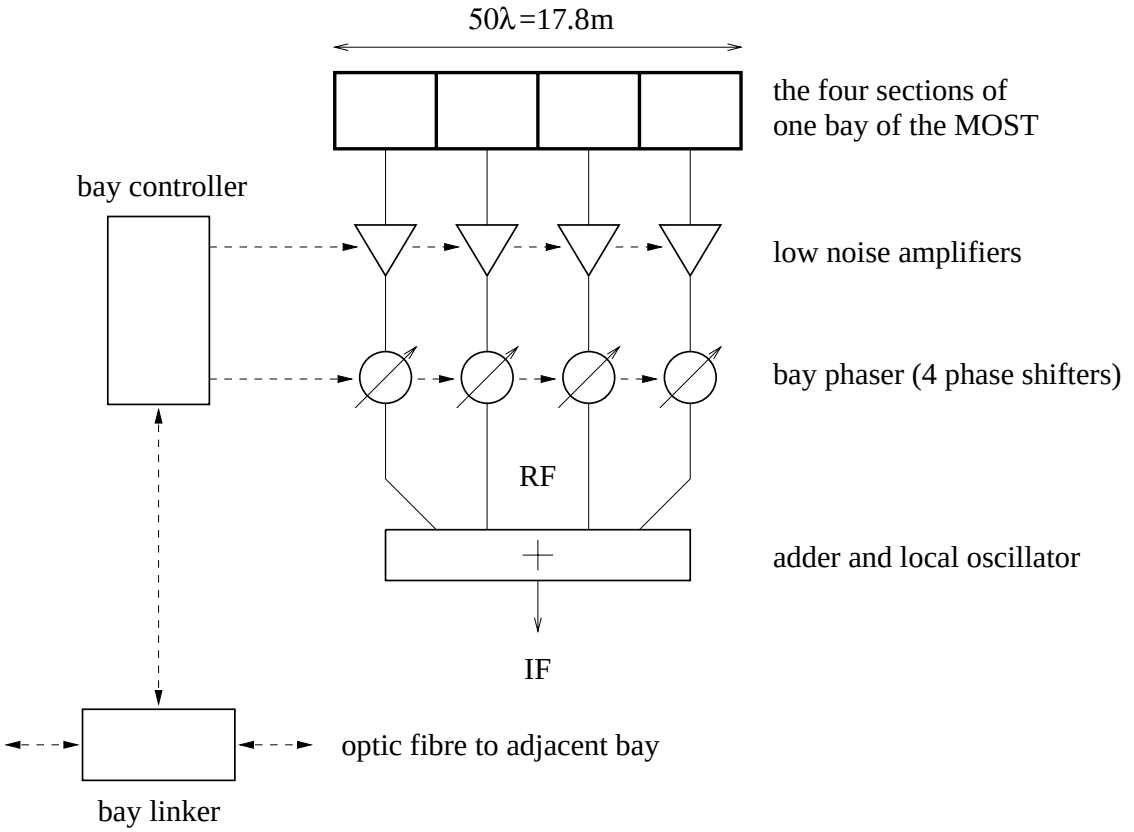

Figure 2.4 Hardware implementation of the Wide Field system. The low noise amplifiers, bay phaser, bay controller and bay linker form the new hardware required at each bay to implement the Wide Field upgrade. The radio-frequency (RF) and intermediate-frequency (IF) signal paths are shown with solid lines. Dashed lines indicate control signal paths. Omitted for clarity are gain compensation circuits in the bay phaser and ancillary control inputs and outputs on the bay controller.

switch are then averaged. Hence there are $64 \times 14 = 896$ measurements in each 28 s sample.

2.4 New radio-frequency hardware

The elements of the new system will now be discussed. Installation and testing is covered in chapter 3.

The radio-frequency components required at each bay to enable the wide field mode of operation are shown schematically in figure 2.4. The *line feed* comprises four 12.5λ sections each driving a low noise amplifier (LNA). The amplified 843 MHz signals from each LNA are combined via adjustable electronic phase shifters. There are

table 2.1. Its operation is compensated for in the data acquisition software.

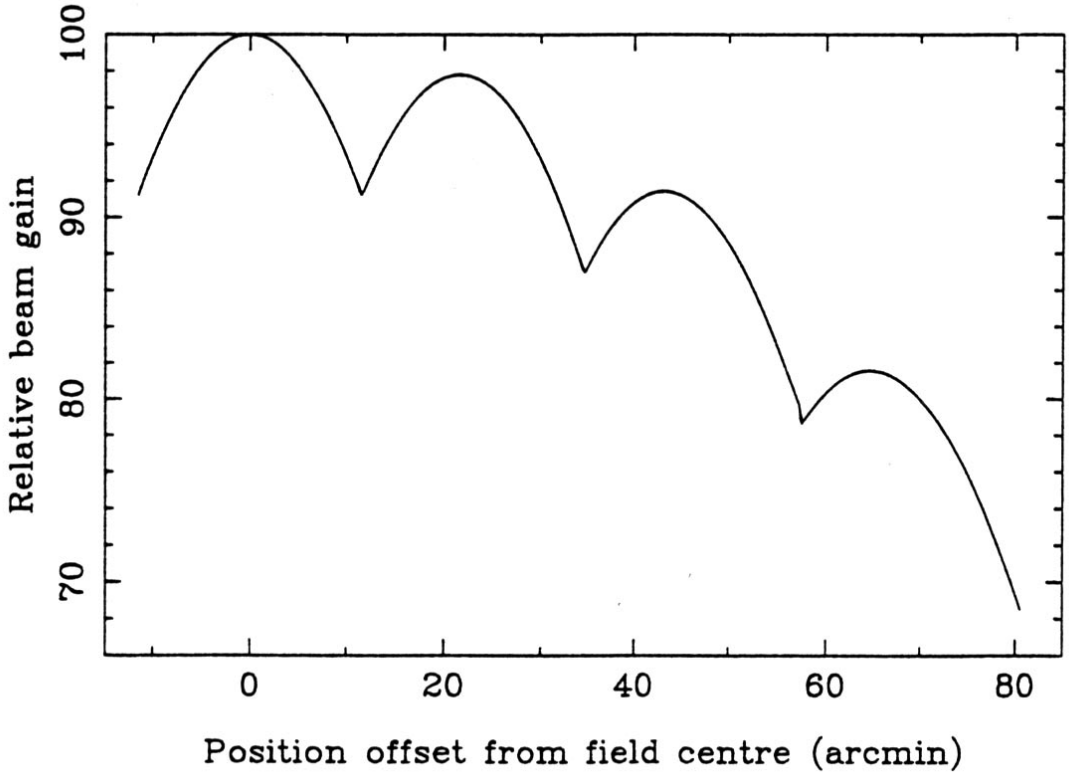

Figure 2.5 The theoretical bay beam response as a function of offset from the field centre for a 7–block Wide Field observation. Only the centre and three offset beams are shown here: the actual responses are symmetrical around the field centre. Reproduced from Large et al. (1994).

thus 352 LNAs and phase shifters installed on the entire telescope. A microprocessor-based control system (section 2.5) provides the voltages required to set the required inserted phases. In operation, phases of 0, $30n$, $60n$ and $90n$ are inserted into the four signal paths from the bay. To realise the stepped offset of the bay beams, n is taken cyclically through seven values $(-3, -2, -1, 0, 1, 2, 3)$, switching once per second. The corresponding offsets of the bay beams in meridian distance are $23'n \sec |MD|$. The phase gradient providing this offset is approximate: the four sections of the line feed are still individually phased by the rotating ring antennae to point at the field centre. However, the differences between the bay beams are minor. Figure 2.5 shows the theoretical bay beams.

The comb of fan beams formed in the central laboratory is simultaneously set to the same offset by phases switched into a second local oscillator. These offsets are all in meridian distance, and are relative to the field centre, which is being tracked continuously in meridian distance (by rotation of the ring antenna elements) and tilt (by movement of the antennae).

2.4.1 Low noise amplifiers

The replacement of the old GaAsFET preamplifiers with the new low noise amplifiers has additional advantages. First, the new LNAs have substantially improved performance, with an excess noise temperature of $\lesssim$20 K, compared with 60 K for the old preamplifiers. This performance enhancement compensates for the reduced observing time per unit area in Wide Field observations (a factor of $\sqrt{7/3}$ in signal-to-noise of a 7–block observation compared with a 3–block observations) inherent in the additional time-sharing which is part of making Wide Field measurements. Secondly, the new LNAs have a reduced temperature coefficient of gain and improved stability. Furthermore, each LNA has a noise diode installed for testing purposes. This may be activated remotely through the control system. Figure 2.6 (following page 20) shows a new LNA.

2.4.2 Bay phasers

The bay phaser located at each bay applies the 4 step phase pattern necessary for offsetting the primary beam of the bay each second, to follow the comb of fan beams as they are switched to point in turn to each of the up to seven positions in a Wide Field observation. The bay phaser comprises three signal-path controls for each quarter bay: continuously variable phase from 0° to 180°, an additional fixed step of a further 180°, and a gain stage of 0–5 dB. Each function is controlled directly by the bay controller (part of the WF distributed control system described in the following section), which interprets observing commands to set the desired phase and to compensate appropriately for the phase-dependent gain variation. Each bay phaser is matched with an erasable programmable read-only memory (EPROM) chip on the bay controller, which stores 'lookup tables' for translation between desired phases and gains, and the voltages required to achieve these settings. Figure 2.7 shows half of a single bay phaser, providing a view of two of the four quarter-bay signal paths.

2.4.3 Further improvements

The new low noise amplifiers and bay phasers, together with associated cabling, complete the new radio-frequency hardware essential for the operation of the MOST in Wide Field mode. However, work continues on other improvements to the signal path aimed at further enhancing the performance of the MOST for the Wide Field sky surveys.

Intermediate-frequency (IF) system[6] The IF system in place until 1997 uses parts of the original system installed in the 1960s for the Molonglo Cross. The upgrade to the MOST preserved the use of 11 MHz for the intermediate frequency,

[6]In this thesis I include the following components when I refer to the new IF system: hybrid combiner, frequency doubler, mixer, image-reject (interdigital) filter, IF amplifier.

thus allowing the same IF amplifiers to be used. However, superior reliability and performance can be obtained from modern components. A replacement system is underway: details may be found in section 3.1.3.

Local oscillator (LO) distribution The local oscillator system in present use is also original, operating at 416 MHz, with a copper pipe inner and a galvanised iron troughline outer. It is exposed to the weather along the telescope. Phase stability is poor during bad weather, with high humidity, and during periods of extreme temperature variation. Work is in progress to improve the system (section 3.1.4).

2.5 A distributed control system

With the above scheme for upgrading the radio-frequency system in mind, a system for its control was required. In this section I will briefly outline the eventual choice of system. A fuller discussion is given by North (1994). I will describe the system as actually implemented, particularly developments subsequent to North's work which ended with the presentation of the first software and hardware prototypes for the the master and bay controllers. These developments took place over the period March 1994 to February 1995, involving a team consisting of M. I. Large, W. J. I. Skillen and the author, generally meeting weekly.

The requirements of the system were well-defined, based on the need to control the low noise amplifiers and the bay phasers. The phase shifters installed in 1989 (Amy & Large 1990) to reduce the grating response of the telescope for observations of $70'$ fields used a simple single-wire tri-state system to introduce the 60° phases which offset the bay beam to each side of the field centre. A minimum Wide Field upgrade might have included a three-wire system with seven states to set the bay phasers to offset the bay beam to point at each of seven positions required for a Wide Field observation. However, this system would have precluded sophisticated individual control of the bay phasers, which are capable of applying arbitrary phases to each signal path at each bay. It would also have necessitated laborious individual adjustments to calibrate the phases and gains required for *each* pointing position at *each* bay.

Instead, a distributed control system was chosen which can devolve much of the work to each bay (North 1994, p9). This system implements the complete flexibility inherent in the bay phaser design with a microprocessor-driven *bay controller*, while requiring only minimum instruction from the observing computers during an observation. A Phillips 80C552 microprocessor was chosen as the basis of the system (North 1994, p16). The bay controller provides the additional functionality of sensor inputs and spare control outputs at each bay. A *master controller* in the control room oversees the operation of the bay controllers.

2.5.1 The master controller

The master controller is the 'central intelligence' of the Wide Field system, and is implemented on a standard PC, running MS-DOS. Custom-designed software, `MC.EXE`, runs on the master controller, interpreting commands received from the observing computer (an HP-A700) or directly from the keyboard, and issuing instructions to the bay controllers. Commands may be directed to individual bay controllers: for example, one may be asked to turn off power to the low noise amplifiers for diagnostic purposes. Alternatively, commands may be broadcast to all bay controllers: for example, stepping commands during observations.

The master controller is connected to the communications system by a standard RS-232 link. Flow control is implemented within the master and bay controllers in software, so Xon/Xoff or hardware flow control is not required.

Connection to the A700 observing computer is made via a serial port. At present a unidirectional link is in place, allowing the A700 to issue instructions to the master controller. A parallel port is used for a connection to the station clock, which strobes the master controller once per second. During normal observations, the master controller polls the clock strobe to determine when stepping commands (received from the A700 during the previous second) should be broadcast to the bay controllers.

Modifications to the master controller software since the publication of North (1994) include:

- a command to send a bay controller reset signal, interpreted by the bay linkers;
- a command to send a communications system test pulse;
- new short stepping commands, e.g. 's1';
- additional bay controller status polling each second;
- support for the A700 and station clock interfaces;
- addition of a power-fail recovery mode;
- addition of a reset indication LED;
- discontinuation of use of the '9th' (parity) bit as a control bit in transmissions from the bay controllers to the master controller;[7]
- a separate program to determine astronomically the appropriate phase and gain origin settings for each of the four signal paths at each bay ('phasing-up');
- the correction of a number of minor bugs.

[7] This step was necessary as the master controller hardware occasionally failed to check the parity status of the message. In normal PC usage, such a failure would simply reduce the detection of errors. However, in the Phillips 80C552 protocol the parity bit is used to convey the bay controller address.

2.5.2 Bay controllers

The bay controllers are slaves of the master controller, interpreting commands from the master controller and controlling the bay phasers and through them the low noise amplifiers. They have a capacity for expansion, with spare digital outputs to control future hardware and spare digital and analogue inputs. The new IF system will make use of one of these by providing a detected IF power output to the bay controller for diagnostic purposes.

The most important task of a bay controller is to direct its bay phaser to apply the appropriate phases and gains to the signal paths. It has several analogue and digital outputs dedicated to this purpose. Voltage-to-phase and voltage-to-gain conversions for the bay phaser (measured in the laboratory before installation) are stored on the bay controller EPROM in a lookup table within the bay controller software. Astronomical phase and gain calibrations are downloaded to the bay controller at the start of each observing session. These compensate for the length of the low noise amplifier/bay phaser RF cable and for the individuality of the low noise amplifiers. Sequences specifying the appropriate phase for each signal path to achieve each of the desired bay beam offsets are also downloaded before observations. Commands from the master controller to move the bay beam may then be broadcast globally. The bay controller translates these to the appropriate phases and gains, and thence to the required voltages.

Several changes have been made to the bay controller since the work of North (1994). They include:

- modifications to the hardware to reduce power consumption;
- alterations to the power-up hardware reset sub-circuit;
- software support for changes to the MC software mentioned above;
- provision of an analogue-to-digital converter reference voltage;
- a new ability to interrupt the LNA power supply;
- the elimination of several minor software errors.

A populated bay controller circuit board is shown in figure 2.8.

2.5.3 The communications system

The first prototypes of the master and bay controllers, and of their software, were developed independently of and earlier than the communications transport connecting them (North 1994, p13). The Wide Field communications system was developed in parallel with the second prototype developments to the controllers which were presented above.

The communications system was specified to connect each bay controller to the master controller with a reliable, cost effective system, using optic fibre for lightning protection and interference minimisation. The chosen configuration consists of interface panels in the control room and in the local oscillator hut (at the central

point between the two arms of the telescope), connected with an RS422 link. The control room interface panel is connected directly to the separately-located master controller by an RS232 link. The local oscillator hut interface panel houses the start of the optic fibre links to the east and west arms. A diagram of the communications system may be found in figure A.1.

2.5.4 Bay linkers

At each bay of the telescope, the optic fibre is terminated by a bay linker, the basic element of the communications system. This device (figure 2.9) detects the light signal and passes it to the local bay controller. It also re-transmits it by optic fibre to the next bay linker along the arm. This is done *asynchronously*, i.e. the level changes in the signal are passed on directly: no pulse shaping or resynchronisation is done. This keeps the linkers simple and the communications system fast. The linkers return bay controller responses to the master controller along another optic fibre. Additional features of the linker include a circuit to decode a long (reset) pulse on the communications link and then apply a signal directly to the reset line of the bay controller, and a facility to 'lock out' malfunctioning bay controllers from the communications system.

This concludes my description of the principle behind the Wide Field system and of its components. In the following chapter I continue with the installation and commissioning of the system. A full description of the communications system and the bay linkers, including design considerations and performance evaluation, may be found in appendix A (Molonglo Technical Report 97.009).

Figure 2.6 (following page, top) Both sides of a new low noise amplifier (LNA). The RF section is above and the DC section is below. The RF cable to the bay phaser connects at the left and the waveguide connects at the right through a choke coupler. Power to the LNA is supplied from the bay phaser via the inner of the RF coaxial cable.

Figure 2.7 (following page, bottom) One half of a bay phaser (BP). The lower right quadrant performs RF phase shifting for input 1. The lower left quadrant switches in or out the extra 180° path. Gain control and signal combination are at the far left. Connections to the LNAs and the bay controller are made on the reverse.

Figure 2.8 (second page, top) A bay controller. The removable EPROM is the labelled integrated circuit. The connectors along the lower side of the printed circuit board are for (left to right) the power supply, bay linker and bay phaser connections.

Figure 2.9 (second page, bottom) A bay linker. The port for connection to the bay controller is on the upper edge, alongside the four activity indicating LEDs. The white transmitters and black detectors make connection with the optic fibre.

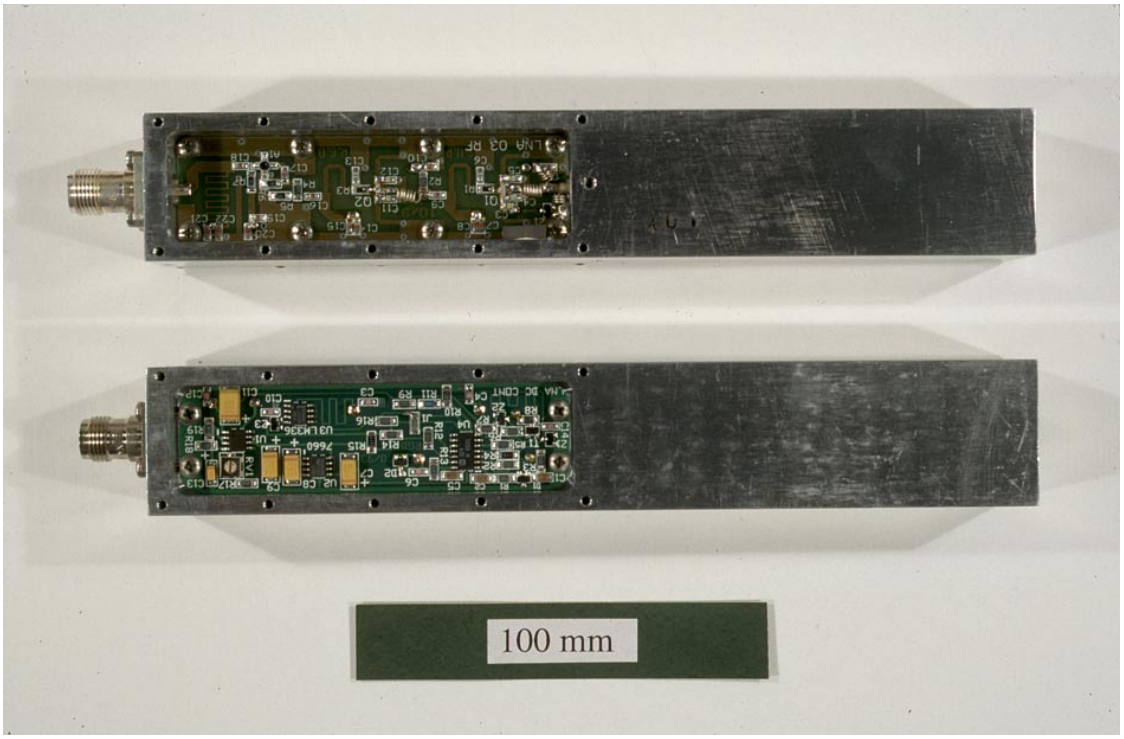
100 mm

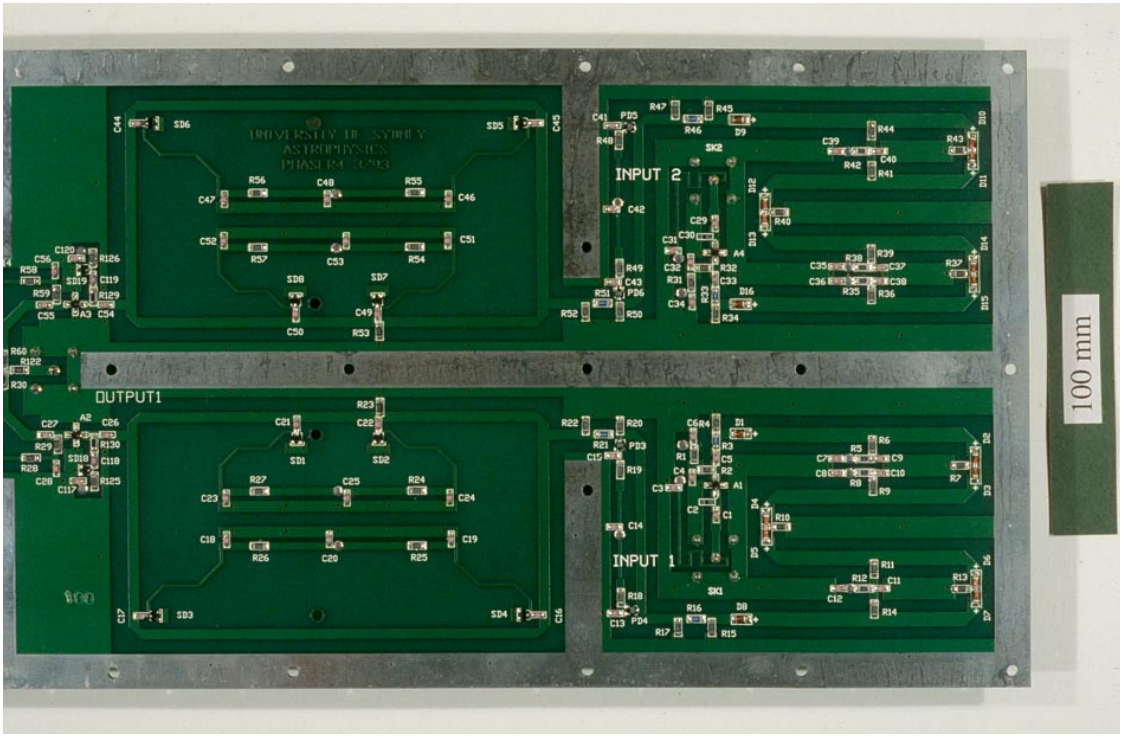
INPUT 2
INPUT 1
OUTPUT1
100 mm

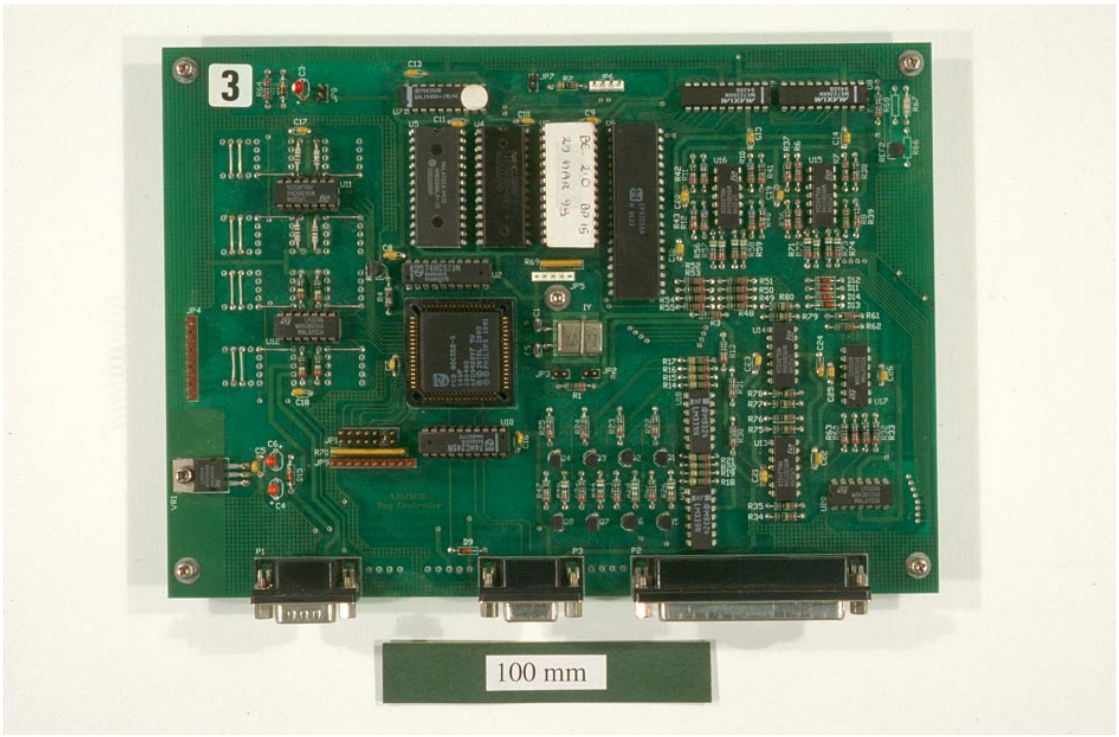
3
100 mm

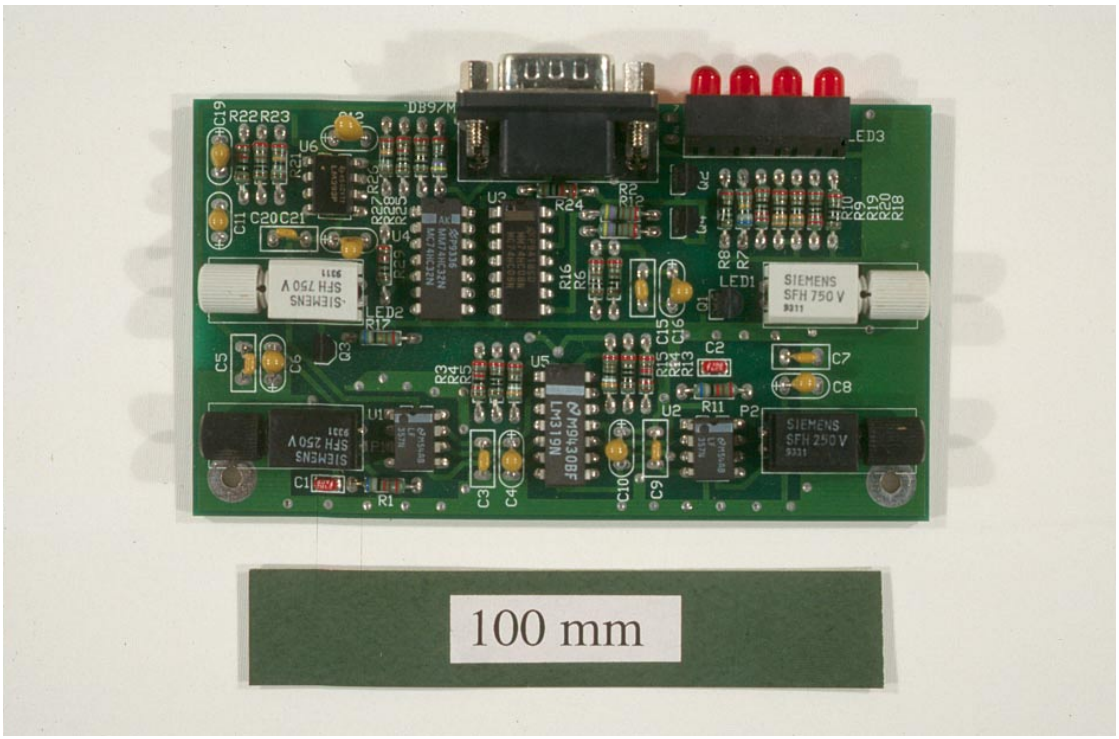
100 mm

Chapter 3

Upgrading the MOST

The previous chapter described the principle of the MOST Wide Field system and presented the hardware modifications required to implement the new observing mode. In this chapter I discuss the implementation of the system on the telescope.

I joined the Wide Field project at the time when the decision to proceed with the implementation had just been made. In addition to participating in the control system development and taking overall responsibility for the communications system, my role was to take on the day-to-day coordinating role in the biggest aspect of the project, manufacture and installation of the new hardware, which I describe in section 3.1. This role involved general task scheduling and resource allocation, as well as an overall responsibility to keep the group aware of progress and to identify possible problems and bottlenecks. Later sections discuss the engineering commissioning of the new system and the initial astronomical tests, for which I was primarily responsible.

3.1 Manufacture and installation of the new hardware

The complete upgrade of the MOST consists of many interrelated tasks, but it is convenient to think of them grouped into four stages, involving the radio-frequency, control, intermediate-frequency and local oscillator systems. The first two stages are fundamental to the Wide Field observing mode—the latter two stages improve the telescope's performance further.

3.1.1 Stage one: New radio-frequency hardware

A priority in stage one was to continue observing as much as possible during the lengthy installation of the radio-frequency hardware. The devices installed at each of the 88 bays of the telescope as part of this stage were the four low noise amplifiers (LNAs), a bay phaser (BP) and *temporary controller* (discussed below), and ancillary cabling and conduit. Manufacture of the key components began in January 1994,

and installation was complete by March 1995, with a concentration of effort in the period of good weather during the summer of 1994–95, when observations were made only at weekends.

Observations were able to continue normally during much of stage one of the upgrade, using a combination of new and old hardware. The new hardware was installed one bay at a time, in parallel with a feed overhaul for each bay. The new components were tested and commissioned at a bay level, as part of the installation process. To make this possible, the new RF hardware was designed to emulate the existing RF hardware with comparable signal path delays.

Proper management of the group's effort during this stage was important, taking into account the complex dependencies involved in the manufacture, testing and installation of the hardware, in order to make sure that labour resources were used appropriately. Progress charts were employed to provide an overview of the current state of the upgrade. An example is shown in figure 3.1. Charts like this helped the group direct effort to tasks leading towards the main outdoors (weather dependent) tasks: the LNA installation and feed overhaul. These tasks would have been virtually impossible in winter. Missing the summer would have delayed the project by up to a year, since tracking the sun is required for equalising the phase in the four RF signal paths at each bay (called 'phasing-up'). For 4.5 months during the winter the sun is not observable by the MOST.

Temporary controllers The temporary controllers were devices which allowed normal observations to continue during the installation phase of stages one and two of the upgrade. A temporary controller at each bay provided the power supply for the bay phaser, and hence for the four low noise amplifiers. It also held the control inputs to each bay phaser at appropriate values for continuing observations. The new system initially had to simulate the old, hence the bay phasers were set so as to provide no additional phase gradient. Continuing observations of 3–block (70′) fields during the upgrade used the old phase shifting system.[1] The temporary controllers have now been replaced by the centrally-controlled bay controllers as part of stage two.

3.1.2 Stage two: Computer controlled phase shifting

Stage two of the Wide Field upgrade involved the manufacture and installation of the computer control system for the radio-frequency hardware which had been installed as part of stage one. The main components of the computer control system are the master controller, the bay controllers and the communications system (shown in figure A.1). The system allows remote control of the phase gradient applied at each

[1]For compatibility between the old and new systems during stages one and two of the upgrade, the bay phaser provides two outputs to the IF system: the summed inputs from the two east-most and the two west-most low noise amplifiers. The relative phase of these two independent signals is controlled as part of the old phase-shifting system; this facility will no longer be available when the the new IF system (see stage three below) is installed.

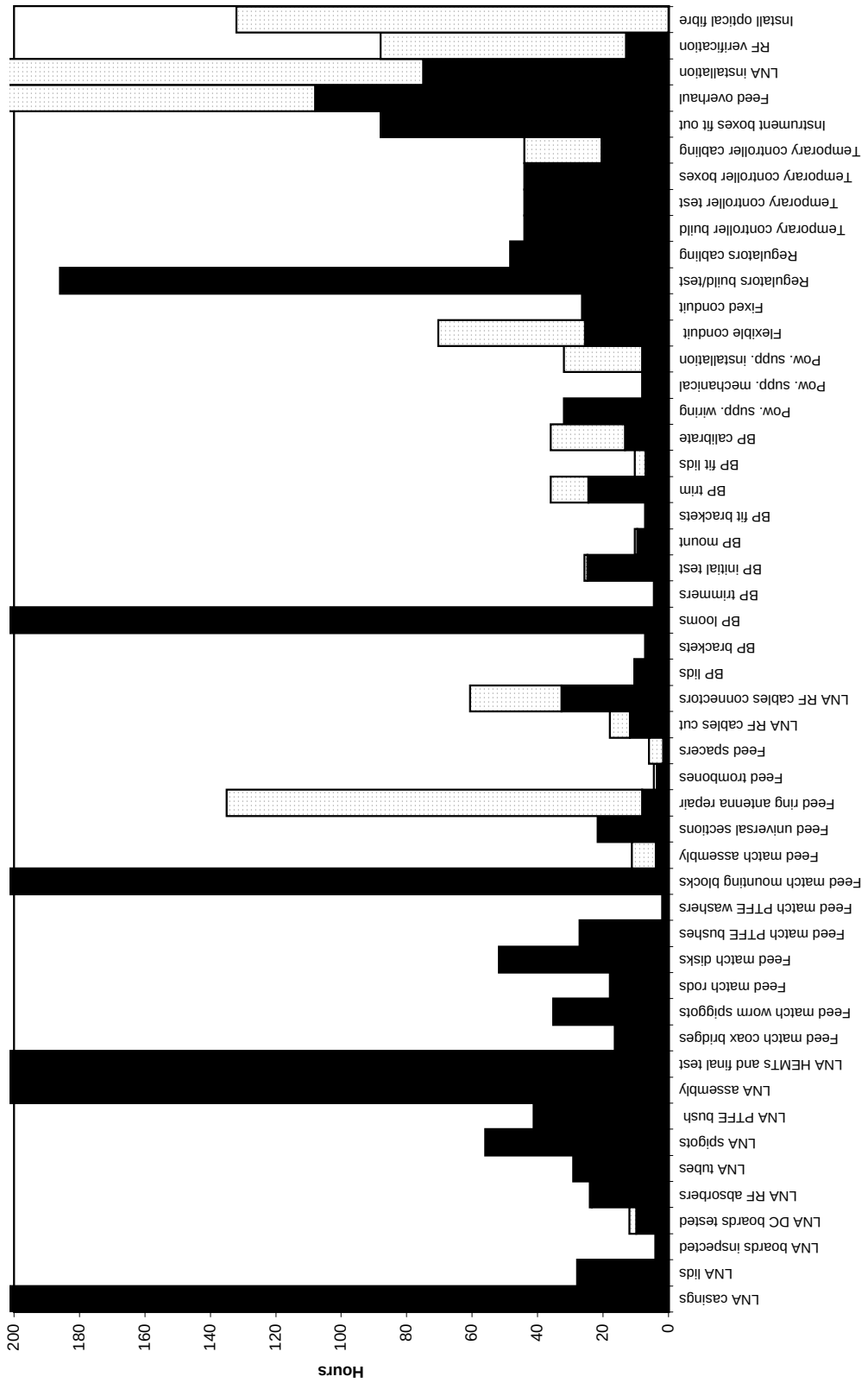

Figure 3.1 A sample Wide Field progress chart, for 1995 October 10—just before completion of stage 1 of the upgrade—showing various tasks requiring completion. Some tasks required a total of more than 200 hours work, and are off-scale on this chart. Charts such as these, updated fortnightly, assisted planning and allowed identification of potential problems. The portion of each task completed is shown black; the uncompleted part is shaded. The tasks shown here are for stage 1 of the upgrade, except installation of the optic fibre, which was a task for stage 2.

bay to change the pointing of the bay's primary beam. It also controls the noise diodes on the low noise amplifiers and provides a facility for driving and monitoring other local devices. This facility is being used as part of stage three of the upgrade to monitor received IF power at each bay, allowing computer controlled phasing-up of each bay remotely during observations of the sun. Manufacture of the components of this system was spread over the second half of 1996. The master controller is an off-the-shelf 486 personal computer.

Installation of the control system involved the laying of optic fibre and the bay linkers within a new galvanised steel ducting, which replaced a fibrous cement ducting already carrying cabling along the telescope. A transparent window in the ducting allows observation of the activity monitoring LEDs on each bay linker. The bay controllers were installed in new instrument boxes. Cabling connecting to the bay linkers made use of existing conduit. The interface panels for the communications system had been installed in the control room and the local oscillator hut during 1995 to allow tests using a few prototype bay controllers and bay linkers.

Unlike stage one, the activation of the hardware installed as part of this stage had to take place all at once, with the replacement of the temporary controllers by the bay controllers. This meant that the installation, which took place over the summer 1995–1996, was done 'cold' with comprehensive testing taking place only from the changeover time. The communications system was partially tested during the installation by the exchange of commands between the master controller and bay controllers at bays east-1 and east-2. Duplicate power supplies had been installed to supply both temporary controllers and bay controllers at these locations. The commissioning of the control system is described in section 3.2.

3.1.3 Stage three: New intermediate-frequency (IF) system

Stage three is underway at the time of writing. The replacement IF system is not essential to the operation of the Wide Field system. However, it will improve the performance and reliability of the system significantly.

The existing IF system has been in continuous use since it was installed for the Molonglo Cross in the early 1960s. It uses outdated germanium technology that is becoming increasingly difficult to maintain. It has insufficient bandwidth definition for the modern, increasingly hostile, spectral environment; and it does not well tolerate level variation in the local oscillator system. A replacement IF system is highly desirable for these reasons alone. However, many additional benefits will flow from the replacement system in production at present, since the new hardware will:

- improve gain stability with temperature by tolerating signal level variation in the local oscillator system;
- be very stable with temperature change;
- allow additional individual temperature compensation of each LNA;

- reduce interference by providing improved bandwidth definition after the pre-amplifiers but before the subsequent non-linear stages, and better rejection of the image;
- provide field IF power detectors, which may be monitored by the local bay controllers for quick performance checks;
- allow remote phasing-up of each bay simultaneously via the bay controller;
- improve the dynamic range of the signal path.

Implementation The new IF system comprises an inter-digital filter, mixers and IF amplifiers at each bay, and compensation amplifiers for cable losses in the central phasing laboratory. The existing coaxial cable will be retained. Following development work by R. G. Davison throughout 1996, production and testing is underway during 1997, with complete installation expected by the end of the year. Unlike the replacement of the RF system (in stage one) most of the IF system changeover must take place all at once, since the signal delays in the new IF system will be quite different from those in the present system. This will take about two weeks. The new compensation amplifiers have already been installed.

3.1.4 Stage four: Local oscillator (LO) distribution system

Like parts of the IF system, the LO distribution system dates from the original Molonglo Cross. One factor in the choice of the present operating frequency (843 MHz) of the MOST, was the ability to reuse the LO distribution system (operating previously at 397 MHz) at the current LO frequency of 416 MHz. The main distribution along the length of the telescope is in an open galvanised iron trough, with a central copper conductor.

Variation of the phase and gain of the LO system is considerable with changing humidity and temperature, despite existing feedback phase control systems. Infestations of spiders also cause a detrimental effect when wet. As a result, the quality of observations made in some conditions can be poor. After the replacement of the IF system, the LO distribution system will most likely be the dominant performance-limiting system of the telescope.

Initial investigations of ways to improve the LO distribution system focussed on a replacement with optic fibre (Walker 1996). The humidity dependence would be removed and gain variations will already be tolerated by the new IF system, but experiments have shown that the temperature coefficient of phase is similar to that of copper. Fibres with a low temperature coefficient (such as those used for the Owens Valley Interferometer) are expensive. Short-term attempts are focusing on sealing and perhaps air-conditioning and gently pressurising the existing coaxial trough-line. Discussions with the Optical Fibre Technology Centre on the design of fibre systems are continuing. More active consideration of this stage of the upgrade will begin once the IF replacement (stage three) is complete.

3.2 Commissioning the Wide Field system

As outlined above, the RF hardware installed at each bay as part of stage one had been commissioned during installation to allow continuing observations during the changeover period. Tests by J. G. Robertson (personal communication, 1996) confirmed that the noise figure of the telescope was improving with progress of the installation. The main commissioning required was that of getting the stage two hardware to control phases at the bays and then putting the hardware (via the master controller) under the control of the existing observing computers.

3.2.1 Linking the master controller to the bays

The first step in commissioning the Wide Field control system, before putting it under the control of the observing computers, was to ensure that it was performing satisfactorily on its own. The optic fibre and bay linkers had been pre-installed, leaving the replacement of the temporary controllers with the bay controllers as the final step. With the connection of each bay controller it was possible to test optic fibre communications incrementally by interrogating the bay controllers one at a time, working outwards from the centre of the MOST, with simple commands from the master controller. The bay linkers derived their power from the bay controllers.

Pulse shaping When changeover was complete, it was possible to measure the change in pulse shape of the control signal along an entire arm of the telescope. The minimisation of this change was an important design feature (sections 2.5.4 and A.6). To make this measurement, a short fibre was connected from the outwards transmitting LED to the inwards receiving photodiode on the last bay linker (east-44) on the east arm. These devices are normally unused on the last bay linker as they are intended to connect to the next bay linker in the chain. This gave a chain of 88 transmitter/receiver pairs from the local oscillator hut out along the east arm and back again. A test pulse was sent from the master controller. It was measured twice on the local oscillator hut linker: once before being sent out along the arm and again as received back after the 88 stages. The total delay of a rising edge was 32 μs, and of a falling edge 35 μs. The differential delay, 3 μs, is the change in the width of the standard 100 μs pulse—well within the maximum tolerable differential delay for detection of 46 μs (for half this distance) set by the 80C552 microprocessor on the bay controllers. The actual differential delay will be somewhat temperature dependent, but certainly will never approach the maximum tolerable value. See appendix A for additional procedures, circuit diagrams, and details of the laboratory delay measurements which these field measurements confirm.

Phasing delay During observations data acquisition is suppressed for the first 60 ms of each solar second, to allow the electronics to stabilise after a pointing change. The change in phase gradient applied at each bay by the new Wide Field system has to take place close to the beginning of this dead time. A key measurement

was the delay between the start in transmission of the master controller command setting phases and the actual change in voltages controlling the phases on the bay phaser. This delay is dominated by the length of time it takes to send and receive the command, so a very short master controller command '`s1`' was used for this task. The measured delay was 22 ms, with a jitter of about 1 ms. This significant delay was one factor in the adoption (described in the next section) of a procedure to supply the master controller with a predicted stepping position which it then issues as a stepping command in advance of the next solar second, thus ensuring that the beams stepped at the start of the 60 ms dead time.

3.2.2 Interfacing the master controller

With the new hardware for the Wide Field upgrade all apparently working correctly, the next task was to arrange for it to be controlled by the observing computers which normally run a MOST observation.

The observing computers Two computers control observing with the MOST: the telescope control computer (TCC) and the 'A700'. The TCC is a purpose-built computer that handles all the real-time aspects of observing such as coordinate transformations, movement of the telescope, and the calculation and application of phase and delays. It is physically rather fragile and uses assembler language programs which are difficult to modify. It was highly desirable to leave its operation unchanged after the Wide Field upgrade. The Hewlett Packard A700 minicomputer (the 'A700') controls the observing at a higher level, demanding sky positions from the TCC and looking after data acquisition and logging.

Interfacing with the A700 With the aim of avoiding any interface to the TCC, it was decided to drive the master controller from the A700. A further aim was to have the master controller a closely-supervised slave of the A700, so that there could be no conflict between the machines. For reasons of simplicity, the communication was made unidirectional: the A700 issues instructions to the master controller telling it which standard switching pattern to load to the bay controllers, and sends stepping commands each second thereafter. An operator may take charge of the master controller at any time and issue alternative instructions. When some experience operating the Wide Field system has been gained, modifications to the master controller/A700 interface will be contemplated. An obvious one would be to provide a two-way communications path and have the master controller make the A700 aware of the results of routine diagnostics of the communications system and (through the bay controllers) measurements of IF power, local temperature, etc.[2]

[2] At present the master controller cycles through all the bays, one per step (i.e. one per second), checking that the previous message was received. Errors are logged on the master controller, but not reported to the A700. Direct action, like resetting the bay controllers or recording the errors directly in observing logs could be implemented by a two-way link.

The disadvantage of driving the master controller directly with the A700 came from timing. In the initial implementation, A700 stepping commands to the master controller were sent a variable 20–80 ms after the solar second, with data acquisition from the previous second taking priority in the A700. This meant that the bays would step as much as 100 ms late, corrupting the data. The solution adopted was to have the A700 predict the stepping position one second in advance and send it to the master controller each second after completing its other tasks. The master controller was then strobed by a delayed pulse derived from the station clock to send the command out the the bay controllers. The pulse delay was adjusted to make the bay controllers change the phase gradient at each bay 6 ms after the solar second, allowing 54 ms settling time before the beginning of data acquisition.

3.3 Astronomical testing

The testing of a complex system like the MOST after major modifications necessarily proceeds incrementally, in order to demonstrate in turn that each component is working, or to isolate those sub-systems which are giving trouble.

The astronomical tests discussed below were essentially acceptance tests, with each test leading to the next.

3.3.1 A sweep observation on the sun

Sweep observations with the MOST are made in a similar fashion to the observations made with the Molonglo Cross: the telescope is held still and the sky is observed as it sweeps past (hence the term 'sweep'). An observation of the sun was made in this fashion using only one bay of the telescope. This observation (made in collaboration with M. I. Large) was the first astronomical test of the fundamental concept of the Wide Field system, using the new computer controlled electronic phase shifting hardware to offset the primary beam of the bay from the position set by the rotating ring antenna elements. Seven beam positions were chosen (as in figure 2.5).

The observation The observation was made on 1994 November 3, measuring the total power detected from bay east-4, which was under the control of a prototype bay controller, two prototype bay linkers and production-version low noise amplifiers and bay phaser. A prototype master controller connected to the bay linker provided the step signals, manually activated once every two seconds. The 7-step pattern set phases equivalent to subtracting signal path lengths of $0°, 30°n, 60°n, 90°n$, from the four quarter bay signal paths (1–4, east to west respectively), with n an integer ranging from -3 to 3 providing the seven positions used.[3]

[3]By 'subtracting' signal path length I ensure that the values specified here are in the same sense as those used in the phase stepping file (`.stp`) on the master controller.

The telescope was driven to a point with the same declination as the sun but 7.5 minutes in advance in right ascension, and held stationary for the duration of the observation. A square-law detector was used to measure the total power received by the bay giving a signal which drove a chart recorder. The chart record is shown in figure 3.2.

Interpretation The observation is a quantitative test of the bay phasing system for which the effective radio size and position of the sun has not been taken into account. Furthermore, the tilt motors of the telescope were also stopped for the observation, causing the sun not to pass exactly through the central bay primary beam (beam 4 in the chart, corresponding to $n = 0$ above). However, the observation provided three elementary tests of the system:

1. It tested the overall operation of the Wide Field hardware and software from the master controller through to the low noise amplifiers, by demonstrating conclusively that the bay's primary beam moves on the sky as expected.
2. It provided a check on the spacing between the bay primary beams set up by the new phase shifters on the sky. The time difference between the sun being central in beam 6 to being central in beam 5 was 97 ± 6 s. Calculating the sun's motion in the meridian distance direction during the observation, this implies a distance between the beam positions of $24\farcm5 \pm 1\farcm5$, in satisfactory agreement with the intended separation of $23' \sec |MD| = 24\farcm3$ on the sky.[4]
3. It checked the *sense* of the switching pattern, which was confirmed to be 1 (west) to 7 (east). It was useful to have this confirmed at an early stage before adding the complication of switching the array beams to follow the bay primary beams during a full synthesis.

3.3.2 Preliminary tests on 3–block fields

An early test of the hardware and data acquisition processes was made during August 1996, while observing 3–block (i.e. $70'$) fields. This was the most commonly observed field size before the Wide Field upgrade. The purpose of the test was to check for any gross errors in synthesised images introduced by the new phase shifting and control hardware and/or the new data acquisition computer software (`WFSYN`), by simulating the pre-1989 mode of observing (with no primary beam offsetting) and the 1989–1996 mode of phase shifting to offset the bay primary beams (section 2.3; Amy & Large 1990) with the new electronic phase shifting of the Wide Field system.

Observations Two versions of the data acquisition software were used for the tests, `SYN` and `WFSYN`. `SYN` is the program which was used for all MOST 12 hour

[4]These beam positions were chosen for this measurement as their peaks are approximately equal: the attenuation due to the envelope of the quarter bay's primary beam is partially offset by the sun not passing centrally through the set of beam positions.

Figure 3.2 (following page) A copy of the chart record made during the sweep observation of the sun. The points corresponding to each of the 7 bay pointing positions have been joined to make the envelope of the bay's primary beam (convolved with the sun) at each of the seven bay pointing positions. Note the overall envelope of the quarter-bay response. The horizontal scale is 4 divisions per minute.

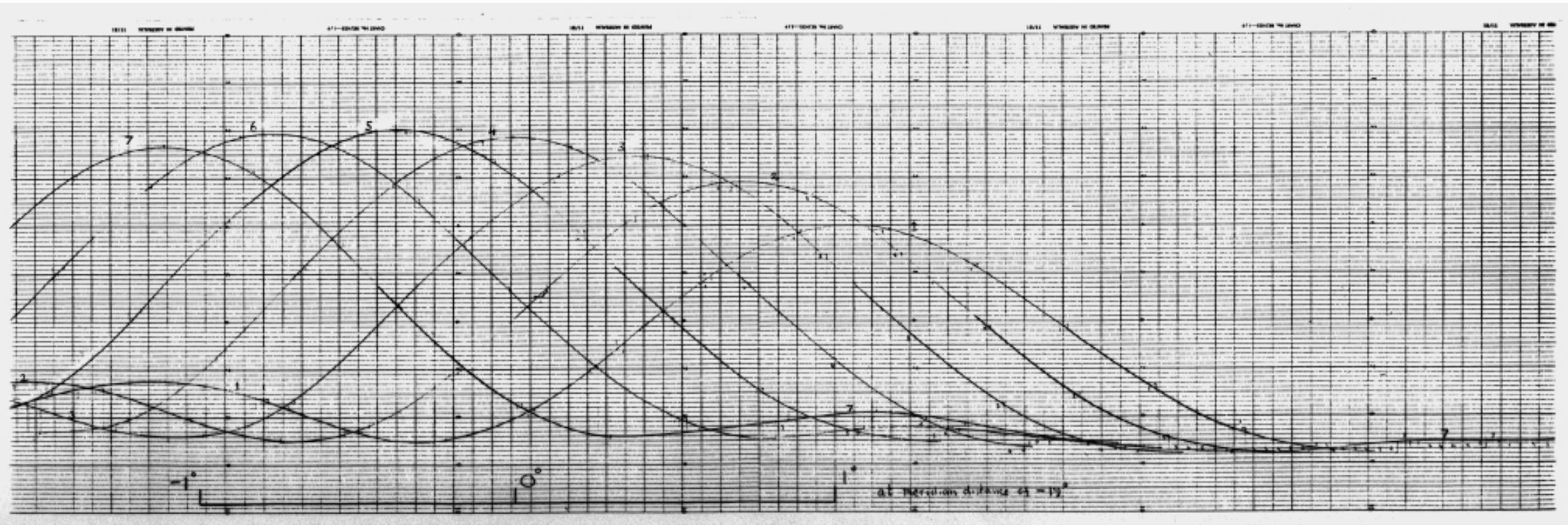
7
6
5
4
3
2
1
-1°
0°
1°
at meridian distance q = 12°

synthesis observations in the period 1987–1995 with meridian distance bay primary beam calculations made (by J. G. Robertson) for the installation of the 60° phase shifters in 1989. `WFSYN` is a modification of `SYN` by Lawrence Cram designed specifically for the Wide Field system. Observations using `SYN` were made with the 60° phase shifters installed in 1989 (Amy & Large 1990). Observations using `WFSYN` were made with the new phase shifters (i.e. the Bay Phasers) (a) 'off' (i.e. with no bay primary beam movement), (b) simulating the 60° pattern of the old phase shifters and (c) making the new 30° step pattern intended for the Wide Field system. The MOST calibrator B2049−368 (2.66 Jy: Campbell-Wilson & Hunstead 1994) was in the field for each of the tests, as was a nearby source at about 10% of the calibrator's flux density ($20^{\rm h}49^{\rm m}17^{\rm s}$ $-36°26'04''$, B1950). Further details of the observations, including the applied SCAN-derived calibrations, may be found in table B.1.

Measurements The observations were made in 1996 August, during the lengthy maintenance and upgrade period which continued for much of 1996, and the pointing and synthesised beamshape were not fully optimised for observing. Measurements from these observations were used to seek position or flux density errors introduced by the beamshape changes made with the new phase shifting system, or gross problems with the data acquisition software. Errors in the calibration of the telescope generally during the maintenance and upgrade period have not been considered.

Each observation was imaged using David Crawford's program `mstimg` to produce a dirty map. In the imaging process, the meridian distance (MD) gain correction[5] applied to the data at acquisition time (Burgess 1989) was removed. The meridian distance gain correction is a measurement of how the forward gain of the fan-beam response of the telescope varies with distance from the meridian. It was replaced with the same correction applied to each fan beam according to its actual MD, rather than the MD of the field centre. The tilt primary beam corrections derived by Crawford (1996) were applied to the data. During the synthesis, the usual SCAN calibrations were applied. The two sources described above were fitted with the synthesised beam produced by `mstimg` using the fitting program `mstflx`. Table 3.1 shows the results.

Interpretation The position scatter of the measured sources is within a few arcseconds. This is a larger scatter than might normally be expected from MOST observations (Hunstead 1991). However, it does imply that there were no obvious errors in the timing of the new data acquisition program, `WFSYN`, which has had its timing relationship to the telescope control computer (TCC) extensively modified, and which now controls a new time-critical system (i.e. the new bay phase switching system) via the master controller. If present, such timing errors were expected to show up as errors of order 1 s in the right ascension of sources measured to the north or south of the field centre. These position errors are probably due to poor observ-

[5]Note that this is distinct from (a) the correction for the meridian distance primary beam (figure 2.5) and (b) the correction applied to compensate for differing IF signal-path gains.

MOST archive name	Source	Acquisition software	Phase switchers	ΔRA ($''$)	$\Delta\delta$ ($''$)	$\frac{S}{S_{\rm ref}}$	$\frac{S_A}{S_B}$
D20493619	A	`SYN`	old	–	–	–	10.8
	B			–	–	–	
D20493616	A	`SYN`	old	−3.0	−0.3	1.12	11.7
	B			−2.7	0.4	1.02	
D20493617	A	`WFSYN`	none	−0.6	−1.1	0.77	8.7
	B			1.2	−0.1	0.94	
D20493618	A	`WFSYN`	new	−4.7	1.4	0.94	10.6
	B		(simul. old)	−2.9	1.5	0.96	
D20493620	A	`WFSYN`	new	−2.4	0.0	1.08	11.1
	B		(normal)	−0.8	0.6	1.05	

Table 3.1 Tests of the phase shifting system and data acquisition software on 3–block fields. The observation D20493616 was made with the calibrator (A: B2049−368) centred; the others were made with the field centre $50'$ to the south of the calibrator. Source B is the weaker second source in the field (see text). The table shows the position difference and flux density ratios of the sources compared with the 'reference' observation, D20493619, which was made using the pre-existing system. The ratio of the flux densities of the two sources in each image is also shown.

ing or telescope conditions (as mentioned above). This conclusion is supported by a change of several arcseconds in the average MD offset correction derived from SCAN observations before and after each observation. Furthermore, the scatter in the individual SCAN MD offset measurements was significant. The discrepancy in position between the two observations made with the old system also adds support to this.

The flux densities, on the other hand, are in good agreement. Typical MOST flux density calibration is within 10% (Hunstead 1991), and the measurements are consistent with this. One discrepant flux density measurement (source A in D20493617) is due to an incorrect meridian distance primary beam correction. A lookup table in `WFSYN` corrects assuming the new phase shifting hardware is in operation, which is not appropriate for this test. Furthermore, the ratio of the flux densities of the two sources for D20493620 is in good agreement with that for D20493619 and D20493616. These are the three observations made which have had appropriate meridian distance primary beam corrections applied in synthesis.

In summary, the tests indicate that flux density and position accuracy was preserved by the introduction of the new data acquisition software and the new phase-shifting hardware. Final tests await full optimisation of the MOST.

3.3.3 Preliminary tests on 7–block fields

The next test of the system was to examine position and flux density reliability of the much larger Wide Field images. Initially, observations of MOST calibrators were made, to look for gross errors in flux and position. This test necessarily made use

of versions of synthesis software still under development. Consequently, the results described here should be considered preliminary, indicating the gross performance level of the system. As mentioned in chapter 6, errors have since been corrected in the synthesis and data acquisition software. If repeated, the numerical results of these tests would now differ. However, the basic conclusions at an 'acceptance' level would not change.

Observations Twelve-hour synthesis observations of the MOST calibrator B0409−752 were made using the MOST in Wide Field mode in October 1996. On each occasion the field centre was offset from the calibrator in different directions. It was difficult to reconcile measurements from these observations with the adopted position of B0409−752. Problems with the synthesis software were suspected. To focus more on this, further observations were made in 1997 with the MOST calibrator B1215−457 centred in Wide Fields and with the MOST calibrator B1934−638 offset from the field centre to the north and south. Table B.1 gives details of the observations and the SCAN-derived calibrations that were applied.

Measurements Each of the 1997 observations was analysed using `newsyn`, a modification for Wide Field analysis by Lawrence Cram and Taisheng Ye of `fitsmsyn` (a multi-author program). This program uses the tilt primary beam of Reynolds (1986, p20), with the scaling factor $\cos^{-1}$(MD) rather than Reynolds' original $\cos^{-1.2}$(MD), when making a CLEANed image. As for the tests on 3–block data above, the meridian distance gain correction of Burgess (1989) was applied to each fan-beam according to its meridian distance. At the time of making these measurements (1997 June 20) `newsyn` gave positions and flux densities more consistent with the adopted values than the alternative program, `mstkln` (by David Crawford). Since the test was not intended specifically to compare the performance of the two programs, only the `newsyn` results are presented here. Section 6.1 describes these two synthesis software programs.

In each image the calibrator's position and flux density were fitted using the `MIRIAD` program `maxfit`. This fits a 2-dimensional parabola to a 3×3 pixel box. Gaussian fits to larger areas were unsuccessful since the beamshape produced by the preliminary synthesis software was not symmetrical. The measured position of the calibration source was derived from the fitted profile. In the case of I12154548 and I1934651 the flux density of the source was also determined from the fitted profile. For the other observations the flux density was that of the brightest pixel, which was placed almost exactly at the fitted position. Table 3.2 gives the results. In each case the positions and flux densities shown are relative to the accepted values from Campbell-Wilson & Hunstead (1994).

Discussion The results above show that the positional accuracy of the MOST in Wide Field mode has been essentially preserved. The position errors are only slightly worse than those found in the test observations of $70'$ fields. Further work on the synthesis software will be required to achieve the expected accuracy. One

MOST archive name	Source	Calibrator position	ΔRA ($''$)	$\Delta\delta$ ($''$)	$\frac{S}{S_{\rm adopted}}$
I12154548	B1215−457	centred	1.6	0.0	1.15
I12154549	B1215−457	centred	−2.7	0.2	1.34
I12154550	B1215−457	centred	−1.0	0.3	1.19
I1934622	B1934−638	south	−2.8	−1.2	0.97
I1934651	B1934−638	north	−1.1	−0.4	0.75

Table 3.2 Preliminary measurements of the position and flux density accuracy of the MOST in Wide Field mode, observing calibrators in 7–block fields. The positions and flux densities are relative to the adopted positions of the calibration sources (Campbell-Wilson & Hunstead 1994). The fields centres were offset from the calibration sources for some of the observations: the indicated direction is that of the source relative to the field centre. Since the time of making these measurements (1997 June 20) several errors in the synthesis and data acquisition software have been corrected. As a consequence, the results here would differ from the results obtained with more recent software. See section 6.6 for further discussion. For further observational details, see table B.1.

factor contributing to these errors may be the precession algorithm in `newsyn` which uses approximations that were adequate for earlier modes of operation, using a simple displacement and rotation to simulate precession (Ye 1996). A more accurate calculation is now required for Wide Field operation. Additionally, the observations of B1934−638 were made with the source very close to the field edge. As a result the significantly lower signal-to-noise affects measurements of this source.

The flux density accuracy is somewhat poorer. Some of the Wide Field data taken before April 1997 may have poor calibration. Further investigations of this aspect will need to be made in conjunction with more detailed tests of the Wide Field imaging software and a better determination of the tilt primary beam model of the telescope.

3.3.4 A test survey region—The MOST Vela supernova remnant survey

Having completed engineering tests of the Wide Field system (section 3.2) and the basic astronomical tests described above, the next step was to assess the performance of the telescope in the mode of its primary use as a survey instrument. The MOST Wide Field surveys comprise two major projects: a Galactic survey and an extragalactic survey (section 1.3). At the resolution and frequency of the MOST the majority of galactic emission is extended, but the bulk of extragalactic sources are compact. Thus it is necessary to evaluate carefully the response of the MOST both to extended and compact sources.

For this thesis it was possible to complete only the initial tests of telescope responses. Performance assessment of the MOST will continue for the life of the survey and the survey parameters will doubtless continue to be refined on the basis

of an improved understanding of the telescope. In fact, this is a process which has occurred continuously since the MOST began operation. The present tests serve to indicate that the upgrade has, as expected, preserved the essential features of the MOST, while increasing by a factor of up to five the area of sky that can be imaged each night. As well, they indicate the need for further investigations of the telescope and reduction software methods.

At declination $-45°$, the Vela supernova remnant region provides a good testing ground for the telescope. It contains regions of extended emission and many unresolved sources a few degrees from the Galactic Plane. It is also in the mid-range of declinations which will be observed for the surveys. To allow a comparison of the performance of the telescope in the Wide Field mode with its previous performance, a survey of the Vela supernova remnant was carried out using the MOST before the upgrade.

The Vela supernova remnant was chosen early as a topic for study within this thesis, combining Wide Field testing with scientific investigation. I will now discuss the Vela SNR and the $70'$ mosaiced survey made with the MOST, before returning to Wide Field testing in chapter 6.

Chapter 4

The Vela Supernova Remnant

The study of supernova explosions (supernovae) and their remnants is a key part of the study of our Galaxy, and increasingly of other galaxies. Supernovae are the sole source of elements heavier than iron and provide a majority of the abundances of many of the lighter elements. They are among the most energetic events known: type Ib, Ic and II supernovae typically release about 10^{53} ergs (Cooperstein & Baron 1990). Most of this is released in the form of neutrinos. About 10^{51} ergs makes up the kinetic energy of the explosion. Type Ia supernovae are less energetic, releasing about 10^{51} ergs in total.

This chapter begins (section 4.1) with a brief review of the basic theory governing the evolution of supernova remnants. Then, from the observational perspective, section 4.2 discusses the wide variety of supernova remnants in the context of the standard classification based on radio properties.

The Vela supernova remnant (SNR) is one of the closest remnants (about 500 pc), enabling us to study it in great spatial detail. Because it is classified as a composite remnant (meaning it has both an expanding shell and a central synchrotron nebula), we are able to observe features due to a wide variety of emission mechanisms. As well, Vela is one of only a few SNRs conclusively associated with a pulsar, the compact stellar remnant of the progenitor. In spite of these qualities, the Vela SNR has been much less studied than other close remnants such as the Crab Nebula and the Cygnus Loop, on account of its southern declination. Inconsistent models and unsolved problems motivate further study of this remnant.

The ability of the MOST to image low surface brightness extended emission over large areas makes it ideal for studying the Vela SNR. At 843 MHz non-thermal emission dominates, making the high sensitivity of the MOST enormously useful. Yet the observing frequency is not so low that free-free absorption becomes important. Section 4.3 provides an overview of previous work on the Vela SNR, leading into a discussion of the particular problems in our understanding of the relationship between the supernova remnant and the Vela pulsar (section 4.4).

4.1 The evolution of supernovae

The life of a massive star ends in a supernova, leaving an expanding remnant, which is typically observable in the radio bands because of the synchrotron radiation produced during its interaction with the interstellar medium (section 4.1.1). This remnant is relatively short-lived in astronomical terms ($< 10^6$ yr: Reynolds 1988b). Optical, X-ray and even γ-ray emission may be observable from an SNR, but primarily due to absorption and extinction the majority of SNRs are visible only in the radio.

Supernovae (SNe) have been classified into several groups based on their maximum light optical spectra, although the spectra at age about six months have been used for alternative classifications. The standard classification system separates supernovae into types Ia, Ib, Ic and II, based on the presence or absence of certain elements in the spectrum. Type II SNe show evidence of hydrogen, while type I SNe do not. Type Ia SNe show Si II absorption, whereas types Ib and Ic do not and are distinguished by the presence or absence respectively of He I in the spectrum. A comprehensive review of SNe classifications is given by Harkness & Wheeler (1990). Other authors have used variants on this scheme, a selection being published in the same volume (Petschek 1990).

Type Ia SNe occur in population II stars, among old stars such as white dwarfs. They occur when carbon burning in the core provides more nuclear energy than can be carried away by plasma neutrino losses (Woosley 1990). Type Ib, Ic and II SNe result from the core collapse of younger more massive ($> 8M_\odot$) stars. Nuclear reactions in these stars continue until the central core of iron is unable to generate sufficient radiation pressure to prevent the outer layers gravitationally falling back. A shock wave rebounds from the dense core, ejecting the outer layers of the star (Cooperstein & Baron 1990). Usually, a compact remnant, such as a neutron star or black hole, is left behind after a type II SNe. The compact remnant is most easily observable when it is a rapidly rotating neutron star, called a *pulsar*. Pulsars are believed to power the central nebulae seen in some SNRs. The supernova rate in our galaxy has been estimated to be about one every 40 ± 10 years (Tammann et al. 1994).

The interaction of supernova explosions with the interstellar medium means the resulting remnants lead to an improved understanding of the composition of the interstellar medium. Two groups of models have been proposed to explain SNR evolution. I will briefly describe the 'standard' version of each, although many variations and refinements have been proposed.

4.1.1 The interaction of supernova ejecta with the ISM

Woltjer (1972) has summarised the standard model, derived from the theory of explosions in a uniform medium. The model comprises four phases, presented below. In practice the ISM is not a uniform medium: inhomogeneities such as molecular clouds and cavities made by stellar winds dominate all stages of the evolution. Hester

(Hester & Cox 1986; Hester 1987) among others has examined the effects of these inhomogeneities on SNR evolution. Governed by the local environment, SNRs are thought to go through these stages with wide variety in timing. We see each SNR at a snapshot in time, sometimes with features attributable to more than one stage. A recent review is given by Reynolds (1988b).

Free expansion phase: The blast wave expands at constant radial velocity. The swept up material has sufficiently small mass that the kinetic energy imparted to it is a small fraction of the total kinetic energy released in the explosion. Evolution during this phase is dominated by initial conditions such as explosion energy and progenitor mass.

Adiabatic or Sedov-Taylor phase: The mass swept up by the explosion is now significant, but radiative cooling is still relatively minor and so kinetic energy is effectively conserved. The shock is now decelerating:

$$v = \frac{2}{5}\frac{r}{t},$$

with v and r the radial expansion velocity and radius at time t. Interior thermal X-ray emission is intensified by the passage of a *reverse shock* from the deceleration. The radio emission takes the form of a shell.

Radiative or snowplow phase: At about $v = 200\,\mathrm{km\,s^{-1}}$ radiation dominates, as the cooling time becomes less than the age of the remnant. Momentum of the shock is conserved but energy is not. About half the thermal energy of the shock has been dissipated. The remnant consists of cool, dense shell with a hot interior, and has $r \propto t^{1/4}$. Optical filaments may form, indicating recombination cooling of denser material swept up.

Dissipative phase: Now the shock has slowed to a velocity comparable with random motions in the interstellar medium ($10\,\mathrm{km\,s^{-1}}$). It dissipates at an age of about 10^5 years, and is no longer observable in the radio continuum.

4.1.2 Pulsar-powered nebulae

Plerionic or *filled-centre* SNRs are thought to be powered by a pulsar left by the SN. The rate of energy loss of a pulsar is directly measurable as a slowing of its rotation. This energy is thought to be released in the form of relativistic electrons sweeping along a strong polar magnetic field, which gives rise to the beamed (hence observationally pulsating) radiation (Goldreich & Julian 1969; Backer 1988; Gangadhara 1996). How this energy actually powers an SNR is poorly understood (Kennel & Coroniti 1984). The standard model of the evolution of pulsar-powered nebulae is due to Reynolds & Chevalier (1984) and depends strongly on initial properties of the pulsar, such as its magnetic field and rotation period (Bhattacharya 1990). Reynolds & Chevalier propose four phases in their model.

Phase I: The supernova ejecta are expanding (as in section 4.1.1), and an expanding bubble of relativistic particles and magnetic fields is formed within the expanding remnant by the rotational energy lost by the pulsar.

Phase II: The expanding bubble has swept up all the slow-moving ejecta and accelerates with the continued energy input from the pulsar.

Phase III: When the age of the remnant is comparable to the characteristic spin-down time of the pulsar the bubble no longer has sufficient energy to continue accelerating. If this happens before the slow-moving ejecta are all swept up, this phase follows directly from phase I.

Phase IV: The reverse shock, which is formed when the fast-moving supernova ejecta begin to slow significantly and sweep up significant amounts of the ISM, passes through the bubble which then dissipates. The expanding shell from the fast ejecta may remain an observable manifestation of the remnant.

4.2 Diversity among supernova remnants

It is sometimes remarked that there are as many classifications of SNRs as remnants themselves, with an incredible diversity of observable properties. Nevertheless, a basic classification scheme based on generally accepted models for SNR evolution has been found useful. The classification relies primarily on radio observations, which are the main method of SNR discovery (e.g. Day et al. 1972; Taylor et al. 1992; Duncan et al. 1995; Whiteoak & Green 1996). Three classes have been proposed: shell, plerion (or filled-centre) and composite. A fourth class is beginning to emerge (Rho 1996) comprising SNRs which are shell-like in the radio but have a filled-centre thermal X-ray morphology. Of the three well-established classes, shell SNRs comprise the majority, about 85% of those in the Galactic SNR catalogue of Green (1996). The composite and plerion classes contain about 10% and 5% respectively of the observed Galactic SNRs. Serious selection effects may disguise these statistics (Green 1991; Gaensler & Johnston 1995), and these figures should be considered a very rough guide only. The following presentation considers examples from our Galaxy. Many well-studied remnants also exist in the Magellanic Clouds and other other galaxies.

4.2.1 Shell supernova remnants

Dominant among the classes by number, shell supernova remnants are also probably the best understood theoretically (section 4.1.1). Although the basic models are of a spherical shell expanding after a supernova explosion, shell SNRs (e.g. IC443: Duin & Van Der Laan 1975; HB3: Fesen et al. 1995; the Cygnus Loop: Green 1990) are observed in any number of irregular shapes deviating from the spherical ideal. In the majority of SNRs this is thought to be due to the inhomogeneity of the

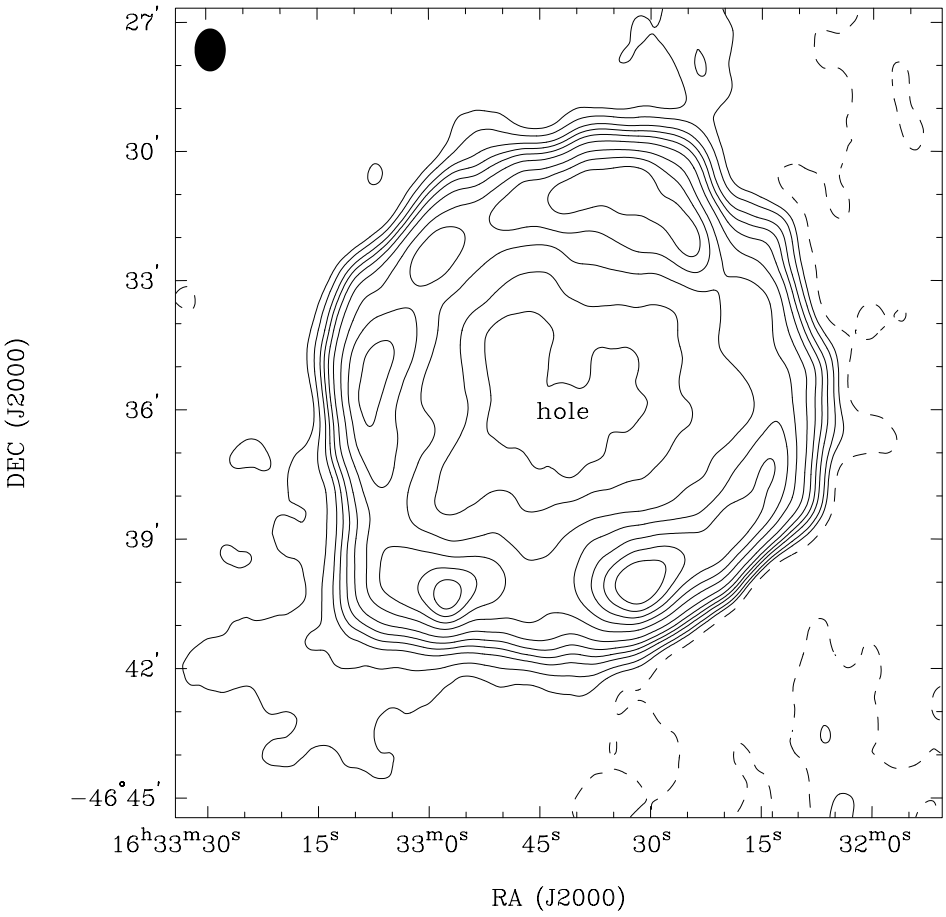

Figure 4.1 MOST 843 MHz of a classic shell SNR, G337.3+1.0 (Kes 40), reproduced from Whiteoak & Green (1996). The remnant has an integrated spectral index of −0.55. Contour levels are at −5, 10, 20, 35, 50, 70, 100, 150, 200, 250, 300, 350, 400 mJy beam^{-1}: the FWHM beam is given at the upper right.

interstellar medium, with which the expanding supernova shock wave is interacting. The observable features of a shell-type remnant in the radio regime are regions of steeper-spectrum (spectral index $\alpha = -0.4$ to -0.8, $S_\nu \propto \nu^\alpha$) polarised synchrotron emission, seen in projection on the limbs of the expanding shell. The polarisation arises from magnetic fields which are oriented radially in younger remnants and randomly or tangentially in older remnants away from the Galactic Plane (Milne 1987). The polarisation is typically at levels of 3–15% (Lozinskaya 1992, p233). Optical filaments and knots are associated with some of the remnants, and these are sometimes correlated with the radio emission. This correlation is thought to be due to the Duin and van der Laan mechanism (Duin & Van Der Laan 1975). X-ray emission from the shocked gas interior to the main blast wave is also detectable from many shell remnants (Seward 1990).

Figure 4.1 shows a classic shell SNR, G337.3+1.0. The shell is complete and

nearly circular, with several enhancements around the rim and a spectral index of -0.55 (Whiteoak & Green 1996). Polarimetric observations by Milne et al. (1989) indicate a probable radial magnetic field and hence that the remnant is probably in the free expansion phase.

4.2.2 Plerionic supernova remnants

Plerionic (or 'filled-centre') supernova remnants differ from shell remnants in that their radio morphology is smooth and centrally peaked, rather than a shell structure. Like shell remnants, they are found in a wide variety of shapes. Plerionic remnants have been found to emit synchrotron emission with a flatter spectrum than shell remnants, with spectral indices ≥ -0.3 (Weiler & Sramek 1988), consistent with recent injection from the pulsar. Both morphology and spectral index have been useful in separating plerionic and composite remnants from the more numerous shell remnants. Plerions generally exhibit a greater degree of polarisation than shell remnants, typically around 20%, but sometimes even higher (e.g. the Crab Nebula: Bietenholz et al. 1991). It has been proposed that plerions may be an early evolutionary stage of a subset of those shell remnants originating from type II supernova explosions (Lozinskaya 1986). As mentioned in section 4.1.2, plerions are generally thought to be powered by pulsars.

The most widely studied of the plerionic supernova remnants is the Crab nebula, the remnant of the historical supernova AD 1054. There is evidence (Wallace et al. 1994) that the Crab exploded into a low-density region of the ISM, possibly a pre-existing cavity blown out by the stellar winds of the progentitor and other OB stars in the region. The blast wave of the supernova explosion is then supposed not yet to have reached the higher density ISM which gives rise to the characteristic shell structure seen in shell-type remnants. Recent observations (Frail et al. 1995) confirm that there is no shell surrounding the Crab to a limit much lower than is usual for composite remnants. Observations of other plerionic remnants (Wallace et al. 1997) do not show a pre-existing cavity, so some filled-centre remnants may result from much lower energy supernova events (Nomoto 1987) which may not form a visible shell. A radio and optical image of the Crab Nebula is shown in figure 4.2. In the image, note the similarity between optical and radio emission. This is not seen in the plerion of the Vela SNR, which is at least an order of magnitude older.

4.2.3 Composite supernova remnants

Composite supernova remnants (Caswell 1977b; Helfand & Becker 1987) share morphological characteristics with both the shell and plerion classes above. Aspects of the theory of both shell and plerionic remnants probably apply to the shell and filled-centre regions respectively. Composite remnants have been proposed as an intermediate stage between the plerionic and shell remnants (Wallace et al. 1994; Lozinskaya 1986); but this has not been conclusively shown. What is more clear is that composite remnants are likely to evolve to become shell remnants as the pulsar is no longer able to sustain the plerion by the release of rotational energy. Composite

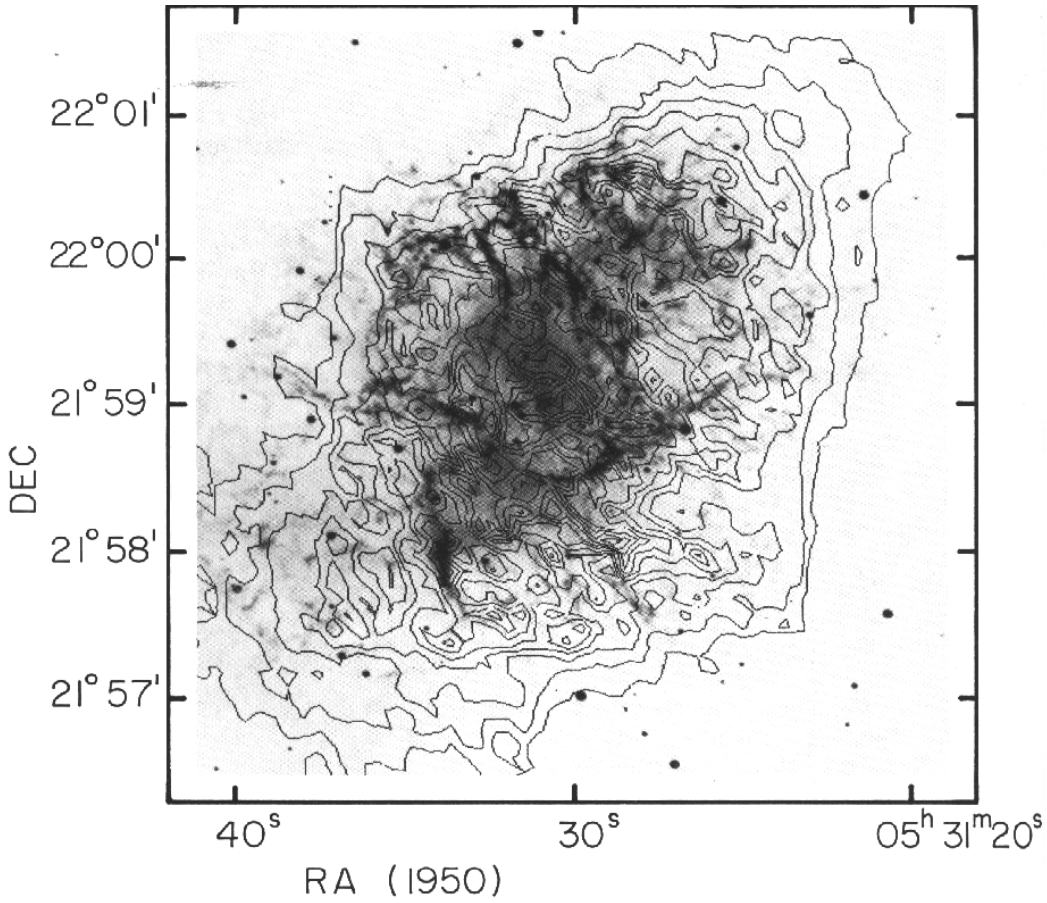

Figure 4.2 A radio and optical image of the Crab Nebula, reproduced from Wright & Forster (1980). The contours are from a radio observation at 23 GHz, and are overlaid on the brightest optical filaments, showing how the brightest radio structure is found around the optical filaments.

remnants are the least studied class, having been relatively recently identified, and the Vela SNR may well become the archetypal Galactic example. Figure 4.3 shows a MOST 843 MHz image of the composite SNR G326.3 − 1.8. This remnant has an optical counterpart (van den Bergh 1979). Soft X-ray observations (Kassim et al. 1993) show thermal emission within the radio shell, but not a non-thermal analogue of the radio plerion.

4.3 The radio remnant of Vela

The Vela supernova remnant (G263.9 − 3.3) is one of the closest ($\sim$ 500 pc) and brightest supernova remnants. Its brightness and large angular size ($\sim 8^\circ$) has made possible its study at many wavelengths. However, many issues remain controversial. Among these has been the key question of whether it is a shell or a composite

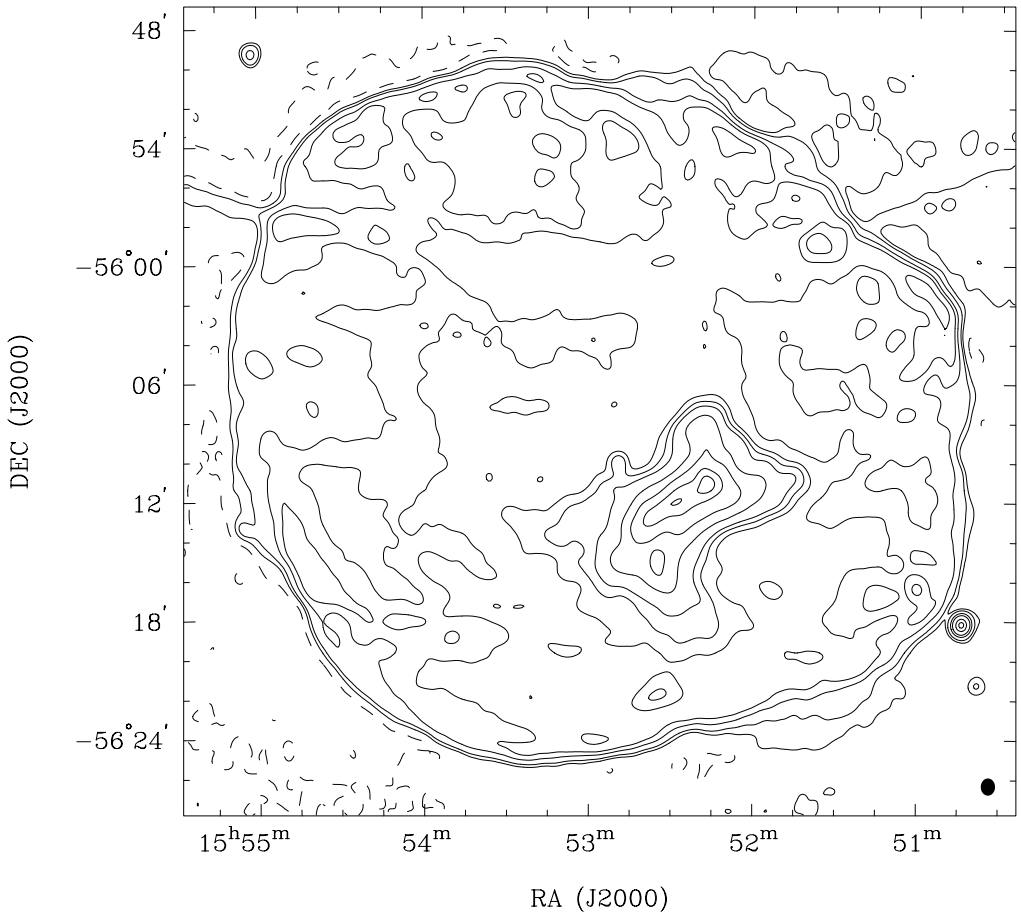

Figure 4.3 MOST 843 MHz image of a composite SNR, G326.3 − 1.8 (MSH 15 − 56), reproduced from Whiteoak & Green (1996). Optical filaments have been detected associated with the shell, but not the plerion. Contour levels are at −4, 14, 25, 50, 75, 125, 160, 200, 300, 400, 500, 550 mJy beam^{-1}. The FWHM beam is shown at the lower right.

remnant. Spectral index arguments have been used to conclude that it is a composite remnant, but the results have not gone uncontested. The work to be presented in chapter 5 clearly shows the shell and central nebula as being quite different in structure, lending strong morphological support to the argument that the Vela SNR is a composite remnant. Accepting this conclusion leads us naturally to make detailed measurements of the Vela SNR, as a means of understanding the way pulsars are able to power nebulae over significant distances.

The Vela pulsar, discovered in 1968, was immediately associated with the Vela supernova remnant (Large et al. 1968). Calculations by Bailes et al. (1989) indicate that there is only a 0.1% probability that the pulsar and the supernova remnant are in chance superposition. The discovery that the speed and direction of the pulsar's proper motion implies that it was born near the centre of the 8° Vela SNR shell

(Aschenbach et al. 1995), confirms the association. This is one of only a few reliable SNR/pulsar associations (Kaspi 1996).

Previous radio studies of the Vela SNR region have mainly been lower resolution single dish experiments over a frequency range from 408 MHz to 8.4 GHz (Milne 1968b; Day et al. 1972; Milne 1980; Milne 1995; Duncan et al. 1996). The earliest observations showed the Vela SNR to be comprised of three main areas of radio emission, called Vela X, Y, and Z, with a diameter 5°, corresponding roughly with the bright, filamentary structure of the nebula Stromlo 16 (Gum 1955; Milne 1968a). The most recent of these observations (Milne 1980; Milne 1995) began to resolve Vela X at higher frequencies (5–8.4 GHz) and uncovered highly polarised structure. The flatter spectral index of Vela X (compared to the rest of the SNR) has led to the remnant's classification as a composite, with Vela X a plerion directly powered by the Vela pulsar (Dwarakanath 1991; Weiler & Sramek 1988). Vela Y and Z were thought to be bright regions of the shocks from the original SN event as they interact with surrounding molecular material.

4.3.1 Morphology

Until the late 1980s, the Vela SNR was widely accepted to be limited in the radio to an angular diameter of about 5°, with the nebula Vela X, containing the pulsar, offset to one side. Relatively recently, Kundt (1988) suggested from the 408 MHz survey of Haslam et al. (1982) that the Vela SNR may be much larger than previously realised, in fact about 8° across, with the pulsar approximately at the centre. ROSAT observations (Aschenbach 1992) and later radio observations (Duncan et al. 1996) confirmed this. However, it should be noted that the earlier 29.9 MHz Fleurs Galactic survey of Jones & Finlay (1974) (reproduced in figure 4.4) clearly shows the entire 8° remnant. The lower left quadrant of the shell is significantly fainter than the rest of the Vela SNR, but still much brighter than the surrounding region. The steeper spectral index of the Vela shell (-0.53: Dwarakanath 1991) causes the shell to be fainter by a factor of seven compared to the central nebula (Vela X) at a higher frequency of 1.4 GHz. Free-free absorption of the radio emission has only a small opposite effect: the shell remains highly visible in the Fleurs image.

The fact that the shell of the Vela SNR is brightest towards the Galactic Plane probably indicates that the ISM is most dense in this direction, with a greater mass of material swept up by the SN blast wave. It has been found (Caswell 1977a; Kesteven & Caswell 1987; Gaensler 1997) that bilateral or 'barrel-shaped' supernova remnants are aligned preferentially with the Galactic Plane. The enhanced Vela shell near to and aligned with the Galactic Plane may be due to the same mechanism. Figure 4.4 shows the X-ray and 29.9 MHz radio images to the same scale. The radio peaks known as Vela X, Y and Z are marked on the radio image.

Radio observations of the Vela shell published before the present work have been at relatively low resolution. For example, the observations of Duncan et al. (1996) have a resolution of $10'$, much lower than the available X-ray (Aschenbach et al. 1995) and optical (Elliott et al. 1976) observations. The MOST observations of the

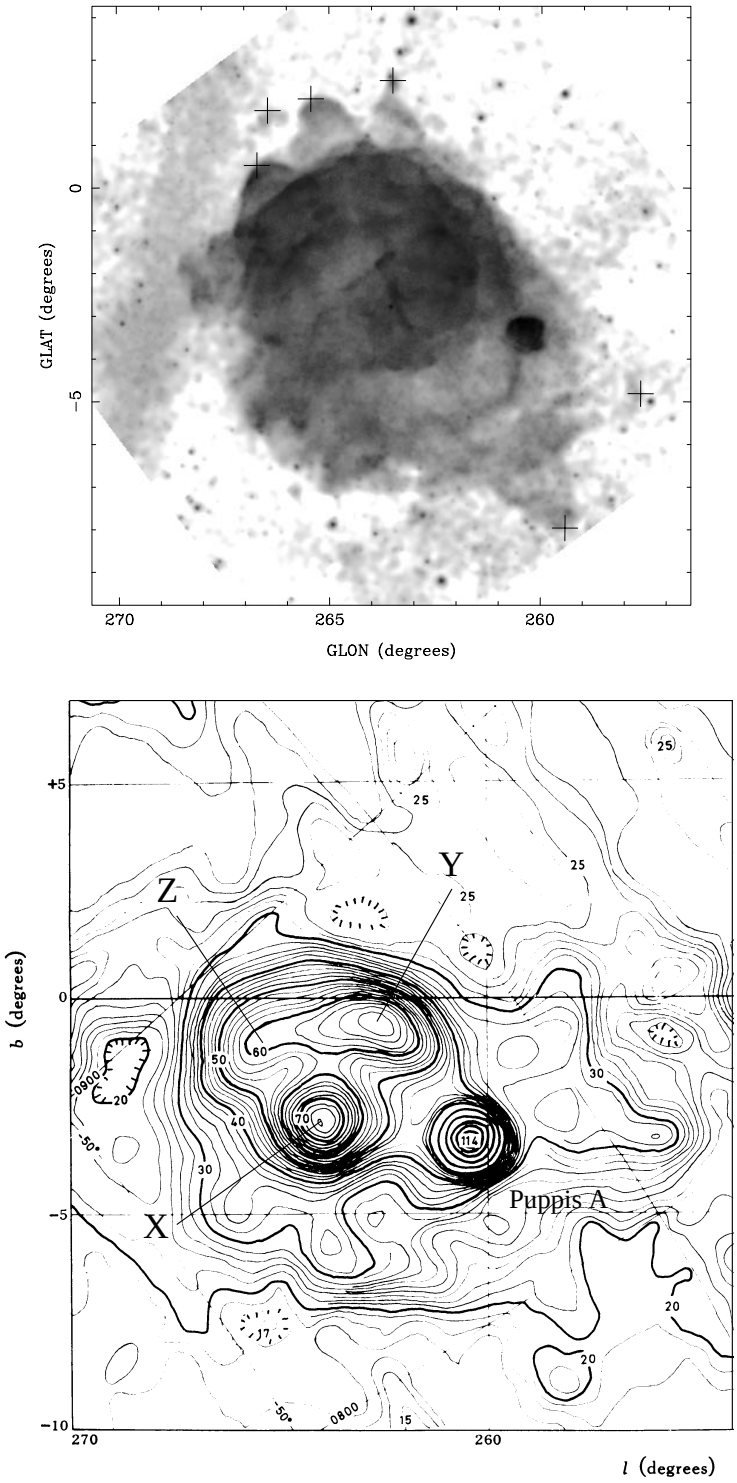

Figure 4.4 X-ray (0.1–2.4 keV) and 29.9 MHz (Fleurs) images of the Vela SNR, showing its 8° extent. The images are approximately at the same scale. The X-ray data are courtesy of B. Aschenbach (originally published in Aschenbach 1992). Note the protrusions from the shell (dubbed 'bullets') marked with crosses. The radio image is reproduced from Jones & Finlay (1974); on it the radio peaks Vela X, Y and Z are marked.

Vela SNR presented in chapter 5 allow for the first time a multiwavelength study of the shell of a composite remnant at scales a small fraction of a parsec (chapter 7).

The interaction of the Vela SNR with the interstellar medium is apparent also outside the 8° boundary, now the accepted edge of the Vela SNR. Aschenbach et al. (1995) discovered several extended X-ray features outside the boundary, which they interpret to be fragments from the original supernova explosion. The axes of symmetry of these objects intersect close to the centre of the SNR. Aschenbach et al. used this position as an estimate for the location of the original explosion.

Strom et al. (1995) followed this up with radio observations of one of the explosion fragments, detecting a synchrotron shell coincident with the outermost edge of the X-ray emission.

4.3.2 Distance and age

Historically, the distance to Vela was used to calibrate the surface brightness–diameter ($\Sigma - D$) relationship (Milne 1979), which is now known to be unsuitable as a predictor of distance (Green 1984b). However, the distance is actually quite uncertain: foreground H I to the pulsar is negligible, so its distance cannot be predicted using Galactic rotation models (Frail & Weisberg 1990 and references therein). Estimates from pulsar dispersion measures give about 500 pc, but suffer from inaccuracies in electron distribution models at these sort of distances (Frail & Weisberg 1990). Oberlack et al. (1994) have argued that this distance is an overestimate. For this thesis I will adopt the most commonly accepted value of 500 pc, which is consistent with measurements of extinction of OB stars towards a dark cloud that may be physically associated (Milne 1968b). This value for the distance of the Vela SNR implies a shell diameter of 70 pc and a diameter of 20 pc for the plerion (Vela X). A conclusive value for the distance to the Vela supernova remnant may be obtained by measuring the parallax of the Vela pulsar. Such a measurement is presently underway, using VLBI techniques (J. E. Reynolds, personal communication, 1997).

The age of the Vela supernova remnant has for many years been accepted to be about 12 000 years, with an uncertainty of up to a factor of two. The characteristic age[1] of the pulsar is 11 400 years, but this is only a lower limit to the true age of the pulsar and supernova remnant (Chanmugam et al. 1995). Stothers (1980) gives the most comprehensive review of the early age estimates. Quite recently, both these age estimates have been revised upwards: Lyne et al. (1996) made a measurement of the braking index of the pulsar (a measure of the rate at which it is slowing) which implies an age of 22 000 to 29 000 years. Assuming the pulsar to have moved at constant velocity from the explosion centre determined above, Aschenbach et al. (1995) derive an age for the remnant of $18\,000 \pm 9\,000$ yr using the proper motion of Bailes et al. (1989). The age of the remnant/pulsar pair has important implications

[1]The characteristic age of a pulsar is defined to be $\tau_c = P/2\dot{P}$, where P is the period and $\dot{P}$ is the spin-down rate.

for models of the system. The increased age estimate reduces by up to an order of magnitude the energy required to sustain the X-ray 'jet' of Markwardt & Ögelman (1995) (section 4.4.2). The implied decrease in the velocities of the expanding shell and 'bullets' (Aschenbach et al. 1995), impacts upon any quantitative understanding of the emission in the shocked regions.

4.4 Vela X and the Vela pulsar

Recent research has begun to focus on the central part of the remnant (Vela X) with the aim of investigating the connection between the Vela pulsar and the remnant. The 'traditional' approach to classifying the Vela SNR has been to measure the spectral indices of the putative shell and plerionic components: much of the argument of the nature of the Vela supernova remnant has been based on these measurements. A interesting morphological alternative is permitted by the large size of the Vela SNR, which can be resolved in more detail at more frequencies than almost any other remnant.

4.4.1 Classification of the Vela SNR

Prior to 1995, the majority of the published observations in the radio, X-ray and optical regimes had indicated that the extent of the Vela SNR was 5° (section 4.3). It was somewhat unusual for a pulsar powered component to lie so far from the centre of the emitting region. However, the discovery that the Vela SNR is approximately circular (in projection), with the pulsar and the Vela X nebula near the centre (section 4.3.1) allows for more straightforward models.

Spectral index measurements Milne (1968b) first confirmed with measurements of the spectral index of the Vela SNR that Vela X was different from the rest of the remnant, although Risbeth (1958) had suggested this result from earlier surveys. Milne found the spectral index of the whole remnant to be -0.3, while the spectral index of the shell alone (components Vela Y and Z) was steeper, about -0.6. These results, with the original measurements, were used by Weiler & Panagia (1980) to estimate a spectral index for Vela X of -0.08 ± 0.02. Weiler & Panagia then proposed that Vela had a plerion like the Crab Nebula, but shell-like features (Vela Y and Z) as well. The Vela SNR then became part of the new class of supernova remnants (Weiler 1983) called 'combination' remnants, or more usually now, 'composite' remnants.

However, as pointed out by Milne & Manchester (1986), Weiler & Panagia did not use available 408 and 635 MHz observations (Milne 1968b). The reason was some confusion as to whether the integrated flux density values were for Vela X alone or for the whole SNR. Milne & Manchester (1986) used them to obtain a spectral index of -0.35 ± 0.05 for Vela X, yet Weiler & Sramek (1988) found the peak brightness

temperatures of the 408 and 635 MHz observations were consistent with a spectral index of -0.08.

Dwarakanath (1991) reconciled the arguments as they stood at that time, concluding that from a spectral index perspective, Vela X should be regarded as the plerionic component of the *composite* Vela supernova remnant. New observations at 34.5 MHz established that the spectral index of Vela X was indeed significantly flatter than that of the rest of the remnant, at about -0.16 ± 0.02. Two recent measurements have been added to Dwarakanath's spectrum of Vela X, which is reproduced in figure 4.5 together with his spectrum of Vela Y and Z for comparison. They are from Parkes measurements at 2.4 GHz (Duncan et al. 1996) and 8.4 GHz (Milne 1995). The 2.4 GHz measurement is consistent with the spectrum determined by Dwarakanath (1991). However, the 8.4 GHz measurement is not. It is not clear why this is so. Difficulties in measuring the baselevel in the presence of Galactic emission can significantly affect measurements of this type. The structure of Vela X begins to be significantly resolved at 8.4 GHz, making it harder to determine which emission is background and which is due to the Vela SNR.

The Vela X filaments Recent radio observations (Frail et al. 1997; Milne 1995) have begun to resolve the Vela X region with resolutions as high as $1\farcm8 \times 1'$. These start to show that the Vela X region is comprised of a network of complex filaments, superficially similar to those in the Crab Nebula. Furthermore, the filaments are highly polarised, with the magnetic field directed along the filaments (Milne 1995). The MOST observations presented in chapter 5 are the highest resolution observations yet of the the Vela X region, resolving these synchrotron filaments even further. The MOST observations also cover a substantial portion of the brighter shell (Vela Y and Z). As we will see, the morphology of these filaments is strikingly different from the Vela X filaments.

Unlike the radio filaments in the Crab (cf. figure 4.2), the Vela X filaments have no obvious optical counterpart (Elliott et al. 1976). Reynolds (1988a) has examined mechanisms for the formation of filamentary structure in plerionic SNRs. He concludes that the most likely mechanism relies on pre-existing thermal filaments (such as are seen in the Crab Nebula). With the high resolution radio data available, a new search for optical/radio correlation in Vela X is justified.

4.4.2 A pulsar-powered nebula

The question of how pulsars power plerions is of particular interest. In the Vela SNR we have an excellent opportunity to study the mechanisms at high spatial resolution.

One of the key objections raised by Milne & Manchester (1986) to the composite classification of the Vela SNR was the distance of the Vela pulsar from the centre of Vela X, the nebula it was proposed to power. Although we now accept the Vela SNR as a member of the composite class, the difficulty of the asymmetry of Vela X remains. The proper motion of the pulsar is insufficient to explain this offset. Bailes et al. (1989) have determined that the pulsar is moving approximately north-west at

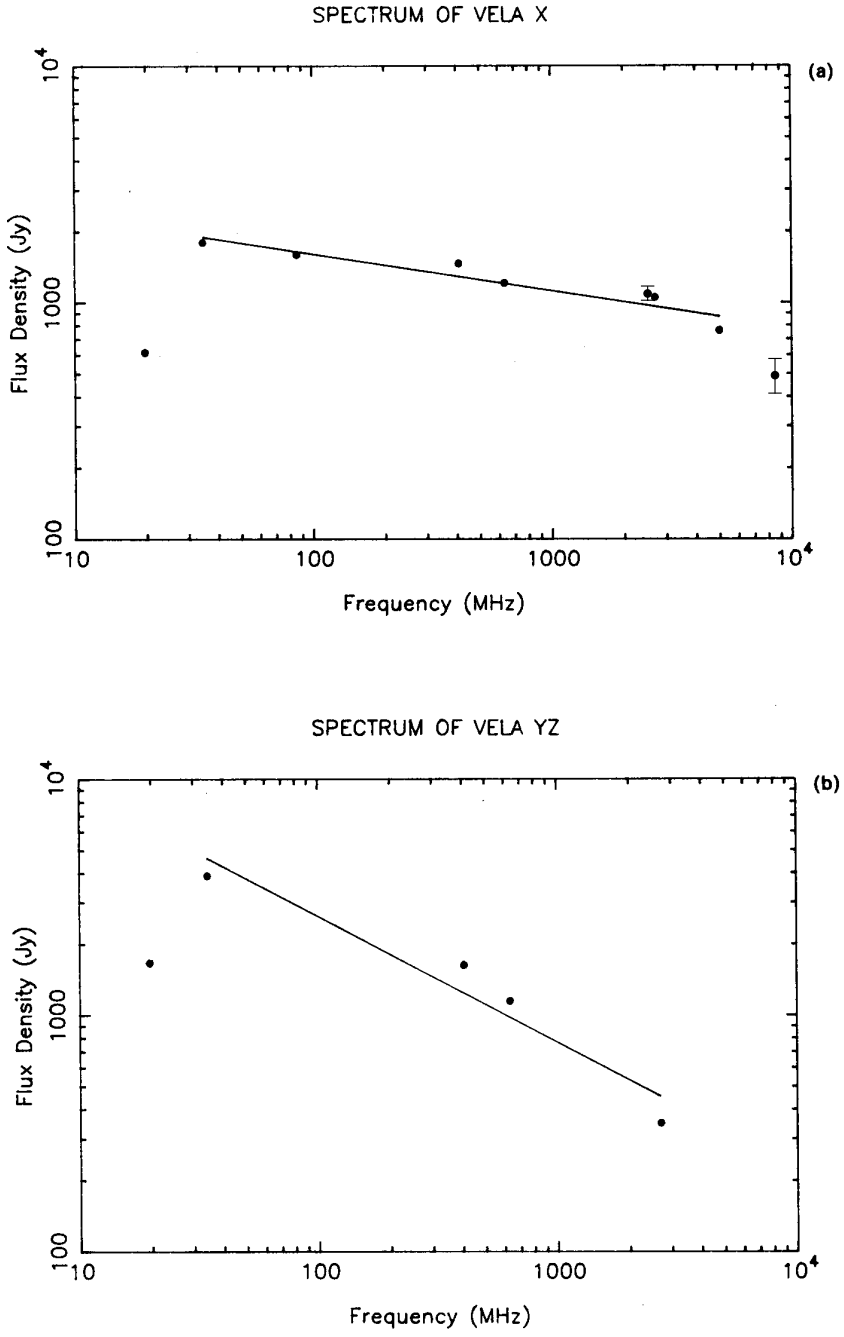

Figure 4.5 The spectra of the integrated flux densities of Vela X and Vela YZ, reproduced from Dwarakanath (1991). Two recent measurements (2.4 GHz: Duncan et al. 1996; 8.4 GHz: Milne 1995) have been added to the spectrum, with error bars indicating the quoted uncertainties. Dwarakanath excluded the 19.7 MHz measurements of Risbeth (1958) (affected by interstellar absorption) from the fits, obtaining spectral indices of -0.16 ± 0.02 and -0.53 ± 0.03 for Vela X and Vela YZ respectively.

$49\,\mathrm{mas\,yr^{-1}}$. This implies a motion of about $9'$ over the SNR's lifetime (assuming an age of 12 000 yr). However, the centre of Vela X is about $40'$ to the south-west of the pulsar's present position.

Recently, Markwardt & Ögelman (1995) have discovered a bright X-ray feature which might provide a clue to the way the pulsar energises the nebula. This feature (which they call a 'jet') extends south from the pulsar to the approximate centre of Vela X. The majority of the X-ray emission from the feature is produced thermally (Markwardt & Ögelman 1997). They propose that the 'jet' is a conduit for the energy to pass from the pulsar to the rest of the Vela X nebula. Using an age estimate for the Vela SNR of 12 000 years, they calculate that half the spin-down energy of the pulsar would be required to sustain the jet. However, recent increased age estimates (section 4.3.2) significantly reduce the energy required to sustain the jet (Lyne et al. 1996). While this discovery appears to point to a mechanism for powering the nebula, the asymmetry of the one-sided jet is surprising.

Frail et al. (1997) have found that the brightest radio filament in Vela X lies along the edge of the X-ray feature discovered by Markwardt & Ögelman. This highly polarised filament (Milne 1995) may indicate magnetic confinement of the jet. If this radio filament is indeed directly related in some way to the jet, it might be somehow different from other filaments in Vela X. Wijers & Sigurdsson (1997) propose an alternative model. They suggest that the 'jet' is part of a bubble of slowly expanding material which 'fell back' from the original SN explosion, and that a companion to the progenitor star is escaping at high velocity, clearing a path for an asymmetric expansion, which manifests itself as the 'jet'. An obvious test of these models is an examination of the radio spectral index of the bright radio filament, with the aim of finding out whether it has significant differences when compared to the other filaments in Vela X.

The region very close to the pulsar is of additional interest. Here, Bietenholz et al. (1991) have discovered a small highly polarised (70%) synchrotron nebula, with a spectral index of -0.6, much steeper than the rest of Vela X. This may be a standing shock from the pulsar wind, comprised of relativistic particles and magnetic field. But there is a distinct lack of any other extended emission in the area. Additional observations of moderate resolution might be able to determine whether this nebula is related to the more extended structure throughout the Vela X region. A little further away, near the projected birthplace of the pulsar (assuming an age of 12 000 yr), high energy γ-rays have recently been discovered (Yoshikoshi et al. 1997). This region is also prominent in the X-ray observations which led to discovery of the 'jet' (Markwardt & Ögelman 1995). The northern end of the 'jet' appears somewhat spread out between here and the current location of the pulsar, indicating that it may be a relatively long-lived feature. Higher resolution sensitive radio observations should clarify our understanding of this area.

With the aims of investigating the nature of Vela X and of providing a higher resolution radio dataset for multiwavelength studies, a survey of the Vela SNR has been made with the MOST, and is described in chapter 5. The survey is compared with Hα observations of the Vela shell and recently-available X-ray data in chapter 7. A study of Vela X, including radio spectral index measurements and optical comparisons is presented in chapter 8.

Chapter 5

The MOST Vela Supernova Remnant Survey

The goals of the MOST Vela supernova remnant survey are two-fold. First, the survey provides a benchmark mosaic of 70′ fields against which to examine performance of the Wide Field system. Secondly it is a study of an intrinsically interesting object in the Galaxy, with the second greatest flux density and angular size of the SNRs listed by Green (1996). This chapter presents the survey and discusses the morphology of the Vela SNR in the light of the general morphological classes of SNRs reviewed in chapter 4. An examination of the astronomical performance of the MOST Wide Field system is given in chapter 6. Further discussion of the shell and plerionic components is contained in chapters 7 and 8.

5.1 Introduction

The Vela supernova remnant has been less intensively studied than other close remnants such as the plerionic Crab Nebula and the shell-type Cygnus Loop, yet it is a key member of the third major class of SNRs, the composite remnants. This chapter aims to show that the Vela SNR can be seen as a composite remnant on morphological grounds and ought to be considered the Galactic archetype. It has recently become accepted that the spectral index evidence also places the Vela SNR in the composite class (Dwarakanath 1991; section 4.4.1). To support the morphological argument, radio observations are presented in this chapter at the highest resolution yet used to image the Vela X region. They are also the first high-resolution radio observations to cover a large fraction of the entire Vela SNR. As the nearest known composite remnant, the Vela SNR is uniquely placed as a laboratory in which to study the interaction of supernova ejecta with the interstellar medium *and* the mechanisms by which pulsars lose energy to surrounding nebulae. The survey includes the first radio observations of the Vela shell at a resolution compatible with currently available optical and X-ray images.

5.2 Observations

The MOST Vela supernova remnant survey covers an area of almost 50 square degrees, consisting of sixty-three 12-hour synthesis observations, each imaging an elliptical field of size $70' \times 70' \operatorname{cosec}|\delta|$. Each observation was made at the MOST's operating frequency of 843 MHz which provides a bandwidth of 3 MHz and a resolution of $43'' \times 43'' \operatorname{cosec}|\delta|$. The MOST receives circularly polarised emission. The observations were made over the period 1984 February 3 to 1996 February 3, before the Wide Field observing mode was commissioned. The elliptical field shape necessitates a substantial overlap in the survey, but this has been used to refine the relative calibration between fields based on the unresolved sources common to more than one field. Twenty-seven of the earlier observations were made for the first epoch MOST Galactic Plane survey (Whiteoak et al. 1989; Green 1994) and some of these data appear in the MOST supernova remnant catalogue (Whiteoak & Green 1996). The observations made especially for the survey were begun on 1992 January 17. All but four of these fields are placed on the same hexagonal grid as the MOST Galactic Plane survey. The four additional observations were special pulsar gating observations in the region of the Vela pulsar required to increase the dynamic range of the image. A complete list of the observations is given in table D.1.

5.2.1 Pulsar gating

Observations initially made in the vicinity (within about 1°) of the Vela pulsar were severely limited in dynamic range by the presence of the pulsar in the primary beam. The pulsar is a strong, unresolved continuum source and is variable over time scales of seconds to hours. Its integrated pulsed emission in ungated observations was 2.2±0.4 Jy, averaged over the entire period. A source will appear in a MOST image with a symmetric point-spread function only if its intensity remains constant throughout the observation. Any time-dependent variation will compromise sidelobe cancellation during synthesis, producing stripes across the image. In a normal 12 hour synthesis the pulsar introduced artefacts which all but masked nearby features. Deconvolution was difficult. To improve the imaging of this region a method of pulsar gating originally developed by J. E. Reynolds (personal communication, 1996) was used.[1]

To make the observations, a predicted pulse arrival time was used to generate a gating signal of width 20 ms in each pulsar period ($\sim$ 89 ms).[2] This was displayed on an oscilloscope simultaneously with the actual detected total power signal of the pulsar. The 50% pulse width of the pulsar signal was 4.5 ms, larger than the observed

[1] Reynolds' observations of the Vela pulsar region were made in 1986 using 23′ fields. He set the gate width at only 8.9 ms. Consequently, the instrumental effects detailed in section C.1 prevented a complete removal of the pulsed emission.

[2] The predicted pulse arrival time was determined from timing measurements of the pulsar kindly provided by R. N. Manchester (ATNF), M. Bailes (University of Melbourne) and P. M. McCulloch (University of Tasmania).

50% width of 2.3 ms at 632 MHz (McCulloch et al. 1978) due to the dispersion (2 ms) over the MOST's bandwidth (following Komesaroff et al. 1972) and to the effect of an integrating low pass filter present in the signal path before the detection point. Data acquisition was suppressed for the duration of the gating signal: from 5 ms before until 15 ms after the peak of the pulse, to allow removal of almost all of the variable pulsed emission. Four observations were made in this manner, each with the pulsar near the edge of the field to the north, south, east and west. These observations were incorporated in the complete mosaic. Overlapping regions in adjacent non-gated images were not used in the mosaic. Although this method removes imaging artefacts due to the pulsar within the four fields observed in the gating mode, some artefacts are present in more remote fields, mainly due to the grating response of the MOST. Further details of the gating procedure may be found in appendix C.

5.2.2 Improving the gating

The survey observations made with the procedure above contained a 40 mJy (2%) residual of the pulsed emission, sufficiently small that the artefacts discussed above are not seen, but large enough to confuse the region very close to the pulsar. Instrumental effects related to the gating were suspected to have caused this residual source. A further observation on 1997 February 13 was made using the improved technique described in section C.3. The pulsar gate was arranged to suppress data acquisition from 9 ms before the arrival of the peak of the emission until 31 ms after the peak. The observation was made using the MOST's $23'$ field size for maximum sensitivity, and is presented in section 8.1.1. The modified observing technique effectively removed the pulsar from the image.

5.3 Imaging

Individual images were made from each of the 63 observations using the back-projection algorithm of Perley (1979) as originally implemented by John Reynolds and modified by Taisheng Ye (`FITSMSYN`: Ye 1996). To provide initial calibration for the reduction process, several strong unresolved sources were observed before and after each 12 hour synthesis observation. These provide a preliminary gain, phase and beamshape calibration of each observation. Each image containing a source stronger than 200 mJy beam^{-1} was then adaptively deconvolved as described by Cram & Ye (1995). The remaining fields were deconvolved using the Högbom CLEAN algorithm as implemented in `FITSMSYN`. Several images with significant extended emission appeared degraded by the adaptive deconvolution: the CLEAN algorithm alone was applied to those fields in the final reduction. CLEANing was stopped in each case when the sum of the previous 100 components was negative, leaving residual images with pixel rms in the range 1–6 mJy beam^{-1}. The CLEAN components were restored with a Gaussian beam of FWHM $43'' \times 43''\mathrm{cosec}\,|\delta|$.[3] The variation in beam

[3]The declination, δ, is of the clean component, not the field centre.

size with declination is significant across the survey (see section 5.3.1), but this is taken into account in fitting programs.

Position and flux calibration uniformity across the whole survey has been achieved by the comparison of unresolved sources common to more than one observation. This step is appropriate since random errors in the calibration of individual images are larger than the global calibration error of the survey after the initial calibration steps.[4] The resulting position calibration in most of the images is consistent to better than $1''$ in right ascension, $2''$ in declination and 5% in flux density. This technique could not be applied to a few fields which had too few point sources in common with nearby fields (by being, for example, at the edge of the mosaic). The calibration parameters that were applied to the survey are given in table D.1.

5.3.1 Mosaicing

The fields were mosaiced using the task `SMJAC` developed within `AIPS` by Taisheng Ye (Ye 1995). A feature of this task is that it uses an ARC projection (Greisen & Calabretta 1995), which is convenient for large surveys, first because it represents with equal area, and secondly because it is the natural optical projection used in Schmidt surveys, with which many large radio surveys are compared. However, it is not easy to measure source sizes and flux densities in an image in the ARC projection, as the beam is not constant when measured in pixels (which are of constant angular size) and it also changes in orientation across the image. These measurements are best made from the images of single observations or from mosaics in NCP or SIN projection. Nevertheless, the mosaic of the Vela SNR survey gives an excellent overall impression of the region.

The NCP projection is the most appropriate projection for future MOST mosaics, since it is the natural geometry for the telescope images. In this projection, the beam of the telescope (expressed in pixels) is constant across the image. If fields are deconvolved individually (as is the case at present), they could then be restored with a beam which is constant (in pixels) over the entire range of the mosaic. This would allow analysis of mosaics with standard packages (such as `MIRIAD` or `AIPS`), which is desirable for publicly released surveys. Furthermore, it would allow full exploitation of the improvement in signal-to-noise made possible by the multiple observations of overlapping fields. For optical comparisons, survey mosaics could be regridded to an appropriate projection.

5.3.2 Sensitivity to extended emission

The MOST is a redundant array sensitive (after deconvolution) to the full range of spatial frequencies to the limit set by its extreme spacings. The minimum geometric

[4] By 'global calibration error' I mean the systematic calibration error in the survey compared with other MOST observations. The systematic uncertainties in the MOST calibration frame, to which all observations are compared, are expected to be less than 5% in flux density and $0\farcs5$ in RA and Dec. (Hunstead, 1991 and personal communication, 1997).

spacing (42.85λ), implies a maximum detectable angular scale of about 1.3°. However, Hogan (1992, p38) has found that the actual synthesised beam of the MOST is best fit with a model including an effective minimum spacing of about 70λ. This parameter varies between observations and appears to be a function of meridian distance. Angular scales greater than about $30'$ are typically poorly detected. The MOST's synthesised beam can also vary significantly during an observation due to environmental effects and minor telescope performance variations.[5] The result is that the theoretical beam used for deconvolution sometimes does not model well the beam of an observation. Deconvolution of very extended structure is more affected as it is in the short spatial-frequency regime that the theoretical and actual synthesised beams differ most. As a result, images can exhibit a 'negative bowl artefact'. In the MOST Vela SNR survey, this effect causes a negative background level of about $-10\,\mathrm{mJy\,beam^{-1}}$ around Vela X.

Two other non-idealities in MOST imaging affect the extended emission in this survey. The first is the lack of short-spacing information characteristic of interferometers. The total flux densities of the Vela SNR and separately of the Vela X region cannot be estimated since much of the flux density is distributed smoothly on scales larger than the MOST's maximum detectable angular scale. The second non-ideality comes from the mosaicing: the image from each of the 63 individual observations was deconvolved separately, yet structure outside a given field can contribute to sidelobes in that field. At present these artefacts are not treated. An improved technique which could be used in future Wide Field surveys would be to deconvolve each image with the relevant synthesised beam while also removing contributions from strong, nearby off-field sources. This method has already been used by Taisheng Ye when developing software for reducing the first epoch MOST Galactic Plane Survey. He modelled and subtracted grating rings due to off-field sources in data observed prior to 1989. Subsequent telescope modifications have substantially reduced the effect of grating rings in MOST images.

Nevertheless, the MOST Vela supernova remnant survey is excellent at detecting very low surface brightness emission. The artefacts and limitations discussed above are well recognised and can generally either be ignored or corrected for the purposes of the present research. Extended structure at levels as low as $6\,\mathrm{mJy\,beam^{-1}}$ is clear in the images. Although the rms in individual pixels is around $2\,\mathrm{mJy\,beam^{-1}}$, typical extended structure covers many pixels and is reliably measured at lower levels than would usually be accepted for point sources. The presence of this low level structure in a VLA image of Vela X made at 1.4 GHz (section 8.3.1) confirms the existence of similar emission seen at 843 MHz elsewhere in the survey.

5.4 The full survey image

An image of the complete MOST survey of the Vela SNR is shown in figure 5.1. To assist in identifying the various objects and emission regions within the survey,

[5] A few bays sometimes lose pointing fidelity during the course of a 12 hr synthesis observation.

a cartoon covering the same area is presented in figure 5.2. In this section I will briefly describe the overall view it gives us of the Vela SNR and other astronomical sources. I will also point out artefacts which affect the image. Further interpretation and intercomparisons of detailed sub-images with data at other wavelengths are presented in chapters 7 and 8.

5.4.1 The Vela supernova remnant

Morphologically, there are several distinct regions apparent in the image. Near the centre is the bright nebula known as 'Vela X', which is thought to be powered by the Vela pulsar (PSR B0833−45). The nebula is composed of a network of complex filaments. Significant extended structure is also present but not detected by the MOST. This region will be seen more clearly in subsequent images and is discussed with those images in chapter 8.

In the north-east quadrant of the image there are several filaments from the shell of the Vela supernova remnant and at least one H II region. There are also partial elliptical artefacts due to strong H II regions outside the survey area. Broadly speaking we can categorise the extended structure in this area on morphological grounds. To the north-east of the Galactic Plane, much of the structure is diffuse and randomly oriented and may be Galactic emission unrelated to the Vela SNR. Most of the extended emission between the Galactic plane and the Vela X nebula *is* due to the Vela supernova event. These shell-like features have some correspondence with optical filaments and X-ray emission in the area (see chapter 7) and they are generally concave towards the centre of the SNR. This is the area known in the literature as Vela Y (see, for example, Dwarakanath 1991; Milne 1968b). Directly to the east of Vela X is the radio peak known as Vela Z—this area is confused by the elliptical sidelobe from the bright H II region RCW38 (Rodgers et al. 1960), not included in the survey. This strong source produces significant artefacts which obscure nearby faint sources. The area around RCW38 is included in the first epoch MOST Galactic Plane survey (Whiteoak et al. 1989; Green 1994).

On the southern side of the central nebula another region of shell-like emission is probably also part of the Vela SNR ($08^{\rm h}32^{\rm h}-49°00'$). Future observations of the area using the MOST in its new Wide Field mode will look for additional shell emission to the west, corresponding to the faint radio shell seen by Duncan et al. (1996), as part of a survey of the entire Vela SNR region.

5.4.2 Artefacts

Various sections of ellipses present in the image are grating rings, artefacts due to the periodic structure of the MOST. These are in general of variable amplitude, since they pass through several individual fields where the grating rings have different relative gains. This is one way we have of separating these artefacts from actual sky emission. Much of the survey is dynamic-range limited; in the less complicated regions the rms noise is of order 1–2 mJy beam^{-1}.

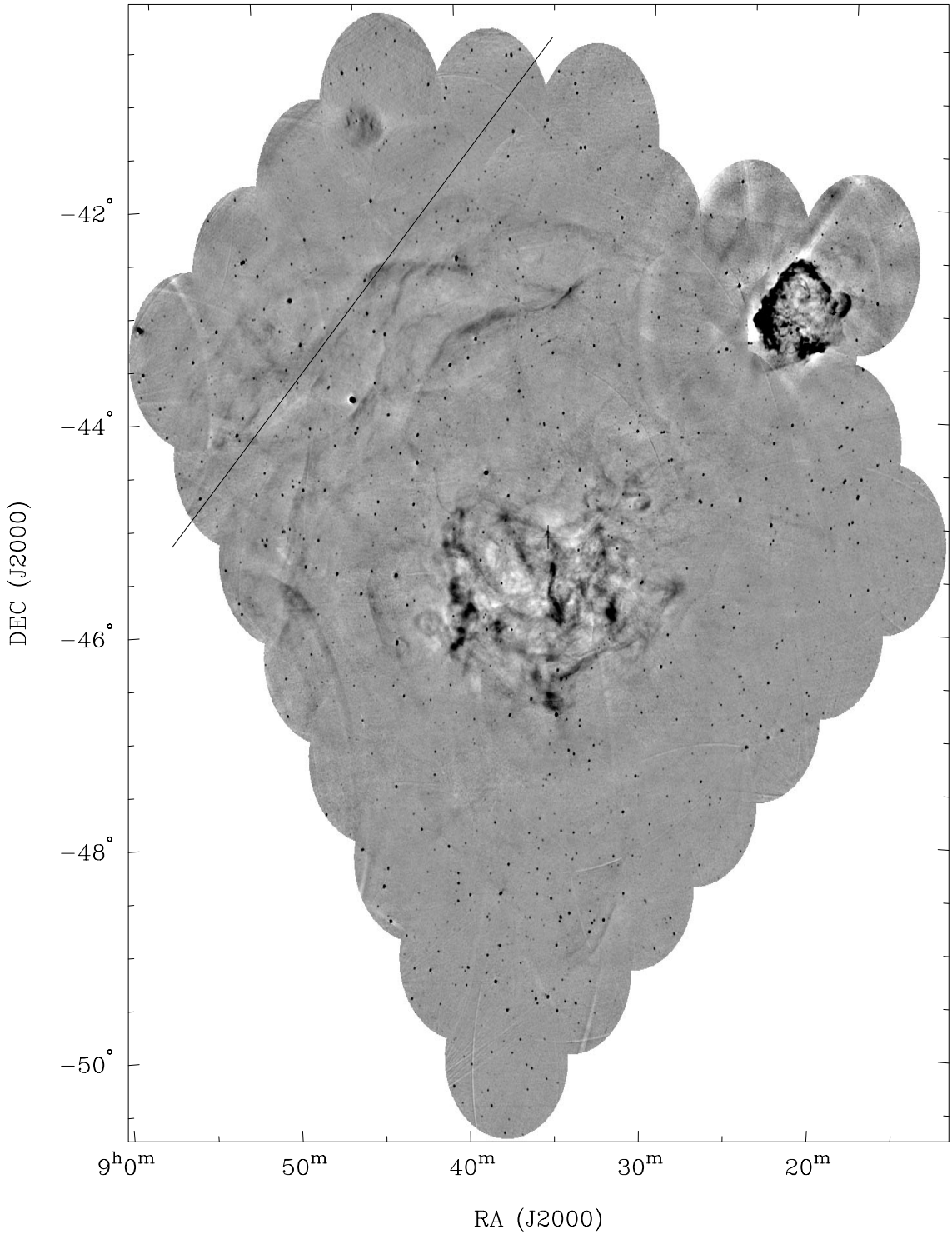

Figure 5.1 The MOST Vela supernova remnant survey. Vela X is the central, nebulous region composed of many filaments in an area about 2° across, centred on $08^{\rm h}35^{\rm m}-45°30'$, with the Vela pulsar (suppressed in this image) offset from the centre of the nebula at a position marked with a cross. The radio shell can be seen most clearly around $08^{\rm h}42^{\rm m}-43°00'$. The separate SNR, Puppis A, is also included in the survey, at $08^{\rm h}22^{m} - 43°00'$. The image greyscale is saturated outside the intensity range of −20 to 30 mJy beam^{-1}. The minimum is −50 mJy beam^{-1} (the negative bowl of Puppis A) and the maximum is a 1.1 Jy unresolved source. The position of the Galactic Plane is marked with a line.

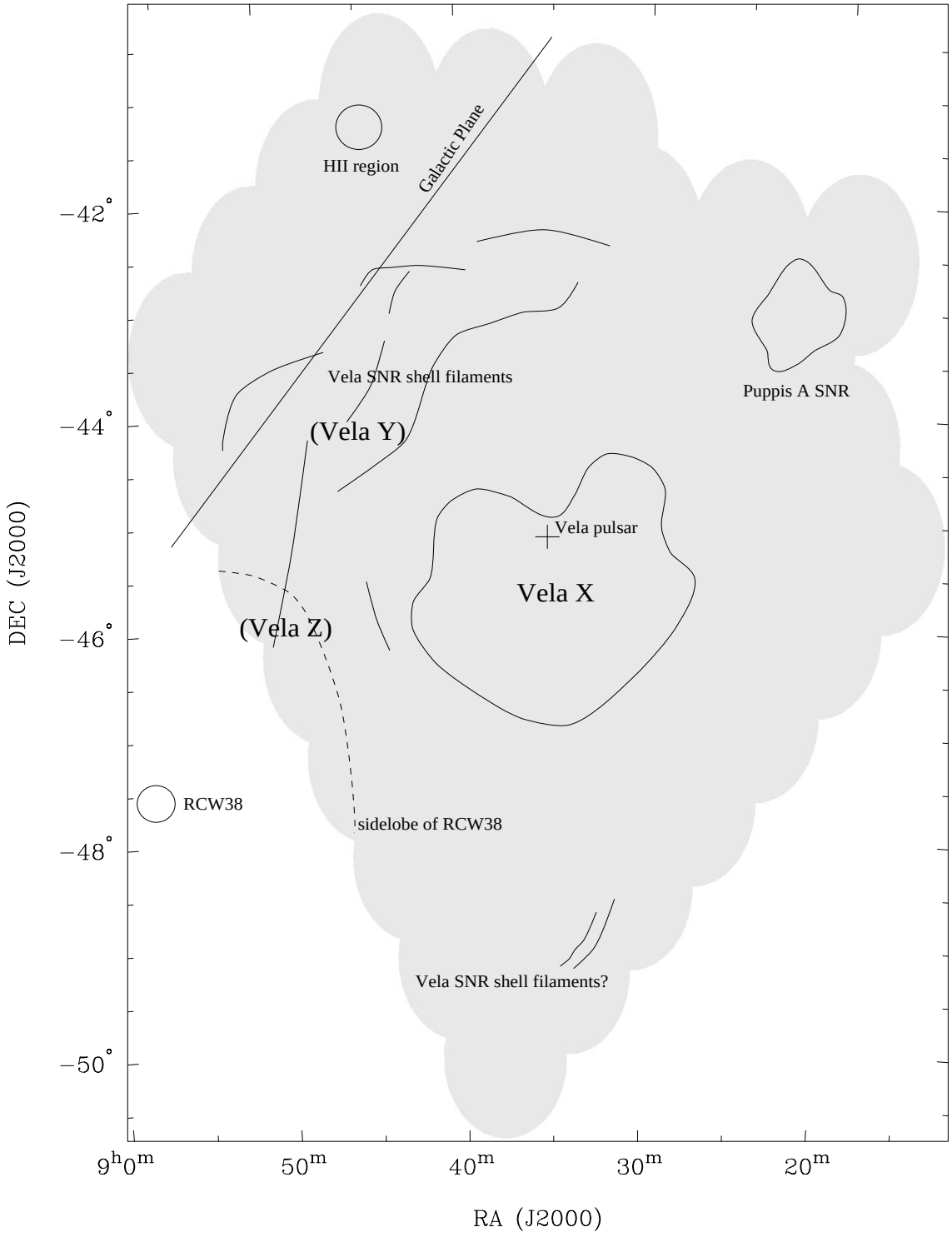

Figure 5.2 A cartoon of the MOST Vela supernova remnant survey. The plot is of the same area as figure 5.1, showing several key features of the survey. The radio peaks (in total power observations) of Vela X, Y and Z are marked at the positions adopted in the literature (see, for example, Dwarakanath 1991; Milne 1968b). The names Vela Y and Z are superseded now that these regions have been resolved to show the filamentary structure.

In the region of Vela X the image is affected by a lack of short spacing information and by the presence of a 'negative bowl' caused by incomplete deconvolution. These effects are discussed in chapter 8, where the close-up image of the Vela X region is presented.

5.4.3 Astronomical objects not connected with the Vela SNR

The survey contains many unresolved and barely resolved sources, most of which are presumably background sources.[6] In section 6.4 some of these are catalogued for use in assessing position and flux density reliability of the MOST in its new Wide Field mode. Several of these sources have unusual coincidences with extended emission. From the survey it is unclear whether they are in fact background sources, or whether they are 'knots' in the SNR emission. VLA observations of some of these sources are described in section 8.2.

The unrelated supernova remnant Puppis A (figure 5.3) is contained within the survey. It is an oxygen-rich SNR of age about 3700 yr (Winkler et al. 1988), with a usually adopted distance of 2 kpc (Arendt et al. 1990). Puppis A has previously been imaged with the MOST (Kesteven & Caswell 1987; Arendt et al. 1990). Its inclusion in this survey was made to determine whether any of the radio emission in its vicinity is obviously associated with the Vela SNR. No obvious changes in the structure of Puppis A have occurred in the 10 years since the previous observations.

5.5 Discussion

The survey presented contains the highest resolution observations yet made of the bulk of the Vela supernova remnant and resolves the structure of the remnant in more detail than has been possible for any other composite remnant. The resolution of this observation of the Vela X region is a factor of two greater than that presented by Frail et al. (1997), and covers the entire plerion, unaffected by primary beam attenuation. Although the survey does not contain information at the lowest spatial frequencies, this structure may be inferred from single dish observations at higher frequencies (Milne 1995; Duncan et al. 1996), which show that the filamentary emission in the survey covers the same area as the more diffuse emission from Vela X seen in total power images. A future project will be to combine the 1.4 GHz VLA image of Vela X (presented in section 8.3.1) with a Parkes image at approximately the same frequency.

As discussed in section 4.4.1, spectral index measurements have in the past been used to distinguish between two distinct regions of the Vela SNR: the shell and plerion. This puts Vela in the composite class with supernova remnants such

[6] About 37 small-diameter sources above 5 mJy are found per square degree in MOST images away from the Galactic Plane (Large 1990).

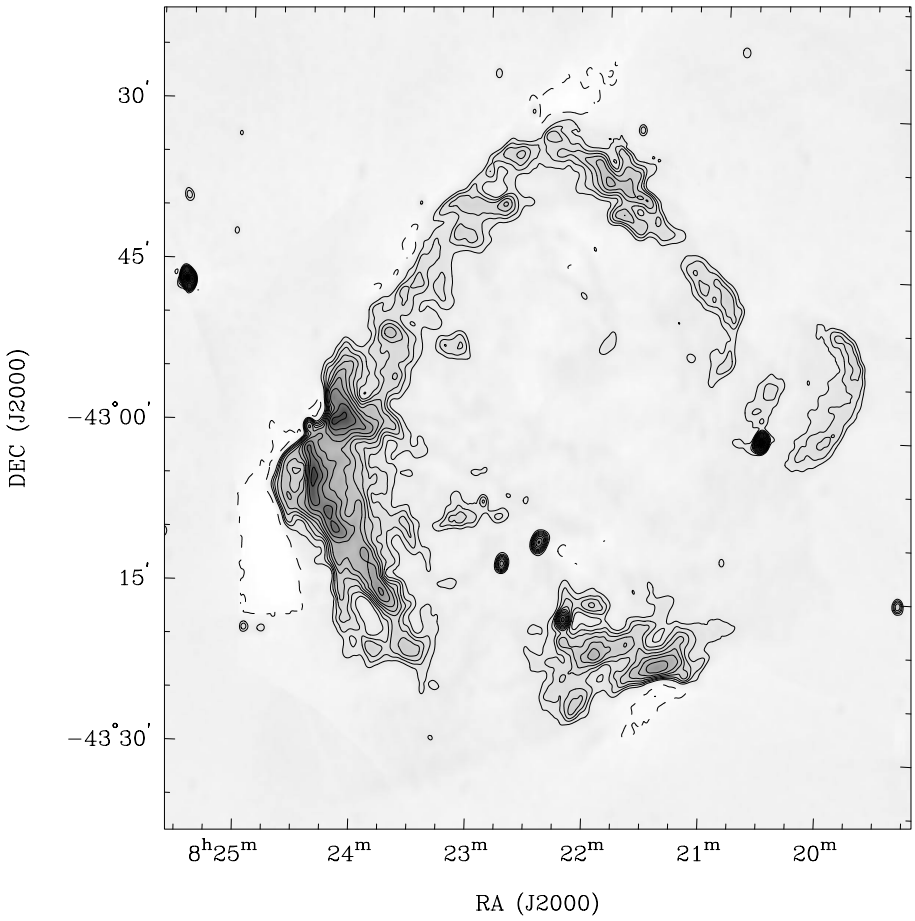

Figure 5.3 A detailed view of the supernova remnant Puppis A within the Vela supernova remnant survey. Contours are the same as used by Arendt et al. (1990): −20 (dashed), 20, 35, 50, 70, 95, 125, 170, 230, 300, 400, 530 mJy beam^{-1}. Note that Arendt et al. added single dish data to their image. The contrast between the images highlights the significant additional flux present at low spatial frequencies.

as G326.3 − 1.8 (MSH 15 − 56: Clark et al. 1975; Whiteoak & Green 1996) and G0.9 + 0.1 (Helfand & Becker 1987). In the survey presented in this chapter, we now see the shell and plerion in much finer detail. Indeed they separately show strong similarities with what we see in the few well-studied supernova remnants observed at similar resolutions: the shell filaments are comparable to those seen in the Cygnus Loop (Green 1984a; Straka et al. 1986), while the filamentary structure within the plerion is reminiscent of the filaments in the Crab SNR (see, for example, Bietenholz & Kronberg 1990). It is clear morphologically that the Vela SNR has both a shell and a plerion and hence belongs unassailably in the composite class.

Given this classification and our ability to study the Vela SNR in detail, it can now be considered as the archetypal Galactic member of the composite class. In angular extent, the Vela SNR is respectively 50 and 12 times larger than G0.9 + 0.1

and G326.3 − 1.8. In this thesis, attention is further focussed on the Vela supernova remnant in chapters 7 and 8.

Chapter 6

Vela and the MOST Wide Field System

This chapter continues the description of the testing process which has formed part of the commissioning of the MOST Wide Field system. This process uses the successful observation of the MOST Vela Supernova Remnant Survey (chapter 5) as a testbed. The chapter begins (section 6.1) with a brief description of the main reduction software. Section 6.2 presents a MOST Wide Field observation of part of the Vela SNR and uses it to describe the main features of WF images. Discussions of the performance of the WF system when imaging extended and small-diameter sources are given in sections 6.3 and 6.4. The results of preliminary noise measurements (section 6.5) are followed by conclusions (section 6.6).

6.1 Wide Field reduction software

Two programs have been developed for the reduction of MOST Wide Field observations, `newsyn` and `mstkln`. They are briefly described below. Each has characteristics which make it appropriate for certain tests and each is still under development at the time of writing (1997 July). The earlier tests in chapter 3 also made use of these programs. In the investigations described in this chapter, I have specified in each case which program was used for synthesis. In section 6.4 I have provided results from the MOST Vela SNR survey (a mosaic of 3–block fields) which may be compared with Wide Field data when the synthesis programs are further advanced. Unless otherwise stated, all analyses below use the meridian distance (MD) gain correction of Burgess (1989), applied to each fan beam according to its actual MD, rather than the MD of the field centre.

`mstkln` David Crawford's program `mstkln` (Crawford 1997a) is the latest in the suite of `mst` programs and implements an algorithm for determining CLEAN components from the original beam responses, deriving time-dependent calibration parameters from the strongest sources. Gaussian CLEAN components are restored in

a residual image synthesised using the back projection algorithm (Crawford 1984; Perley 1979) as implemented in `mstimg`, the program which was used for some of the tests described in chapter 3. `mstkln` allows easy control of many image-making parameters.

`newsyn` The program `newsyn` (Lawrence Cram) is an adaptation of `fitsmsyn` (Ye 1996), which has been used for the majority of MOST synthesis observations in recent years. `newsyn` uses the back-projection algorithm exclusively but determines a time-dependent calibration from the original beam responses using the method of Cram & Ye (1995). It allows somewhat less control of certain imaging parameters, such as restoring beam size, primary beam model and output map characteristics (e.g. pixel size, projection etc). `newsyn` uses a restoring a beam of $43\farcs0 \times 43\farcs0 \operatorname{cosec} |\delta|$ FWHM (RA×Dec.) and the tilt primary beam model of Reynolds (1986, p20) with the scaling factor $\cos^{-1}(MD)$ rather than Reynolds' original $\cos^{-1.2}(MD)$.

6.2 Characteristics of MOST Wide Field images

6.2.1 A sample observation

In this section I present two images derived from an early MOST Wide Field observation. The 12 hour observation was made on 1997 January 31, with the MOST collecting data in its Wide Field (7–block) mode. The area chosen for the observation was within the boundary of the Vela supernova remnant (SNR) but away from the brightest emission of the central nebula, Vela X. The area has been covered by a previous MOST survey of the Vela SNR region (chapter 5), allowing a comparison between imaging with the new system and a composite image of $70'$ (3–block) fields made using the old system. The observation (at Galactic latitude $b = -4.4$) is far enough from the Galactic Plane to avoid dynamic range limitations and shows faint structure well.

The first image, shown in figure 6.1, is essentially a 'raw' image, formed directly by back-projection (Perley 1979; Crawford 1984), as has been used at the MOST since observations began in 1982. Samples corrupted by interference have been excised from the data, but the image is uncalibrated. The only corrections that have been made to the observed data are directly measurable gain corrections due to different signal paths in the beam-forming networks and subsequent amplifiers. The image was made with `mstkln` and has not been deconvolved. The image demonstrates immediately one of the key strengths of the MOST: its ability to form an astrophysically usable image directly. Post-processing is used to enhance images but is not *essential* for basic imaging. This makes the extended emission in MOST images inherently reliable.

Image 6.2 is an image post-processed as a typical survey observation might be. The data have had calibrations and astronomically-derived gain corrections for the

frequency	843 MHz
bandwidth	3 MHz
declination range (12 hour synthesis)	$-90^\circ \leq \delta < -30^\circ$
image	elliptical, $163' \times 163'$ cosec $\lvert\delta\rvert$
resolution	$43'' \times 43''$ cosec $\lvert\delta\rvert$
polarisation	right circular (IEEE)

Table 6.1 Key characteristics of a MOST Wide Field observation

MD of observation, for temperature, and for the tilt and MD primary beamshapes applied. The image, made with `newsyn` of 1997 June 20, has been deconvolved but not self-calibrated.

The basic characteristics of a Wide Field observation are summarised in table 6.1.

6.2.2 Features of the images

Size and resolution At declination δ, a 7–block MOST Wide Field image has size $163' \times 163'$ cosec $\lvert\delta\rvert$ (right ascension $\times$ declination) and synthesised FWHM beamsize $43'' \times 43''$ cosec $\lvert\delta\rvert$. This aspect ratio is a direct result of the foreshortening of the MOST in the terrestrial east-west direction when observations are made away from the meridian. The images presented here, at declination -48°, are each $163' \times 231'$ in size, with an elliptical fully synthesised area of 8.2 square degrees. The synthesised beam to half power points is $43'' \times 61''$.

Compact sources A typical Wide Field image will contain about 200 extragalactic sources stronger than 5 mJy, of which most will be unresolved.[1] In the image in figure 6.1 the sources towards the edge of the field are attenuated with respect to those at the field centre as the primary beam correction has not been applied. The rays emanating from sources at position angles 80° and 260° show the effect on the point spread function of the removal of data (4% of the total) affected by solar interference. Deconvolution has removed this effect from the image in figure 6.2. The other rays emanating from the sources in both images are due to gain variation over 12 hours see below). Note that both images are scaled in order to show low-level emission and artefacts. As a result strong sources saturate the display levels and appear larger than weak sources.

Noise variation across the image The signal-to-noise ratio in any Wide Field image decreases with distance from the field centre. The uncorrected image in figure 6.1 has constant noise, with lower gain towards the edge of the field. After

[1] A determination of the source density expected in MOST images was made by Large (1990) from data presented by Subrahmanya & Mills (1987).

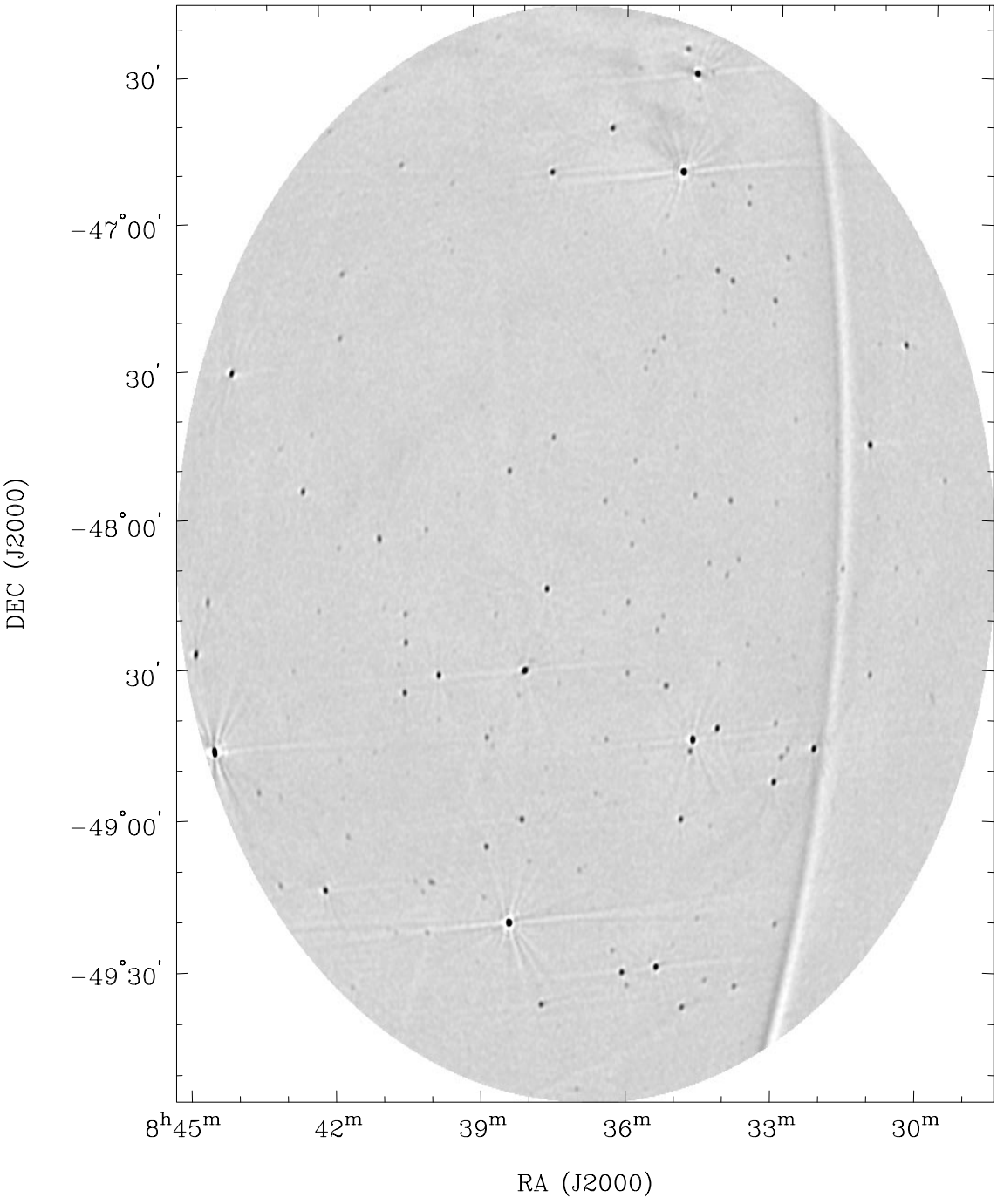

Figure 6.1 A raw MOST Wide Field image of a part of the Vela supernova remnant region, produced directly from the raw data using the back-projection algorithm as implemented in `mstkln`. The greyscale is from −20 (white) to 100 (black) mJy beam^{-1}.

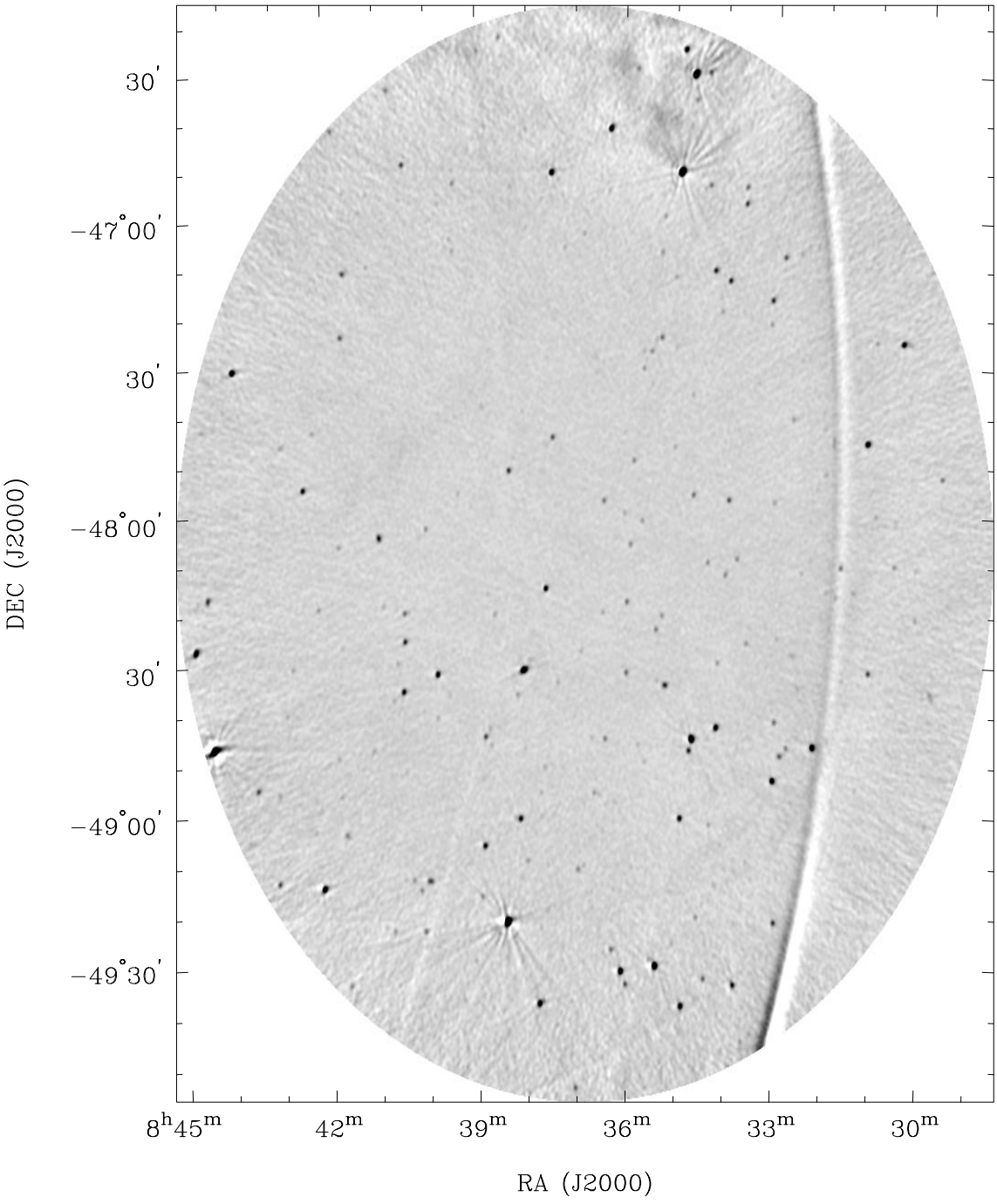

Figure 6.2 A deconvolved image made from the same data as figure 6.1 using `newsyn`, with astronomically measured calibrations and beamshapes applied. The greyscale is from −20 (white) to 100 (black) mJy beam^{-1}.

corrections, the image in figure 6.2 clearly shows a higher noise towards the edge of the image, but the gain is more uniform across the whole field.

Gain variation The brighter sources in both images have 'rays' emanating from them. The causes are random position offsets due to ionospheric variation, and gain variations due to humidity changes and the unmodeled components of temperature variation. The effect is emphasised by the scaling of the images. In fact the rays are at the 2% level. This effect is usually reduced using the adaptive deconvolution of Cram & Ye (1995).

Extended emission The MOST is sensitive to emission on spatial scales up to about $35'$, set by the effective distance between the innermost elements on the east and west arms of $70\,\lambda$ (section 5.3.2). Its continuous u-v coverage from this spatial scale up to its resolution limit makes the telescope excellent for detecting low brightness extended emission such as supernova remnants (see Whiteoak & Green 1996). Extended emission from the central nebula of the Vela supernova remnant is visible faintly at the top of the images. Figure 6.2 shows the emission with the correct gain. Negative regions around the extended emission are the signature of the *negative bowl* which results from the inability to completely deconvolve extended emission. An incomplete model of the synthesised beam of the MOST has caused this. If the distant sidelobes of the assumed synthesised beam were correct the bowl would not be present. A radial profile of the theoretical u-v weighting in the MOST's synthesised beam (assumed in CLEANing) is given in figure 6.3.

Grating rings Following the upgrade to the Wide Field mode, the strongest grating response of the MOST is now an ellipse of size $4.6^\circ \times 4.6^\circ \operatorname{cosec}|\delta|$, set by the regular quarter-bay waveguide spacing of 4.45 m. The obvious elliptical grating ring crossing the image in figure 6.1 is the result of an off-field source. The synthesised amplitude of the grating ring in the figures ranges from 0.1% to 0.8% of the flux density of the source causing it.[2]

6.2.3 Quality of MOST Wide Field images

Position and flux density accuracy The absolute position and flux density calibration of the MOST depends on the observation of calibration sources (see section 2.2.1) before and after the 12 hour observation. The overall calibration of a single Wide Field observation should be maintained within approximately 10% in flux density and $1''$ (1σ) in each of right ascension and declination, degraded by lower signal-to-noise and reduced resolution in the declination direction when made away from the south celestial pole. A source list derived from the MOST Vela SNR

[2]This source is RCW38 (Rodgers et al. 1960), imaged in the first epoch MOST Galactic Plane survey (Whiteoak et al. 1989; Green 1994) with peak flux density $9\,\mathrm{Jy\,beam^{-1}}$.

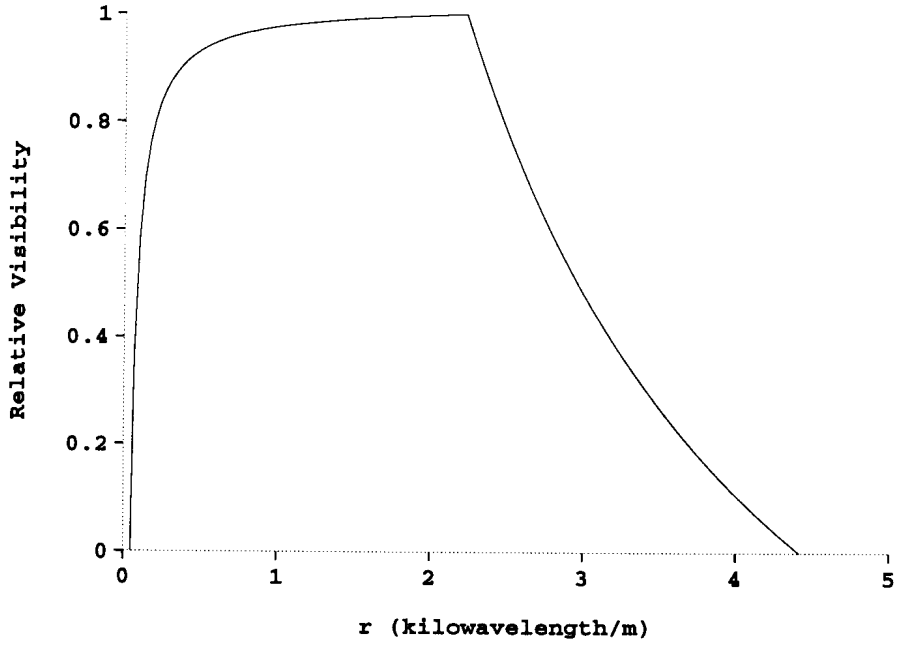

Figure 6.3 A radial profile of the ideal u-v weighting of the MOST's synthesised beam (after Durdin et al. 1984)

survey is presented in section 6.4 for comparison with the observation presented in figure 6.2 when the reduction software (section 6.1) is fully developed.

Source broadening Smearing due to finite bandwidth and time averaging (Bridle & Schwab 1989) broaden the synthesised beam away from the field centre. The effect was negligible in 70′ fields and will be small in Wide Field images: point sources will be broadened by up to 0.″4 in the direction tangential to the field centre and by up to 3.″3 in the radial direction. Peak flux densities may be reduced by up to 1%, but this is well-defined and will be corrected for in large-scale statistical source analyses. Integrated flux density will be preserved. Further details are presented in section 6.4.2.

Dynamic range Gain variations and artefacts limit the effective dynamic range of raw MOST images to about 100:1 (Cram & Ye 1995). It has been possible to improve this by up to a factor of ten for many MOST images using the technique of Cram & Ye (1995). This technique, *adaptive deconvolution*, solves for three telescope parameters (gain, pointing offset and east-west arm relative phase) as a function of time and will be a valuable part of the analysis pipeline.

Signal-to-noise Noise in MOST images is a function of declination, maintenance, interference and weather conditions. It varies with respect to position in the field and is a combination of thermal noise and source confusion from the main beam and sidelobes of the MOST. Wide Field survey images will be mosaiced to recover sensitivity and dynamic range in the overlap regions. Preliminary noise measurements are presented in section 6.5.

6.3 Low brightness filamentary emission

To evaluate the performance of the MOST when imaging extended emission in the Wide Field mode, a 7–block observation of a filamentary region in the Vela supernova remnant was made. In this section I compare this image with a section of the MOST Vela SNR survey covering the same area.

6.3.1 Observations

The single 7–block observation of the Vela X region in the Vela SNR was made on 1997 February 12, employing the technique of pulsar gating which was used for the original MOST Vela SNR survey. Pulsar gating (described in appendix C) suppresses data acquisition during the reception of pulsed emission, attenuating it (in the case of this observation) by a factor of about 50. Artefacts from the intense and variable pulsar would otherwise affect imaging of the weak extended structures in the region. The calibration (SCAN) observations were also gated for consistency. Data were collected for a constant fraction (approximately 620 ms) of each second.[3]

The program `newsyn` (version of 1997 June 20) was used to synthesise and deconvolve the image of the Wide Field data, and the result is shown in figure 6.4. Figure 6.5 shows the corresponding region of the MOST Vela SNR survey (from chapter 5) for comparison.

6.3.2 Discussion

The two images agree in many respects. Extended structure is reproduced by the Wide Field system and the relative surface brightnesses of various regions are approximately preserved. The most obvious difference between the two images is the increased noise in the Wide Field image, a tradeoff of the reduced observing time—the Wide Field image was made with one-fifth of the observing time devoted to the same area of the MOST Vela SNR survey. The rms noise near the edge of the Wide Field image is about 5 mJy; at the edge of the mosaiced image it is 1–1.5 mJy. Near the centre of the image the rms noises are more similar, 3 mJy for the Wide Field image and 2 mJy for the mosaiced image. Some of this increase in noise appears to be due to an error in gain calibration of the Wide Field image: the extended

[3]Normal observations collect data for 940 ms each second. A 60 ms dead time allows the system to stabilise after a pointing change.

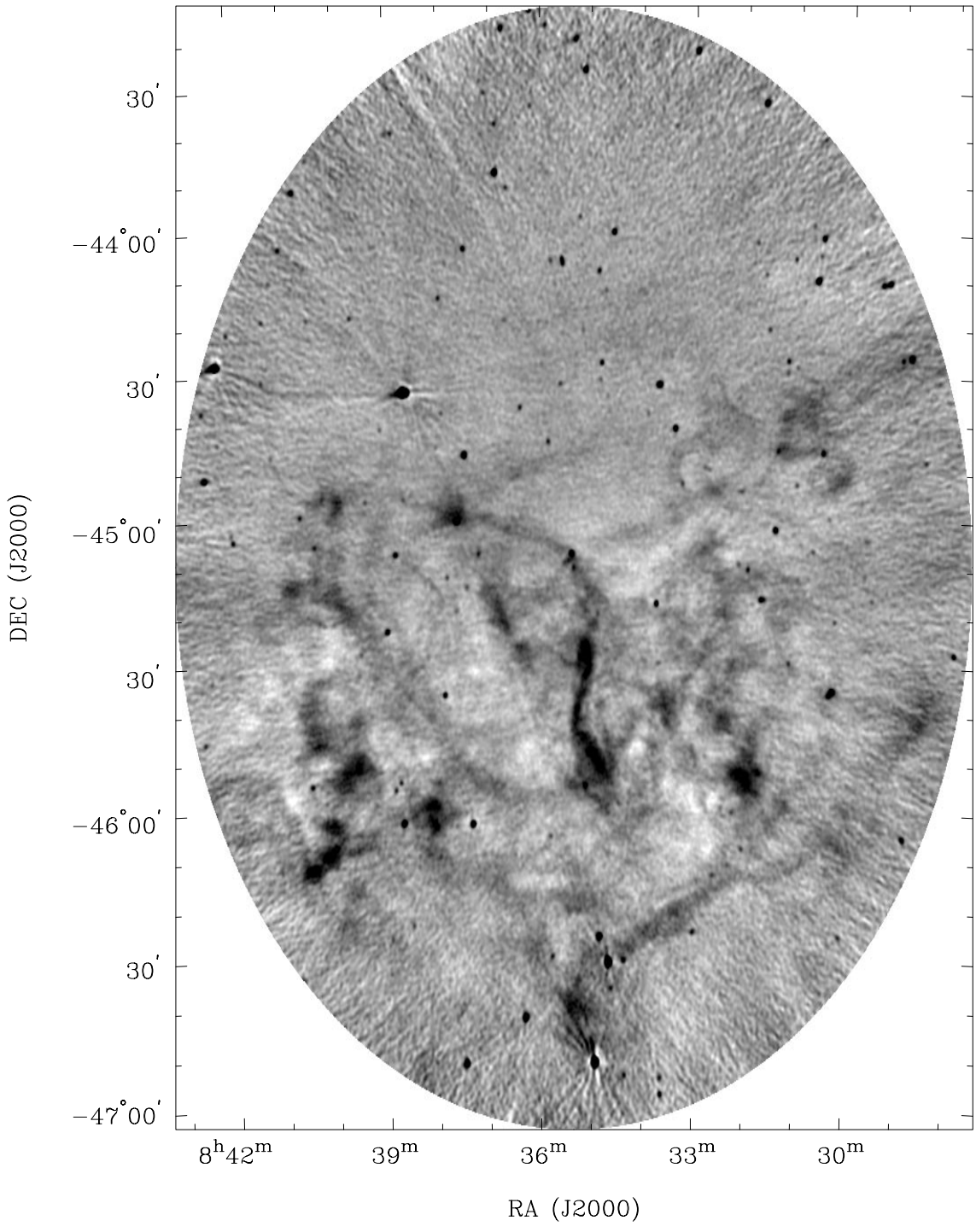

Figure 6.4 A Wide Field image of the Vela X region. The image is saturated with an intensity range of −32 (white) to 50 (black) mJy beam^{-1}. Note that the calibration of this image is not completely secure as the synthesis program was still under development.

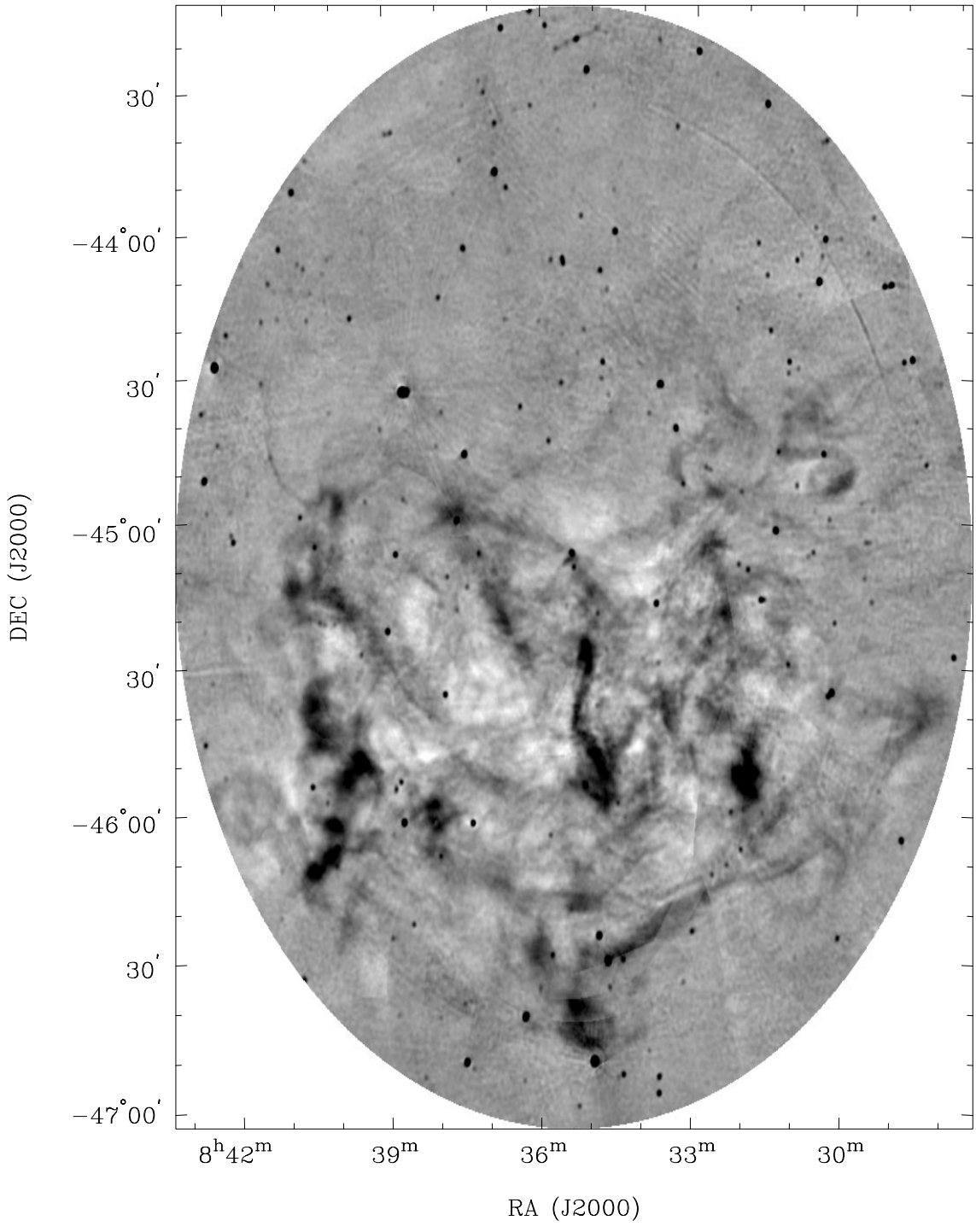

Figure 6.5 A composite of 70′ (3–block) images (from the MOST Vela SNR survey) covering the same area as figure 6.4. The image is saturated with an intensity range of −20 (white) to 30 (black) mJy beam^{-1}.

emission is about 50% brighter in that image. Noise analyses of 'quiet' fields are presented in section 6.5.

The extended structure in the Wide Field image has been more reliably reproduced because deconvolution of the images forming the mosaic was hampered by the presence of off-field sources in the primary beam. Deconvolution of Wide Field images could be further improved with a better tilt primary beam model and by the use of a maximum entropy technique for deconvolving extended emission. The Wide Field image is without the mosaicing artefacts that appear in the mosaiced image, and without the grating ring of the pulsar, since all the data for the image were obtained using pulsar gating. These improvements make the Wide Field observing mode superior for imaging large regions of extended structure.

6.4 Position and flux density reliability

At the time of writing, none of the available synthesis programs appeared to be giving sufficiently accurate positions and flux densities to make detailed comparisons across an entire Wide Field image useful. Here I present a catalogue of sources in a region of the MOST Vela supernova remnant survey (a mosaic of the 70′ fields) which may be used for comparison with Wide Field data in future Wide Field tests. One such comparison field has already been observed: MOST archive field I0835471. A preliminary image was presented as figure 6.2. The effect of bandwidth and time-average smearing on Wide Field images is also discussed below.

6.4.1 Source measurement

The program `mstflx` (Crawford 1997a) was used for all the source measurements described in this section. It allows multiple measurement passes by providing an ASCII format output file that can be also be used as an initial source list for a further measurement pass.

To form the catalogue an initial source list was produced by requiring `mstflx` to find and fit all sources with integrated flux densities above 10 mJy. This list contained several spurious and extended sources. A careful visual inspection of the image was used to separate various classes of sources. From the original list of 94 sources, 73 unresolved or just-resolved sources were retained for the catalogue. Twelve spurious and 9 extended sources were discarded.

Results Flux densities and positions for the sources selected are given in table 6.3. The errors quoted in the table are formal errors of fit. Additional errors in the calibration of the MOST Vela SNR survey were described in section 5.3.

6.4.2 Bandwidth and time-average smearing

The effects of bandwidth and time-average smearing (Bridle & Schwab 1989) become significant in Wide Field images.

Time-average smearing Time-average smearing in images from the MOST is a result of the averaging of data collected over several (up to 28) seconds into a single sample. The stepping pattern of the MOST for 7–block observations was given in table 2.1. Each datum in the 28 s sample consists of two measurements, made with each sense of the low phase switch. These 1 s measurements are made for each possible combination of block number and interlacing offset and may be made up to 27 s apart. Simulations of the effect of time-average smearing were made by adding artificial Gaussian point sources corresponding to individual single-second measurements into blank images at appropriate spacings.[4] These show that this effect is small: sources would be broadened by at most $0\farcs6$ and have peak brightnesses reduced by about 1%. Positions of the broadened sources will still be correct, since the switching pattern is symmetric.

Bandwidth smearing Bandwidth smearing in MOST images arises because the delays inserted in the signal paths returning from each bay are correct for the beam at the field centre, while all the other beams are generated using a frequency-independent phase gradient. This is appropriate for the central observing frequency of 843 MHz. At other frequencies, the inserted delays will be inappropriate for those beams pointed away from the field centre. It is possible to estimate the maximum effect: a source will be broadened as if convolved in the radial direction by a rectangular function of width

$$\frac{\Delta\nu}{\nu} R = 17'',$$

where $\nu = 843$ MHz is the observing frequency, $\Delta\nu = 3$ MHz is the bandwidth and $R = 4900''$ is the radius of a (near-polar) Wide Field. This corresponds to a source broadening in the radial direction of $3\farcs3$. To first order, the average position will still be correct. The component of the broadening in the declination direction scales as $\mathrm{cosec}\,|\delta|$.

This effect could be reduced with modifications to the Telescope Control Computer code: the inserted delays could be changed each second to be correct at the centre of each block. The magnitude of the effect at the edges of 7–block observations would be reduced by a factor of seven.

6.5 Noise levels in Wide Field images

Knowledge of the noise levels in MOST Wide Field images is an important aspect of telescope performance for planning the extragalactic survey since one of the major

[4] One second of time corresponds to $0\farcs353$ in position at the edge of a 7–block image.

scientific objectives is to detect the faint population of radio sources below 5 mJy. The purpose of the tests described here was to quantify the noise levels in MOST Wide Field images by observing quiet regions of the sky.

6.5.1 Observations

Observations were made of four fields in areas of the sky free of strong sources, spread over a range of declinations. To select the fields the following procedure was adopted. A grid was made of possible field centres in the region of each preferred right ascension (night-time observations typically suffer less interference and result in images with lower noise) and desired declination. The 5 GHz Parkes–MIT–NRAO survey catalogues (zenith and southern regions: Wright et al. 1994; Wright et al. 1996) were searched for the strongest source which would fall in the chosen 7–block field ($S_{\mathrm{max(5\,GHz)}}$); and for the strongest source which might cause a 4.°16 grating ring to fall in the field ($S_{\mathrm{grating(5\,GHz)}}$). In each region a field was selected which approximately minimised $10\,S_{\mathrm{max(5\,GHz)}} \times S_{\mathrm{grating(5\,GHz)}}$.[5] The fields selected, with $S_{\mathrm{max(5\,GHz)}}$ and $S_{\mathrm{grating(5\,GHz)}}$ listed, are shown in table 6.2. These fields were observed in normal Wide Field mode on 1997 March 5, 10 and 17, and 1997 June 6. Details of the observations and of the calibrations applied in synthesis are given in table B.1.

6.5.2 Analysis

An image of each observation was synthesised using `newsyn`. Residual images were obtained by the removal of CLEAN components using the CLEAN algorithm as implemented in `newsyn`, which stops when the previous 100 components have a negative sum. For each field, the peak in the residual map at which CLEANing terminated is shown in table 6.2. Note that corrections for meridian distance gain and the bay primary beam have been applied.

To examine the variation of noise with position in the residual images, each image in turn was divided into boxes of 20×20 pixels. The rms in each box was calculated. The results were used to make new 'rms' images, which are shown in figure 6.6. This box size was chosen to minimise the impact of real sources not fully deconvolved while retaining reasonable resolution in the rms image. Each rms image is overlaid with a single elliptical contour. This contour indicates a locus of $\sqrt{2}$ increase in noise derived from a single elliptical Gaussian fit to the image. The shape of the rms image is influenced by the primary beam model and is actually only approximately fitted by a Gaussian. However, the residual of the fit was small within the contour shown in each case. Table 6.2 shows the parameters of the fit: the semi-axes of the ellipse in right ascension and declination directions and the minimum rms noise. The elliptical Gaussian was constrained to be centred at the

[5]This criterion reflects two facts. First, the magnitude of artifacts is proportional to the flux density of the source responsible. Secondly, the incidence of a grating ring due to an off-field source is less serious than the presence of a source of similar flux density in the field.

MOST archive name	Dec. (J2000)	$S_{\max(5\,\mathrm{GHz})}$ (mJy)	$S_{\mathrm{grating}(5\,\mathrm{GHz})}$ (mJy)	S_{resid} (mJy)	$\sigma_{\min}$ (mJy beam^{-1})	$R_{\sqrt{2}\sigma}$ RA (′)	Dec. (′)
I2027321	$-32\overset{\circ}{.}2$	194	2058	28.1	1.90	53	69
I1200481	$-48\overset{\circ}{.}0$	156	2383	8.3	1.62	61	72
I0936661	$-66\overset{\circ}{.}0$	135	1193	8.1	1.47	68	74
I1014711	$-71\overset{\circ}{.}8$	115	1183	7.1	1.38	78	80

Table 6.2 Characteristics of Wide Field noise test observations. The flux densities of the maximum source in each image and of the maximum source which might cause a grating ring within the image ($S_{\max(5\,\mathrm{GHz})}$ and $S_{\mathrm{grating}(5\,\mathrm{GHz})}$) are from the Parkes-MIT-NRAO survey. S_{resid} is the peak flux density of the *residual* image. The fitted minimum rms noise measurements ($\sigma_{\min}$) and semi-axes of $\sqrt{2}$ increase in noise ($R_{\sqrt{2}\sigma}$) are derived from a fit of an elliptical Gaussian to the noise images.

field centre. At the time of analysis, the gain calibration of images from `newsyn` was somewhat uncertain. The version of 1997 June 20 was used for this analysis.

6.5.3 Discussion

Several trends are apparent in the noise measurements. First, there is an obvious trend towards higher noise in the field centre at more northerly declinations. These noise measurements, which are approximately linear with cosec $|\delta|$, indicate that the noise at the centre of a Wide Field observation increases by a factor of about 1.4 from declinations $\delta = -90°$ to $\delta = -32°$. Secondly, the noise increases with distance from the field centre more rapidly at more northerly declinations, and this effect is more pronounced in the right ascension direction than the declination direction. In the declination direction the increased field size due to the east-west foreshortening of the MOST partially offsets the increase in noise resulting from the tilt primary beam.

The rms images presented here show considerable small-scale fluctuation. A model with more parameters than a Gaussian would be more difficult to fit. However, a better *a priori* model derived from primary beam measurements would be helpful. Alternatively, several observations of fields at the same declination but (preferably) different right ascension could be analysed.

Crawford (1997b) has measured the correlation of noise between adjacent pixels in MOST images, which arises from the near-identical contribution in the synthesis of beams at certain hour angles. He calculates that the rms in the measurement of a point source in the presence of this noise in a MOST image will be a factor of 0.66 lower than the rms of the image. This leads to typical 5σ detection limits of 4.5 mJy to 6.3 mJy near the centre of images analysed here.

The area *on the sky* of the ellipse of $\sqrt{2}$ increase in rms noise is less at more northerly declinations. This factor, along with the increased rms noise at the *centre* of northern fields, indicates that the extragalactic survey will be significantly more efficient if conducted close to the south celestial pole. Furthermore, at northerly de-

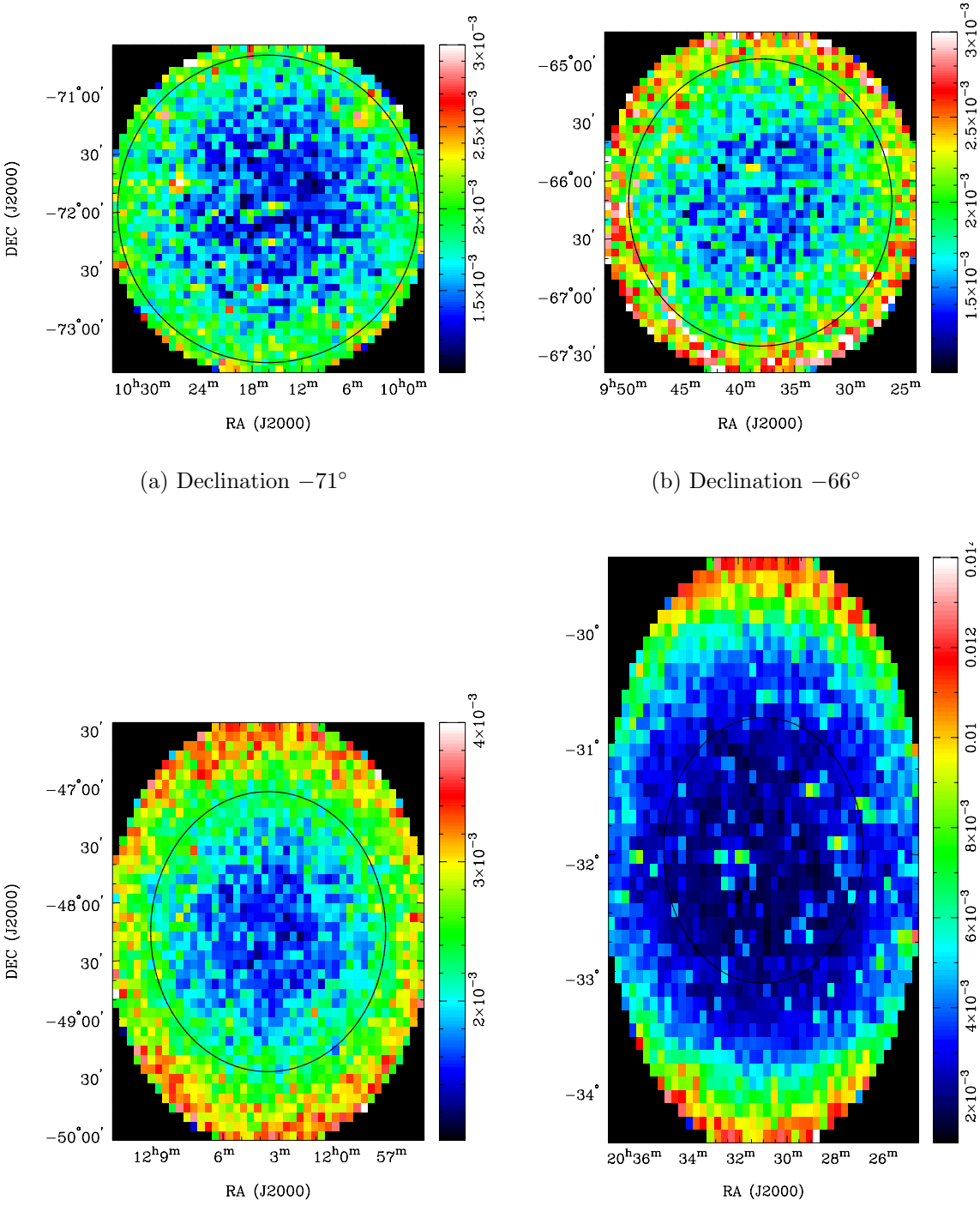

(a) Declination −71°

(b) Declination −66°

(c) Declination −48°

(d) Declination −32°

Figure 6.6 Noise images of four Wide Field observations made in quiet regions of the sky. Each pixel in these images represents the rms (in mJy beam^{-1}) calculated over a box of 20×20 pixels in the residual image. The contour is of an elliptical Gaussian fitted to each image, at a level $\sqrt{2}$ higher than the fitted minimum.

clinations, the choice of survey centres will be complicated by the strong declination-dependence of noise increase with distance from the field centre.

6.6 Postscript

All the tests mentioned in this chapter depend intrinsically upon the data reduction software, which is still under development. Testing of this software will continue for some time. The Astrophysics Department has adopted the approach of developing two alternative reduction programs (`mstkln` and `newsyn`) in parallel to aid the identification of errors and to compare alternative imaging algorithms. However, the tests detailed here and in chapter 3 do show that the performance of the MOST in the Wide Field system is essentially as expected. The reproduction of extended structure is excellent, the artefact levels are low, and the noise performance is as expected.

Since the above test reports above were written, significant progress has been made improving the positional accuracy of Wide Field images. Errors introduced into the data acquisition software caused the solar time in data headers to be wrong by 27 s. This has now been corrected and the positional accuracy of strong images has been improved. Analysis of one field (at $\delta = -35°$) has determined a field offset of $1\overset{s}{.}51$ in right ascension and $1\overset{''}{.}06$ in declination (Crawford 1997c). Flux density weighted rms values for individual sources were $0\overset{s}{.}38$ for right ascension and $0\overset{''}{.}67$ for declination, normalised for a source of 350 mJy. The next task will be the improvement of flux density accuracy in Wide Field images. The dominant uncertainty here centres on the model of the tilt primary beam (which varies with meridian distance). An improved determination of this, or the derivation of an empirical correction to synthesised fields, will be the key to accurate WF flux densities. Every indication is that further development of the synthesis software and telescope models will lead to WF images of exceptional quality. Accordingly, the Wide Field survey observing programme has now commenced.

Recent noise measurements have been made on images derived from 24 observations for the extragalactic survey in 1997 June and July (E. M. Sadler, personal communication 1997). The results are lower than those found in section 6.5 above. Typical northern ($\delta \approx -34°$) images have noise levels of about 1.5 mJy beam^{-1}, while southern ($\delta \approx -70°$) images have noise levels of about 0.9 mJy beam^{-1}. These results confirm the expected noise performance of the Wide Field system.

Table 6.3 Unresolved and just-resolved sources in an 8 square degree region of the Vela SNR survey (a mosaic of 3–block fields). These sources are those detected in a region of the survey covering the same area as a 7–block observation centred on RA(B1950) = $08^{\rm h}35^{\rm m}13\overset{\rm s}{.}9$, Dec.(B1950) $-47°57'59''$ (e.g. MOST archive I0835471). The quoted errors are formal errors of fit. For a discussion of other errors in the MOST Vela SNR survey see section 5.3.

Position (J2000)		RA error	Dec. error	Peak flux density	Flux density error
RA (h m s)	Dec. (° ′ ″)	(s)	(″)	(mJy beam^{-1})	(mJy beam^{-1})
08 29 40.43	−47 52 26.8	0.03	0.5	42.7	0.9
08 30 29.67	−47 25 19.5	0.03	0.4	123.3	2.0
08 31 06.12	−48 31 53.6	0.03	0.5	67.8	1.2
08 31 41.13	−48 10 52.1	0.07	1.1	45.3	2.0
08 32 12.72	−48 46 53.7	0.02	0.3	189.0	1.9
08 32 44.82	−48 47 09.4	0.26	4.1	32.5	5.1
08 32 50.96	−47 08 12.7	0.04	0.6	55.8	1.3
08 32 52.40	−48 48 44.0	0.05	0.7	55.5	1.5
08 32 57.65	−49 21 43.8	0.03	0.5	58.7	1.2
08 32 59.37	−48 42 01.9	0.04	0.6	38.9	0.9
08 33 01.08	−48 53 39.8	0.02	0.3	161.2	1.8
08 33 05.42	−47 17 00.9	0.02	0.4	94.5	1.4
08 33 37.19	−46 53 59.6	0.13	2.0	48.1	3.7
08 33 37.36	−46 57 18.3	0.03	0.4	64.2	1.1
08 33 47.24	−49 34 04.9	0.03	0.5	95.5	1.8
08 33 56.17	−47 13 06.2	0.02	0.3	79.3	1.0
08 33 56.48	−47 57 36.8	0.03	0.4	55.2	0.8
08 34 00.43	−48 12 40.3	0.08	1.2	28.3	1.3
08 34 10.38	−48 43 11.4	0.02	0.3	138.7	1.5
08 34 13.91	−47 11 03.6	0.02	0.3	86.6	1.1
08 34 20.19	−46 53 35.3	0.05	0.8	40.9	1.3
08 34 21.24	−46 30 28.8	0.13	2.0	36.2	2.9
08 34 24.20	−49 33 03.5	0.04	1.0	50.4	1.1
08 34 33.59	−49 20 53.5	0.07	1.1	31.2	1.2
08 34 38.92	−47 56 35.2	0.03	0.4	46.4	0.7
08 34 39.21	−46 30 42.9	0.04	0.6	429.7	10.1
08 34 40.15	−48 45 31.0	0.04	0.6	290.6	6.9
08 34 43.29	−48 47 48.2	0.10	1.6	63.4	3.8
08 34 50.04	−46 25 42.5	0.02	0.4	152.0	2.2
08 34 51.81	−49 38 21.1	0.03	0.4	133.7	2.1
08 34 54.01	−49 01 20.2	0.03	0.4	111.3	1.8
08 34 54.95	−46 50 58.4	0.02	0.3	750.6	8.9
08 35 12.69	−48 34 47.9	0.05	0.8	74.4	2.2
08 35 17.36	−47 24 45.0	0.10	1.6	42.8	2.7
08 35 23.68	−48 23 41.1	0.11	1.8	29.6	2.0
08 35 23.98	−49 30 29.2	0.02	0.3	264.4	3.4
08 35 45.61	−46 29 39.1	0.08	1.2	31.8	1.5
08 35 59.04	−48 18 09.8	0.03	0.5	45.6	0.8
08 35 59.70	−48 32 22.1	0.04	0.6	40.2	0.9
08 36 00.28	−49 34 07.2	0.57	9.4	49.2	17.2
08 36 05.98	−49 31 33.1	0.01	0.2	198.1	1.6

continued on next page

continued from previous page

Position (J2000)		RA error	Dec. error	Peak flux density	Flux density error
RA (h m s)	Dec. (° ′ ″)	(s)	(″)	(mJy beam^{-1})	(mJy beam^{-1})
08 36 17.72	−49 27 14.1	0.04	0.7	40.3	1.0
08 36 25.32	−48 45 35.3	0.05	0.9	31.6	1.0
08 36 26.79	−47 57 52.5	0.04	0.7	36.1	0.9
08 36 58.29	−49 11 20.9	0.06	1.0	32.0	1.2
08 37 01.20	−49 54 29.1	0.04	0.6	48.4	1.1
08 37 28.25	−47 45 00.4	0.04	0.6	48.8	1.1
08 37 36.95	−48 15 27.1	0.02	0.3	132.1	1.3
08 37 45.84	−49 37 52.3	0.02	0.4	144.7	2.1
08 38 21.13	−47 51 42.0	0.03	0.5	72.4	1.2
08 38 25.01	−49 21 43.1	0.01	0.1	847.6	4.2
08 38 50.74	−48 45 00.8	0.06	0.9	59.3	2.1
08 38 52.24	−49 06 39.8	0.02	0.3	100.4	1.2
08 39 26.35	−46 53 09.7	0.04	0.6	33.3	0.8
08 39 48.46	−48 32 26.7	0.02	0.3	140.3	1.4
08 40 01.36	−48 03 16.3	0.05	0.9	29.9	1.0
08 40 06.03	−49 23 25.8	0.03	0.5	47.3	0.9
08 40 25.72	−46 49 08.9	0.03	0.5	60.0	1.1
08 40 27.71	−48 25 48.3	0.02	0.4	77.5	1.2
08 40 28.01	−48 20 04.3	0.05	0.9	47.0	1.5
08 40 29.88	−48 35 48.3	0.02	0.4	101.8	1.3
08 41 37.57	−47 11 14.8	0.04	0.6	53.8	1.3
08 41 38.76	−49 33 52.6	0.04	0.8	33.9	1.0
08 41 41.19	−47 24 11.5	0.05	0.9	47.0	1.5
08 41 41.25	−49 04 12.3	0.07	1.1	33.8	1.4
08 41 49.55	−46 41 55.4	0.05	0.9	36.8	1.2
08 42 10.15	−49 14 35.0	0.02	0.3	200.4	2.4
08 42 28.75	−47 54 54.9	0.02	0.4	106.3	1.6
08 43 05.26	−49 13 22.3	0.05	0.8	63.7	1.9
08 43 29.29	−48 54 47.6	0.03	0.5	58.3	1.1
08 43 50.55	−47 30 30.5	0.02	0.3	198.5	2.3
08 44 22.15	−48 46 23.0	0.01	0.2	1044.2	6.8
08 44 25.79	−48 16 22.4	0.05	0.9	73.8	2.4

Chapter 7

The Vela SNR Shell

This chapter focuses on the shell of the Vela supernova remnant. As the closest composite remnant, with a well-resolved shell (the resolution of the MOST observations correspond to physically interesting scales of 0.1 pc), the Vela SNR is ideal for studying the interaction of expanding shells from middle-aged[1] SNRs with the surrounding interstellar medium. The most well-studied middle-aged shell remnant, the Cygnus Loop, is significantly further away at about 800 pc (Minkowski 1958).

The northern Vela shell is a region bright both at 843 MHz (chapter 5) and in Hα emission (Elliott et al. 1976). Furthermore, it has recently been imaged in X-rays as part of the ROSAT all-sky survey (Aschenbach et al. 1995). The availability of a digital Hα/continuum image made during commissioning of equipment for the Mount Stromlo and Siding Spring Observatories/University of Sydney wide field imaging Hα survey, has allowed a study at comparable resolution in the three wavelength regimes. In section 7.1, I present and discuss the datasets available for the study. In section 7.2, comparisons are drawn, and the observations are considered in the light of observations of similar remnants, and of simple theoretical models. Supplementary MOST observations of the X-ray bullets discovered by Aschenbach et al. are presented in section 7.3.

7.1 Observations of the northern Vela shell

7.1.1 MOST 843 MHz observations

The MOST Vela SNR survey, presented in chapter 5, covers much of the brightest region of the Vela shell. The image in figure 7.1 is a portion of the survey, a cross-section of the northern part of the Vela SNR shell. In this region, the radio emission

[1]The term 'middle-aged' has been used sporadically in the literature. Here, I use it to specify evolved remnants which show significant interaction with the inhomogeneous ISM, so are partly in the radiative phase, but which may still also be partly in the adiabatic stage (as spherical X-ray shells imply in some cases). I specifically exclude 'young' remnants with morphology still dominated by the original explosion, such as Tycho's remnant, and old remnants in the dissipative phase.

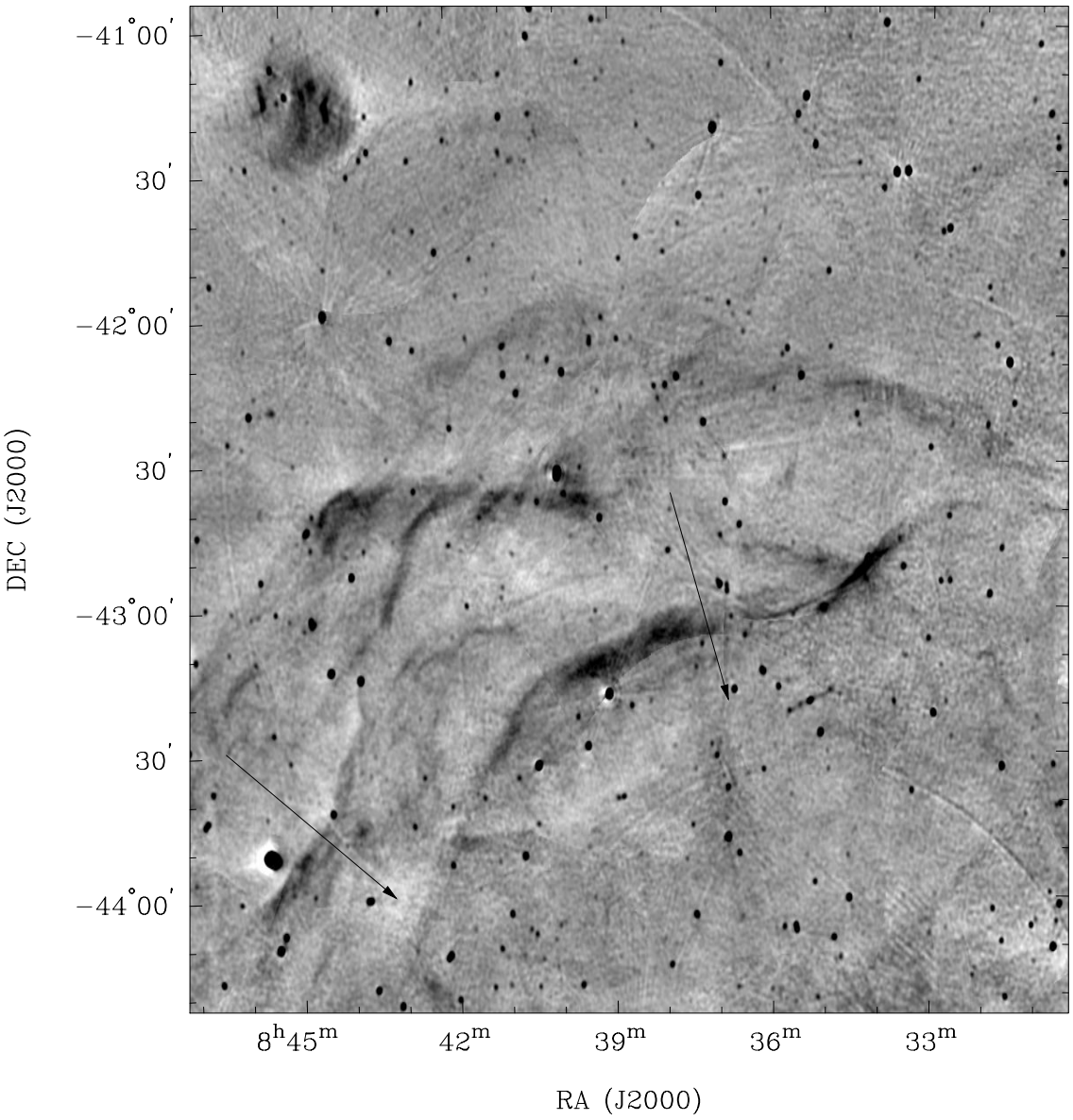

Figure 7.1 MOST 843 MHz image of the northern Vela SNR shell, from the MOST Vela SNR survey (chapter 5). The intensity scale is linear, from −10 (white) to 15 (black) mJy beam^{-1}. The arrows indicate the approximate direction of the centre of the SNR.

from the shell is most prominent, and not confused by emission from unrelated Galactic objects or by artefacts. Recall (from section 5.2) that the survey is of continuum emission, with the MOST receiving circularly polarised radiation. Thus unpolarised and linearly polarised emission will be detected without complication. The image has a resolution of $43'' \times 43''\mathrm{cosec}\,|\delta|$ with rms noise $1\,\mathrm{mJy\,beam^{-1}}$ or less.

The ability of the MOST to image extended structure (section 5.3.2) is crucial to this investigation. Much of the emission present in the image would be undetected by the VLA or the ATCA, even in compact configurations. In this image extended structure above $3\,\mathrm{mJy\,beam^{-1}}$ is visible. The majority of the extended structure is received Galactic radiation and not instrumental artefacts. The authenticity of the observation is confirmed by repetition and by a comparative VLA/MOST study, presented in section 8.1.2. Artefacts in MOST images are relatively easy to identify: the continuous u-v coverage precludes such problems as clean stripes (Cornwell & Braun 1989).

The most commonly seen artefacts are grating rings, sections of ellipses of dimension $1\overset{\circ}{.}15 \times 1\overset{\circ}{.}15\,\mathrm{cosec}\,|\delta|$ with width dependent on the source producing them. The absence of strong sources in the image means a minimal effect. Three other artefacts are easily recognisable: a negative bowl around the bright compact source to the south-east, instances of interference-affected data visible as regions of faint parallel structure, and an abrupt elliptical brightness change in background at $08^{\mathrm{h}}42^{\mathrm{m}}-41°20'$ (a mosaicing artefact). The bright extended source in the north-east corner of the image (seen also in the Hα image) is an H II region. The image contains many unresolved or barely resolved sources, most of which are probably extragalactic. However, some may be Galactic objects, such as compact H II regions, planetary nebulae, pulsars or distant SNRs.

The remaining extended radio emission in the image is presumed part of the Vela SNR. The proper motion of the explosion's stellar remnant, the Vela pulsar (Bailes et al. 1989), indicates that the origin of the explosion was $10'$ to the south-east of the pulsar's present position, using an age for the remnant of 12 000 years. This origin is $2\overset{\circ}{.}5$ away from the centre of this image at position angle = 170°. Greater age estimates (e.g. Aschenbach et al. 1995; Lyne et al. 1996) change this slightly as they increase the distance moved by the pulsar by up to a factor of two. The extended structure in this image is in a series of filamentary arcs across the image at position angles ranging from 70° to 170°. The structure is generally concave towards the centre of the SNR: there are no significant radial filaments. The majority of the filaments are resolved by the MOST, with widths ranging from $1'$ to $6'$ and peak surface brightnesses up to $20\,\mathrm{mJy\,beam^{-1}}$. These filaments generally have a sharp edge on the side away from the centre of the remnant, while towards the remnant centre they may fade over several arcminutes. This probably indicates that the filaments are in fact *edges*, spatially filtered by the MOST so that only the sharp transitions appear. The sharper outside edge is also consistent with the 'projected sheet' picture of filamentary emission (Hester 1987). Both these effects may be important. The degree of the spatial filtering effect is indicated by the small

proportion of the total flux density present in the MOST image. The integrated flux density of the filaments in the MOST image is difficult to measure in the presence of the varying background level, but is about 10 ± 3 Jy. The spectrum of Dwarakanath (1991) (reproduced in figure 4.5) indicates that the main shell components of emission in the Vela SNR should have a total flux density of about 900 Jy. However, it is difficult to measure what fraction of the shell emission is from the area covered by this image, and what part of that is Galactic background emission. The 408 MHz survey of Haslam et al. (1982) implies that as much as 40% of the Vela emission could be Galactic background. In any case the MOST is probably measuring about 10% of the total flux density. The response of the MOST to extended structure was discussed in more detail in section 5.3.2.

7.1.2 Hα observations

An Hα image of the northern Vela shell is shown in figure 7.2, covering the same area as the radio image in figure 7.1. The Hα image is from a test observation[2] made for the MSSSO/University of Sydney Hα Survey (Buxton et al. 1997). This survey has been specifically designed to obtain low resolution ($\sim 25''$) wide field images of approximately the size of a standard Schmidt plate for easy comparison with data from the second epoch MOST Galactic Plane survey.

The observation was made using a 2048×2048 $24\,\mu$m pixel CCD though a 400 mm, f/4.5 Nikkor-Q lens, at the 16-inch telescope facility at Siding Springs Observatory. Pixel spacing in the image is $12''$, giving a field size of 7° square. The portion of this image presented here is taken from the central ($5^\circ \times 5^\circ$) region, where vignetting in the 15 Å filter is not significant.

The image has been derived from two frames with a total exposure time of 1400 s, which were bias-subtracted and flat-field corrected before averaging. No correction has been made for the effect of cosmic rays. No continuum observation was made for subtraction. Consequently the image presented here contains a continuum component in the extended emission and many stars.

A coordinate system was applied to the image by comparison with a Digital Sky Survey image (Morrison 1995) using `koords`, part of the `KARMA` package (Gooch 1996). Within a $25' \times 25'$ box centred on $08^{\rm h}31^{\rm m}58^{\rm s}{-}42^\circ 17' 41''$ (in the centre of the filamentary emission) a coordinate solution was determined to better than $3''$. Beyond this region the solution is compromised, with positions in error by up to $\sim 1'$, comparable with the resolution of the radio image ($43'' \times 64''$).

The optical filamentary structure in the image agrees well with that seen by Elliott et al. (1976), whose observation was significantly deeper with greater resolution (from a 5 hour exposure with the UK Schmidt Telescope). The advantage of the present observation is that it is a digital image of comparable resolution to the MOST 843 MHz data.

[2]The Hα observation of the Vela SNR shell was made and reduced by M. S. Bessell, Mount Stromlo and Siding Springs Observatories (MSSSO).

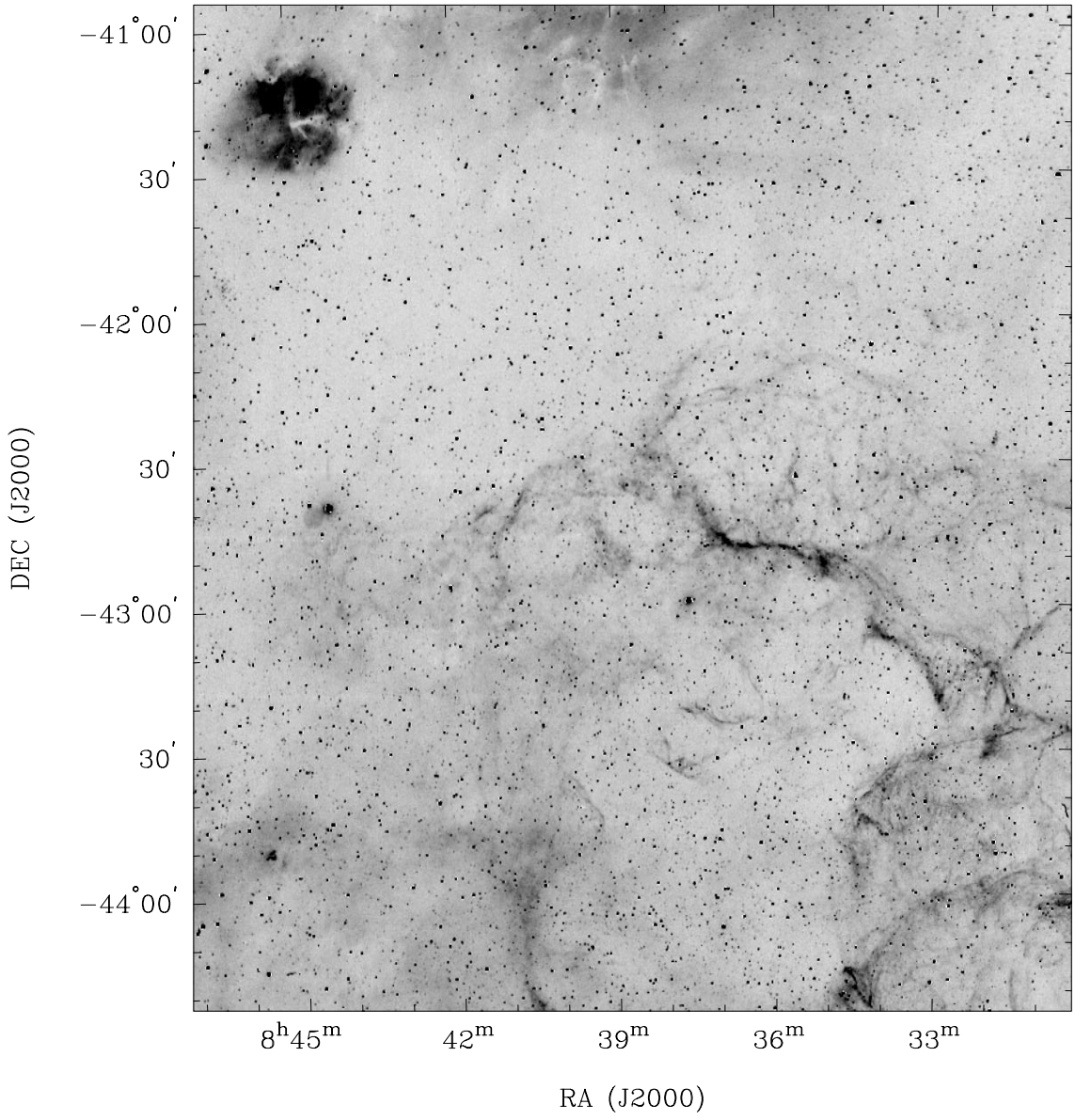

Figure 7.2 Hα image of the northern Vela SNR shell, part of a test observation made as part of the MSSSO/University of Sydney wide field imaging Hα sky survey. The registration of this image with the MOST image (figure 7.1) is within about 1′.

7.1.3 The ROSAT all-sky image

The Vela SNR was observed as part of the ROSAT all-sky survey between 1990 October and 1991 January. An image of the Vela SNR (0.1–2.4 keV, with angular resolution 1′) from the survey has been presented by Aschenbach et al. (1995), and is reproduced with permission in figure 4.4. The image clearly shows the 8° extent of the Vela SNR shell and the six bullets beyond it. In the top right quadrant the shell is most clearly defined, without bullets or the protrusions/instabilities that dominate the remainder of the X-ray shell. This region of the X-ray shell is enlarged and presented in figure 7.3 together with MOST 843 MHz and Hα overlays.

In figure 7.3, the top section of the X-ray image (black) is the Galactic background. The edge of the SNR shell appears first in light blue, with surface brightness $7 \times 10^{-15}\,\mathrm{erg\,cm^{-2}\,s^{-1}\,arcmin^{-2}}$ (Aschenbach et al. 1995). To the south, the surface brightness increases by a factor of 500 at the brightest part (white), which is the brightest X-ray emission region in the entire SNR. The very sharp transition region marks the edge of the main shock, seen in projection. The bright X-ray emission 'bullets' seen outside the shock are interpreted by Aschenbach et al. as being due to supersonic ejecta from the original explosion.

7.2 Multiwavelength analysis

With three datasets of comparable resolution in different emission regimes there is the opportunity to understand the spatial relationship between the underlying physical processes. The radio image shows primarily the non-thermal synchrotron emission, the optical filaments result from recombination in cooling processes and are seen as line emission, while the X-ray image portrays the thermal continuum due to shock heating. To see clearly the distribution of emission in the observed regimes, the three images are shown together in figure 7.3. In this section I will first discuss the correlations we see in a comparison of the three available datasets. Following this, I will place them in the framework of what is expected theoretically and compare the results to what is seen in other SNR shells.

7.2.1 Morphological comparisons

By considering only the radio and Hα images it is possible to see immediately the most striking aspect of the comparison, namely the contrast between the optical and radio emission regions. As will be discussed below, this is not without a simple theoretical basis, but is contrary to the picture seen in other SNRs, where the shell structure has been well-resolved in the radio and comparisons with optical emission made. The brightest radio filaments are (as noted earlier) generally oriented tangentially to the SNR centre and are without optical counterparts. Likewise, many of the optical filaments are without radio counterparts. However, one of the brightest optical filaments (at $08^{\mathrm{h}}36^{\mathrm{m}}-42^{\circ}50'$) *does* have a faint radio counterpart. In contrast, the equally bright optical filaments in the south-west corner of the image

are without radio counterparts in the MOST image. These filaments are generally not tangential to the SNR centre in the same way as the radio filaments. The optical filament with the most obvious counterpart *is* aligned tangentially.

In addition to the optical filamentary structure, diffuse optical emission is also present. This is concentrated to the eastern side of the image, in the general area of the strong radio filaments, but there is no obvious correlation between the diffuse optical emission and the radio filaments. No measure was available of the effect of extinction on the the Hα image.

The complete X-ray image (figure 4.4) indicates by its near-circular shape that it delineates the projected edge of those parts of the main shock that are still expanding into a relatively homogeneous medium. The regions of optical and radio emission described so far are interior to this main X-ray shell. At the western side of the main X-ray boundary in figure 7.3, we see the only significant optical and radio emission clearly present close to the X-ray edge. Here the radio and optical emission agrees quite well, in an arc with apex at $08^{\rm h}35^{\rm m}{-}42^\circ10'$, which is near but still behind the edge of the brightest X-ray emission (coloured red), and further behind the fainter outer X-ray emission.

The X-ray emission is quite different in form to the emission we see in the optical and radio regimes. Apart from the main edge, it is relatively diffuse and smooth. By contrast, the radio and optical images are dominated by filamentary structure. However, both the radio and optical images have reduced sensitivity to smooth structure, the MOST from its spatial response and the Hα from extinction.

With the exception of the strikingly radial optical filament at the south of the image, much of the optical filamentary emission is exterior (with respect to the remnant expansion) to the brightest peaks of the X-ray emission. The diffuse optical component has no such obvious relationship in the image to the X-ray emission, although it appears where the X-ray emission is not quite so bright, to the east. The radio filaments are also partially correlated with the X-ray emission. Several follow changes in X-ray brightness. However, the most central filament ($08^{\rm h}39^{\rm m}{-}42^\circ10'$) is less well correlated: it crosses a bright region of X-ray emission.

7.2.2 Discussion

In SNRs, optical and X-ray emission are both due to thermal processes. However, quite different physical conditions are involved. Thermal X-ray emission is the result of fast shocks propagating through a rarefied medium, with density 0.1–1 $\rm cm^{-3}$, shocked to temperatures of 10^6–10^7 K (Lozinskaya 1992, p188). The optical emission typically observed is produced by hydrogen recombination of material at lower temperatures, $\sim 10^4$ K, with density a few times $10^2\,\rm cm^{-3}$.

One model which has had success explaining optical and X-ray observations of the Cygnus Loop (Hester & Cox 1986; Graham et al. 1995; Levenson et al. 1996) invokes large ($\gtrsim 10^6$ cm) molecular clouds with which the expanding shock is interacting. The optical emission comes from the shocked cloud, where the dense material is not heated to temperatures as high as those which are maintained in the less dense

Figure 7.3 (following) ROSAT X-ray image of the northern Vela SNR shell with Hα and MOST 843 MHz overlays. The images cover the same area as the images in figures 7.1 and 7.2, which are presented again here as transparent overlays, allowing any combination of the three images to be viewed with the assistance of a sheet of blank paper. Surface brightness in the X-ray image is colour-coded, increasing in the order light blue, yellow, red, white. Light blue (7×10^{-15} erg cm^{-2} s^{-1} arcmin^{-2}) to white represents a factor of 500. These data were kindly provided by B. Aschenbach (originally published in Aschenbach et al. 1995) and are presented with the same colourmap as the complete image there. The intensity scales of the overlays have been adjusted from those used in their previous presentations. Registration of the X-ray and optical images with the MOST image made use of `MIRIAD regrid`. The ARC projection has been used.

0.1–2.4 keV

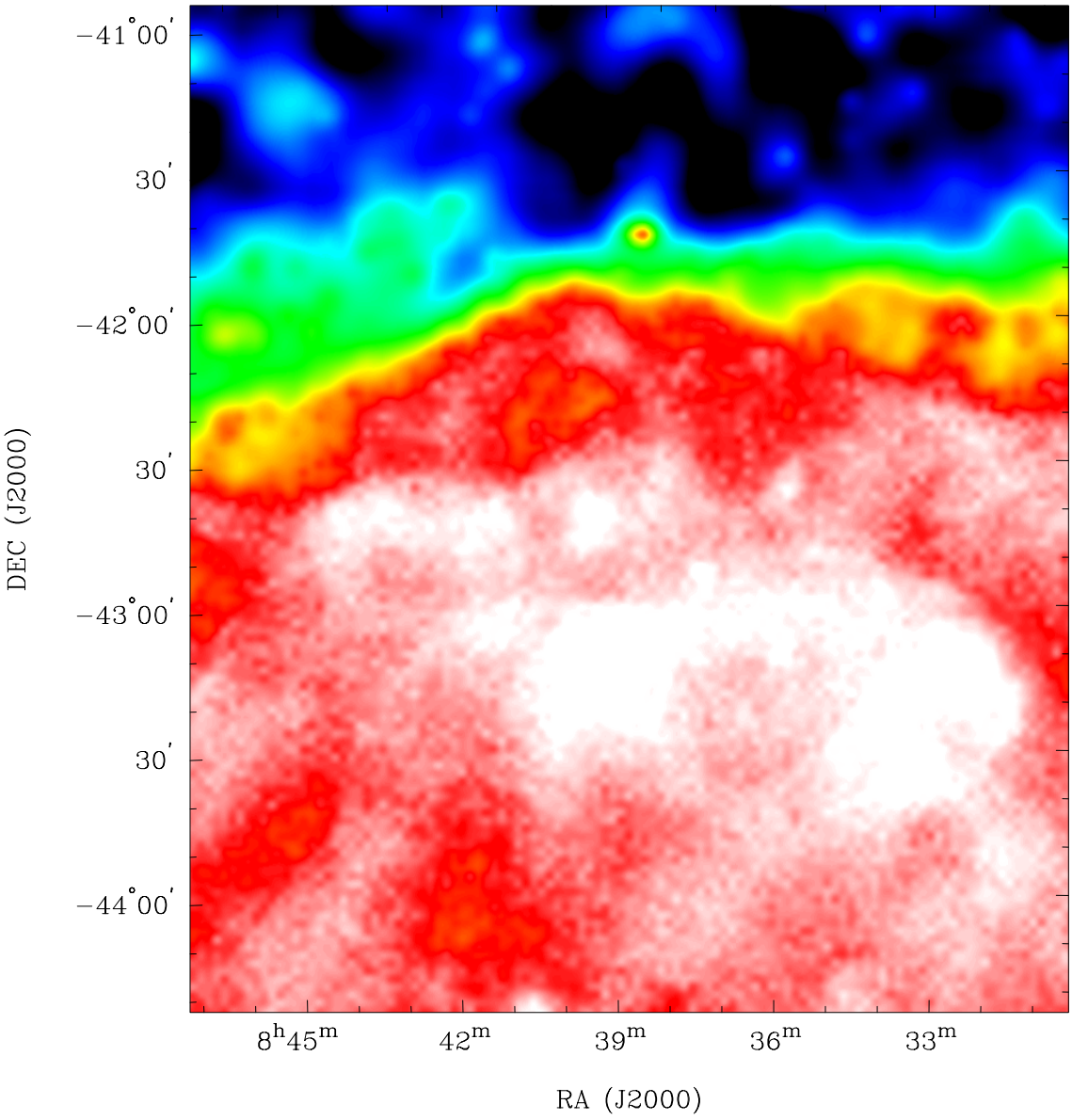
−41°00′
30′
−42°00′
30′
−43°00′
30′
−44°00′
DEC (J2000)
8h45m
42m
39m
36m
33m
RA (J2000)

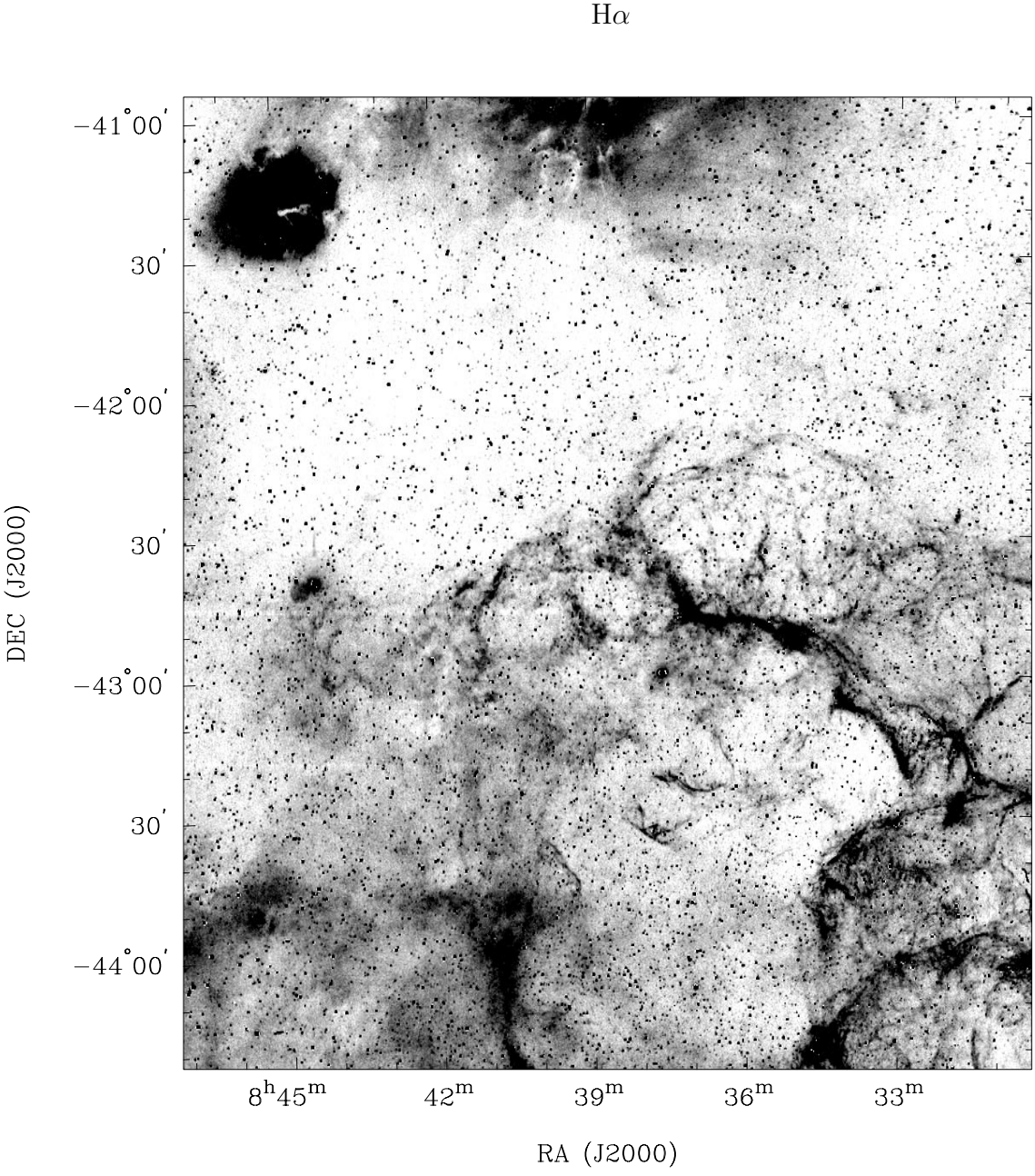
Hα
−41°00′
30′
−42°00′
30′
−43°00′
30′
−44°00′
DEC (J2000)
8h45m
42m
39m
36m
33m
RA (J2000)

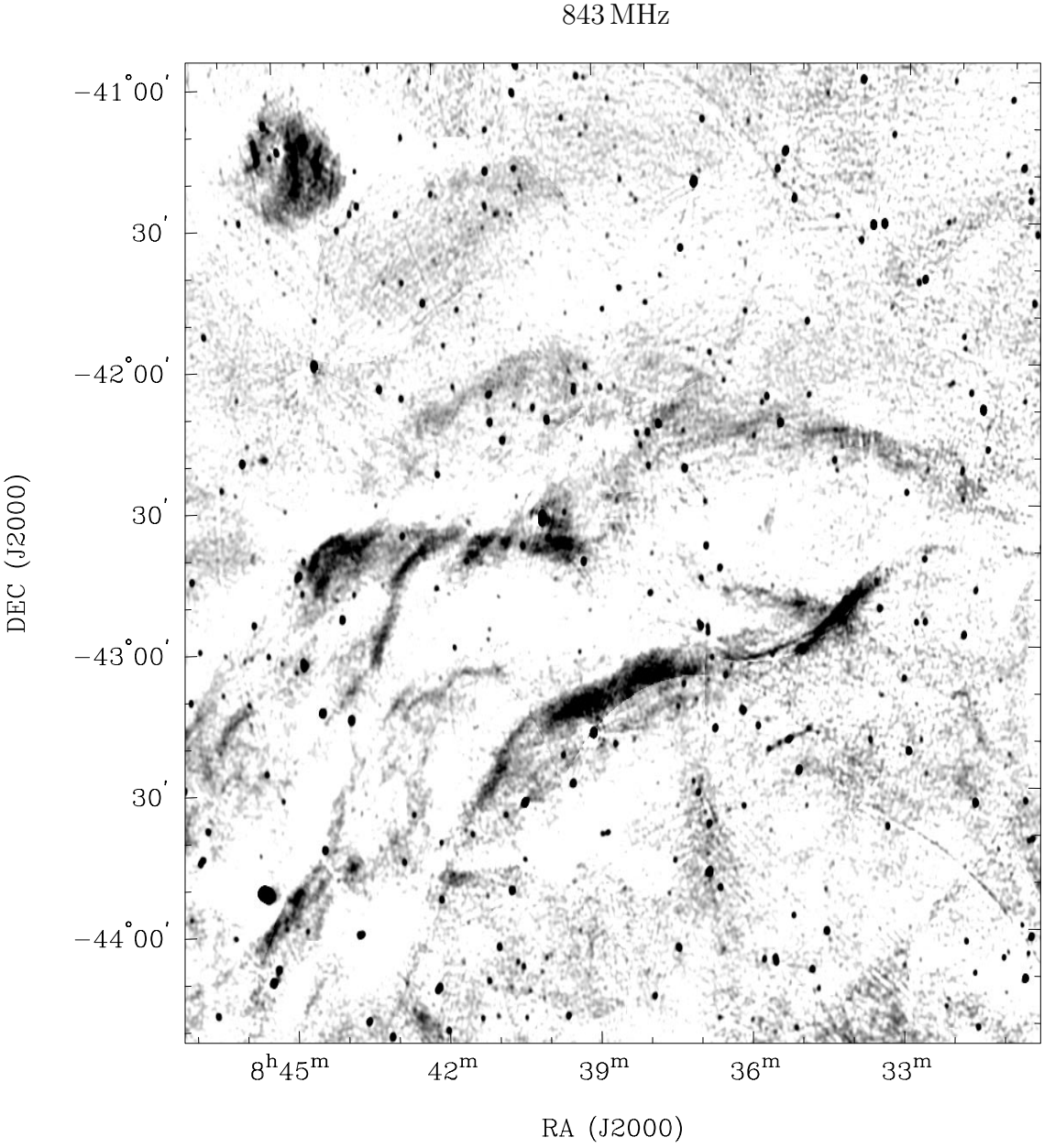
843 MHz
−41°00′
30′
−42°00′
30′
−43°00′
30′
−44°00′
DEC (J2000)
8h45m
42m
39m
36m
33m
RA (J2000)

X-ray emitting regions. The optical emission is due to recombination cooling after the passage of the shock. Behind the optical recombination emission, the X-ray emission is further brightened by the passage of a reflected (or *reverse*) shock due to the density contrast between the cloud and the less dense inter-cloud material. Where the main shock does not encounter molecular clouds, we do not expect to see recombinative cooling. Instead the fainter non-radiative (Balmer) filaments may be apparent (Hester et al. 1994).

The present observations of the northern Vela shell fit nicely into this picture. If the majority of optical emission was from the main shock interacting with a relatively uniform medium, but seen here in projection, we would expect also to see it along the entire edge of the X-ray shell, where accentuation of sheet-like emission in projection would be strongest. This is not observed, implying the emission is localised: due to some interaction with inhomogeneities with a filling factor much less than unity. The cloud interaction model of Hester & Cox (1986) is supported by the presence of X-ray brightened regions immediately behind many of the bright optical filaments in figure 7.3. We might be seeing this emission in projection, significantly in front of or behind the plane of the explosion centre transverse to the line of sight. This would indicate local density enhancements very close to the main shock. Alternatively, it could be nearly in the plane of the explosion centre, with a shock velocity significantly reduced by interactions with more dense material. Some of the emission could be from regions already passed and energised by the main shock.

As a check on the thermal nature of the X-ray emission, the digital 60 μm images in the IRAS Sky Survey Atlas (Wheelock et al. 1994) covering the same area as figure 7.3 were inspected. In general infra-red images are less useful thermal diagnostics than X-ray images near the Galactic Plane, since the infra-red observations are dominated by diffuse Galactic emission and confusion from other sources (White & Long 1991). However, much of the X-ray structure does have an infra-red counterpart, supporting a thermal emission model.

An alternative model for SNR optical/X-ray emission (McKee & Cowie 1975), which has not been explored further here, explains SNRs with centrally-peaked X-ray emission (White & Long 1991). In this model cold dense clouds with a small filling factor have been passed by the main shock and are evaporating by conductive heating from the postshock gas.

Both these models rely on molecular clouds to explain the observed features. Molecular clouds have been detected in the direction of the Vela SNR (May et al. 1988). The basic survey was of ^{12}CO and ^{13}CO $J = 1 \rightarrow 0$ line emission with a resolution of $0\overset{\circ}{.}5$. Higher resolution follow-up observations (Murphy & May 1991) covered only the eastern part of the Vela SNR shell. A cloud with a barely resolved peak at $08^{\rm h}41^{\rm m}-41°20'$ is seen, with a distance estimated to be 0.5–2.0 kpc, i.e. immediately behind the Vela SNR. However, this cloud appears coincident with a bright H II region seen optically in figure 7.2, and might not be responsible for the observed optical features in the Vela shell. H I may be a better tracer of density in the Vela shell region. Dubner et al. (1991) find an H I distribution which implies

that the Vela SNR is expanding into a cavity and has formed optical filaments where it has reached the higher density material at the edge of the cavity.

All the radio emission seen in the MOST image from the Vela SNR region is presumably non-thermal. The standard mechanism for non-thermal radiation in SNRs, synchrotron emission, requires the presence of relativistic electrons and a magnetic field. The background non-thermal radiation in the Galaxy leads to estimates of pre-existing Galactic magnetic field and relativistic particle densities. Expanding SNR shells compress magnetic field lines and accelerate electrons giving rise to the observed emission intensities, probably by the diffusive shock mechanism (Fulbright & Reynolds 1990). The tangential magnetic field present in the shells of some barrel-shaped (Kesteven & Caswell 1987) SNRs (Milne & Haynes 1994; Lalitha et al. 1984) may be a signature of magnetic field compression by the expanding shock. However, in many evolved remnants the field is less ordered. Milne (1987) suggested that this may be due to local inhomogeneities in the ISM or to projection effects. The structure of magnetic fields found in younger remnants is quite different (e.g. Tycho's remnant: Dickel et al. 1991). These magnetic fields are generally radial, probably formed in Rayleigh-Taylor instabilities at the contact surface between the swept-up ambient gas and the stellar ejecta (Jun & Norman 1996a & b).

In the simple radio emission model for the interaction of supernova explosions with the ISM (Woltjer 1972), Vela is in the *radiative* or *snowplow* phase of evolution, having swept up significant matter and dissipated much of the original explosion energy. A cool dense shell surrounds a hot interior. This model can account for the faint radio emission seen behind the X-ray shock, which indicates the presence of compressed magnetic fields and accelerated particles. It does not account for the brighter localised filaments apparently well behind the main shock.

Duin & Van Der Laan (1975) present a consistent picture for the coincidence of radio and optical emission which is observed in middle-aged shell remnants. This model, based on observations of IC443, proposes that the magnetic field required for synchrotron emission is frozen into condensations forming in the cooling instabilities which then give rise to the optical emission. If this process is active in Vela, then we can infer that the cooling material around the radio filaments is not at an appropriate temperature for the emission of recombination radiation. Furthermore, at the site of the optical filaments, either the magnetic field has not been sufficiently compressed or accelerated particles are not present.

The applicability of these models may be able to be investigated further with magnetic field information, provided by polarimetry. Polarised intensity has been observed in the Vela shell (Duncan et al. 1996), but high resolution measurements at several frequencies will be required to examine the magnetic field structure in this area in detail. The emission may be too faint for effective polarimetry.

Good agreement between optical and radio emission has been found in other middle-aged shell SNRs such as IC443 (Duin & Van Der Laan 1975), the Cygnus Loop (Straka et al. 1986) and HB3 (Fesen et al. 1995). The situation in Vela is quite different and the reason for this is not apparent. Extinction may be a culprit, obscuring some of the Hα emission. Eggen (1980) determined from stellar

reddening measurements that a dark cloud lies in the direction of the Vela SNR, immediately behind a sheet of stars at 425 pc; this is consistent with the distance (500 pc) commonly adopted for the Vela SNR. However, the coincidence of diffuse optical emission with bright radio filaments, noted above, argues against severe extinction in this direction.

This work does not constitute a detailed investigation of the optical/radio/X-ray correlations. However, this preliminary presentation indicates that a fuller investigation would be profitable. A first step would be to obtain optical spectral information to separate non-radiative and radiative filaments.

7.3 The X-ray 'bullets'

The idea that the Vela SNR might have an X-ray extent as large as 8°, with the pulsar near the centre, was first suggested by the Einstein observations of Seward (1990). ROSAT all-sky survey imaging of the same region (Aschenbach et al. 1995) confirmed this and revealed some unusual structure outside the approximately spherical boundary, namely a collection of apparently supersonic 'bullets' shock heating the ambient medium by their expansion (figure 4.4). Aschenbach et al. suggest that these bullets are high-speed ejecta from the original explosion. An alternative model (Stone et al. 1995) is that they are condensations resulting from hydrodynamical instabilities in the stellar outflow. Follow up VLA observations of one of these bullets by Strom et al. (1995) detected synchrotron emission at the putative 'head' of the bullet in an arc closely following the X-ray emission. Furthermore, three steep-spectrum radio sources were found in the trailing Mach cone of the bullet.

Observations were made of three of the brighter bullets with the MOST in early 1995 to search for radio counterparts and to continue the investigation of bullet A. Additionally, an existing image forming part of the MOST Galactic Plane survey (Whiteoak et al. 1989; Green 1994) and covering the area of one of the bullets was re-examined. The results are reported below.

7.3.1 Observations

The observations comprising the investigation are listed in table 7.1, using the naming convention from the X-ray results. The observation of the region of bullet D had already been made as part of the first epoch MOST Galactic Plane survey. The other observations were made especially for this investigation. Initial observations were made of bullets B, D and E on the basis of their greater X-ray flux (see table 7.2) and of bullet A (on the basis of prior radio detection). Scheduling constraints prevented observation of bullets C and F. Reduction of the three special observations followed the standard procedure used for the individual survey observations of chapter 5. The observation of bullet D had been reduced as part of the Galactic Plane survey.

Bullet	Observation date	Field centre (J2000) RA (h m s)	Dec (° ′ ″)
A	95/04/17	08 57 55.0	−41 49 22
B	95/03/04	09 02 02.1	−43 33 05
D	89/01/30	09 10 11.4	−44 57 00
E	95/03/19	07 58 07.3	−44 37 60

Table 7.1 Summary of MOST observations of the X-ray bullets. The observation of bullet D was made for the Galactic Plane survey; the subsequent observation (93/03/23) suffers more severely from artefacts. Bullets C and F were not observed with the MOST.

7.3.2 Results and discussion

MOST images of the regions surrounding the X-ray bullets A, B, D and E are given in figures 7.4–7.7. In each image the position of the X-ray bullet given by Aschenbach et al. (1995) is marked with a cross. A faint radio counterpart arc is seen corresponding to each of the X-ray bullets A, B and D. While artefacts are present in these images, these are distinguishable from the radio arcs. MOST artefacts are usually rays from strong sources or ellipses around them. Sources which could give rise to artefacts of the form of the radio arcs are not present. No counterpart is seen to bullet E, which would be just at the detection limit if its radio/X-ray flux density ratio was similar to that of the other bullets. However, while the X-ray emission is thermal, the radio arcs are non-thermal, probably resulting from particle acceleration at the shock front (Strom et al. 1995). So projection effects and the local environment will also affect the relative intensities of radio emission.

It is difficult to measure the total flux densities or thickness of the arcs due to the substantial artefacts present in these fields (bullets A, B and D are very close to the Galactic Plane). However, the characteristic shock-like structure of the arcs does indicate non-thermal emission at 843 MHz. The peak flux density of the radio counterpart to each bullet is shown in table 7.2. The rms noise measurements on each image are made over regions comparable with the size of the arc. Typical noise measurements over smaller regions are of order 1 mJy. Note that while the radio emission from bullets A and D is at the X-ray arc positions quoted by Aschenbach et al., the radio emission from bullet B is about 3′ 'behind' the shock. This may be due to a projection effect.

The point sources behind bullet A Strom et al. (1995) have discovered three small-diameter sources behind the 'head' of bullet A. In figure 7.4 these are marked '1', '2' and '3'. While the spectral indices are consistent with these being extragalactic, Strom et al. argue that a chance coincidence is unlikely. In the MOST image, these three sources do not appear to be preferentially distributed and reflect typical background source densities. Large (1990) has determined typical small-diameter source counts in MOST 843 MHz images from the data of Subrahmanya & Mills (1987). His results imply that about 17 sources above 5 mJy should be present in

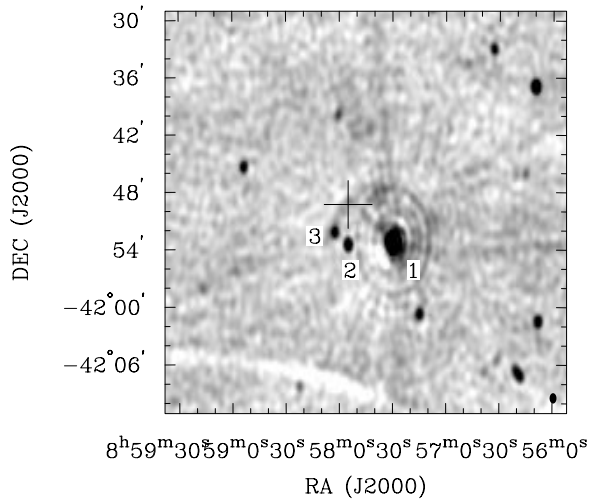

Figure 7.4 MOST observation of the Vela SNR X-ray bullet A (cross). The image is of the same area as the X-ray/VLA image given by Strom et al. (1995), with the bullet's X-ray position coincident with the radio arc at the position marked by a cross. Sources 1, 2 and 3 are those seen by Strom et al. and have 843 MHz flux densities of 1 Jy, 40 mJy and 24 mJy respectively. The ellipses around source 1 are artefacts. The greyscale is from $-4\,\mathrm{mJy\,beam^{-1}}$ (white) to $16\,\mathrm{mJy\,beam^{-1}}$ (black), and the HPBW ellipse is shown on the lower right.

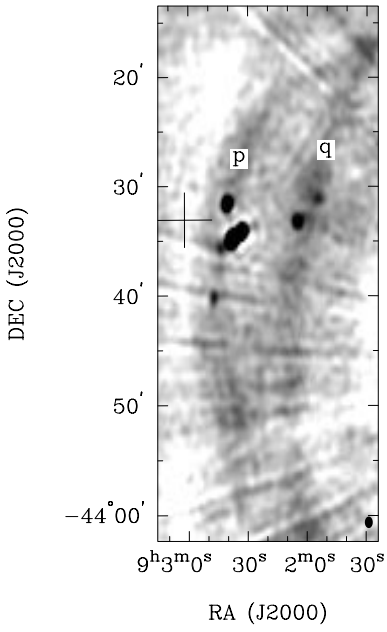

Figure 7.5 MOST observation of the Vela SNR X-ray bullet B (cross). The position of the radio arc corresponding to (and behind) the X-ray bullet is marked 'p'. An artefact of the strong HII region to the west is marked 'q'. The greyscale is from $-5\,\mathrm{mJy\,beam^{-1}}$ (white) to $15\,\mathrm{mJy\,beam^{-1}}$ (black), and the HPBW ellipse is shown on the lower right.

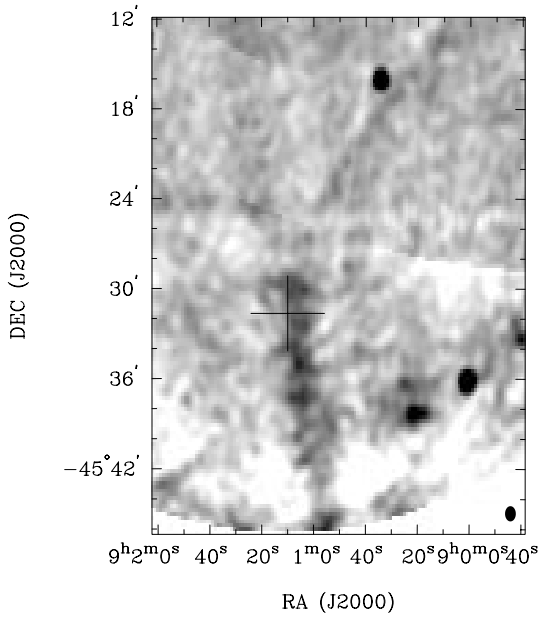

Figure 7.6 MOST observation of the Vela SNR X-ray bullet D (cross). An arc of emission is seen coincident with the X-ray position. The greyscale is from $-5\,\mathrm{mJy\,beam^{-1}}$ (white) to $15\,\mathrm{mJy\,beam^{-1}}$ (black), and the HPBW ellipse is shown on the lower right.

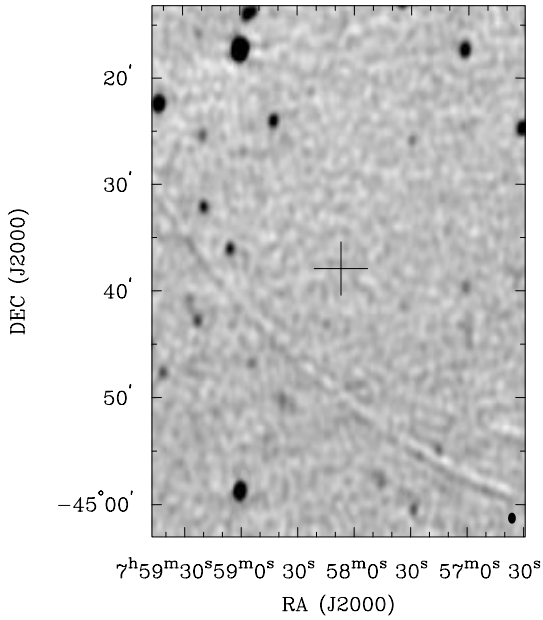

Figure 7.7 MOST observation of the region of the Vela SNR X-ray bullet E (cross). The greyscale is from $-5\,\mathrm{mJy\,beam^{-1}}$ (white) to $15\,\mathrm{mJy\,beam^{-1}}$ (black), and the HPBW ellipse is shown on the lower right. No radio counterpart has been found.

Bullet	843 MHz peak flux density (image rms) (mJy)	X-ray flux (10^{-12} erg cm^{-2} s^{-1})
A	5 (1.3)	3.0
B	8 (2.0)	44.9
D	13 (1.3)	66.0
E	*not detected* (1.0)	19.7

Table 7.2 Summary of results from MOST observations of the Vela SNR X-ray bullets. The X-ray fluxes are taken from Aschenbach et al. (1995).

Source	$S_{843\,\mathrm{MHz}}$	$\alpha_{20\,\mathrm{cm}/6\,\mathrm{cm}}$	$\alpha_{843\,\mathrm{MHz}/6\,\mathrm{cm}}$
1	1.0 Jy	−0.7	−1.4
2	40 mJy	−0.7	−0.9
3	24 mJy	−1.3	−1.0

Table 7.3 MOST 843 MHz flux densities and spectral indices of the unresolved radio sources behind X-ray bullet A. The 20 cm/6 cm spectral indices and the 6 cm flux densities used are from Strom et al. (1995).

this image. Eighteen are found.

The MOST data provide an opportunity to confirm the spectral index measurements of these sources. Spectral indices derived from the MOST data and 6 cm flux densities are compared with the 20 cm/6 cm spectral indices in table 7.3.[3]

The new spectral index measurements for sources 2 and 3 are consistent with those of Strom et al. (1995), given the expected errors. However, the strongest source gives discrepant results. The 408 MHz Molonglo Cross flux density is 1.8 Jy (Clark & Crawford 1974). The position of this source in the lower resolution 408 MHz survey agrees with the 843 MHz position to within a few arcseconds, indicating that confusion at 408 MHz is probably not affecting that measurement. Excluding the 20 cm point from the spectrum, the available data support a spectral index of −1.3, indicating an origin more likely to be extragalactic. However the possibility of variability or of an unusual spectrum is not ruled out. It may be possible to resolve this source with the VLA in BnA configuration to reconcile these results (see, for example, section 8.2).

7.4 Conclusions

The investigations in the early sections of this chapter focussed specifically on the northern part of the Vela shell. Like parts of the Cygnus Loop, this region can be explained by a model of a fast shock heating interstellar material to X-ray emitting temperatures and interacting with denser clouds to produce Hα recombination line

[3]Exact observing frequencies were not quoted by Strom et al. (1995); 4.9 GHz has been assumed for 6 cm.

emission (Hester 1987; Graham et al. 1995; Levenson et al. 1996). However, the expanding shock produces non-thermal radio emission in *different* regions, in contrast with the optical/radio agreement seen in many middle-aged SNRs.

To continue investigating this region, observations of other optical emission lines are needed to separate projected Balmer filaments produced at the outer shock from recombination line emission at molecular cloud interactions. High-resolution polarisation observations of the radio shell filaments are the obvious next step to investigate the magnetic field producing the non-thermal emission.

The presence of a radio arc found by Strom et al. (1995) and associated with the X-ray bullet 'A' (Aschenbach et al. 1995) has been confirmed. Radio observations of some of the other X-ray bullets have revealed possible synchrotron-emitting shocks at the head of two further bullets. Higher resolution multi-frequency studies would be helpful.

Chapter 8

The Vela X Region

As the closest composite remnant, the Vela supernova remnant deserves particular attention. Studies of its plerionic component, Vela X, should help us to understand how the Vela pulsar transfers its rotational kinetic energy to the nebula. With an age at least ten times that of the Crab nebula, the best studied plerion, we might expect the Vela plerion to show evolutionary trends. The absence of obvious correlations between radio emission and the optical filaments (Elliott et al. 1976) already contrasts Vela X with the Crab nebula, where the radio filaments surround the optical filaments (Bietenholz & Kronberg 1991). A re-examination of optical emission in the Vela X region with the higher resolution radio observations now extant is appropriate. The recent discovery of a possible X-ray 'jet' from the pulsar (Markwardt & Ögelman 1995) further contrasts Vela X with other plerions. Markwardt & Ögelman propose that the X-ray feature may be a conduit for the energy transfer to the nebula from the pulsar, which is offset $40'$ from the centre of Vela X. Frail et al. (1997) have presented radio observations of the region at 327 MHz, which show a filament to the east alongside the X-ray feature. They hypothesise that the filament may be a 'shocked sheath' around the X-ray structure, where the expanding X-ray gas compresses material already energised by the pulsar wind. Frail et al. note that shocked gas would be expected to have a steeper spectral index (around -0.6) than the rest of the plerion (-0.16: Dwarakanath 1991) and suggest spectral index measurements to test their hypothesis.

This chapter draws together several investigations with the aim of further understanding the Vela X region. Initially, images from the MOST Vela SNR survey (chapter 5) are presented. An investigation of the nature of small-diameter sources within the Vela X region follows in section 8.2. VLA observations made in collaboration with D. A. Frail and A. J. Green (section 8.3) enable spectral index measurements of the filament alongside the 'jet' and of another filament in Vela X (section 8.4). Section 8.5 presents the results of a search for radio/Hα correlations in Vela X.

8.1 MOST observations of Vela X

A view of the central nebula of the Vela SNR (from the survey of chapter 5) is shown as a greyscale in figure 8.1, as a contour image in figure 8.2 and as a ruled surface plot in figure 8.3. Each representation emphasises different characteristics. The greyscale plot gives a good overall view of the region, while the contour plot highlights the filamentary structure and provides a more quantitative representation. The hidden line plot helps to show the nature of the filamentary structure and emphasises the small-diameter sources.

The first thing to note in the images is that at the resolution of the MOST the nebula is seen to be composed of many filaments or wisps, at a variety of orientations and on many angular scales. However, it is important to realise that the flux density detected by the MOST is only a small fraction of the total flux density of the remnant, because of absent low spatial frequency information. The flux density in this image summed over the pixels in the area of Vela X is 28 ± 2 Jy.[1] An estimate, corrected for the negative bowl, of the total flux density detected by the MOST within its spatial frequency range is about 130 Jy. For comparison, the total flux density of Vela X at 843 MHz estimated from the spectrum of Dwarakanath (1991) is 1100 Jy. Hence the MOST is detecting about 12% of the total flux density.

A benefit of the MOST acting as a spatial filter is the prominence it gives to higher resolution features with size of the order of the X-ray features shown in Markwardt & Ögelman (1995). In figure 8.1, the central radio filament overlaid on the X-ray feature by Frail et al. (1997) is marked '2'. This filament does not look strikingly different from other filaments in the region, for example the filament marked '1'. However, we see in the 8 GHz Parkes image of Milne (1995) that it is located at the brightest part of the Vela X nebula. Frail et al. (1997) have argued that the radio filament may be associated with the X-ray feature, but it is morphologically indistinguishable from other filaments in the image. The central radio filament looks so prominent in the 327 MHz VLA image of Frail et al. (1997) partially because that image is uncorrected for the VLA primary beam attenuation at the edge of the field. Also, the MEM deconvolution of the VLA data has been more successful at restoring flux density at low spatial frequencies than the CLEAN algorithm used to deconvolve the MOST observations. The issue of whether the central radio filament (i.e. filament '2') is related directly to the pulsar or the X-ray feature will be considered further in section 8.4.

Several further objects in the region should be noted at this stage. In figure 8.1 a filament ('3') extends through the pulsar to the south and may connect to filament '2'. The axis of symmetry of these two filaments is closely aligned with the direction of motion of the pulsar (Bailes et al. 1989), shown on the image with an arrow. Some very faint structure around the edge of Vela X stands out as unusual: object '4' (the Loop) has a shape reminiscent of many shell supernova remnants, but if it

[1] The flux density has been integrated over the area of Vela X as seen in the image of Milne (1995), which is the highest resolution single dish dataset.

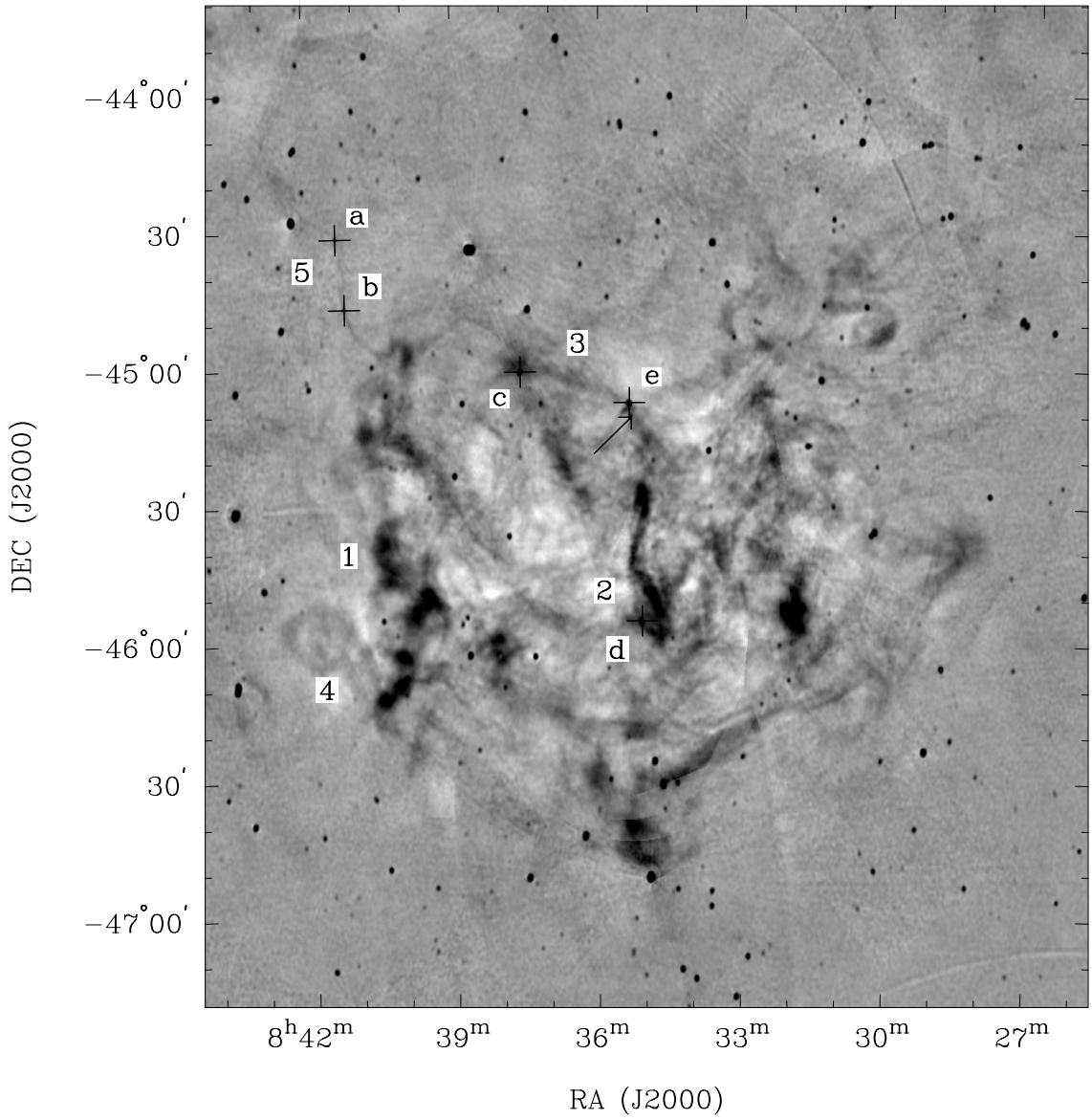

Figure 8.1 A portion of the image in figure 5.1 showing Vela X, the central nebula of the Vela supernova remnant. This greyscale image gives the best overall representation of the extended structure in the Vela X region. The arrow shows the direction and magnitude of the proper motion of the pulsar over 12 000 yr, assuming constant velocity as measured by Bailes et al. (1989). The arrow's head is at the present location of the pulsar (suppressed in this image). Other features of the image are: (1) the brightest filament in the image (peak brightness 49 mJy beam^{-1}); (2) a filament thought to be a 'jet' from the pulsar by Markwardt & Ögelman (1995); (3) another filament stretching away from the region of the pulsar, approximately symmetric with feature 2 across the pulsar's proper motion axis; (4) a faint shell, possibly an unrelated source or part of Vela X ('the Loop'); (5) an unusually thin filament stretching away from Vela X ('the Wisp'). The unresolved sources marked with the letters (a) to (d) are those further investigated in section 8.2. Source (e) was investigated by Bietenholz et al. (1991).

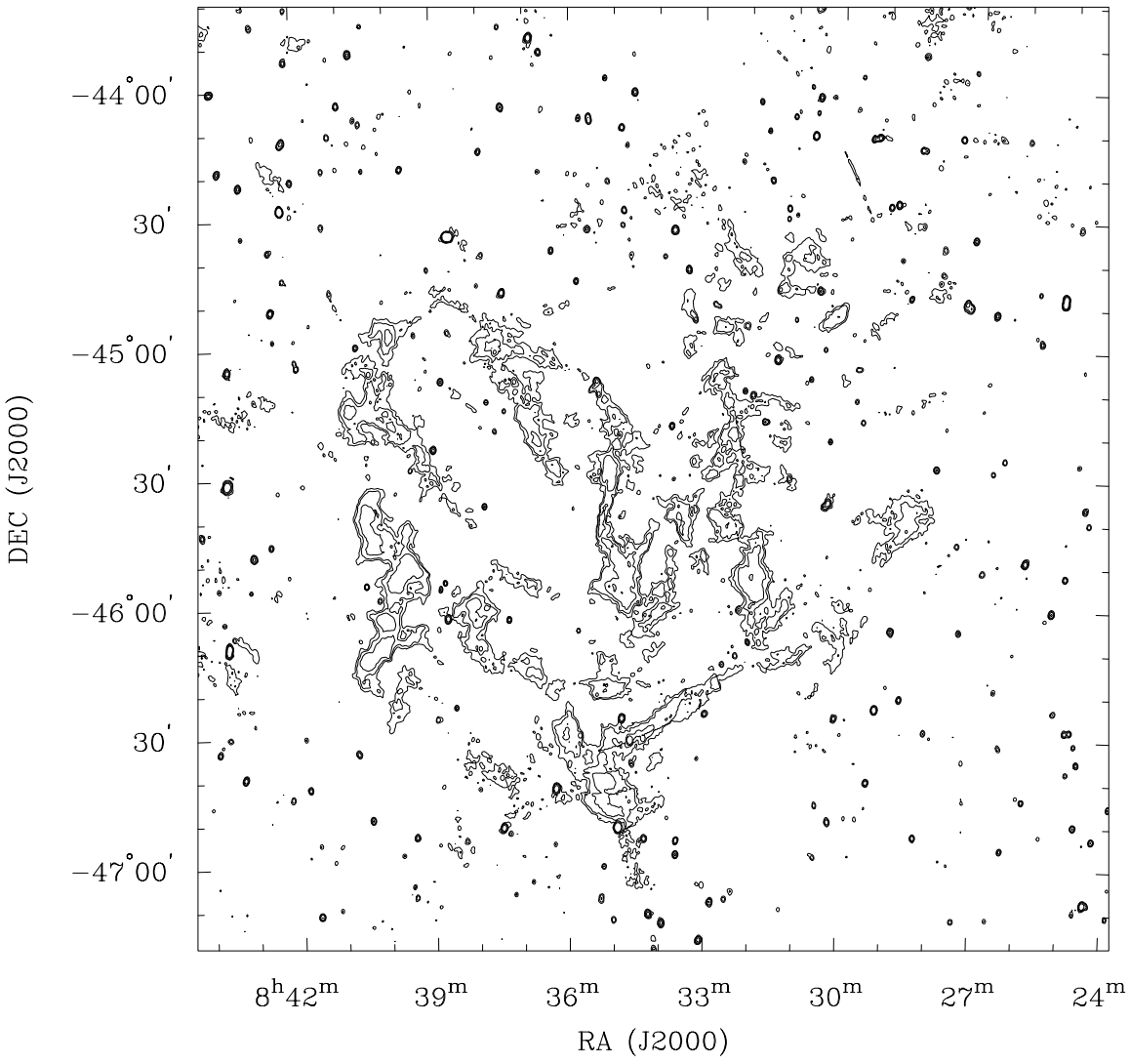

Figure 8.2 A contour plot of the Vela X region, covering the same area as the previous image, and showing how the brighter filaments (with the exception of one to the south) are oriented with a similar position angle of about 10°. Contour levels are at 5, 10, 20 and 50 mJy beam^{-1}.

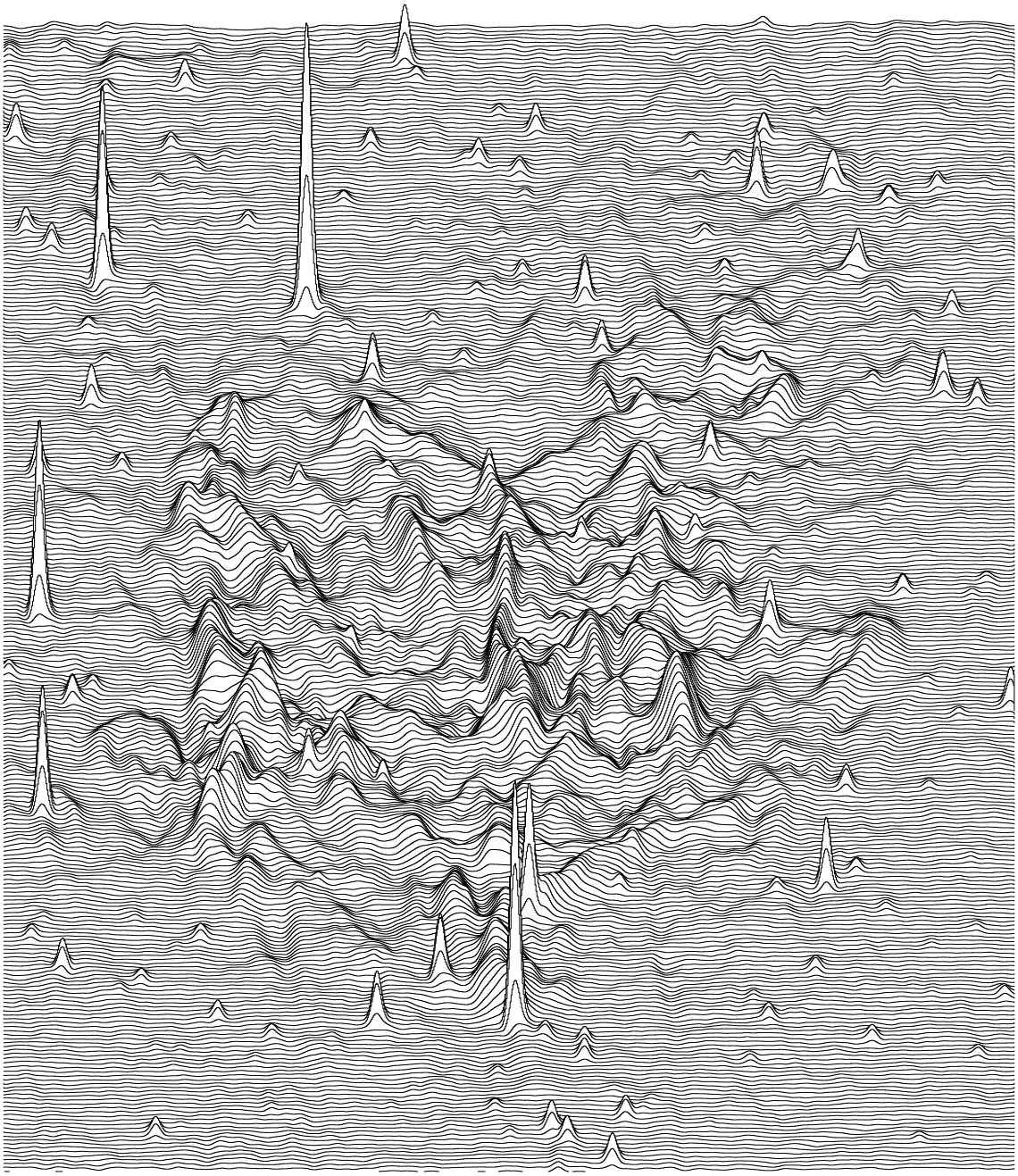

Figure 8.3 A ruled surface plot of the Vela X region in the MOST Vela SNR survey, emphasising the disordered nebulosity of the complex and highlighting the relative strengths of the point sources and the extended structure. In this image the Vela plerion looks like a confined region of uniform 'turbulence' or chaos: the filaments could merely be random concatenations. The plot is of the same area as figure 8.1. The data have been convolved to a circular beam of $120'' \times 120''$ to reduce the noise, which also accentuates the extended emission relative to the compact sources. The brightness scale is $132\,\mathrm{mJy\,beam^{-1}/cm}$.

is associated with Vela X, could it be a blowout from the nebula? Object '5' (the Wisp) is a faint streamer which appears to connect Vela X to the Vela shell (look back to figure 5.1). It might be argued that it is actually a foreground or background projection of the surface of a shock 'bubble', but it is thinner than any of the shell filaments and appears to connect with Vela X. Detailed images of these two objects are presented in section 8.1.2. The nature of two point sources along the Wisp (one apparently located at an elbow in the streamer) is examined in section 8.2.

8.1.1 The region around Vela pulsar (B0833−45)

Figure 8.4 shows the region around the Vela pulsar, from a pulsar gating observation of 1997 February 13, when the data were collected only during the 'off' part of the pulsar's period (see section 5.2.2 and appendix C). Reduction of the data used the same procedures as for the whole MOST Vela SNR survey (chapter 5). The rms noise of the image varies, but is around 1 mJy beam^{-1}. In the image, the position of the pulsar is marked by a circle. At its location, the brightness of the image is 11 mJy beam^{-1}, which all appears to be due to extended emission. A SE-NW slice across the image at the position of the pulsar reveals that there is no residual unpulsed point source of more than 2 mJy. Using the proper motion measurement of Bailes et al. (1989), we notice that over its lifetime (assuming an age of 12 000 yr) it has moved to its present position from a bright region to the south-east. An excess of high-energy γ-rays has been detected from near this putative birthplace (Yoshikoshi et al. 1997). Now, the pulsar is apparently located just behind a sharp edge which is unique within the Vela X region. The pulsar's direction of motion almost bisects the corner between this edge and another structure to the north-east, which could be a bow shock of the pulsar. The wide opening angle indicates that such a shock, if it existed, would be travelling much faster than the proper motion of the pulsar. Just to the north of the pulsar is a 3′ crescent-shaped synchrotron nebula, seen originally by Bietenholz et al. (1991). They resolved out the extended structure in the region, whereas here we see that the crescent is one bright region of much extended emission around the pulsar.

8.1.2 Unusual objects in the Vela X region

In this section I present images of two unusual objects at the edge of the Vela X region, which I have named 'the Wisp' and 'the Loop'. These results are part of the image of the whole of Vela X presented in figure 8.1. Although faint, these objects are both present in the VLA 1420 MHz mosaic of the same region (figure 8.9).

The Wisp This object (figure 8.5) is unique in the Vela X region for its thin, elongated structure. It stretches from the edge of the plerion outwards towards the shell of the Vela SNR. The most similar Galactic object is probably 'the Snake' (G359.2 − 00.2: Gray et al. 1991; Gray et al. 1995). It too is long and thin and prominent at 843 MHz, and contains a clear cusp. However, the Snake has length

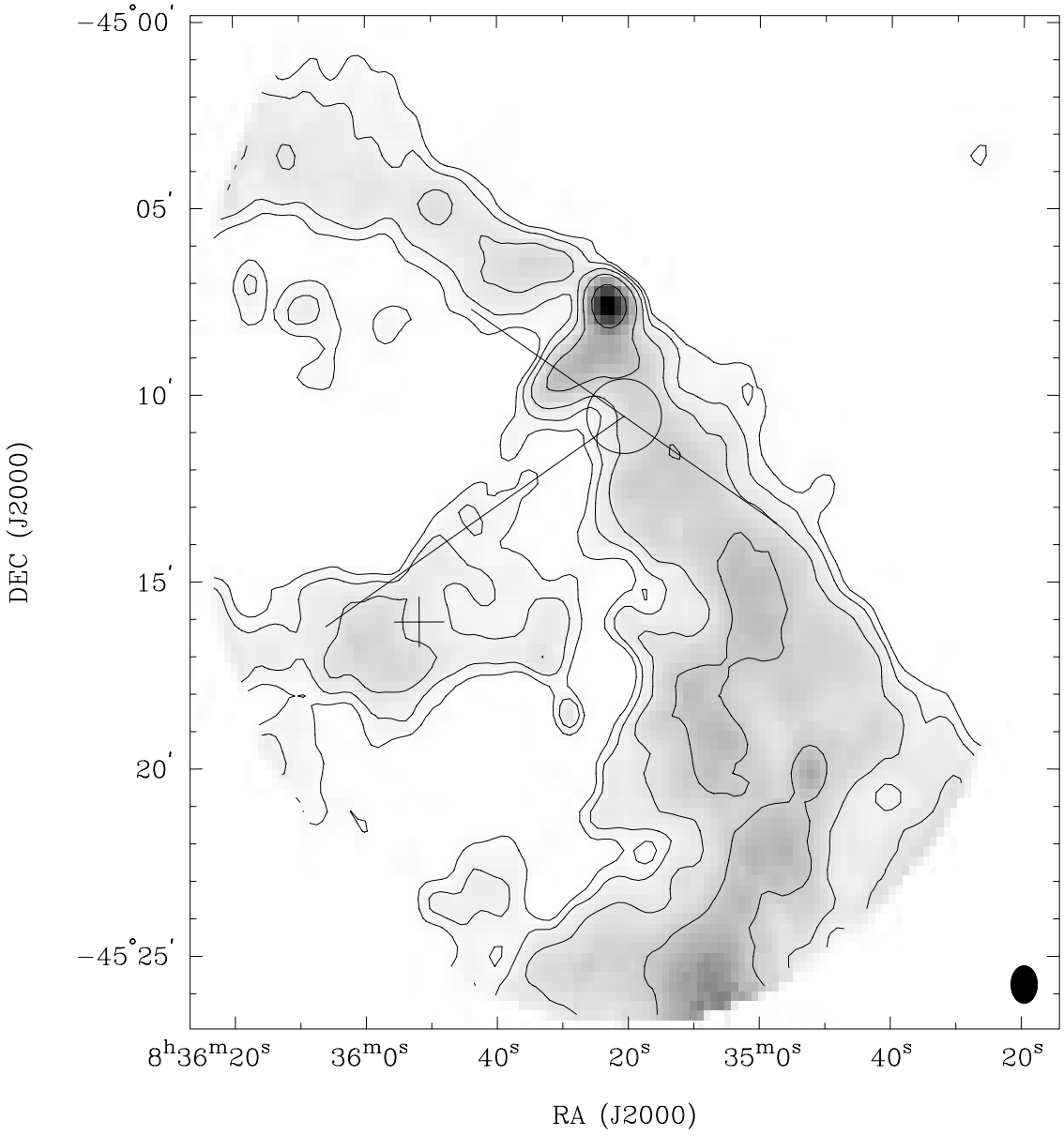

Figure 8.4 The MOST image of the region around the Vela pulsar (PSR B0833−45). Data for the image were obtained during the 'off' part of the pulsar's period. Its position is at the centre of the circle. The contours are 2, 5, 10, 20 and 50% of the peak, 90 mJy beam^{-1}, which corresponds to an unresolved extragalactic source (Bietenholz et al. 1991). The pulsar's proper motion (Bailes et al. 1989) is indicated by a solid line at $PA = 305°$ from its extrapolated birthplace (assuming an age of 12 000 yr). Its rotation axis is indicated by the line at $PA = 55°$ (Bailes et al. 1989). The cross marks the location of an excess of γ-rays detected by Yoshikoshi et al. (1997).

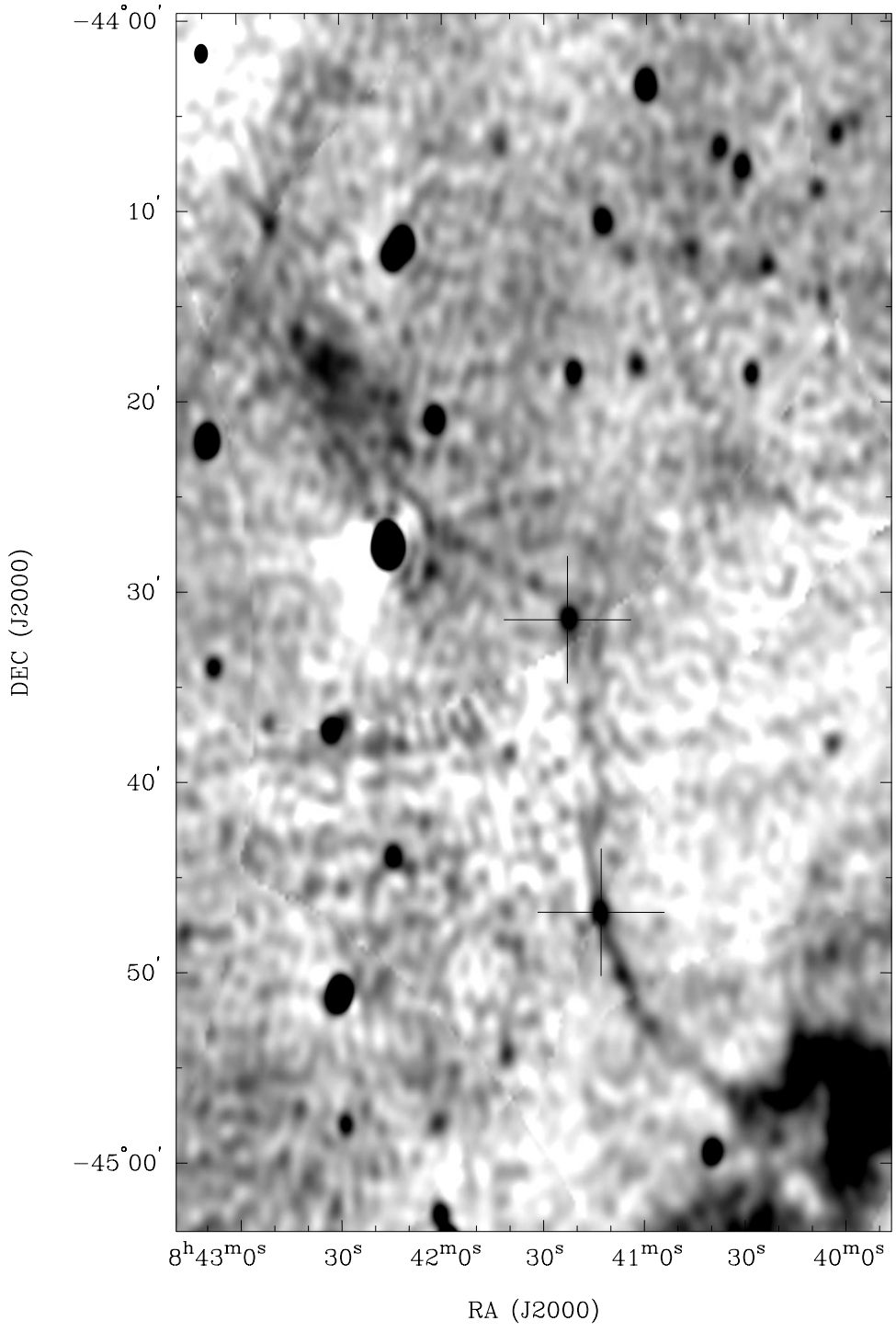

Figure 8.5 The Wisp, which extends from the bright edge of Vela X (lower right) to the closest shell filament (top right). Two unresolved sources along the Wisp (investigated in section 8.2) are marked with crosses. The scale is linear, from −4 (white) to 9 (black) mJy beam^{-1}. The HPBW ellipse is shown at the top left. This image is taken from the data shown in figure 8.1.

60 pc, whereas the Wisp would have length only 9 pc if at the distance of the Vela SNR. The Snake has a peak flux density of $\sim 20\,\mathrm{mJy\,beam^{-1}}$ at 843 MHz, with a non-thermal spectrum and linear polarisation up to 50%. The Wisp is much fainter—if a synchrotron source, it will be very difficult to image in polarisation or at high frequencies. Nevertheless, the *a priori* knowledge of its existence could make a search in existing polarisation datasets (like those in section 8.3.1) worthwhile. The Wisp might be just a filamentary part of the shell seen in projection, but it is unresolved in width unlike the main shell filaments (see chapter 7). Two unresolved small-diameter sources situated on the Wisp, one near its cusp, are considered further in section 8.2. The presence of the Wisp in the Hα image of the Vela X region (section 8.5) supports the association with the shell.

The Loop Seen on its own (figure 8.6), the Loop resembles a shell SNR (cf. Whiteoak & Green 1996). However, its proximity to the edge of the Vela X nebula indicates that we must consider the possibility that it is instead a feature of the plerion itself. Faint features on the other side of the nebula (to the north-west of figure 8.1) are similar in appearance, but not so clearly shell-shaped. Whiteoak et al. (1994) have used the ratio of 60μm to 843 MHz flux density as a thermal/non-thermal discriminator when evaluating SNR candidates. In this case, however, a non-thermal spectrum is expected for both hypotheses. The Loop has no obvious counterpart in Hα (figure 8.11).

8.2 Unresolved sources within Vela X

In his analysis of sources found in the first epoch MOST Galactic Plane Survey, Whiteoak (1992) notes a significant excess ($21 \pm 8\%$) of small-diameter ($< 60''$) sources in the Galactic Plane, when compared with a sample region away from the Plane. He concludes that the majority of these are probably HII regions and planetary nebulae. However, the fraction of sources not identified as thermal objects appears to be larger than can be accounted for by expected non-thermal sources such as small SNRs, radio stars and pulsars.

In the Vela X region, about 5–6 compact Galactic sources with $S_{843} > 50\,\mathrm{mJy}$ might be expected, based on Whiteoak's estimated excess of $1.4 \pm 0.6\,\mathrm{deg^{-2}}$ (one of these is the Vela pulsar!).[2] In the MOST images the morphology of local extended emission might be an indicator of the Galactic nature of some of the unresolved sources. Several sources in the Vela X region have an unusual juxtaposition with the extended emission of Vela X. This section reports on a brief investigation undertaken with the VLA to examine the nature of these sources, unresolved in the MOST Vela SNR survey. The purpose was to determine whether they were local condensations in the extended emission of the Vela SNR or chance coincidences of background sources. The sources investigated are labelled (a) to (d) in figure 8.1.

[2]There is a total of about 25 small-diameter source above 50 mJy in the region: the exact count is affected by the negative bowl.

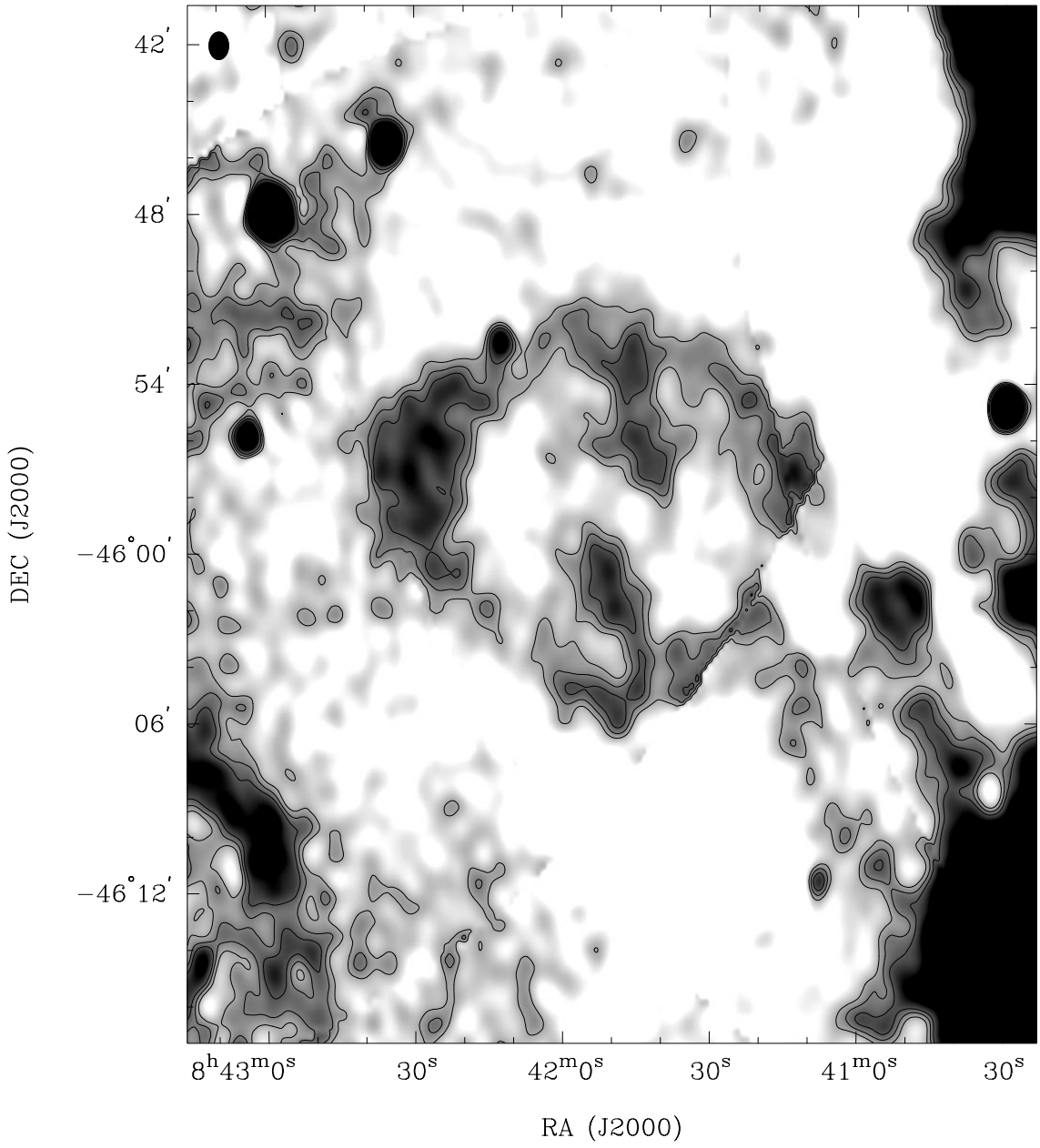

Figure 8.6 The Loop, protruding from the bright edge of Vela X (lower right). The abrupt transitions in flux density to the west of the Loop are artefacts of the mosaicing process. The scale is linear, from −3 (white) to 6 (black) mJy beam^{-1}, and the contours are at 0, 1.5, 3, 6, 10, 20 and 50 mJy beam^{-1}. The HPBW ellipse is shown at the top left. This image is a portion of the image in figure 8.1.

Sources (a) and (b) are along a thin filament (the Wisp: section 8.1.2) extending away from Vela X, with source (a) located where the Wisp changes direction. Although the Wisp is faint, its existence has been confirmed by the VLA 1.4 GHz observation of Vela X presented in section 8.4. Source (c) is in a region of bright extended emission within Vela X where several filaments meet, including one apparently emanating from the region of the pulsar. Source (d) is on a bright part of the X-ray 'jet' first seen by Markwardt & Ögelman (1995). Source (e) was found to be extragalactic by Bietenholz et al. (1991) using similar techniques to those used here and was not re-investigated.

8.2.1 Observations and reduction

The Very Large Array (VLA) was used in its BnA configuration to observe the sources on 1997 February 10.[3] This configuration has the highest resolution of the VLA at extreme southerly declinations, with the antennae spaced further apart on the northern arm to make the beam as nearly circular as possible. At the observing declination of $-45°$ the beam is elongated by a factor of approximately two. A snapshot observation of each source was made for six minutes at each of the three observing frequencies: 1.4649 GHz, 4.8851 GHz and 8.4351 GHz. The sources J0542+498 (3C147) and J0828−375 were observed for flux density and phase calibration, respectively. Standard NRAO procedures (Greisen 1996) in `AIPS` were used to edit and calibrate the data and then, imaging, cleaning and self-calibration were performed in `MIRIAD` (Sault et al. 1995). The restored half-power beamwidths were approximately $9'' \times 4''$, $3'' \times 1''$, $2'' \times 0.6''$ (RA×Dec.) respectively: the exact beams are shown in the images.

8.2.2 Results

Images of the four sources at the three frequencies of observation are shown in figures 8.7 and 8.8. The resolution of the observations at the three frequencies differs, but the images are shown to the same angular scale. The dynamic range of the images also varies due to changing confusion characteristics from the extended emission, as well as variations in receiver performance at the different observing frequencies. The contour intervals are at fixed percentages of the peak in all the images; the captions give the value of the peak (mJy beam^{-1}) and the lowest contour (%) in each case.

Spectral indices To measure the spectral index of each source, the clean components derived from observations at each frequency were restored with the corresponding beam of the 1.5 GHz observation. The u-v coverage of the VLA in the BnA configuration is such as to give (after deconvolution) complete flux density

[3] D. A. Frail kindly assisted with the planning of these observations and wrote the observing file.

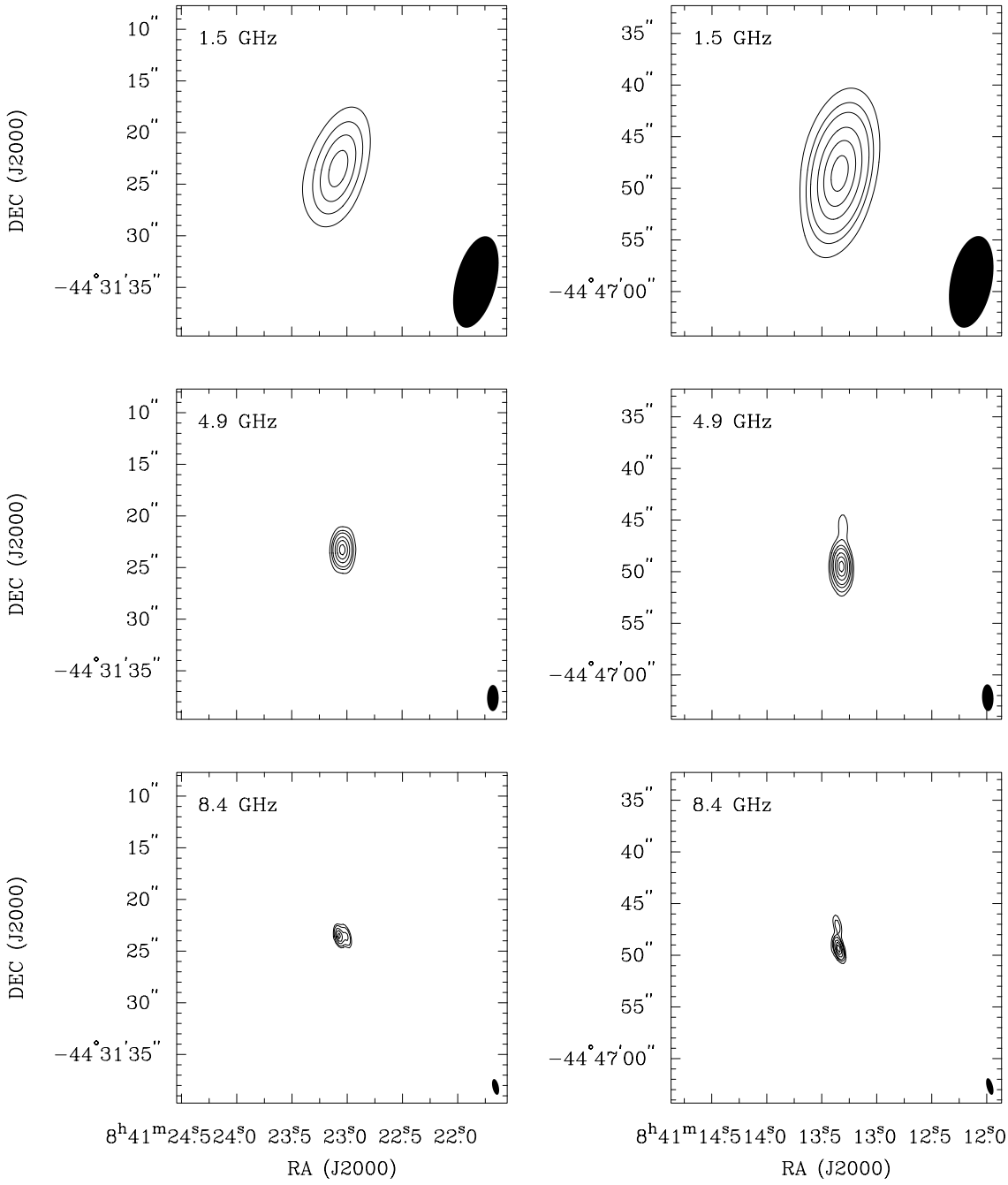

Figure 8.7 VLA images of source (a) (left) and source (b) (right) from the MOST Vela SNR survey. The contour levels are at 2, 5, 10, 20, 30, 50, 70, 90 % of the peak brightness, with the lowest level plotted dependent on the dynamic range (and at least 3σ in each case). The HPBW ellipse is plotted in the lower right corner of each image. The peak brightness and lowest contour plotted for each image are:

1.5 GHz	5.2 mJy beam^{-1}	30 %	5.6 mJy beam^{-1}	10 %
4.9 GHz	2.8 mJy beam^{-1}	10 %	5.4 mJy beam^{-1}	5 %
8.4 GHz	1.0 mJy beam^{-1}	20 %	3.9 mJy beam^{-1}	10 %

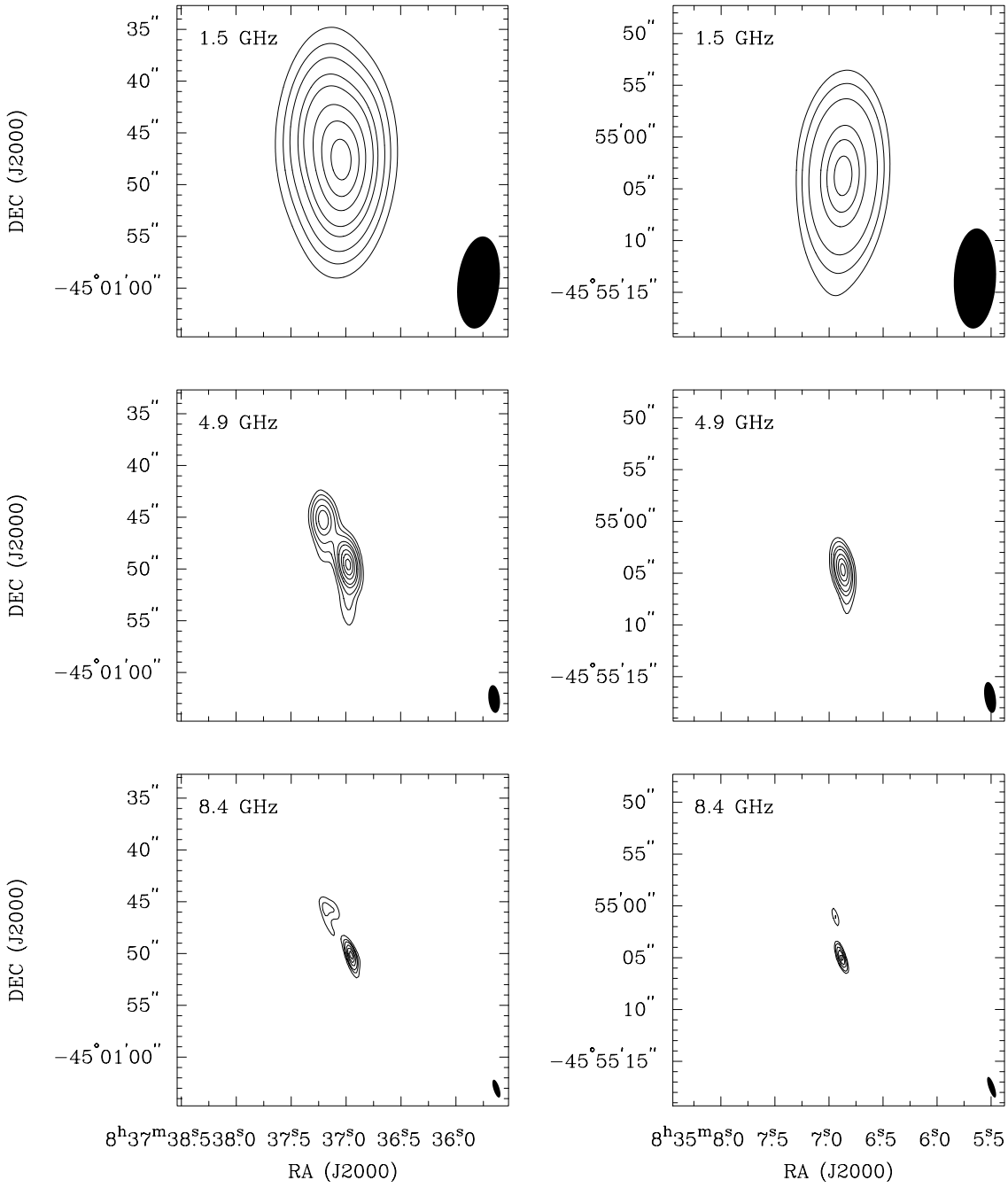

Figure 8.8 VLA images of source (c) (left) and source (d) (right) from the MOST Vela SNR survey. The contour levels are at 2, 5, 10, 20, 30, 50, 70, 90 % of the peak brightness, with the lowest level plotted dependent on the dynamic range (and at least 3σ in each case). The HPBW ellipse is plotted in the lower right corner of each image. The peak brightness and lowest contour plotted for each image are:

1.5 GHz	45 mJy beam^{-1}	2 %	18 mJy beam^{-1}	5 %
4.9 GHz	9.5 mJy beam^{-1}	2 %	4.4 mJy beam^{-1}	5 %
8.4 GHz	3.7 mJy beam^{-1}	10 %	1.5 mJy beam^{-1}	20 %

Source	Spectral index
(a)	-0.64 ± 0.17
(b)	-0.07 ± 0.07
(c)	-1.13 ± 0.03
(d)	-1.24 ± 0.07

Table 8.1 Spectral indices for each of the sources observed with the VLA

measurement of sources with size of the order of the 1.5 GHz beam even at 8.4 GHz. After taking into account differing background levels, the flux densities were used to determine the spectral index of each source. This procedure includes in the measurement any faint emission near the noise limit which would have appeared away from the main emission at high frequency and high resolution but which is included in the beam at 1.5 GHz. The spectral indices for each source are shown in table 8.1. The error estimate in each case is from the linear regression fits applied to the data, and may be an underestimate of the total uncertainty.

8.2.3 Discussion

Source (a) Partially resolved at 4.9 GHz, the morphology of this source at 8.5 GHz is typical of a double-lobe radio source. The spectral index is consistent with this. It is surprising that this apparently extragalactic source is located at the cusp of the Wisp (section 8.1.2). The axis of the source is aligned with the northern part of the Wisp.

Source (b) This is the source which is located on the southern section of the Wisp. With a flat spectral index, it could be either Galactic or extragalactic. Its morphology is consistent with it being extragalactic. The resolution of the observation at 8.5 GHz is insufficient to resolve the southern peak; however, the limit on source size and its flux density of 4.0 mJy implies $T_B > 1600$ K.

Sources (c) and (d) These two sources have classic double source morphologies and very steep spectral indices, so that there is little doubt that they are radio galaxies.

8.3 Complementary radio surveys of the Vela X region

Several complementary radio observations of the Vela SNR, have been made following the MOST observations discussed in section 8.1. The two major investigations have been a spectral index study of the Vela X region and attempts to measure better the polarisation characteristics of the radio filament corresponding to the X-ray 'jet'.

In this section I present these complementary observations of the Vela X region. Only the 1.4 GHz VLA radio observations are considered further in this thesis. However, I will describe each of them and the role they will play in continuing study of the Vela supernova remnant.

8.3.1 VLA 1.4 GHz observations

The Very Large Array in its DnC configuration was used to survey the Vela X region. This configuration approximately matches the resolution of the data to the resolution of the MOST 843 MHz image (section 8.1). The area of the Vela X nebula is much larger than the area of the VLA primary beam (4 square degrees compared with 0.2 square degrees), so a mosaicing technique was employed. Seventy-two pointing centres were observed on a 9×8 rectangular grid spaced equally at $15'$ intervals, half the HPBW of the primary beam at the observing frequency. Each pointing was observed for 25 s on four occasions spaced as widely as possible in hour angle. At the extreme declination limit of the VLA, the most southern pointing centres were observed over a smaller range of hour angles. Although the observing time at each pointing was not uniform, the mosaic is limited by confusion (both instrumental and astronomical) and thermal noise does not limit any of the pointings. The calibration sources 3C48 (gain), 3C286 (polarisation) and J0828-375 (phase) were observed.

To prevent the pulsar affecting the quality of the observations (as discussed for the MOST observations in section 5.2.1), the High Time Resolution Processor (Perley 1996) was used to implement pulsar gating. A configuration was chosen which caused the correlator to acquire data from the first IF when the pulsar was 'on' and from the second IF when the pulsar was 'off'. In this way, data without the pulsar could be used for imaging, while data with the pulsar could be used for self-calibration. This method has been previously used to image the region very close to the Vela pulsar (Bietenholz et al. 1991). The observations were made in two 4-hour sessions on 1996 June 2 and June 5. In the first of these, mosaic pointings closer to the pulsar were observed, and the pulsar gating was employed.[4] In the second, pointings more distant from the pulsar were observed and the gating procedure was not required. The pulsar was re-observed to allow self-calibration.

Editing and calibration of the data was performed in `AIPS`, using the standard methods described by Greisen (1996). Self-calibration was performed on the field containing the Vela pulsar and the derived calibrations were then applied to the other data.

Imaging and deconvolution made use of the `MIRIAD` system (Sault et al. 1995). The image was made with a taper to force the synthesised beam to a resolution similar to that of the MOST synthesised beam at the same declination ($43'' \times 60''$). Superuniform weighting (`sup`=1800) was applied to minimise the sidelobes at the expense of sensitivity. Deconvolution, using the 'joint' approach (Sault et al. 1996) made use of the maximum entropy method, which failed to converge in 90 iterations.

[4] D. A. Frail made the gating observation at the VLA.

However, after this many iterations improvements were minimal. No 'model' was provided in the deconvolution process. In future work the 1.4 GHz Parkes image of the area (see below) will be used as a model in order to add low spatial frequency content to the image. The image was restored with a beam of size $50'' \times 75''$ at a position angle of 10°.

Although data were collected in all Stokes parameters, software allowing joint deconvolution of multiple Stokes parameters is not yet available. The polarisation data will be analysed as a separate project.

Results The VLA image of the Vela X region is presented in figure 8.9. One immediately notes the strong similarity over many angular scales with the MOST image of the same area (figure 8.1). At first sight the image guides us in two clear ways. First, the spectral index of the remnant is reasonably uniform, as the structure is well-preserved between the two images. This aspect is investigated quantitatively in section 8.4. Secondly, the very faint structures noted around the remnant—such as 'the Loop' and 'the Wisp' mentioned in section 8.1.2, and the low-level emission at the northeast edge of Vela X—exist at both frequencies and are consequently not low-level artefacts.

8.3.2 Other available datasets

Various other observations have been taken and additional datasets been made available by other observers for future studies of the Vela X region. Although detailed analyses have not yet been carried out, they are presented here for completeness.

ATCA observations A project to study the spectral index distributions and polarisation of the central filament (the 'jet') in Vela X using the Australia Telescope Compact Array (ATCA) commenced in 1995. The project is a collaboration between the author, R. J. Sault and D. K. Milne (ATNF), and A. J. Green (University of Sydney). The project has comprised 12 hour mosaicing observations with each of the 750 m array configurations of the ATCA to form images of the filament at 1.4 and 2.3 GHz. One additional observation using a 6 km configuration was made of two of the mosaic pointings closest to the Vela pulsar to examine the emission in this area in greater detail and with greater sensitivity. For each of the observations, the 'pulsar binning' mode of the ATCA correlator was used to make images with and without the pulsar. The images containing the pulsar were used to self-calibrate the entire dataset. All the data have now been edited and calibrated. The joint-deconvolution process (Sault et al. 1996) is required to deconvolve the polarised structure in this highly complex region. Work on software to enable the joint deconvolution of polarised intensity images is still in progress.

VLA 327 MHz observations Observations of Vela X at 327 MHz were made using a single pointing of the VLA in the CnB and DnC configurations (Frail et al.

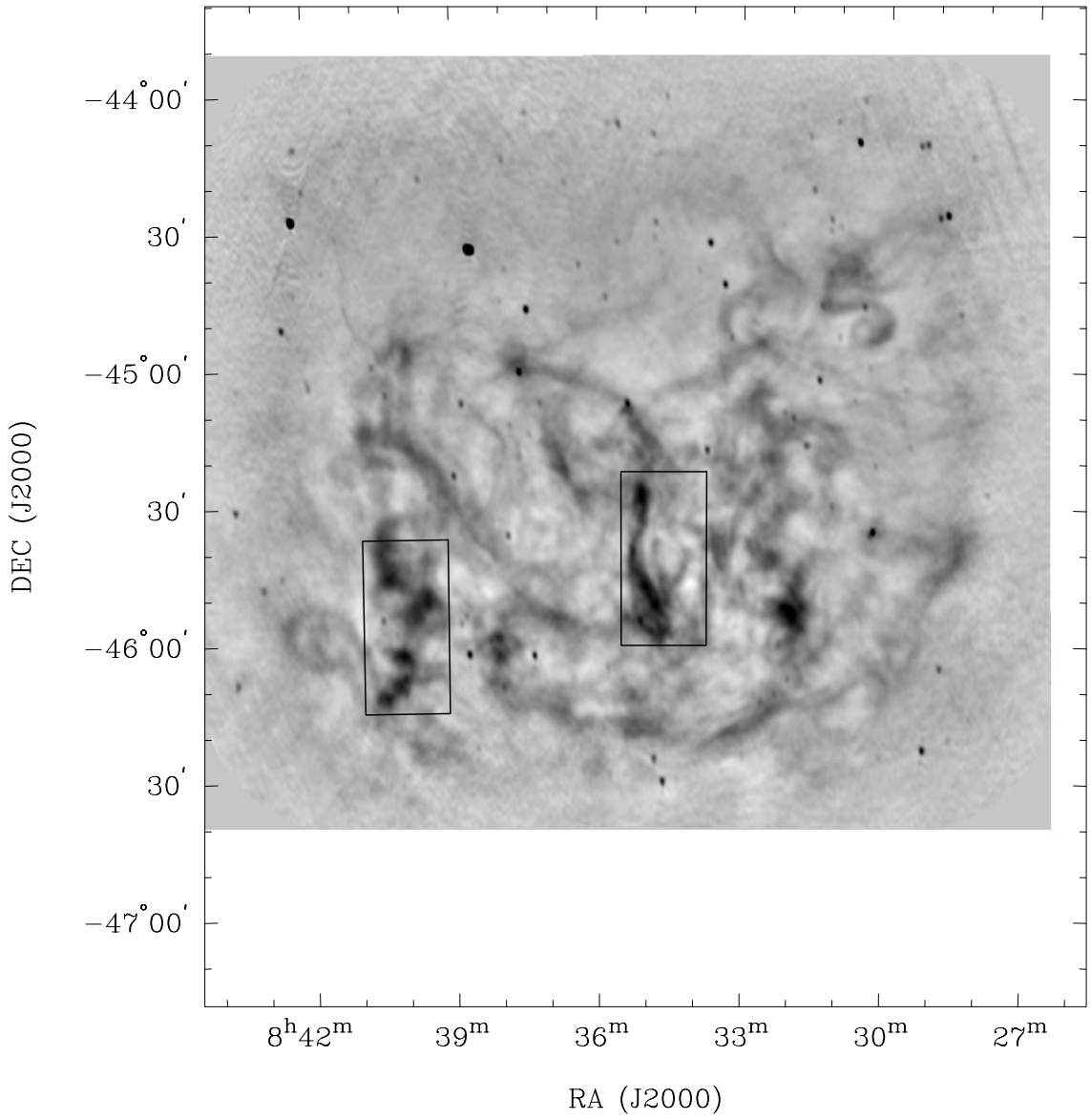

Figure 8.9 The 1380 MHz VLA image of the Vela X region. The image is on the same scale as the MOST image of the same region in figure 8.1, but covers a smaller area. Observation of the southern extremes are precluded by the declination limit of the VLA. The maximum entropy method of deconvolution has restored significantly more flux density than in the MOST image: the negative bowl artefact is absent. The boxes show the regions over which 843 MHz/1380 MHz spectral index was evaluated (see section 8.4)

1997). These data have been imaged with a resolution of $1' \times 1\farcm8$. Imaging problems with the non-coplanar baselines of the VLA (Perley 1989) appear to be affecting the registration of the images. However, work is in progress to improve the imaging algorithms to handle this case (D. A. Frail, personal communication, 1996). The accurate flux density calibration of the VLA will make these data valuable in a future extension of the spectral index assessment of the Vela X region.

Parkes 1.4 GHz observations Observations with the Parkes 64 m telescope were made of the Vela X region at 1.4 GHz with a $15'$ beam (FWHM) in 1996. These observations were part of a collaboration (A. R. Duncan, University of Queensland; R. F. Haynes, ATNF; and the author) to map the entire Vela supernova remnant in total and polarised intensity. The observations have been presented by Duncan et al. (1997). It is intended that these data will be combined with the VLA data for Vela X (section 8.3.1) to make a 1.4 GHz image with complete spatial frequency content up to the limit set by the restoring beam of the VLA observations, allowing a greater spatial frequency coverage in future spectral index studies. It is unfortunate that equivalent 843 MHz single dish data cannot be obtained to complement the MOST data in a similar way, since the 843 MHz Parkes receiver used by Roger et al. (1984) is no longer available.

Parkes 8.4 GHz observations Milne (1995) presented observations (already mentioned in chapter 4) of Vela X in polarised and total intensity with the Parkes Telescope at 8.4 GHz. Electronic versions of the observations were kindly provided by Milne and have now been converted to FITS format. Artefacts limit the usefulness of the data over the range of spatial frequencies in common with the MOST and VLA 1.4 GHz datasets. However, when the 327 MHz data has been imaged with software which takes the non-coplanar baselines sufficiently into account, the 8.4 GHz and 327 MHz images should provide useful additional data at lower spatial frequencies.

8.4 The Vela X filaments

The network of filaments comprising the Vela X plerion (figure 8.1) are considered to be due to the Vela pulsar's continuing energy loss. This section presents measurements of the spectral indices of two of these filaments. One filament is near the X-ray 'jet' found by Markwardt & Ögelman (1995). It has been suggested that this filament may be a 'shocked sheath' of the X-ray feature (Frail et al. 1997). The other filament is near the eastern edge of the plerion, well-removed from the X-ray feature. While the plerion overall has a spectral index of -0.16 (Dwarakanath 1991), a different spectral index for an individual filament might indicate an alternate origin.

8.4.1 Measuring spatial spectral index variation

The measurement of spectral indices of extended objects from interferometer data is a notoriously difficult task. This is mainly because one has to ensure that flux density measurements at different frequencies (often using different telescopes) are made with similar spatial frequency coverage. The Very Large Array has scaled array configurations for this purpose, which match spatial frequency coverage over a variety of observing bands. When imaging objects much smaller than the maximum spatial scale recorded by an interferometer, it is possible to restore complete spatial frequency coverage from zero up to the maximum determined by the resolution of the instrument, using deconvolution algorithms such as CLEAN or the maximum entropy method.

The Vela supernova remnant, by contrast, contains a significant proportion of its flux density in very extended structure, which is is not measured by interferometers such as the MOST or the VLA. Deconvolution algorithms attempt to remove artefacts caused by sidelobes, but have to extrapolate below the low spatial frequency cutoff set by the minimum interferometer spacing. If the synthesised beam is well known, allowing good deconvolution, the result will often be visually pleasing. However, the flux density at low spatial frequencies will typically be significantly underestimated. In section 8.1 we saw that the CLEAN deconvolution of the MOST survey sub-images was able to reconstruct about 12% of the total flux density of Vela X. Deconvolution of the VLA image (figure 8.9) has done somewhat better, by virtue of the better knowledge of its synthesised beam.

To measure spectral indices under these conditions, it is important that images at separate frequencies have identical spatial frequency (i.e. u-v) coverage, otherwise any measurement of spectral index is going to give spurious results. It is also generally accepted that the coverage should extend to the zero spacings in order that the total flux densities faithfully represent the source emission at each wavelength. The standard approach to this problem has been to add single dish data to interferometer data, filtering and scaling to ensure uniform spatial frequency coverage and correct relative calibration. This approach has commonly been applied in the study of supernova remnants, angularly some of the largest non-thermal emitters (Leahy & Roger 1991; Green 1990). An exception is that by using 'T–T plots' (described below) it is possible to make measurements in the presence of unknown total flux density, that is, an uncertain zero spatial frequency weighting in the image.

For the present study of the Vela supernova remnant, images of a very large area were produced, with sufficient resolution to separate emission from different regions of the remnant. At the declination of the Vela SNR ($-45°$), the possible instruments for such an observation are the MOST, the Australia Telescope Compact Array (ATCA), the VLA and the Parkes radiotelescope. The Parkes telescope has sufficient resolution only at high frequency, but the extant image at 8 GHz (Milne 1995) has significant imaging artefacts at spatial scales comparable to those available from the MOST 843 MHz data. Although at the limit of its declination range, the VLA has superior spatial frequency coverage to the ATCA, especially valuable when

imaging extended structure.

The image of the Vela SNR made with the VLA and presented in section 8.3.1 was obtained at 1380 MHz to facilitate mosaicing with the larger primary beam, although a greater difference from the MOST frequency of 843 MHz would have been desirable for this spectral index study.

8.4.2 T–T plots

T–T plots (Turtle et al. 1962) allow spectral index determination for regions of extended emission in the presence of zero-level errors in images. Originally they were made on contour plots calibrated in brightness temperature: the T–T stands for temperature–temperature. On the plots, the brightness temperature at many locations (such as at each pixel) within a region of an image is plotted against the brightness temperature of the same location on an image at a different frequency. Today, it is usual to make images measured in surface brightness with units Jy beam^{-1}, and the plot is of B_{ν_1} versus B_{ν_2}, where ν_1 and ν_2 are the observing frequencies. For historical continuity I will continue to refer to these plots as T–T plots.[5] On such a plot, the slope of the line of best fit is

$$\left(\frac{\nu_1}{\nu_2}\right)^{\alpha}$$

where the spectral index is α, using the spectral index as defined by $B_\nu \propto \nu^\alpha$.

This method of measuring the spectral index has two chief advantages. First, zero-level uncertainties in one or both of the images in the region of interest do not affect the result. This is because the slope is used to measure the spectral index, rather than the ratio B_{ν_1}/B_{ν_2}, which would not be constant in the presence of a zero-level error. As a result, the line of best fit need not pass through the origin of the T–T plot. Secondly, the action of fitting a line of best fit allows the inclusion of many points (pixels) in each measurement with a determination of error from the fit. A useful diagnostic is the distribution of the points on the graph. For example, a non-linear distribution of points on the graph could indicate poorly matched u-v coverage (as might occur where the baselevel of one image was locally sloping due to excess low spatial frequency coverage). Regions of different spectral index show up as distinct linear groupings of different slope (see, for example, Green 1990).

8.4.3 The adopted recipe

To make spectral index measurements using the MOST 843 MHz and VLA 1380 MHz images, the following procedure was adopted. This method has aspects in common with other recent approaches (e.g. Green 1990; Leahy & Roger 1991; Anderson & Rudnick 1993). The primary difference is that the data here are filtered to achieve

[5] Also because one of my supervisors has the colloquialised initials TT, and was amongst the earliest proponents of the method.

uniform spatial frequency coverage, rather than being deconvolved to similar models (Anderson & Rudnick 1993), or having had total power data added (Green 1990; Leahy & Roger 1991). Like Anderson & Rudnick, the plots are of surface brightness in Jy beam^{-1}, rather than of brightness temperature as often used earlier.

1. The images were interpolated onto the same projection with identical pixel sizes using `AIPS HGEOM`. The registration was confirmed to be within a few seconds of arc, better than 10% of the resolution of the images.
2. The MOST image was convolved to the same resolution as the VLA image: $50'' \times 75''$ (right ascension $\times$ declination) using `MIRIAD convol`.
3. A filter was created in the spatial frequency domain to eliminate low spatial frequencies from the data with a smooth cutoff from $10'$ to $15'$ (one quarter of a cosine function was used in the transition region).
4. The filter was fast Fourier transformed into the image domain and convolved with the images (`MIRIAD` tasks `fft` and `convol`).[6]
5. T–T plots were made using a subset of the pixels in each image: each fourth pixel in the direction of right ascension and each third pixel in the declination direction. This ensured that fit estimates were not affected by the correlated noise in adjacent pixels. The plots were made using data from regions spanning as large an intensity range as possible, while covering a morphologically similar region.
6. A line was fitted to each plot, using the routine `fitexy` (Press et al. 1992, p666), which allows for errors in each coordinate when making the fit. The estimates of error in the data provided to the routine were the approximate scatter of points on the plots.
7. The spectral index was calculated using the relationship above, with an error estimate from the formal error of the fit.

8.4.4 Results

T–T plots were made of the central 'jet' filament and the bright filament to the east of Vela X: the exact regions used are shown in figure 8.9. Tests using plots made over smaller regions (for example to search for spectral index variation along the central filament) were also done. However, there were insufficient data points to make reliable measurements of spectral index in these smaller areas. The T–T plots of the two regions are shown in figure 8.10. In each plot, the line of best fit (which provides the spectral index) is shown, along with a line showing for comparison the slope for a region of spectral index -0.5 (the flattest allowed by a simple strong shock: Longair 1994 and references therein). The derived spectral indices are $\alpha = 0.01 \pm 0.03$ for the central filament, which may be directly associated with the X-ray 'jet', and $\alpha = -0.09 \pm 0.03$ for the filament at the eastern edge of Vela X.

[6] Although `convol` actually operates in the Fourier domain, this method most easily preserves image headers within `MIRIAD`.

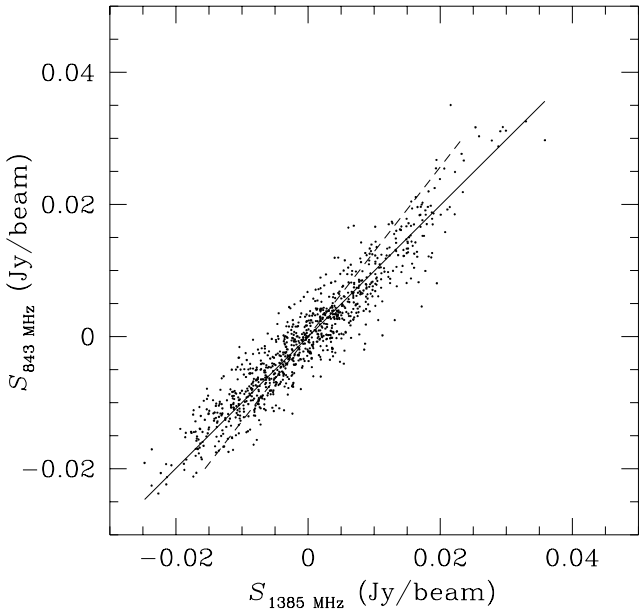

(a) the filament possibly associated with the 'jet' of Markwardt & Ögelman (1995), $\alpha = 0.01 \pm 0.03$

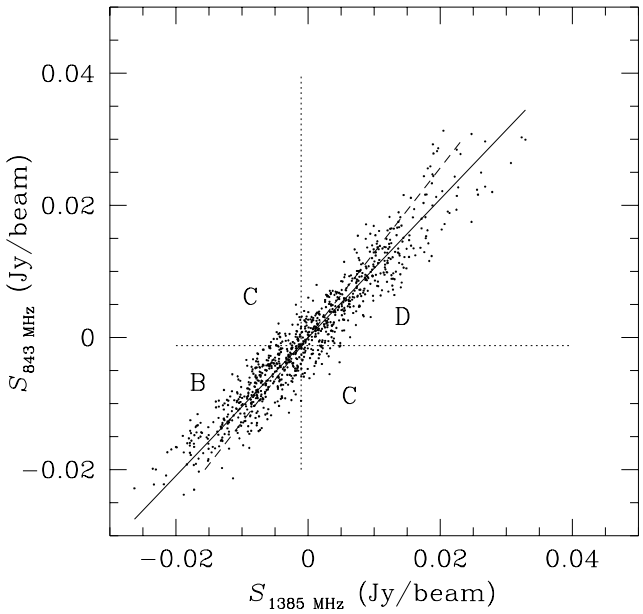

(b) another unassociated filament in Vela X (marked '1' in figure 8.1), $\alpha = -0.09 \pm 0.03$

Figure 8.10 T–T plots of two filaments in the Vela X region of the Vela SNR. The solid line is the line of best fit, from which the spectral indices (α) were derived. The dashed line in each plot is for $\alpha = -0.5$, the expected spectral index of a simple strong shock. In (b) the three classes into which the data were divided to form a contingency table are marked A, B and C (see text).

Error estimates The error estimates quoted, ± 0.03 in α, were derived from formal errors in fitting the line. However, these do not take into account calibration errors of either telescope. The MOST survey calibration accuracy is about 5%, while the absolute MOST flux density scale carries an additional uncertainty of 5% (section 5.3). Absolute calibration of the VLA is within 2% using the scale of Baars et al. (1977), while the bootstrapping calibration of individual observations introduces an additional 2% error (Taylor 1997). So, relative calibration of the two datasets should be within about 15%. R. W. Hunstead (personal communication, 1997) has confirmed this directly. He determined MOST/VLA (1420 MHz) spectral indices of 195 extragalactic point sources using the standard flux density scales and obtained a median spectral index of -0.8. Measurements of this parameter over longer frequency ranges typically fall in the range -0.8 to -0.9 (e.g. Murdoch & Hoskins 1973).

A further check on the method assessed the sensitivity of the measurements to a small movement of the region from which the data to make the plots were drawn. For this test, the measurement regions were shifted by three pixels in the declination direction or four pixels in the right ascension direction (corresponding to moving one sampling interval) to the north, south, east and west of the original position. The spectral indices derived in each case were within 0.01 of the values at the central position, indicating that the fit errors were not grossly underestimated. So the errors of fit quoted are appropriate for comparing the spectral index of one filament with the other. When comparing these spectral indices with measurements from other datasets, a more comprehensive error estimate, taking calibration errors into account, is about ± 0.3 in α.

Significance level tests In order to formally assess the likelihood of the data being consistent with the 'shocked sheath' model proposed by Frail et al. (1997), the statistical significance of this model with respect to the data was evaluated. Additionally, the significances of a model allowing a calibration error of up to 15% and of the fitted spectral index were also tested.

The data were divided into three distinct classes: those with value above the median of the data in each frequency, those below the median in each frequency and those remaining. The three classes are marked A, B and C respectively in figure 8.10 (b). For each model these classes were further divided into two classes according to whether the data were above or below the predicted values for the model, thereby forming a 3 by 2 contingency table (i.e. where the three rows correspond to the initial three classes and the two columns correspond to whether the data were above or below the predicted value for the model in question).

If the model in question fits the data well, we would expect that the rows and columns of the contingency table would be statistically independent (i.e., the proportion of data above the predicted value for the model would be approximately the same in each of the three initial classes). Pearson's χ^2 test (Agresti 1990, p47) was

used to test this. The results of the χ^2 test for the models are shown in table 8.2.[7] The analysis shows that the simple shock model ($\alpha = -0.5$) is not significant, even when allowing for a calibration error of up to 15%. The significance of the model estimated from the data is high, indicating that the fitting process was appropriate.

	Significance level	
Spectral index model	Filament near the 'jet'	Filament near edge of Vela X
$\alpha = -0.5$	1×10^{-40}	2×10^{-31}
$\alpha = -0.5$ with 15% calibration error	1×12^{-13}	3×10^{-5}
α estimated from data	0.39	0.52

Table 8.2 Significance levels of the data with respect to spectral index models for the two strongest filaments within Vela X. The filaments are labelled '2' and '1' respectively in figure 8.1.

8.4.5 Discussion

Although the method of selecting a limited u-v range over which to measure spectral index is not common practice, it is at least as appropriate as the method of Anderson & Rudnick (1993), who use a common model to reconstruct consistent low spatial frequencies at each of the observed frequencies, using a maximum entropy method deconvolution. Indeed, it seems preferable to discard the low spatial frequencies if they are to be reconstructed to an identical model. The structure at low spatial frequencies will be well-correlated after deconvolution, possibly masking any poor correlation at higher spatial frequencies which might be detected in the T–T plots, and which might indicate errors in the analysis.

The spectral indices derived for the two filaments in the central nebula of the Vela SNR are essentially the same, at the 2σ level, indicating that the central filament is probably produced by the same mechanism as the other filaments in Vela X. Hence, it may not be related to the pulsar in any special way. The central filament may be behind or in front of the pulsar in the nebula, although there is no limb-brightening to indicate that the observed filaments are concentrated to the outside of a spherical structure. Rather, the single dish images of Vela X, of which the image by Milne (1995) has the highest resolution, indicate a brightening towards the centre of the remnant, consistent with other 'filled-centre' remnants that are thought to be pulsar-powered. An evaluation of the detected flux density in the MOST Vela SNR survey image of Vela X (section 8.1) indicates that the majority of the emission is in extended structure.

[7]Note that this χ^2 statistic is not the same as the one used to estimate the best-fit spectral index. The Pearson χ^2 statistic makes no assumptions about data distributions or correlations, but nevertheless supports the estimated model for these data.

The two filaments have similar spectral indices to the accepted value for the whole of Vela X, -0.16 ± 0.02 (Dwarakanath 1991), within the larger error estimate (of ± 0.3) which includes an estimate of calibration uncertainty. This suggests that the emission from the filaments is due to the same mechanism as the rest of Vela X. These filaments could be just the brightest of a network of filaments making up Vela X. This idea is supported by the view of the nebula seen in figure 8.3, in which the whole of Vela X looks like a chaotic collection of smaller nebulous regions, some of which happen to appear as filaments. Alternatively, the plerion could consist principally of a homogeneous, approximately spherical object, resolved out by interferometers, with several filamentary condensations, possibly instabilities at the contact discontinuity between the pulsar-powered nebula and the supernova ejecta. Such a scenario is observed optically in the younger Crab Nebula, where O III filaments have been found in a thick shell surrounding the central nebula (Lawrence et al. 1995). HST observations (Hester et al. 1996) indicate that these are Rayleigh-Taylor instabilities at the contact discontinuity. It is difficult to see how to obtain three-dimensional information about the Vela filaments as correlated line emission has not yet been detected.

8.5 Vela X in Hα

8.5.1 Observations

Test observations from the Mount Stromlo and Siding Springs Observatory/University of Sydney wide field Hα imaging sky survey (section 7.1.2; Buxton et al. 1997) provide the opportunity to compare the Hα emission from the Vela X region with the 843 MHz radio emission.

The Hα image presented in figure 8.11 has been derived from six 600 second exposures, three taken through a 15 Å Hα filter and three through a continuum filter.[8] After flat-fielding and bias-subtraction the observations taken with each filter were combined to form single images, removing the effect of cosmic rays and CCD defects. The continuum emission was then subtracted from the data taken through the Hα filter. The subtraction was imperfect: median filtering applied within 3×3 pixel boxes has removed some of the artefacts. For further details of the observing apparatus, see section 7.1.2.

A coordinate system was applied to the image by comparison with a Digital Sky Survey image (Morrison 1995) using `koords`, part of the `KARMA` package (Gooch 1996). Within a central $50' \times 50'$ box in the image, a coordinate solution was determined to better than $12''$. Beyond this region the solution is poorer, with positions in error by up to $\sim 1'$ due to the geometry of the optical system. This error is comparable with the resolution of the radio image ($43'' \times 60''$).

[8]The observations were made by A. J. Walker, University of Wollongong, who also did the bias-subtraction and flat-field correction.

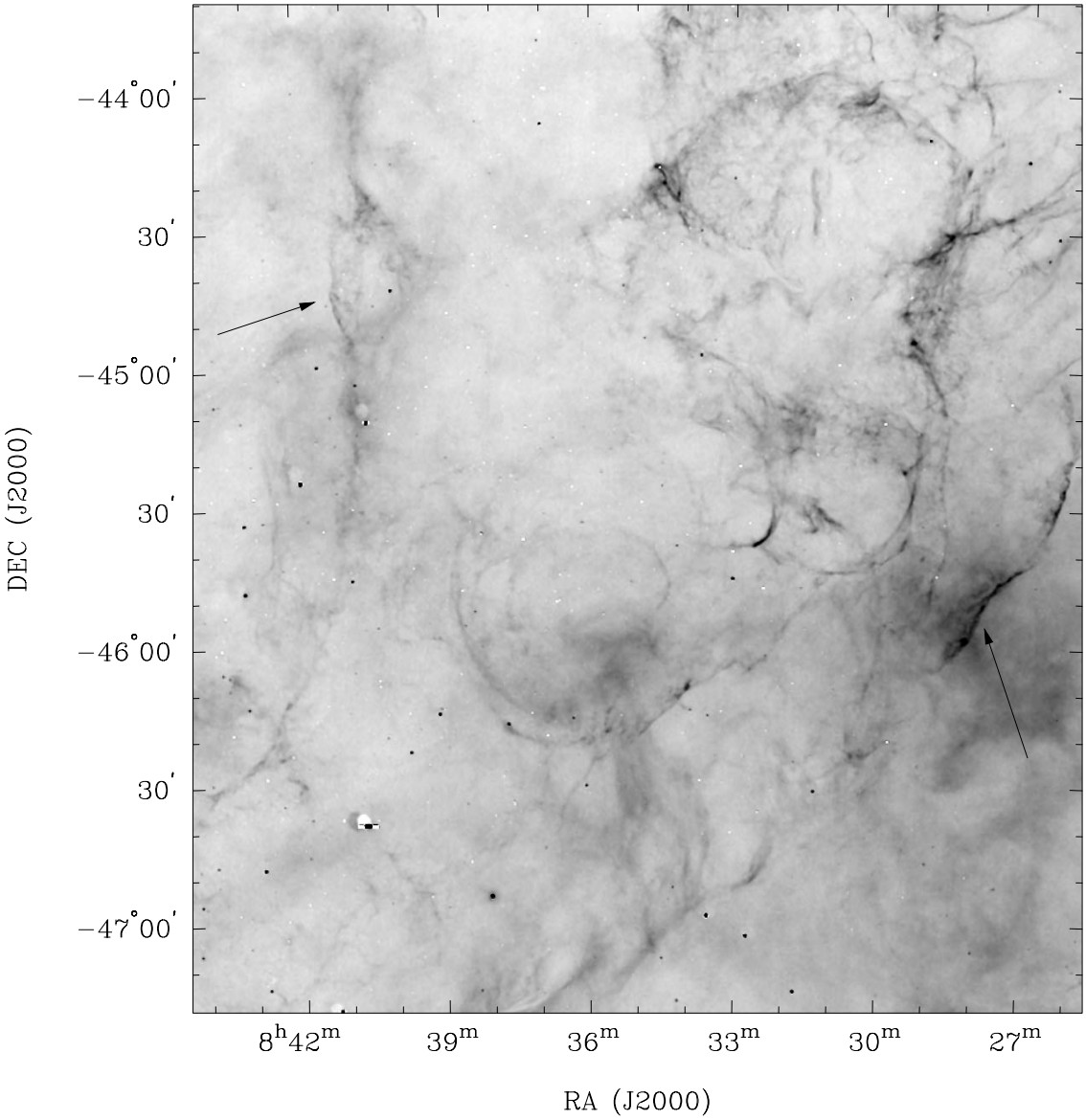

Figure 8.11 Hα emission in the Vela X region, from the MSSSO/University of Sydney wide field Hα imaging survey. The MOST image of the same area is repeated in the following figure for easy comparison. The arrows point to two of the Hα filaments with most obvious 843 MHz counterparts. The eastern of the two is coincident with part of the Wisp (figure 8.5).

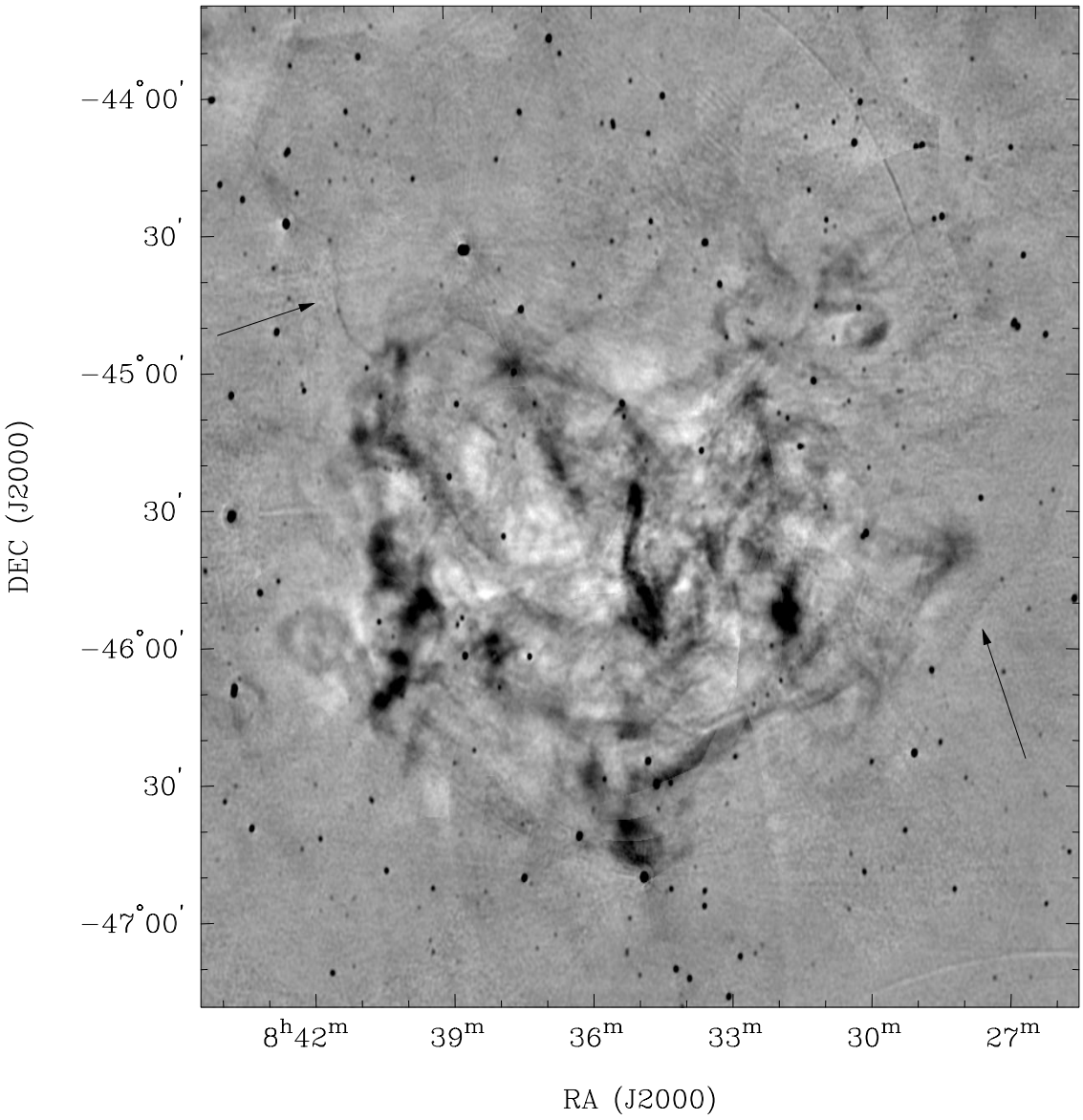

Figure 8.12 Vela X at 843 MHz in the MOST Vela SNR survey. This is a repeat of figure 8.1 for comparison with the Hα emission in figure 8.11. The arrows indicate the filaments with Hα counterparts.

8.5.2 Discussion

The Hα image of the Vela X region is remarkable in its contrast to the radio observations. Initial inspection shows gross differences. There is no visible Hα counterpart to the strongest radio filaments (1 and 2 in figure 8.1), nor to the X-ray jet seen by Markwardt & Ögelman (1995). In general the bulk of the radio emission, which is on scales greater than $1'$, has no optical counterpart. Much of the Hα emission is thin and filamentary, similar in structure to that seen in the shell region (chapter 7). A few of these Hα filaments do have counterparts in the 843 MHz image, generally they are the thinnest of the radio filaments. In figure 8.11, two of these are marked with arrows. In the radio, these filaments are also thin—one of them is the Wisp (section 8.1.2). This coincidence may indicate that these radio filaments (already different in structure from the majority of radio emission in Vela X) are shell filaments seen in projection, and not directly associated with the pulsar-powered Vela X nebula. Much of the optical emission could be from the shell of the SNR, since we saw in chapter 7 that there is relatively poor agreement between the Hα and non-thermal components of the shell emission.

This lack of agreement is in contrast to that observed in the Crab Nebula, where excellent agreement is found on scales greater than about 0.1 pc (e.g. Wright & Forster 1980). The Crab is a much younger remnant, and the emission mechanisms may be quite different.

There is some position coincidence between diffuse low-level Hα emission and radio emission in the plerion, but this preliminary survey image is not suitable for a deep study. Note also that some emission may be affected by absorption in the direction of Vela (Eggen 1980).

8.6 Conclusions

In this chapter I have presented radio observations of the pulsar-powered nebula in the Vela SNR at the highest resolution yet available, a spatial resolution comparable only with the Crab Nebula among SNR plerions. The images display a remarkable array of interesting filaments and structures. The region immediately surrounding the Vela pulsar contains much non-thermal emission in addition to the possible pulsar wind nebula seen by Bietenholz et al. (1991). Unlike the Crab, the Vela plerion at radio frequencies displays little correlation with Hα emission. The origin of the radio filaments remains unclear.

The Vela plerion in the radio consists both of diffuse and filamentary emission. The spectral indices of selected filaments are consistent with the flat spectral index previously determined for the whole of Vela X, indicating that the filaments are probably powered by the same mechanism used by the pulsar to power the entire nebula. Specifically, the X-ray 'jet' discovered by Markwardt & Ögelman (1995) appears *not* to be shock heating the adjacent radio filament as suggested by Frail et al. (1997), nor is there Hα emission to indicate cooling postshock material in the

region. In fact, the radio filament seems not to be different from other filaments in the Vela nebula. This implies that the 'jet' may not be magnetically confined as suggested by Markwardt & Ögelman and that alternative explanations should be investigated. Furthermore, the problem of how the Vela pulsar can power a nebula when situated so far from the centre is still unresolved.

Chapter 9

Final Discussion and Future Prospects

9.1 The MOST Wide Field project

The conversion of the MOST to an instrument capable of imaging fields five times the maximum area observable before 1996, has been a major task which has required significant resources from the Astrophysics Department over several years. This thesis has shown that, with the essential features of the Wide Field observing system in place, the MOST can now image elliptical fields of area up to $5\overset{\circ}{.}8 \operatorname{cosec} |\delta|$, accurately reproducing extended and compact emission.

This process has involved the removal of the 176 preamplifiers installed on the antennae of the MOST and their replacement by 352 new low noise amplifiers. Computer controlled phasing circuits apply phase gradients to the signals from these amplifiers in such as way as to offset the primary beam of each bay from the central position set by the phase gradient applied mechanically in the feed. This allows time-sharing during a 12 hour synthesis observation to fully synthesise each sky point within the area approximately circumscribed by the $2\overset{\circ}{.}2$ tilt extent of the primary beam of the MOST.

Initial testing of the new observing mode has focussed on ensuring that the hardware components of the system are working as expected, and on checking that the telescope performance after conversion is maintained at a high level. Observations of extended emission and of small-diameter sources have confirmed these objectives. Measurements made in quiet regions of the sky have been used to determine that the noise performance of the MOST is near the 0.5–1 mJy beam^{-1} attained by the MOST when it was observing smaller fields before the conversion (Robertson 1991). Observations for the Wide Field extragalactic and Galactic surveys (to be called the Sydney University MOST Sky Survey, SUMSS) have begun.

To optimise the quality and reliability of the survey images, attention is now being focussed on three key areas.

Telescope modelling The complex phasing system of the MOST leads to interrelated telescope parameters which vary in complicated ways. The meridian distance gain correction of the MOST has now been well determined (Burgess 1989), but its theory is still not well understood. The meridian distance (terrestrial east-west) component of the primary beamshape of a bay may be calculated from theory. Measurements of the pre-1989 MD beamshape agreed reasonably well with the calculation (Reynolds 1986, p14): a measurement of the Wide Field MD primary beamshape is now in order. However, the tilt (terrestrial north-south) primary beamshape is not as well known. It is strongly dependent on meridian distance, and is reasonably well correlated with the MD gain curve (Reynolds 1986, p20) at $MD \lesssim 20°$. In most syntheses to date, Reynolds' original formula has been used with only minor amendments to model the tilt primary beamshape with a single parameter, the half-power width. It is now appears that this is not sufficient for Wide Field images. Recent attempts to provide a better model for the tilt primary beam (Crawford 1996 and personal communication 1997) have indicated that more observations are necessary to refine further the tilt primary beam model for Wide Field observations.

Reduction software The two MOST synthesis packages `mstkln` and `newsyn` have now each been used to make Wide Field images. They adopt alternative imaging algorithms which have different advantages. A further synthesis method, under investigation by L. E. Cram (personal communication 1997), involves placing individual measurements in the Fourier plane and producing an image by the Fourier transform imaging methods used with interferometers such as the ATCA and VLA. The evaluation and refinement of image production methods will doubtless continue well into the observing period of the MOST Wide Field surveys.

IF and LO systems Although not essential to the implementation of Wide Field observing, replacement intermediate-frequency and local oscillator systems are nevertheless an important part of the Wide Field upgrade. They will significantly improve the performance of the MOST, particularly during periods of changing temperature and humidity. The new IF system is scheduled to be installed by the summer of 1997–98, while improvements to the existing LO system are presently under investigation. Following the completion of these projects, quality enhancement of MOST images will depend primarily on improvements to the telescope models and enhancements in the reduction software.

9.2 The Vela supernova remnant

The MOST Vela supernova remnant survey, presented in this thesis, is the first radio survey of the Vela SNR to cover the bulk of the remnant at high resolution ($\sim 43'' \times 60''$). The proximity of Vela (500 pc) allows us to see structure within the remnant on scales of 0.1 pc, while the comprehensive spatial frequency coverage of the MOST still allows imaging of extended structure on scales up to about 4 pc

(30′). Although very diffuse structure is not present in the survey, this emission has been well-imaged in earlier surveys. Indeed, its absence in the MOST survey lends clarity to the structure present on smaller scales.

Two fundamentally different regions of the Vela SNR are exposed morphologically at this high resolution. The shell of the remnant appears as a series of lengthy tangential filaments, principally near the Galactic Plane, while the region near the Vela pulsar is comprised of brighter, more nebulous filaments at various orientations but offset as a group with centre 40′ south of the pulsar itself. The identification of the Vela SNR as a composite remnant on this clear morphological evidence leads naturally to the proposition that it be considered the archetypal composite SNR in the Galaxy for future detailed study.

The Vela shell The Vela shell provides an excellent laboratory in which to study SNR shocks. It is bright at radio, optical and X-ray wavelengths, allowing an investigation of each of the major emission mechanisms found in SNRs. The optical/X-ray emission regimes broadly support the cloud interactions which have been successfully used to explain the optical/X-ray structure in the Cygnus Loop (Hester & Cox 1986; Graham et al. 1995; Levenson et al. 1996). The radio emission has presented more of a challenge. Although it is due primarily to non-thermal processes, in contrast with the thermal processes which give rise to the X-ray and optical emission, radio emission has been found generally to follow optical emission in other middle-aged remnants such as the Cygnus Loop, IC443 and HB3. In the Vela shell, the situation is different. Although we see some optical/radio agreement, the majority of emission in each of these regimes is without counterpart in the other. At least in the case of the optical emission, this cannot be explained by a lack of observing sensitivity, since some weaker optical emission has a radio counterpart, while much of the stronger optical emission does not. Although absorption might be suspected, there is optical emission in the area where the main radio emission is observed, but it is not correlated with the optical emission.

More sensitive radio observations are unlikely to uncover much more in the radio regime: confusion from Galactic emission limits images made this close to the Galactic Plane. However, it may be possible to detect polarisation of the faint shell filaments, allowing a detailed study of the magnetic fields responsible for the synchrotron emission. Possibilities for future study lie more with the bright optical filaments. Spectral analyses of these should allow us to separate Balmer filaments due to the fast non-radiative shock from the radiative filaments present where the shock interacts with more dense material. A better theoretical understanding of how the radio emission is related to the optical emission is desirable to clarify the question of why optical and radio filaments should sometimes occur together, and why in Vela they are not well-correlated. A three-dimensional picture of the Vela shell would assist these investigations.

Vela X The mystery of how the Vela pulsar can power the plerionic component of the Vela SNR when it is so far from the centre of the nebula is still with us. Investigations in this thesis indicate that the radio filament of Frail et al. (1997) probably has no unique function within the remnant. This casts doubt on the interpretation of Markwardt & Ögelman (1995) that the 'jet' seen in X-ray observations is magnetically confined, and acting as a conduit to power Vela X.

The origin of the rest of the filaments in Vela X is not clear either. In contrast to the filaments seen in the Crab Nebula, the distinctly nebulous radio filaments in Vela have no optical counterparts. Detailed polarisation measurements of several of these filaments will be in reach when reduction software is in place to deconvolve ATCA mosaics in all Stokes parameters. A more comprehensive spectral index study will be enabled when the 327 MHz VLA data can be imaged correctly and when the VLA and Parkes 1.4 GHz images have been combined. A detailed investigation of the region very close to the pulsar in polarised and total intensities may lead to a better understanding of the way pulsars power the nebulae seen in composite and plerionic SNRs.

Appendix A

The MOST Wide Field Communications System

Chapter 2 outlined the idea of the Wide Field system and gave an overview of the development of the sub-system components. This appendix describes specifically the system which provides the communications link between the master controller and the bay controllers and doubles as the technical documentation for the system. I took sole responsibility for this project, from development to manufacturing and commissioning.

A.1 System requirements

The overall design considerations leading to the choice of a distributed control system and the use of optic fibre as the transport medium have been mentioned in section 2.5. These aspects of the system are discussed more fully by North (1994). Specific requirements of the communications system which resulted from North's work or subsequent considerations are given below.

Low cost The project as a whole had a limited budget. Excluding in-house labour, the main production costs were the bay linkers (A$50 each) and the optic fibre (A$40/bay).

Reliability The daisy-chain design meant that the failure of a single link would result in the failure of an entire 12 hour synthesis observation. Hence it was essential that each unit operate reliably under a wide range of environmental conditions.

Ease of installation and maintenance As with all of the Wide Field upgrade, it was desirable to limit interruption to observing as much as possible during installation. Low maintenance is especially desirable given the small Molonglo staff.

Use of optic fibre Optic fibre was required to provide immunity from interference, lightning and ground loops, and to reduce electro-magnetic radiation, which would cause radio-frequency interference.

Duplex low speed data The data rate[1] of the bay controllers was set at $9600\,\mathrm{bit\,s^{-1}}$—fast enough to allow many simple commands each second, and to allow the loading of user code to the bay controllers in a reasonable time—yet slow enough to enable daisy-chaining without the need for pulse shaping at each bay.[2] A return path was required for acknowledgement by the bay controllers of commands received and for the return of data collected by the bay controllers.

Carriage of the hardware bay controller reset signal A hardware reset is desirable for any microprocessor-based system. In order to make this as basic and reliable as possible it was preferred to have the communications system carry out this task, by applying a reset pulse directly to the bay controller, without expecting the bay controller to be able to decode commands in the usual way.

Isolation of faulty bay controllers It was realised early in the development of the system that the bay controllers, containing microprocessors and directly linked to several other systems, would be vulnerable to failure. The communications system had to be designed to detect faulty bay controllers and ignore them, thus preventing isolated bay controller failures from disabling the entire system.

Low power consumption At the time of the communications system design, the power supplies for the new Wide Field hardware at each bay were already in production, putting strict limits on the available power supply.

A.2 System description

A schematic of the system as actually implemented appears in figure A.1. The system consists of three main components: the bay linkers located at each bay; the optic fibres, which carry communications between the bays; and the control room/local oscillator hut link, which consists of interfaces in the control room and at the beginning of the optic fibre run. These components are described in the following sections. The only external connections to the system are the connections to the master controller, bay controllers and to the 240 V mains in the local oscillator hut and control room. This helps to keep the system secure from unexpected interactions.

[1] This is the data rate of the control system. Radio-frequency data returns via a separate 11 MHz coaxial system with a 3 MHz bandwidth.

[2] This would involve a local clock to maintain pulse widths, requiring more hardware and increased complexity.

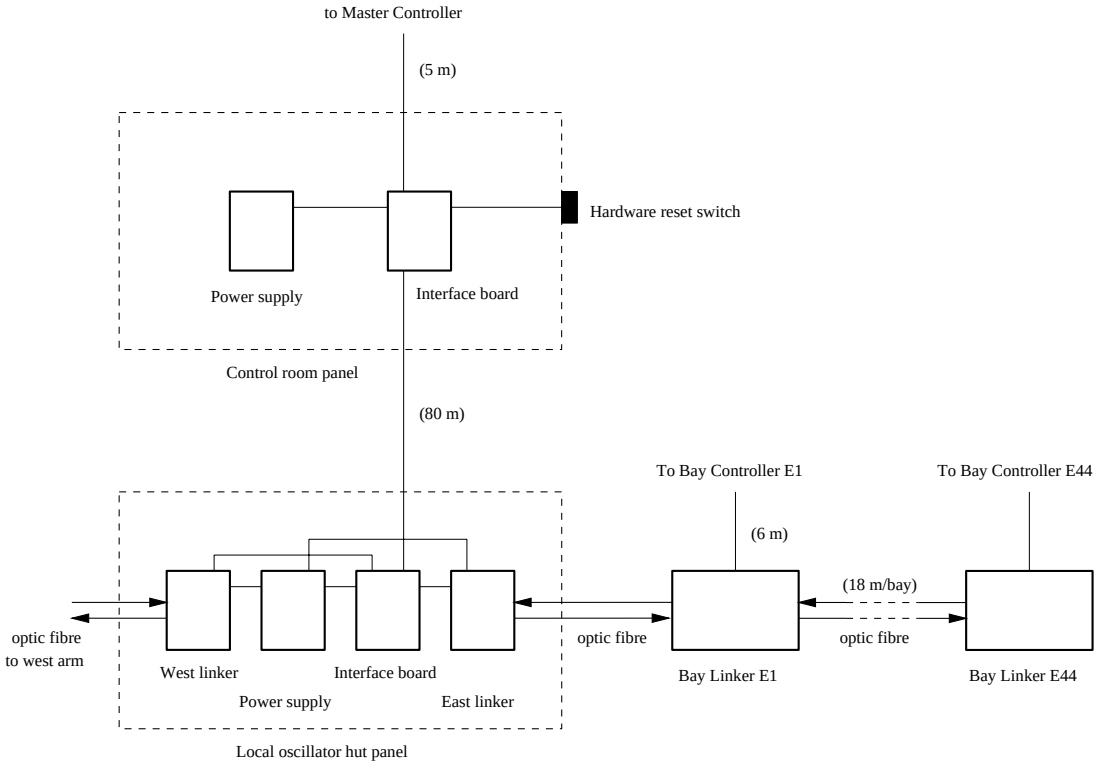

Figure A.1 Schematic of the MOST Wide Field communications system. Data connections are made with 'wire' except where the use of optic fibre is indicated. The hardware reset transmits a pulse to the bay linkers, which then reset the bay controllers.

A.3 Bay linkers

The bay linkers form the core of the Wide Field communications system. They use a mix of complementary metal-oxide-semiconductor (CMOS) digital logic and analogue circuitry to achieve the translation between the signal on the optic fibre and the digital bay controller. There are eighty-eight bay linkers installed on the telescope, and seventeen spares. This section outlines the principal features and specifications of the bay linkers and discusses the tests that were used to verify their operation prior to installation. A photograph of one bay linker is given in figure 2.9. The printed circuit board layout used is shown in figure A.2; the linkers were wired according to the diagram given in figure A.3.

A.3.1 Transmitters and detectors

The transmitters and detectors available for the project were Siemens devices SFH750V (LED1, LED2)[3] and SFH250V (P1, P2), each mounted in cases which secure the optic fibre directly with knurled fasteners. The transmitters, light emitting diodes (LEDs), emit at 660 nm with operating currents up to 30 mA at 50°C. It was found experimentally that they have significant temperature coefficients, and there is great variability between individual devices, necessitating the individual matching of the driving resistors (R7, R17) to the transmitters. Furthermore, the received signal at a linker can vary by up to 15% when the fibre is rotated in the transmitter on the previous linker, indicating asymmetry in both the fibre and transmitter. The detectors are photodiodes sensitive over a wide range of wavelengths, peaking at 850 nm. The sensitivity at 660 nm is about 70% of the peak value. Their high output impedance makes significant amplification necessary before detection: fast LF357 operational amplifiers (U5:A, U5:B) were used for this purpose.

A.3.2 Pulse shaping

The dominant delay in a bay linker is due to the rise and fall times at the output of the operational amplifiers which follow the photodiode detectors. The rise and fall times are set by the feedback resistors (R1, R2), which also control the gain. The choice of value for these resistors is a compromise between speed and signal levels: too small and coupling between outward and inward signal paths (i.e. crosstalk: section A.3.3) becomes large; too large and the circuit becomes too slow. The eventual choice (68 kΩ) provides 90%/10% rise and fall times of 190 ns and output levels of ∼600 mV (with resistors appropriately chosen to match the transmitting LEDs). The feedback capacitors (C1, C2) have been chosen for critical damping of the response.

The variation in light coupling with fibre orientation mentioned above (section A.3.1) leads to a significant variation in the signal received by each bay linker when installed on the telescope, even after the matching of resistors to individual transmitters. The installation specification required the detected signal to be between 600 mV and 700 mV.

The difference between the rise and fall delays determines the change in width of pulses (and so whether they are properly detected by the bay controllers). For one bay linker, this difference is

$$t = \frac{t_r}{V_{\max}}(V_{\max} - (V_{t^-} + V_{t^+})),$$

where t_r is the '100% rise time' (defined here as 1.25 times the 90%/10% time), V_{t^-} and V_{t^+} are the detection thresholds and $V_{\max}$ is the the signal voltage.

[3] Where I note pairs of component designators for the bay linkers, I will place the designator for the 'inwards' component (i.e. the one in the signal path *to* the control room *from* the bays) before the 'outwards' component designator.

For the adopted detection and light levels, the differential delay for one linker is 130 ns, leading to a pulse *broadening* of about 6 μs for each arm. The actual value will generally be lower, as many bay linkers have detected signals less than 700 mV. Actual measurements of many linkers in series (section A.6.2) confirm this.

A.3.3 Crosstalk immunity

Digital logic designed to run at high speed can radiate significantly at levels detectable by standard analogue circuitry. The mix of high speed digital logic and the small signals detected by the photodiode necessarily causes crosstalk: from the relatively high currents driving the transmitter of one signal path to the high-gain inputs to the operational amplifiers detecting the photodiode current in the other signal path. Ordinarily this can be tolerated, as it is of short duration ($< 1\mu$s). However, in the presence of low signal levels (due to poor fibre connection, high temperature etc.) the crosstalk could cause bay linkers to oscillate, affecting the entire communications system, and making the fault difficult to locate. To reduce crosstalk to a low level, ground planes were placed on the printed circuit board (PCB) around the LF357 operational amplifiers, and digital circuits were located as far as possible from analogue circuits in which they could cause crosstalk. As finally implemented, crosstalk detected at the input to the comparator was limited to 45 mV. The hysteresis in the detection circuit was set at 95 mV (a positive-edge threshhold of 200 mV and a negative-edge threshhold of 105 mV). No oscillations were detected in the production bay linkers even at marginal input light levels.

A.3.4 Reset pulse detection circuitry

A bay controller reset signal can be sent with a 250 ms pulse in the optic fibre. The purpose of the reset pulse detection circuitry in the bay linkers is to detect this pulse in the normal transmission circuit and apply a pulse to a special circuit leading directly to the reset pin of the 80C552 microprocessor on the bay controller. This is implemented by a capacitive integrating circuit (R21, C19) measured by a comparator (the LM393; U6:A). The time constant is set so that a '1' held on the system will trigger the bay controller reset after 190 ms (when the integrated signal at pin 2 of U6 falls to 1.1 V). Normal transmission does not trigger the reset pulse because bytes (taking about 1 ms) are sent only each 3 ms. The reset pulse on the fibre can be caused either by the hardware reset switch on the control room interface panel or by a command issued to the master controller (`reset bay controllers`), which sends a stream of bytes comprised entirely of '1's at a very low baud rate with no added inter-byte delay.

A.3.5 Bay controller lockout circuitry

The bay linkers have been designed to be insensitive to the most likely fault conditions in bay controllers. Faulty bay controllers could disable the entire communica-

tions system if they were allowed to continuously send a message or if they caused a bay linker to fail in some way. Possible faults could manifest themselves to the bay linker in the bay controller reception or transmission circuits.

Bay controller reception A failed bay controller could hold its receiving line low or high incorrectly. The bay linker supplies the bay controller through a CMOS gate (U3:D) which has a relatively high output impedance. This should not normally fail, but even if it should, only the local observation LEDs (LED3:A/B) would be affected—normal transmission to the next bay linker would be unimpared, as it is made through a separate gate (U3:B).

Bay controller transmission A bay controller which held its transmitting line high would just never send a message. If it was high impedance (or open circuit), then the pull-up resistor (R24) on the bay linker would hold the line high. In the case where a bay controller fails and holds its transmitting line low with low output impedance (i.e. makes a continual transmission), the bay linker will 'lock out' the bay controller. It does this with a circuit which allows bay controller transmission only when the line is low *and* has not been held low for more than 190 ms, using an identical circuit (R26, C12, U6:B) used for the reset detection discussed in section A.3.4.

A.3.6 Power supply

The bay linker receives its power through the connection to the bay controller from the power supply at each bay. The bay controller was designed to provide this directly in its PCB tracks—a chip failure on the bay controller will not affect power supply to the bay linker unless it causes the power supply for all the electronics at the bay to fail. The operating current of the bay linker at each of the three supply voltages is given in table A.1.

Supply voltage	Operating current/mA
+5 V (passive)	21
+5 V (active)	96
+12 V	21
−12 V	13

Table A.1 The operating current of a bay linker. The 'active' measurement is for one channel active, which is the only normal situation.

A.3.7 Production testing

Following PCB manufacture and component placement (both external to the University), The following tests and measurements were made on each bay linker before installation on the telescope.

- A pass/fail measurement of the detected signal at each photodiode detector, from a standard light source and fibre. The scatter in detector performance was found to be about 10%, probably due to manufacturing tolerances in the housing construction: all passed.
- A measurement of the time, τ_R, from the onset of a reset signal in the outwards communications path to the initiation of the BC reset signal. All were in the range 180 ms$\leq \tau_R \leq$205 ms.
- A measurement of the time, τ_L, from the onset of a simulated failure in BC (where the transmit line was held low) to the 'locking out' of the BC from further transmission. All were in the range 180 ms$\leq \tau_L \leq$210 ms.
- A check that the high and low reference thresholds for signal detection in each direction were correct, at 200 mV and 105 mV respectively (all were satisfactory).
- A measurement of the values of R7 and R17 required to transmit into a standard fibre and detector and receive 650 mV. Resistors with 1% tolerance in the range $47\Omega \leq \mathrm{R17}, \mathrm{R17} \leq 82\Omega$ were used—a few transmitters would have been best matched with resistors less than 47Ω, but the operating current would then have been too high. The actual resistors inserted into each linker are shown in table A.2.
- A communications test, to send actual messages to and from a bay controller and to reset the BC through the entire communications system (all passed).

A.4 Optic fibre

The optic fibre in use in the system is duplex plastic multimode fibre, by Hewlett Packard (part number HFBR–RUD500). The diameter of the core and cladding of each strand is 1.00 mm; the diameter including the polyethylene jacket is 2.2 mm. The two strands are joined by thin polyethylene web. Eighty-eight 18.1 m lengths[4] of fibre have been installed in the high galvanised steel ducting along the two arms of the telescope.

[4]This is 0.3 m longer than the inter-bay distance, allowing for movement or repolishing of the fibres without placing stress on the connectors.

linker	R7 (Ω)	R17 (Ω)	linker	R7 (Ω)	R17 (Ω)	linker	R7 (Ω)	R17 (Ω)
A	56	-	38	51	47	74	62	68
B	75	-	39	68	82	75	68	56
C	75	-	40	51	62	76	56	62
D	51	-	41	47*	62	77	51	56
5	62	68	42	56	56	78	47	47*
6	51	68	43	75	62	79	62	56
7	68	62	44	62	68	80	68	56
8	62	56	45	68	68	81	62	51
9	75	62	46	62	47*	82	62	51
10	56	56	47	68	62	83	62	62
11	47*	68	48	51	56	84	56	47*
12	56	62	49	62	51	85	68	56
13	51	62	50	56	56	86	56	68
14	47*	56	51	62	56	87	62	62
15	51	56	52	62	56	88	56	62
16	47*	75	53	56	68	89	56	47
17	47	68	54	51	62	90	56	62
18	56	68	55	75	75	91	56	56
19	51	62	56	68	75	92	68	51
20	56	62	57	47	62	93	75	75
21	51	56	58	68	68	94	68	51
22	51	68	59	68	56	95	56	68
23	62	68	60	56	56	96	62	51
24	56	68	61	68	68	97	62	68
25	68	62	62	56	75	98	56	75
26	56	68	63	51	68	99	51	62
27	56	75	64	62	51	100	56	68
28	62	75	65	68	75	101	56	62
29	51	62	66	68	68	102	56	62
30	75	68	67	51	47*	103	56	62
31	68	62	68	75	62	104	51	56
32	68	68	69	62	62	105	62	75
33	56	56	70	62	56	106	68	68
34	51	62	71	75	51	107	47	68
35	51	62	72	68	75	108	47*	51
36	51	62	73	68	47	109	56	47
37	56	62						

Table A.2 Values of the transmitter driving resistors, R7 and R17, used in the bay linkers (numbered) and the local oscillator hut linkers (A–D). The resistor values have been chosen to provide an approximately similar light output from all the linkers. In some cases, a very low resistor value would have been required, resulting in an excessive transmitter operating current. In these cases (marked with an asterisk) a resistor of value 47Ω was used; these linkers should be used as spares until more experience with the system operating with low transmitted light levels is available.

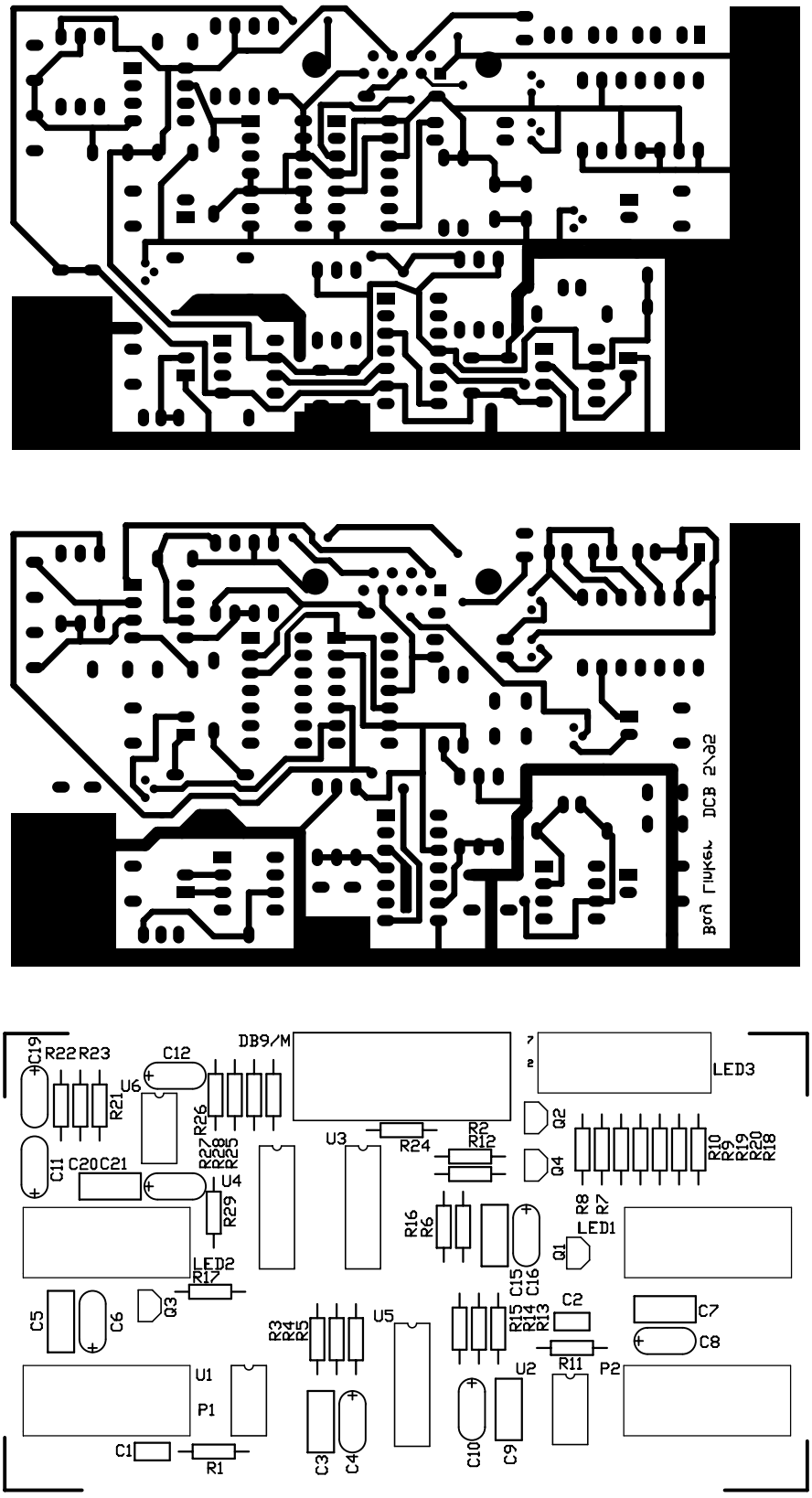

Figure A.2 Printed circuit board layout of the bay linkers (true size). From top to bottom: top layer, bottom layer, component overlay.

A.4.1 Operating conditions

At the operating wavelength of 660 nm, the fibre has attenuation $\alpha = 0.22 + 0.0067(T - 25°\mathrm{C})$ dB m^{-1}. This attenuation is sufficiently low to allow easy inter-bay communication; however, glass fibre would be required over longer distances. This fact led to the choice of an RS422 link for the control room–local oscillator hut link, which is 80 m in length.

Although the fibre is specified to be handled at temperatures up to 70°C, experience during installation has shown that it becomes very soft above about 25°C: opening of the ducting at higher temperatures is undesirable because of the risk of catching and damaging the fibre on the sharp edges of the ducting. The minimum long-term bend radius of 35 mm was a key factor in the decision to locate the bay linkers in the ducting also, thus eliminating the need for rigid low bend radius conduit to take the optic fibre to the instrument boxes.

A.4.2 Polishing

Much experimentation led to adoption of the following procedure for polishing the fibres:

- cut the fibre to length with standard pliers and allow it to relax for 24 hours;
- re-cut the ends at right angles with a sharp, cold blade (such as a scalpel);
- cool (and regularly re-cool) the four fibre ends in iced water;
- place the ends in the specially constructed jig (thus keeping the ends perpendicular to the polishing surface);
- polish in the presence of water with clean 600 grade and then 1200 grade emery paper, taking care not to push so hard as to compress the sheath (which would allow the then overpolished core to relax back into the sheath);
- finish with wet 3 μm lapping film;
- protect the ends from dust until installation.

A.5 The control room/local oscillator hut link

The purpose of the control room/local oscillator hut link is to provide communication between the master controller, situated in the the control room, and the first of the optic fibre 'linkers' situated in the local oscillator hut, some 80 m away. It was initially thought that this link would be made in optic fibre, but several stages would have been required in order to use repeaters (i.e. the linkers) identical to those at each bay. Supplying power to the linkers would have been difficult. Furthermore, such power supplies would have compromised the link's immunity to lightning, thus removing one of the key advantages of optic fibre.

An RS422 interface was chosen for the link. This interface uses balanced signalling (requiring two wires in each circuit) and has greater noise and crosstalk

immunity. The standard RS232 interface (Couch 1990, p708) is not recommended for distances above 16 m. Only the two forward, two return and earth wires were required, as the master and bay controllers implement all signalling protocols in software. A low loss grounded double twisted pair cable with a weatherproof sheath was placed in an existing elevated ducting for the link. In keeping with the usual practice, negative logic (i.e. with a '1' represented by low voltage) is used for all electric protocols (ie RS232, RS422, TTL). This link is terminated by the control room and local oscillator hut interfaces mentioned below. In addition to the installed interfaces, a complete spare of each was also made.

A.5.1 The control room interface

The control room interface has two main functions. Firstly, it translates from the RS232 protocol used to communicate with the master controller to the RS422 protocol used for the link across to the local oscillator hut using a MAX232/DS8921 pair (U3,U6). Secondly, it provides the observer with the hardware reset to all the bay controllers—thus bypassing all computer systems. The reset pulse takes the form of a 250 ms '1', implemented using a monostable multivibrator 74HC221 (U4:A). The interface has its own purpose-built power supply which operates directly from the 240 V mains and has appropriate circuitry to protect the electronics from power supply irregularities. The control room interface is physically located in a rack in the control room. At the front panel several LEDs (LED2–LED5) allow the observer to monitor activity in the communications system. The complete circuit diagram is shown in figure A.4. A photograph of the panel containing the control room interface is given in figure A.7.

A.5.2 The local oscillator hut interface

The local oscillator hut interface translates from the RS422 protocol into TTL (DS8921: U6) for connection with the east and west local oscillator hut linkers with which it is co-located in a rack in the local oscillator hut. It too has its own power supply and activity monitoring LEDs. The circuit diagram for the interface is given in figure A.5. The local oscillator hut linkers are modified bay linkers. They do not require the circuitry to detect the reset pulse, and they need only one transmitter and receiver each. They are built on the same printed circuit board as the bay linkers, with a subset of the components in a bay linker, according to the circuit diagram shown in figure A.6. A photograph of the panel containing the local oscillator hut interface and the local oscillator hut linkers is given in figure A.8.

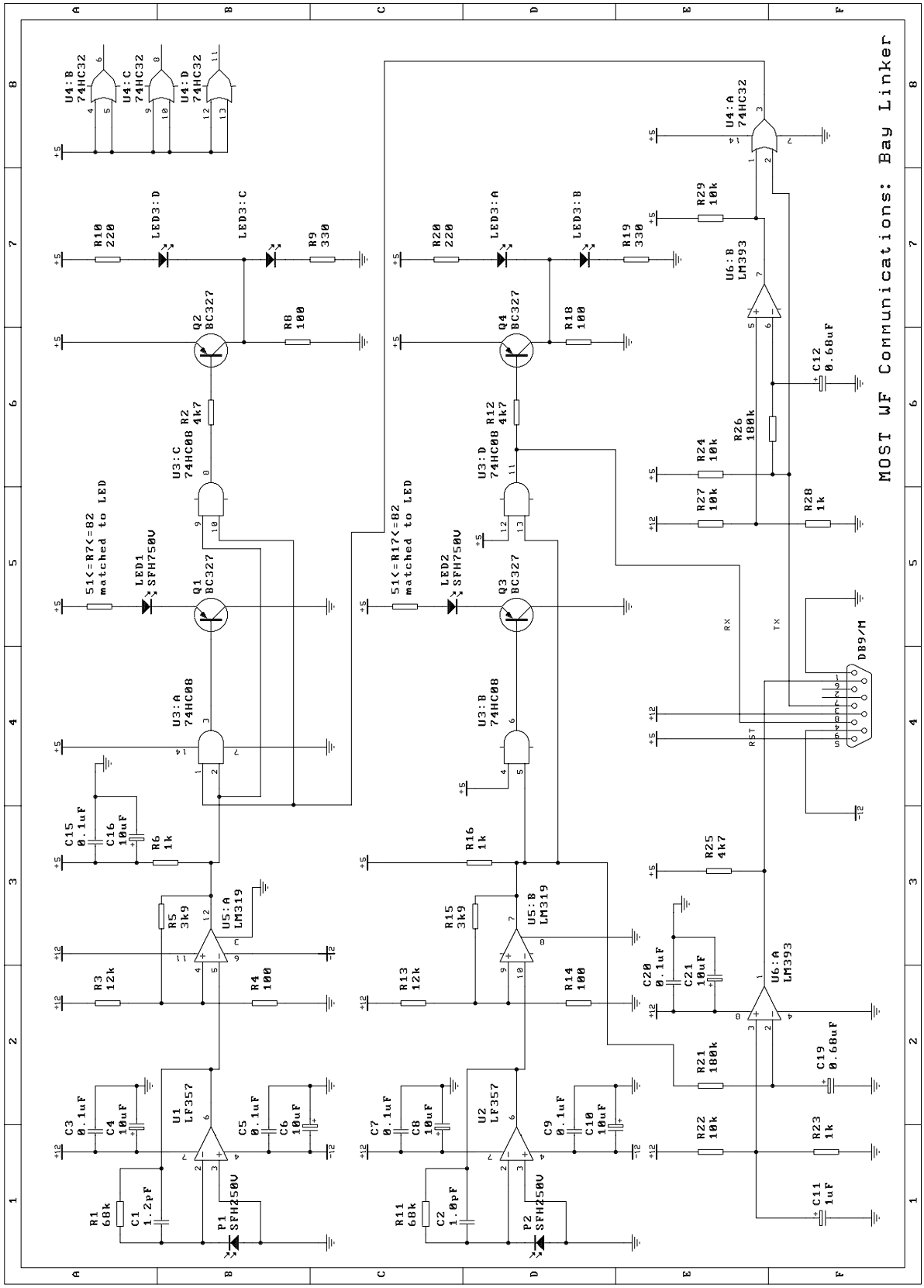

Figure A.3 Circuit diagram for each bay linker. Eighty-eight of these form the optic fibre daisy chain and provide the communications connection to each bay controller.

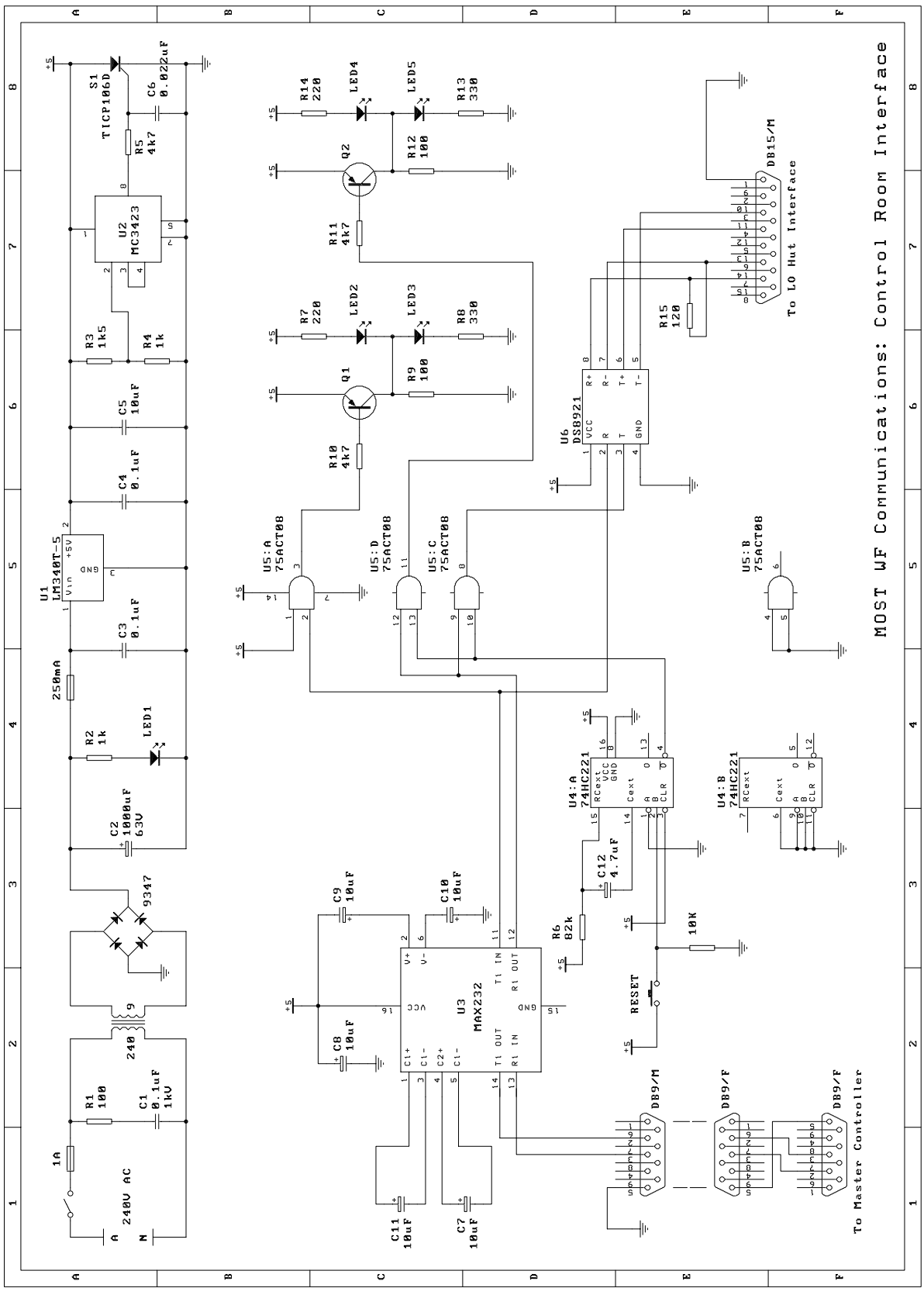

Figure A.4 Circuit diagram for the control room interface. This interfaces the RS232 connection to the master controller with the RS422 connection to the local oscillator hut interface. It also provides activity monitoring LEDs and a hardware reset facility for the bay controllers.

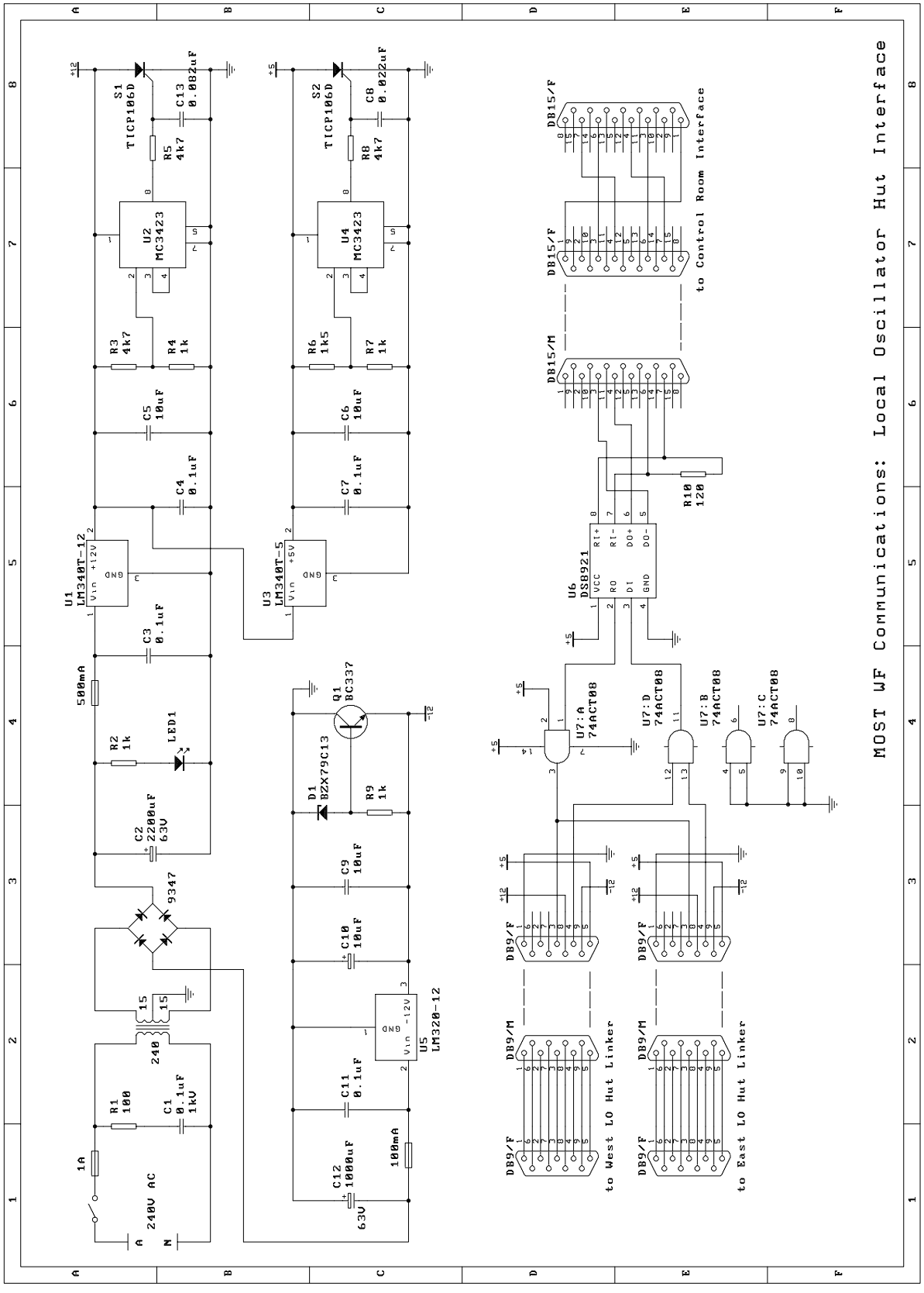

Figure A.5 Circuit diagram for the local oscillator hut interface. This terminates the RS422 link from the control room and connects to the LO hut linkers. It also supplies power to the LO hut linkers. Included in the figure are wiring diagrams for the cables to the LO hut linkers and the control room interface.

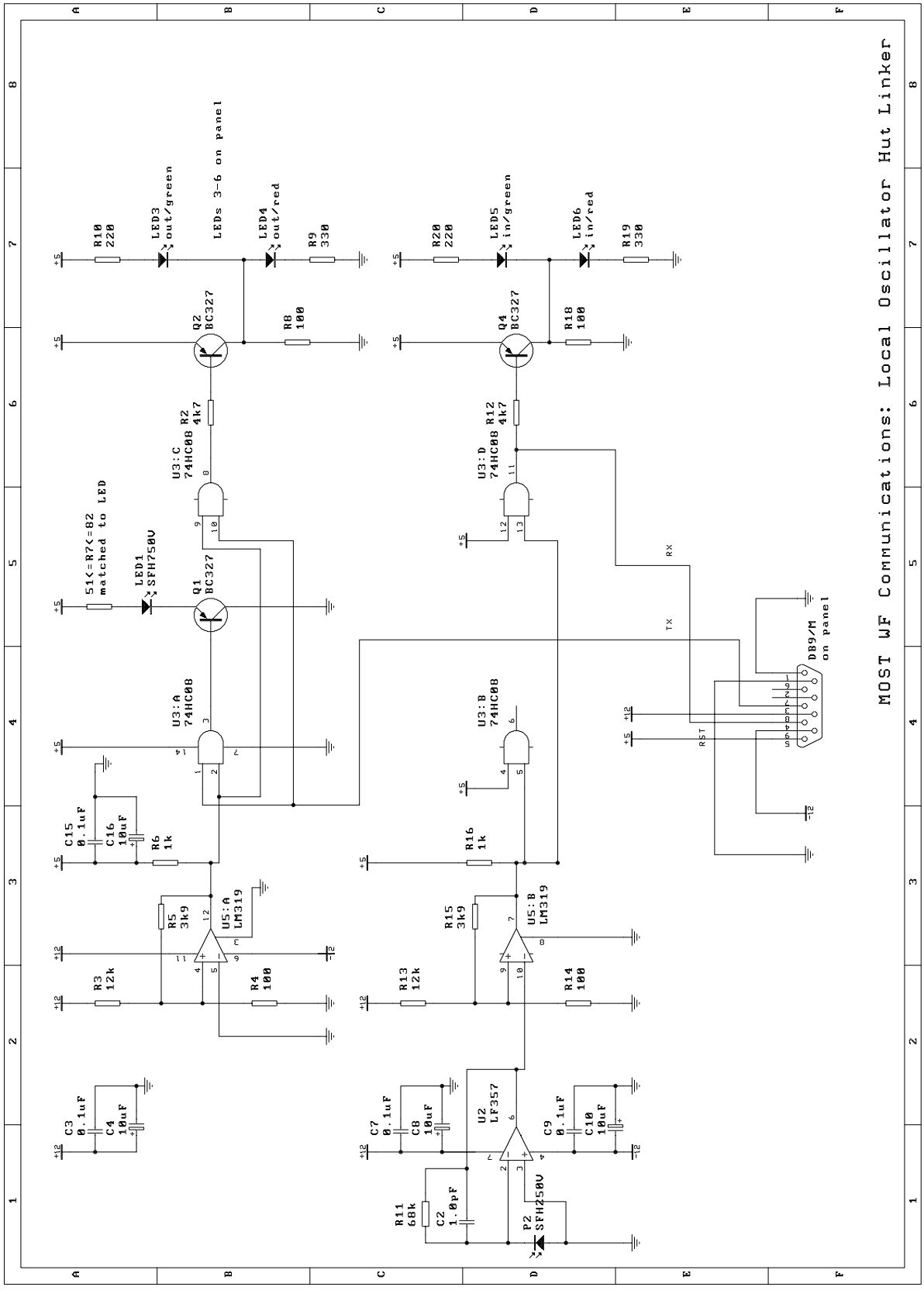

Figure A.6 Circuit diagram for the two linkers in the local oscillator hut. These terminate the optic fibre daisy chains for each arm of the telescope and connect them to the local oscillator hut interface—they are situated in the same panel. The PCB used is as for the bay linkers but a subset of the BL components, as specified here, is used.

A.6 System testing

A.6.1 Soak tests

Soak tests were used for initial diagnoses of the problems with the software protocol used for master controller/bay controller communication (including the famous '9th bit' problem mentioned in section 2.5.1). As part of these tests, many millions of messages were exchanged between bay controllers and the master controller.

A.6.2 Cumulative pulse shape testing

The final design had aimed to keep the rise and fall delays in each bay linker nearly the same to prevent significant pulse shape changes over many links. A bench measurement was made of the actual system delays using the control room and local oscillator hut interfaces and 8 linkers. By using the return path of each linker it was possible to simulate the effect of 16 bay linkers in series. The measured differential delay was $1.35\,\mu$s, implying a differential delay along the entire arm of around $3\,\mu$s. The maximum tolerable differential delay is set by the sampling window of the 80C552 on the bay controller—a delay of less than $46\,\mu$s would be within specification, indicating that the communications system may be able to run at several times its existing speed, and that it is reliable at the present operating rate of $9600\,\mathrm{bit\,s^{-1}}$.

A.6.3 Environmental testing

After some environmental testing of two bay controller/bay linker pairs in place at Molonglo, a clue to the occasional intermittent failures mentioned above was found: they generally occured on hot days. The chief reason was suspected to be the temperature coefficient of the LED transmitters. Controlled temperature tests of four transmitter/fibre/receiver sets in series were carried out with the following results:

- the optic fibre temperature coefficient was found not to be significant;
- the major portion of the temperature coefficient was confirmed to be due to the transmitters;
- the temperature coefficient of the detected power after the transmitter/fibre/receiver set was measured at $-5.2 \pm 0.4\,\mathrm{mV/^{\circ}C}$.

This implies that in hot weather, marginal output voltages from the comparators measuring the photodiodes might intermittently drop below the detection threshhold.

A.7 System maintenance

As discussed in section A.3.1, a potential problem in the system is the connection made between the optic fibre and the receivers/transmitters. These are particularly vulnerable to movement of the fibre during temperature cycling. A slight withdrawal of the fibre from a receiver or transmitter may bring it to the marginal level of failing at high temperature (as a consequence of the large temperature coefficient of the transmitter). The measured temperature coefficient of a transmitter/fibre/receiver combination (above) implies that the absolute minimum detected signal at the bay linker comparators ought to be above 300 mV at 25°C to ensure proper operation at 45°C, the highest temperature expected in the ducting (D. Campbell-Wilson, personal communication, 1997).[5] To ensure reliable performance, the detected signal levels at the bay linkers should be measured at least annually. The best time would be at the end of winter, since failures are more likely to occur in the hot weather of summer.

The easiest way of monitoring the state of the connection is to measure the detected signal level on a bay linker, typically at the right-hand ends of R1 (inwards path) or R11 (outwards path). For the purpose of these measurements a special master controller command has been implemented: `send bay linker test signal`, which sends a continuous stream of regular data to enable convenient pulse height measurement. When making the measurements, the signal should be a regular square wave with amplitude in the range 550–700 mV. If the signal has amplitude below this range, fibre connections should be investigated with a view to achieving the specified level. This allows for some future reduction in the level due to temperature cycling. The measurements made should be noted so that experience with long-term temperature effects on the system may be gained.

A.8 Further work

At the time of writing (June 1997), the communications system has been in place for one and a half years. Following initial commissioning, it has been in daily use for observations for the last year. Only one observation has failed as a direct result of the communications system, when the power supply of the control room interface latched in an unknown state. No actual component failures were detected. Provided the maintenance specified above is undertaken, it is expected that the system will remain reliable for many years.

If desired, it should be possible to upgrade the system by at least a factor of two in speed (see the previous section). Two factors would require particular attention:

- the light should not be 'on' for more than 50% of the time in the outwards path, to avoid the signal appearing as a reset request to the bay linkers. At the existing communications speed (9600 bit s^{-1}) a byte takes about 1 ms, while bytes are sent from the master controller only once every 3 ms;

[5] The instantaneous minimum level for detection is 200 mV.

- The RS232 link between the master controller and the control room interface may need to be replaced with a faster protocol.

Figure A.7 (following page, top) A photograph of the panel containing the control room interface

Figure A.8 (following page, bottom) A photograph of the panel containing the local oscillator hut interface. Only one of the two linkers was installed when this photograph was taken.

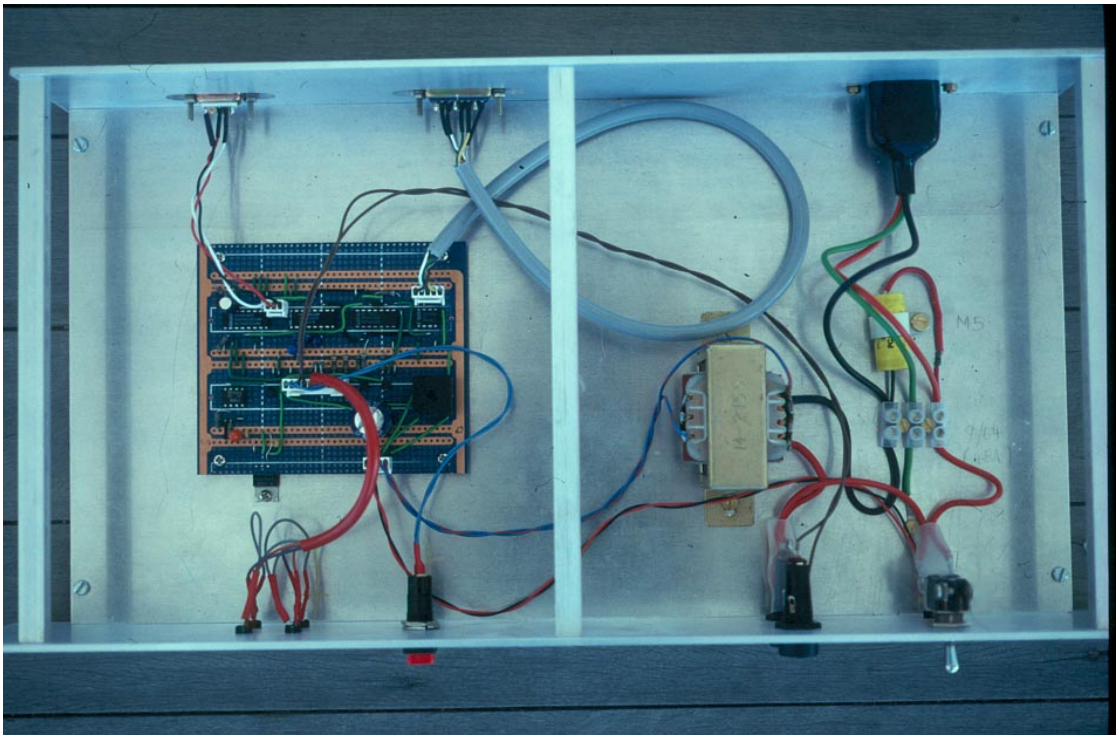

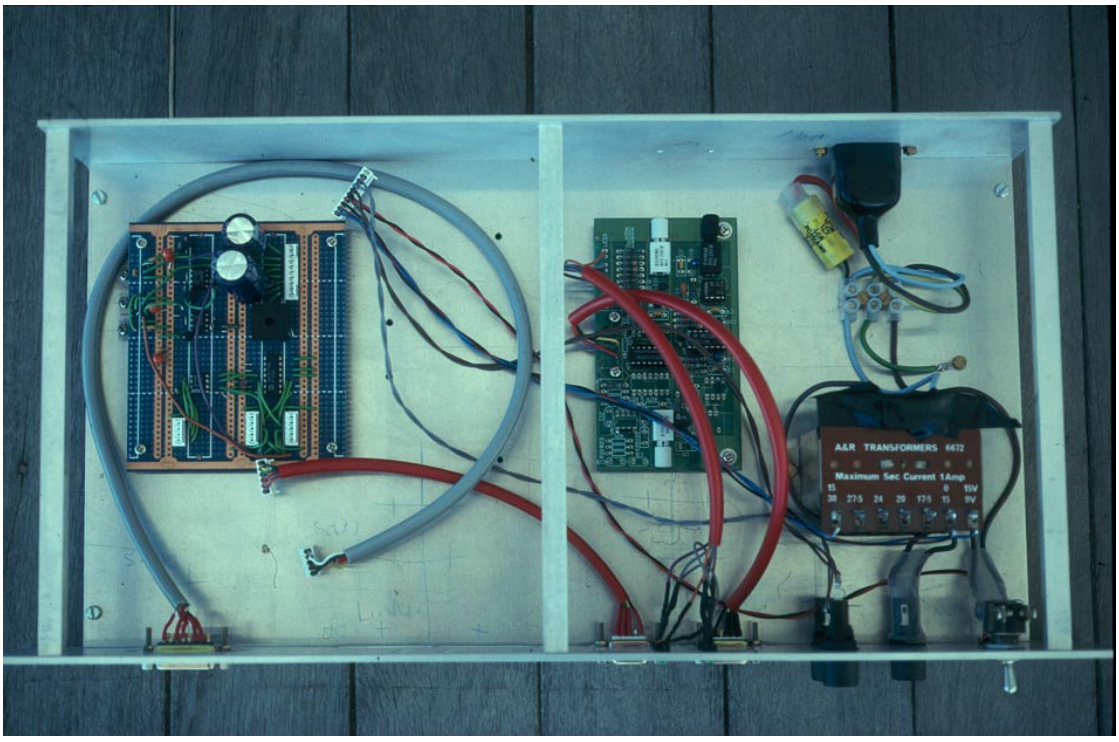
A&R TRANSFORMERS 6672
Maximum Sec Current 1Amp

Appendix B

Summary of Wide Field Test Observations

This appendix consists of a summary of the test observations made as part of the commissioning of the MOST in Wide Field observing mode. Analysis of the observations was presented in chapters 3 and 6. Not all the observations listed here have been analysed in this thesis. However, they may be useful for future tests of the Wide Field system. Excluded are observations which failed or which were made as part of the process of debugging the system.

observation	field centre (B1950)		field	MOST	SCAN calibration				
date	RA (h m s)	dec(° ′ ″)	size	archive name	gain	offset	phase	test purpose	notes
96/08/25	20 49 06.9	−36 51 49	3	D20493616	9.8	−4.9	12.8	test phase shifters	SYN, old phase shifters, cal. centred
96/08/26	20 49 06.9	−36 01 49	3	D20493619	9.7	−3.9	6.5	and software	SYN, old phase shifters, cal. offset S
96/08/27	20 49 06.9	−36 01 49	3	D20493617	10.3	−3.4	2.5		WFSYN, no phase shifters, cal. offset S
96/08/29	20 49 06.9	−36 01 49	3	D20493618	11.0	2.0	−4.7		WFSYN, new phase shifters simulating old system, cal. offset S
96/08/30	20 49 06.9	−36 01 49	3	D20493620	10.1	0.0	−2.5		WFSYN, new phase shifters in normal operation, cal. offset S
96/10/04	03 36 35.9	−35 37 00	7	I0336354	10.4	3.3	−1.9	preliminary	Fornax
96/10/07	04 29 32.8	−75 15 06	7	I0429751	9.2	2.4	7.3	WF test	cal. offset W[a]
96/10/09	04 09 58.4	−74 07 49	7	I0409741	10.2	2.0	4.2		cal. offset S
96/10/10	03 50 24.0	−76 22 23	7	I0350761	9.7	2.5	10.7		cal. offset NE (outside field)
96/10/15	03 56 07.7	−76 10 52	7	I0356761	10.5	0.7	5.9		cal. offset NE
96/10/18	04 09 58.4	−75 42 15	3	D04097550	10.3	1.7	−6.6		cal. offset N
96/10/21	04 09 58.4	−76 36 06	7	I0409761	10.4	−0.1	0.3		cal. offset N
96/01/30	04 09 58.3	−75 15 05	7	I04097557	9.7	2.3	−15.8		cal. centred
97/03/13	12 15 27.3	−45 43 49	7	I12154548	10.0	−2.2	9.6		cal. centred
97/03/14	12 15 27.3	−45 43 49	7	I12154549	8.9	−2.1	−3.7		cal. centred
97/03/15	12 15 27.3	−45 43 49	7	I12154550	8.8	−2.0	−2.3		cal. centred
97/05/10	19 34 55.0	−62 19 28	7	I1934622	10.4	1.2	10.8		cal. offset S
97/05/31	19 34 39.4	−65 18 38	7	I1934651	10.5	1.8	−5.4		cal. offset N
97/01/31	08 35 13.9	−47 57 59	7	I0835471	10.6	0.3	−2.5	Vela SNR re-survey	point sources
97/02/12	08 33 39.2	−45 00 10	7	I08334515	9.5	−0.8	4.4		extended structure in Vela X, pulsar gating
97/02/04	08 24 05.0	−47 53 38	7	I0824472				Vela SNR survey	6 overlapping fields
97/02/05	08 29 49.1	−50 06 09	7	I0829502				extension fields	
97/02/06	08 18 30.5	−50 06 49	7	I0818502					
97/02/07	08 12 46.1	−47 54 19	7	I0812472					
97/02/08	08 40 57.7	−50 05 31	7	I0840501					
97/02/09	08 46 32.4	−47 52 21	7	I0846471					
97/06/06	20 27 52.9	−32 10 00	7	I2027321	10.8	−0.1	4.6	noise analysis	quiet field
97/03/17	12 01 00.0	−48 00 00	7	I1200481	9.1	−0.5	0.6		quiet field
97/03/05	09 37 00.0	−66 00 00	7	I0936661	11.7	−4.1	2.9		quiet field
97/03/10	10 15 00.0	−71 46 12	7	I1014711	9.4	1.3	−6.8		quiet field
97/03/06	10 00 00.0	−73 37 48	7	I0959731					
97/03/11	10 30 00.0	−73 37 48	7	I1029731					these three overlap I1014711
97/03/18	10 45 00.0	−71 46 12	7	I1044711					

[a]i.e. the calibrator is offset to the west with respect to the field centre

Table B.1 Summary of observations for commissioning the MOST Wide Field system

Appendix C

Pulsar Gating with the MOST

The Vela pulsar (PSR B0833-45) is the strongest unresolved source in the Vela SNR survey. Its time variability made initial imaging especially difficult. To minimise the artefacts produced by this variability in the final images, data for fields near the pulsar were collected during the pulsar's 'off' time, when pulsed radio emission was not present. This appendix describes the method used to control data collection. It was employed for the observations in the MOST Vela SNR survey (chapter 5), of the region immediately surrounding the pulsar (chapter 8) and of extended structure for testing the Wide Field system (chapter 6).

C.1 The ADC hold system

The final analogue-to-digital conversion (ADC) stage of data acquisition for each interferometer beam of the MOST is preceded by an integrating low pass filter, which reduces noise fluctuations to below saturation level. The integrator has a time constant of about 3 ms. In normal observing mode, data acquisition is suppressed for the first 60 ms of each solar second. This prevents integrator 'carry over' from one second to the next, which would cause the data taken each second to be contaminated by that taken in the previous second, when the beams are pointing elsewhere. It also allows time for the beams to stabilise in their new positions.

The 60 ms holding time (the 'ADC hold') is controlled by a 60 ms pulse from the station clock which drives the digital logic controlling the ADCs. In order also to suppress data acquisition during the 'on' time of the pulsar, a gating signal, synchronised with the pulsar, was added to the 60 ms pulse train in digital logic.

C.2 Instrumental setup

An HP3325A signal generator provided the initial gating pulse. Its operating frequency was set by a pulsar ephemeris program on the HP-A700 observing computer, which calculated the apparent pulse frequency and updated the signal generator each minute. The barycentric ephemeris of the pulsar for each observing session

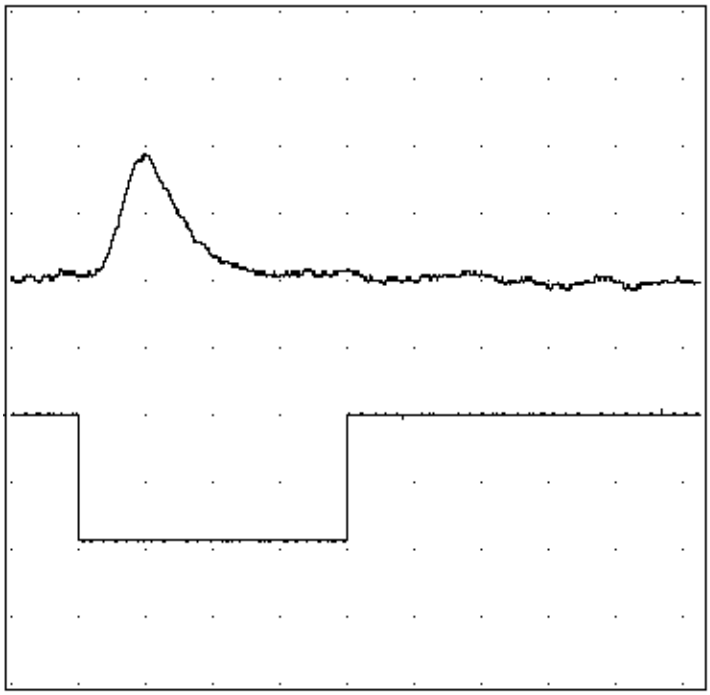

Figure C.1 A sample pulse profile with the gating signal as observed on the cathode ray oscilloscope. Data acquisition is suppressed while the gating signal is low. The horizontal scale is 5 ms/division. The vertical scale is arbitrary.

was derived from observations with the ATNF radiotelescope at Parkes (by Dick Manchester and Matthew Bailes) or from observations at the University of Tasmania's Mount Pleasant Observatory (by Peter McCulloch). For phase stability the signal generator was locked to the station clock. The instrumental setup is shown in figure C.2.

It is possible to access the synchronous demodulation units for each beam of the telescope individually, and display the signal on an oscilloscope. The pulsar is sufficiently strong that it can easily be seen. A device known as the 'Pulsar Zapper' was built by Warren Nicholas of the Astrophysics Department in 1986 for John Reynolds' original experiment. This was used to adjust the phase and width of the gating pulse to be aligned with the pulsar when displayed on the oscilloscope (figure C.1).

For the observations comprising the MOST Vela SNR survey, this signal was added in logic to the ADC hold signal to suppress data acquisition when either was active. However, two problems with this initial method became apparent. First, the width of the gate (set at 20 ms) was such as to suppress the majority of the pulsed emission, but not all. It was realised that the 3 ms time constant of the integrating circuit before the ADC was enough to ensure that a small residual of the pulsar (of order 2%) remained. Secondly, because the MOST records the intensity in each beam averaged over one second of time, and the actual number of pulsar periods

per second slowly changes, the effective data acquisition time was different for each second. This manifested itself as a periodic variation in intensity in the image. The effect was particularly apparent in the outer blocks of Wide Field observations, where an increased noise level resulted.

C.3 Improving the setup

Two improvements were made to the observing technique for observations subsequent to the initial Vela SNR survey.

1. To address the integrator carry over, the pulse suppression time was increased to 40 ms (from 9 ms before the peak of the emission) for a single $23'$ field observation. This allowed a detailed examination of the emission immediately surrounding the pulsar (presented in section 8.1.1).
2. The variation in data acquisition time was addressed using further logic circuits. The circuits provide a new ADC hold input signal which suppresses data not only for the initial 60 ms of each second, but also until the beginning of the first full pulsar 'off' time. Data acquisition is then allowed for nine full pulsar 'off' times before being suppressed until the next second. This is the minimum number of contiguous complete pulsar cycles (starting at the beginning of the pulsar 'off' time) that will fall within the available observing time. The implementation of this scheme is shown in figure C.2. The new hardware was used for the $23'$ field observation of the region around the Vela pulsar and for the wide field test observation described in chapter 6.

C.4 Variation of beam position of a source with hour angle

So that the pulsar could be continuously monitored on the cathode ray oscilloscope, it was necessary to determine in advance the location of the pulsar in the beamset during the observation. Let the field centre (of date) be at RA= α_0 and Dec= δ_0 (both in radians), and a source have position RA= $\alpha_0 + \Delta\alpha$ and Dec= $\delta_0 + \Delta\delta$. Assuming the telescope orientation to be east-west and horizontal, and with $\sin(d) \approx d$, where d is the angular displacement of the source from the field centre (assumed small), we can determine which beam, b, contains the source (in this case the pulsar):

$$b = b_0 + \frac{[(\Delta\alpha \cos\delta_0)^2 + (\Delta\delta \sin\delta_0)^2]^{1/2}}{5.333 \times 10^{-5}} \cos(H_0 - \psi)$$

where

$$\tan\psi = \frac{\Delta\delta \sin\delta_0}{\Delta\alpha \cos\delta_0}$$

with $b_0 = 192.5$ (for 384 beam observations) and H_0 the instantaneous hour angle in radians of the field centre (A. J. Turtle, personal communication, 1995). The

actual deviation of the MOST from a true horizontal, east-west position makes this calculation accurate to about one beam, sufficient for this purpose.

C.5 Observing procedure

Standard observations were made as normal, with the circuitry described above added into the system. However, the 24 second calibration observations (the SCANs) were not gated for the survey observations, as data affected by the gain modulation described in section C.2 would not have become sufficiently time-averaged to allow calibration. Once the improvements of section C.3 were implemented, observations of the calibration sources were also made using the gating system.

The wide (2.2°) tilt primary beam[1] of the MOST meant that the pulsar could be detected for several minutes before it reached the normal starting hour angle of -6^{h}, allowing adjustment of the 'Pulsar Zapper' to provide a gating pulse of the correct phase. Observations using a 20 ms gate (survey and Wide Field test observations) were made with the peak of the pulsar's emission occurring 5 ms after the beginning of the gating pulse. The special $23'$ field observation of the surrounds of the pulsar using a 40 ms gating pulse was made with the peak of the pulsar's emission arriving 9 ms after the beginning of the gating pulse. The pulsar signal was integrated for several seconds on the CRO to assist with this procedure. A sample pulse profile for the 20 ms gating pulse case is given in figure C.1.

The method was successful in removing the pulsed emission to below the confusion level in the final $23'$ image. The procedure is useful where pulsars are sufficiently strong that each pulse may be detected individually and where they have periods much longer than the 3 ms integration time mentioned in section C.1

[1]This value is for $\delta = -45°$ at transit $HA = 0^{\mathrm{h}}$, using the tilt primary beam formula of Reynolds (1986, p20) and the meridian distance gain curve of Burgess (1989)

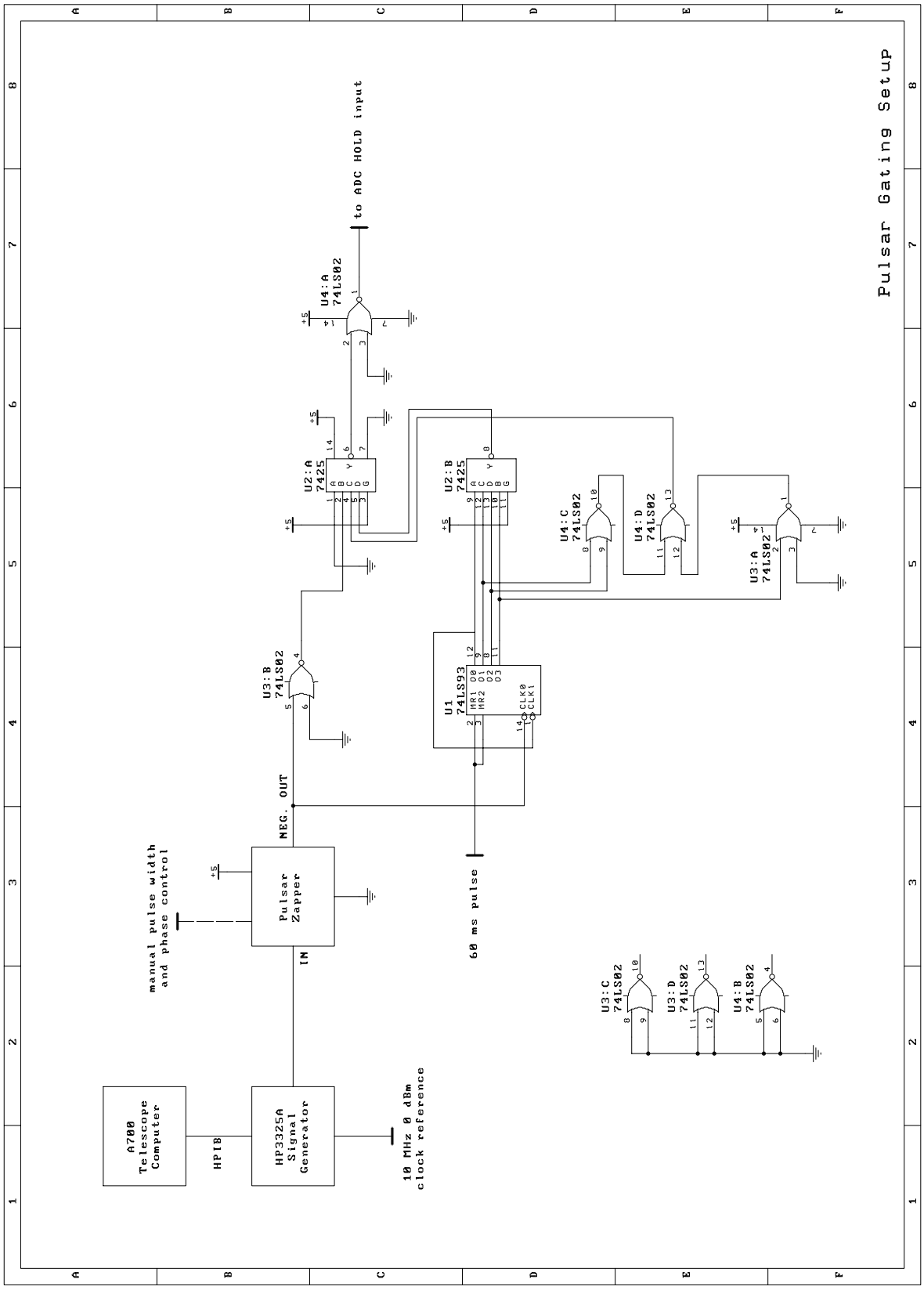

Figure C.2 The instrumental setup for the pulsar gating observations. Note that this diagram includes the improvements to the procedure described in section C.3

Appendix D

Reduction of the MOST Vela SNR Survey

In chapter 5 the MOST survey of the Vela supernova remnant was presented. This appendix contains further details on the reduction of the survey.

D.1 Data reduction and mosaicing

The reduction and mosaicing of MOST survey data is a process which has been largely developed for the MOST Small Magellanic Cloud (SMC) survey (Taisheng Ye and A. J. Turtle). The process was adapted for the Vela survey to include software unavailable at the time of the SMC survey reduction. The data reduction process used is summarised in figure D.1. A comprehensive overview of issues relating to MOST data reduction is given by Gray (1994).

D.2 Summary of observations

A Summary of MOST observations for the Vela supernova remnant survey is given in table D.1. The columns contain the following information:

Observation date Although the date does not always uniquely identify an observation in the MOST archive, each of the observations in the table is the only one near RA $= 8^{\mathrm{h}}$ on that date. The archive names and field centres have been omitted for the sake of brevity.

SCAN calibration Calibration parameters derived from SCAN observations before and after each observation: the overall *gain* (nominal value 10), the pointing *offset* error (in seconds of arc) due to an error in phase gradient along each arm of the telescope, and the *phase* discontinuity (in degrees) between the east and west arms of the telescope. For further details, see section 2.2.1.

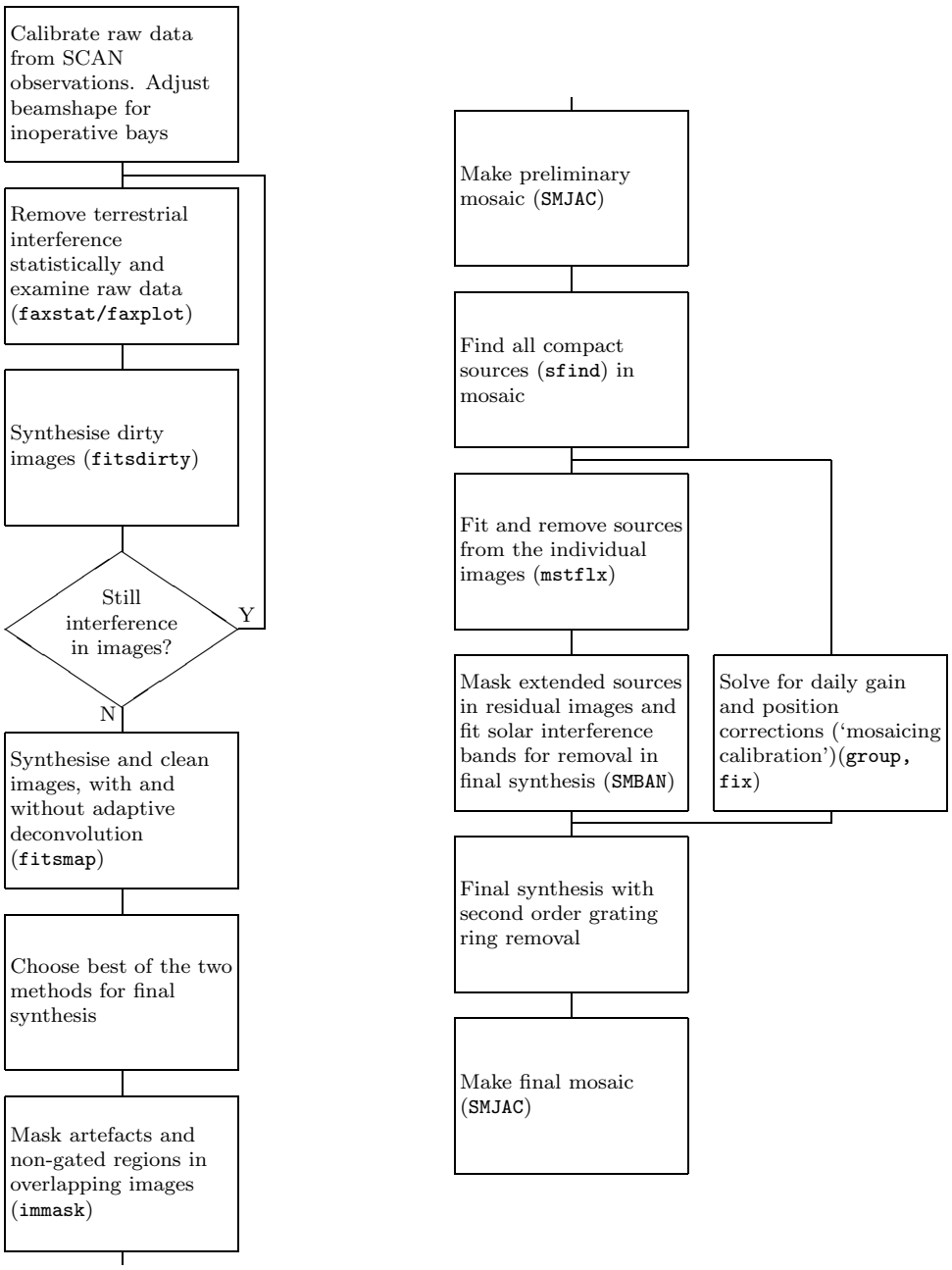

Figure D.1 The data reduction process for the MOST Vela supernova remnant survey. Names of the key reduction programs are shown. With the exception of `sfind` and `immask` (`MIRIAD`) all the software is Astrophysics Department in-house software.

Mosaicing calibration Position and flux density calibration parameters are derived for each observation from multiple observations of sources in regions of overlap. The right ascension and declination errors are measured in seconds of time and arcseconds respectively. It was not possible to calibrate all the fields in this way. Fields with insufficient sources in common with nearby fields were either not calibrated, or, in the case of some Galactic Plane survey fields, calibrated using the Galactic Plane survey calibration parameters corrected for a small systematic difference between the surveys. Galactic Plane survey flux densities were scaled up by 2.0% and positions were adjusted by the addition of -0.013^{s} of right ascension and $0.44''$ of declination. This procedure ensures that the Vela SNR survey achieves the best possible internal self-consistency.

Number of sources This gives the number of sources observed in common with other observations. Small numbers indicate that the mosaicing calibration may be less reliable.

Self calibration Indicates whether or not the imaging used the process of adaptive deconvolution (self-calibration with a reduced number of parameters) as described by Cram & Ye (1995). Whether or not the previously reduced Galactic Plane survey images were self-calibrated is not recorded. However, they were inspected to achieve the best result.

Table D.1 Summary, including calibration and reduction parameters, of the observations comprising the MOST Vela supernova remnant survey

	SCAN calibration			Mosaicing calibration					
Date	Gain	Offset	Phase	Gain	ΔRA	$\Delta\delta$	Sources	Self-cal.	Notes
84/02/03	10.3	3.3	−0.6	1.059	−0.21	0.93	12		1 2
86/02/13	10.2	−0.2	0.3	0.886	0.09	4.77	16		1 2 5
86/02/18	10.6	−0.3	0.4	0.884	0.03	2.77	32		1 2
86/02/20	11.1	0.2	−0.6	0.964	0.06	4.04	25		1 2
86/02/26	10.1	−1.4	8.0	0.949	0.05	1.67	9		1
88/02/16	8.5	2.0	−0.2	1.062	0.13	−1.48	16		1 2
88/02/19	12.4	1.7	−14.2	1.055	0.17	−0.11	11		1 5
88/02/20	12.3	2.8	−16.2	0.957	0.04	−1.76	7		1
88/02/21	11.8	2.2	−13.0	0.964	−0.03	0.37	18		1 5
88/02/22	12.5	1.6	−0.6	0.960	0.03	2.21	10		1 5
89/01/18	10.9	0.4	3.9	0.887	0.01	−2.31	23		1 2 5
89/01/19	10.8	0.6	7.5	1.025	−0.09	−0.85	16		1 2 5
89/01/27	11.3	1.3	−1.1	0.863	0.20	2.33	13		1
89/01/28	11.2	0.8	−1.4	0.927	−0.21	−1.33	8		1
89/01/29	11.9	0.9	0.4	1.014	0.18	0.87	7		1
90/01/19	10.2	0.3	−0.1	0.992	−0.03	−0.18	15		1 2
90/02/09	11.0	1.4	−2.0	1.009	−0.02	0.63	13		1
91/01/03	9.1	−0.4	10.6					N	3
91/02/01	10.2	3.0	−2.2	1.057	0.45	0.27	15	N	
91/11/22	9.6	3.4	−0.5	0.971	−0.08	−1.70	17		1
92/01/17	9.4	−0.4	1.9	0.984	−0.04	−1.19	8	N	
92/01/18	10.7	−1.5	5.2	0.953	−0.02	−0.67	23	N	
92/01/21	8.5	0.4	5.9	0.955	−0.06	−0.09	32	N	5
92/01/28	9.3	0.3	−2.5	0.976	0.05	−1.18	19	N	5
92/01/29	8.7	−1.0	5.4	0.987	−0.02	−0.80	37	Y	5
92/01/30	9.1	−0.9	9.6	1.071	−0.02	−1.01	12	Y	
92/02/03	9.3	−2.8	2.4	1.060	−0.12	0.33	27		1 2
92/02/04	9.9	−0.6	2.2	0.986	0.01	−1.75	10	N	5
92/02/05	10.8	3.0	−1.0	1.041	−0.01	−1.33	9	Y	5
92/02/07	10.7	0.2	1.4	1.088	−0.10	1.90	9		1
92/02/11	8.9	0.5	0.0	1.096	−0.09	−1.41	6	Y	
92/02/12	10.6	−0.7	1.3	1.037	0.05	0.63	14		1 5
92/02/14	9.3	2.0	0.6	1.007	0.02	−0.56	27		1 2
92/02/15	9.3	1.5	3.0	1.029	−0.09	−0.48	14		1
92/02/16	9.0	1.5	8.8	1.077	−0.08	−0.23	5		1
92/02/29	8.9	−4.1	1.2	0.946	−0.20	1.01	9	Y	
92/03/01	8.7	−5.5	3.5	1.056	−0.14	0.78	7		1
93/01/06	9.2	0.4	2.5					Y	3
93/01/11	8.7	1.0	2.1	0.967	0.03	0.07	34	N	
93/01/12	8.8	1.1	0.6	1.068	0.04	0.34	11	N	
93/01/13	8.7	0.5	2.9					Y	3
93/01/14	8.5	−0.4	7.2	0.995	0.03	0.78	16	N	5
93/01/15	8.5	1.5	4.1	0.955	−0.07	0.36	13	N	
93/02/15	8.8	2.2	−0.4	0.942	−0.02	−1.01	8	N	
94/01/18	10.3	1.5	2.6					N	3

continued on next page

continued from previous page

	SCAN calibration			Mosaicing calibration					
Date	Gain	Offset	Phase	Gain	ΔRA	$\Delta\delta$	Sources	Self-cal.	Notes
94/01/19	10.3	0.3	6.6	1.042	0.14	−1.40	15	Y	
94/01/31	9.5	−0.3	1.6	0.967	0.00	1.55	5	Y	
94/02/01	9.9	−0.2	2.6					Y	3
94/05/01	10.6	−0.7	3.7					N	3
95/04/01	9.6	2.8	−10.4					N	3
95/04/02	9.4	4.1	−9.9	0.967	0.14	−0.61	5	Y	
95/04/29	11.3	2.9	−1.4	1.017	0.06	0.73	11	Y	
95/04/30	10.8	4.6	−5.5	0.986	0.00	1.36	8	Y	
95/06/03	7.9	2.1	4.9					Y	3
95/06/17	8.0	−2.6	9.8	0.971	−0.05	−1.41	7	Y	
95/10/20	7.1	1.4	−3.0	0.984	−0.17	−1.21	13	Y	4
95/10/21	7.1	0.8	−1.1	1.038	−0.17	3.91	14	Y	4
95/10/22	6.4	1.3	0.3	1.036	0.07	−0.52	13	Y	4
95/10/23	6.9	1.0	−0.4	0.969	0.00	1.19	12	Y	4
96/01/30	10.6	−2.4	1.8					Y	3
96/01/31	12.1	−0.3	−3.6					Y	3
96/02/01	11.7	0.8	−0.9					Y	3
96/02/03	10.8	−4.0	4.1	0.949	0.10	1.33	5	Y	

notes

1. Galactic Plane survey observation
2. mosaicing calibration taken from the Galactic Plane survey
3. no mosaicing calibration
4. pulsar gating observation
5. part of field not included in mosaic

Felix qui potuit rerum cognoscere causas.

(Happy is he who has been able to learn the causes of things.)

Virgil, Georgics, II. 490

References

Agresti, A., 1990, Categorical data analysis, (New York: John Wiley & Sons)

Amy, S. W. & Large, M. I., 1990, Proc. Astron. Soc. Aust., 8, 308–311

Anderson, M. C. & Rudnick, L., 1993, Ap. J., 408, 514–529

Arendt, R. G., Dwek, E., Petre, R., Dickel, J. R., Roger, R. S., Milne, D. K., & Kesteven, M. J., 1990, Ap. J., 350, 266–274

Aschenbach, B., Egger, R., & Trümper, J., 1995, Nature, 373, 587–590

Aschenbach, B., 1992, in Space Science with particular emphasis on High Energy Astrophysics, ed. J. Trümper, (Garching bei München: Max-Planck-Institut für Extraterrestriche Physik), 28–35

Baars, J. W. M., Genzel, R., Pauliny-Toth, I. I. K., & Witzel, A., 1977, Astron. Astrophys., 61, 99–106

Backer, D. C., 1988, in Galactic and Extragalactic Radio Astronomy, ed. G. L. Verschuur & K. I. Kellermann, (New York: Springer-Verlag), 480–521

Bailes, M., Manchester, R. N., Kesteven, M. J., Norris, R. P., & Reynolds, J. E., 1989, Ap. J., 343, L53–L55

van den Bergh, S., 1979, Ap. J., 227, 497–498

Bhattacharya, D., 1990, J. Astrophys. Astr., 11, 125–140

Bietenholz, M. F. & Kronberg, P. P., 1990, Ap. J., 357, L13–L16

Bietenholz, M. F. & Kronberg, P. P., 1991, Ap. J., 368, 231–240

Bietenholz, M. F., Frail, D. A., & Hankins, T. H., 1991, Ap. J., 376, L41–L44

Bock, D. C., Large, M. I., & Sadler, E. M., 1997, The MOST Wide Field Survey, in preparation

Bridle, A. H. & Schwab, F. R., 1989, in Synthesis Imaging in Radio Astronomy, ed. R. A. Perley, F. R. Schwab, & A. H. Bridle, (San Francisco: Astronomical Society of the Pacific), 247–258

Burgess, A. M. & Hunstead, R. W., 1994, in The First Stromlo Symposium: The Physics of Active Galaxies, ed. G. V. Bicknell, M. A. Dopita, & P. J. Quinn, (San Francisco: Astronomical Society of the Pacific), 359–360

Burgess, A. M., 1989, An attempt to improve the meridian-distance gain curve of the Molonglo telescope, Reseach project report, School of Physics, University of Sydney

Buxton, M. et al., 1997, The MSSSO/University of Sydney wide field Hα imaging survey, in preparation

Campbell-Wilson, D. & Hunstead, R. W., 1994, Proc. Astron. Soc. Aust., 11, 33–38

Caswell, J. L., 1977a, Proc. Astron. Soc. Aust., 3, 130–133

Caswell, J. L., 1977b, M.N.R.A.S., 181, 789–797

Chanmugam, G., Rajasekhar, A., & Young, E. J., 1995, M.N.R.A.S., 276, L21–L24

Clark, D. H. & Caswell, J. L., 1976, M.N.R.A.S., 174, 267–305

Clark, D. H. & Crawford, D. F., 1974, Aust. J. Phys., 27, 713–727

Clark, D. H., Green, A. J., & Caswell, J. L., 1975, Aust. J. Phys. Astrophys. Suppl., No. 37, 75–86

Condon, J. J., Cotton, W. D., Greisen, E. W., Yin, Q. F., Perley, R. A., Taylor, G. B., & Broderick, J. J., 1997, The NRAO VLA sky survey, in preparation

Cooperstein, J. & Baron, E. A., 1990, in Supernovae, ed. A. G. Petschek, (New York: Springer-Verlag), 213–266

Cornwell, T. & Braun, R., 1989, in Synthesis Imaging in Radio Astronomy, ed. R. A. Perley, F. R. Schwab, & A. H. Bridle, (San Francisco: Astronomical Society of the Pacific), 167–183

Couch, L. W., 1990, Digital and Analog Communications Systems, (New York: Macmillan)

Cram, L. E. & Ye, T., 1995, Aust. J. Phys., 48, 113–124

Crawford, D. F., 1984, in Indirect Imaging, ed. J. A. Roberts, (Cambridge: Cambridge University Press), 373–378

Crawford, D. F., 1996, Temperature and gain corrections for the MOST, Molonglo Technical Report 96.010, School of Physics, University of Sydney

Crawford, D. F., 1997a, MSTKLN—a program to analyse MOST data, Molonglo Technical Report 97.005, School of Physics, University of Sydney

Crawford, D. F., 1997b, Noise analysis of Wide Fields, Molonglo Technical Report 97.001, School of Physics, University of Sydney

Crawford, D. F., 1997c, Wide Field positional accuracy (amended), Molonglo Technical Report 97.006, School of Physics, University of Sydney

Day, G. A., Caswell, J. L., & Cooke, D. J., 1972, Aust. J. Phys. Astrophys. Suppl., 25, 1–19

Dickel, J. R., Van Breugel, W. J. M., & Strom, R. G., 1991, Astron. J., 101, 2151–2159

Dubner, G. M., Braun, R., Winkler, P. F., & Goss, W. M., 1991, Astron. J., 101, 1466–1471

Duin, R. M. & Van Der Laan, H., 1975, Astron. Astrophys., 40, 111–122

Duncan, A. R., Stewart, R. T., Haynes, R. F., & Jones, K. L., 1995, M.N.R.A.S., 277, 36–52

Duncan, A. R., Stewart, R. T., Haynes, R. F., & Jones, K. L., 1996, M.N.R.A.S., 280, 252–266

Duncan, A. R. et al., 1997, in preparation

Durdin, J. M., Large, M. I., & Little, A. G., 1984, in Indirect Imaging, ed. J. A. Roberts, (Cambridge: Cambridge University Press), 75–79

Dwarakanath, K. S., 1991, J. Astrophys. Astr., 12, 199–211

Eggen, O. J., 1980, Ap. J., 238, 627–642

Elliott, K. H., Goudis, C., & Meaburn, J., 1976, M.N.R.A.S., 175, 605–611

Fesen, R. A., Downes, R. A., Wallace, D., & Normandeau, M., 1995, Astron. J., 110, 2876–2884

Frail, D. A. & Weisberg, J. M., 1990, Astron. J., 100, 743–757

Frail, D. A., Kassim, N. E., Cornwell, T. J., & Goss, W. M., 1995, Ap. J., 454, L129–L132

Frail, D. A., Bietenholz, M. F., Markwardt, C. B., & Ögelman, H., 1997, Ap. J., 475, 224–230

Fulbright, M. S. & Reynolds, S. P., 1990, Ap. J., 357, 591–601

Gaensler, B. M. & Johnston, S., 1995, M.N.R.A.S., 277, 1243–1253

Gaensler, B. M., 1997, Ap. J., in press

Gangadhara, R. T., 1996, Astron. Astrophys., 314, 853–863

Goldreich, P. & Julian, W. H., 1969, Ap. J., 157, 869–880

Gooch, R., 1996, in Astronomical Data Analysis Software and Systems V, ed. G. H. Jacoby & J. Barnes, (San Francisco: Astronomical Society of the Pacific), 80–83

Graham, J. R., Levenson, N. A., Hester, J. J., Raymond, J. C., & Petre, R., 1995, Ap. J., 444, 787–795

Gray, A. D., Cram, L. E., Ekers, R. D., & Goss, W. M., 1991, Nature, 353, 237–239

Gray, A. D., Nicholls, J., Ekers, R. D., & Cram, L. E., 1995, Ap. J., 448, 164–178

Gray, A. D., 1994, Radio Observations of Sources near the Galactic Centre, PhD thesis, University of Sydney

Green, A. J., 1974, Astron. Astrophys. Suppl. Ser., 18, 267–307

Green, D. A., 1984a, M.N.R.A.S., 211, 433–441

Green, D. A., 1984b, M.N.R.A.S., 209, 449–478

Green, D. A., 1990, Astron. J., 100, 1927–1942

Green, D. A., 1991, Pub. Astr. Soc. Pac., 103, 209–220

Green, A. J., 1994, Proc. Astron. Soc. Aust., 11, 79

Green, D. A., 1996, A catalogue of galactic supernova remnants (1996 August version), Mullard Radio Astronomy Observatory, Cambridge, United Kingdom, (available on the World-Wide-Web at "`http://www.mrao.cam.ac.uk/surveys/snrs/`")

Green, A. J., 1997, Publ. Astron. Soc. Aust., 14, 73–76

Greisen, E. W. & Calabretta, M., 1995, Representations of celestial coordinates in FITS, unpublished

Greisen, E. (ed.), 1996, The AIPS COOKBOOK, (Charlottesville: National Radio Astronomy Observatory)

Gum, C., 1955, Mem. R. A. S., 67, 155

Harkness, R. P. & Wheeler, J. C., 1990, in Supernovae, ed. A. G. Petschek, (New York: Springer-Verlag), 1–29

Haslam, C. G. T., Stoffel, H., Salter, C. J., & Wilson, W. E., 1982, Astron. Astrophys. Suppl. Ser., 47, 1–142

Helfand, D. J. & Becker, R. H., 1987, Ap. J., 314, 203–214

Hester, J. J. & Cox, D. P., 1986, Ap. J., 300, 675–697

Hester, J. J., Raymond, J. C., & Blair, W. P., 1994, Ap. J., 420, 721–745

Hester, J. J. et al., 1996, Ap. J., 456, 225–233

Hester, J. J., 1987, Ap. J., 314, 187–202

Hogan, D., 1992, Improving the Molonglo Observatory Synthesis Telescope, Reseach project report, School of Physics, University of Sydney

Hunstead, R. W., 1991, Aust. J. Phys., 44, 743–757

Jones, B. B. & Finlay, E. A., 1974, Aust. J. Phys., 27, 687–711

Jones, P. A. & McAdam, W. B., 1992, Ap. J. Supp. Ser., 80, 137–203

Jun, B.-I. & Norman, M. L., 1996a, Ap. J., 472, 245–256

Jun, B.-I. & Norman, M. L., 1996b, Ap. J., 465, 800–814

Kaspi, V. M., 1996, in Pulsars: Problems & Progress, ed. S. Johnston, M. A. Walker, & M. Bailes, (San Francsico: Astonomical Society of the Pacific), 375–383

Kassim, N. E., Hertz, P., & Weiler, K. W., 1993, Ap. J., 419, 733–738

Kennel, C. F. & Coroniti, F. V., 1984, Ap. J., 283, 694–709

Kesteven, M. J. & Caswell, J. L., 1987, Astron. Astrophys., 183, 118–128

Komesaroff, M. M., Hamilton, P. A., & Ables, J. G., 1972, Aust. J. Phys., 25, 759–777

Kundt, W., 1988, in Supernova Shells and Their Birth Events, ed. W. Kundt, (Berlin: Springer-Verlag), 1–14

Lalitha, P., Salter, C. J., Mantovani, F., & Tomasi, P., 1984, Astron. Astrophys., 131, 196–199

Lamport, L., 1994, LaTeX: a document preparation system, (Reading, MA: Addison-Wesley)

Large, M. I., Vaughan, A. E., & Mills, B. Y., 1968, Nature, 220, 340–341

Large, M. I., Mills, B. Y., Little, A. G., Crawford, D. F., & Sutton, J. M., 1981, M.N.R.A.S., 194, 693–704

Large, M. I., Vaughan, A. E., Durdin, J. M., & Little, A. G., 1984, Proc. Astron. Soc. Aust., 5, 569–574

Large, M. I., Cram, L. E., & Burgess, A. M., 1991, The Observatory, 111, 72–75

Large, M. I., Campbell-Wilson, D., Cram, L. E., Davison, R. G., & Robertson, J. G., 1994, Proc. Astron. Soc. Aust., 11, 44–49

Large, M. I., 1990, Notes on radio source counts, Molonglo Technical Report 90.003, School of Physics, University of Sydney

Lawrence, S. S., Macalpine, G. M., Uomoto, A., Woodgate, B. E., Brown, L. W., Oliversen, R. J., Lowenthal, J. D., & Liu, C., 1995, Astron. J., 109, 2635–2651

Leahy, D. A. & Roger, R. S., 1991, Astron. J., 101, 1033–1042

Levenson, N. A., Graham, J. R., Hester, J. J., & Petre, R., 1996, Ap. J., 468, 323–329

Longair, M. S., 1994, High Energy Astrophysics. volume 2. Stars, the Galaxy and the interstellar medium, (Cambridge: Cambridge University Press), 2nd edition edition

Lozinskaya, T. A., 1986, Soviet Ast., 30, 542–548

Lozinskaya, T. A., 1992, Supernovae and Stellar Wind in the Interstellar medium, (New York: American Institute of Physics)

Lyne, A. G., Pritchard, R. S., Graham-Smith, F., & Camilo, F., 1996, Nature, 381, 497–498

Manchester, R. N., 1985, Proc. Astron. Soc. Aust., 6, 89–93

Markwardt, C. B. & Ögelman, H., 1995, Nature, 375, 40–42

Markwardt, C. B. & Ögelman, H. K., 1997, Ap. J., 480, L13–L16

May, J., Murphy, D. C., & Thaddeus, P., 1988, Astron. Astrophys. Suppl. Ser., 73, 51–83

McCulloch, P. M., Hamilton, P. A., Manchester, R. N., & Ables, J. G., 1978, M.N.R.A.S., 183, 645–676

McKee, C. F. & Cowie, L. L., 1975, Ap. J., 195, 715–725

Mills, B. Y. & Little, A. G., 1972, Publ. Astron. Soc. Aust., 2, 134–135

Mills, B. Y., 1985, Proc. Astron. Soc. Aust., 6, 72–78

Mills, B. Y., 1991, Aust. J. Phys., 44, 719–727

Milne, D. K. & Haynes, R. F., 1994, M.N.R.A.S., 270, 106–114

Milne, D. K. & Manchester, R. N., 1986, Astron. Astrophys., 167, 117–119

Milne, D. K., Caswell, J. L., Kesteven, M. J., Haynes, R. F., & Roger, R. S., 1989, Proc. Astron. Soc. Aust., 8, 187–194

Milne, D. K., 1968a, Aust. J. Phys., 21, 501–509

Milne, D. K., 1968b, Aust. J. Phys., 21, 201–219

Milne, D. K., 1979, Aust. J. Phys., 32, 83–92

Milne, D. K., 1980, Astron. Astrophys., 81, 293–301

Milne, D. K., 1987, Aust. J. Phys., 40, 771–787

Milne, D. K., 1995, M.N.R.A.S., 277, 1435–1442

Minkowski, R., 1958, Pub. Astr. Soc. Pac., 70, 143–151

Morrison, J. E., 1995, in Astronomical Data Analysis Software and Systems IV, ed. R. A. Shaw, H. E. Payne, & J. J. E. Hayes, (San Francisco: Astronomical Society of the Pacific), 179–181

Murdoch, H. S. & Hoskins, D. G., 1973, Aust. J. Phys., 26, 867–880

Murphy, D. C. & May, J., 1991, Astron. Astrophys., 247, 202–214

Nomoto, K., 1987, in The Origin and Evolution of Neutron Stars, ed. D. J. Helfand & J. H. Huang, (Dordrecht: Kluwer), 281–303

North, A. J., February 1994, A Telescope Control System, Master's thesis, University of Sydney

Oberlack, U., Diehl, R., Montmerle, T., Prantzos, N., & von Ballmoos, P., 1994, Ap. J. Supp. Ser., 92, 433–439

Perley, R. A., 1979, Astron. J., 84, 1443–1457

Perley, R. A., 1989, in Synthesis Imaging in Radio Astronomy, ed. R. A. Perley, F. R. Schwab, & A. H. Bridle, (San Francisco: Astronomical Society of the Pacific), 259–275

Perley, R. A., 1996, Very Large Array observational status summary (1996 July version), National Radio Astronomy Observatory (available on the World-Wide-Web at "`http://www.nrao.edu/vla/obstatus/vlas/vlas.html`"

Petschek, A. G. (ed.), 1990, Supernovae, (New York: Springer-Verlag)

Press, W. H., Teukolsky, S. A., Vetterling, W. T., & Flannery, B. P., 1992, Numerical recipes in C, (Cambridge: Cambridge University Press), 2nd edition

Reynolds, S. P. & Chevalier, R. A., 1984, Ap. J., 278, 630–648

Reynolds, J. E., 1986, Radio Emission from Galaxies in Clusters, PhD thesis, University of Sydney

Reynolds, S. P., 1988a, Ap. J., 327, 853–858

Reynolds, S. P., 1988b, in Galactic and Extragalactic Radio Astronomy, ed. G. L. Verschuur & K. I. Kellermann, (New York: Springer-Verlag), 439–479

Rho, J., 1996, An X-ray Study of Composite Supernova Remnants, PhD thesis, University of Maryland

Risbeth, 1958, Aust. J. Phys., 91, 550–563

Robertson, J. G., 1991, Aust. J. Phys., 44, 729–742

Rodgers, A. W., Campbell, C. T., & Whiteoak, J. B., 1960, M.N.R.A.S., 121, 103–110

Roger, R. S., Milne, D. K., Wellington, K. J., Haynes, R. F., & Kesteven, M. J., 1984, Proc. Astron. Soc. Aust., 5, 560–562

Sault, R. J., Teuben, P. J., & Wright, M. C. H., 1995, in Astronomical Data Analysis Software and Systems IV (ASP Conference Series, Volume 77), ed. R. Shaw, H. Payne, & J. Hayes, (San Francisco: Astronomical Society of the Pacific), 433–436

Sault, R. J., Staveley-Smith, L., & Brouw, W. N., 1996, Astron. Astrophys. Suppl. Ser., 120, 375–384

Seward, F. D., 1990, in Imaging X-Ray Astronomy, ed. M. Elvis, (Cambridge: Cambridge University Press), 241–245

Stone, J. M., Xu, J., & Mundy, L. G., 1995, Nature, 377, 315–317

Stothers, R., 1980, Pub. Astr. Soc. Pac., 92, 145–146

Straka, W. C., Dickel, J. R., Blair, W. P., & Fesen, R. A., 1986, Ap. J., 306, 266–270

Strom, R., Johnston, H. M., Verbunt, F., & Aschenbach, B., 1995, Nature, 373, 590–592

Subrahmanya, C. R. & Mills, B. Y., 1987, in Observational Cosmology, ed. A. Hewitt, G. Burbidge, & L. Z. Fang, (Dordrecht: Kluwer), 569–572

Tammann, G. A., Löffler, W., & Schröder, A., 1994, Ap. J. Supp. Ser., 92, 487–493

Taylor, A. R., Wallace, B. J., & Goss, W. M., 1992, Astron. J., 103, 931–942

Taylor, G. B., 1997, Very Large Array calibrator manual (1997 July version), National Radio Astronomy Observatory (available on the World-Wide-Web at `"http://www.nrao.edu/~gtaylor/calib.html"`

Turtle, A. J., Pugh, J. F., Kenderline, S., & Pauliny-Toth, I. I. K., 1962, M.N.R.A.S., 124, 297–312

Walker, B., 1996, Enhancing the MOST—proposed local oscillator distribution systems, Reseach project report, School of Physics, University of Sydney

Wallace, B. J., Landecker, T. L., & Taylor, A. R., 1994, Astron. Astrophys., 286, 565–578

Wallace, B. J., Landecker, T. L., Taylor, A. R., & Pineault, S., 1997, Astron. Astrophys., 317, 212–222

Weiler, K. W. & Panagia, N., 1980, Astron. Astrophys., 90, 269–282

Weiler, K. W. & Sramek, R. A., 1988, Ann. Rev. Astron. Astrophys., 26, 295–341

Weiler, K. W., 1983, Observatory, 103, 85–106

Wheelock, S. L. et al., 1994, Sky Survey Atlas Explanatory Supplement, JPL Publication 94-11, (Pasadena: JPL)

White, R. L. & Long, K. S., 1991, Ap. J., 373, 543–555

Whiteoak, J. B. Z., 1992, Astron. Astrophys., 262, 251–257

Whiteoak, J. B. Z. & Green, A. J., 1996, Astron. Astrophys. Suppl. Ser., 118, 329–380

Whiteoak, J. B. Z., Large, M. I., Cram, L. E., & Piestryzynski, B., 1989, Proc. Astron. Soc. Aust., 8, 176–179

Whiteoak, J. B. Z., Cram, L. E., & Large, M. I., 1994, M.N.R.A.S., 269, 294–300

Wijers, R. A. M. J. & Sigurdsson, S., 1997, M.N.R.A.S., 290, 276–282

Winkler, P. F., Tuttle, J. H., Kirshner, R. P., & Irwin, M. J., 1988, in Supernova remnants and the interstellar medium, ed. R. S. Roger & T. L. Landecker, (Cambridge: Cambridge University Press), 65–68

Woltjer, L., 1972, Ann. Rev. Astron. Astrophys., 10, 129–158

Woosley, S. E., 1990, in Supernovae, ed. A. G. Petschek, (New York: Springer-Verlag), 182–212

Wright, M. C. H. & Forster, J. R., 1980, Ap. J., 239, 873–879

Wright, A. E., Griffith, M. R., Burke, B. F., & Ekers, R. D., 1994, Ap. J. Supp. Ser., 91, 111–308

Wright, A. E., Griffith, M. R., Hunt, A. J., Troup, E., Burke, B. F., & Ekers, R. D., 1996, Ap. J. Supp. Ser., 103, 145–171

Ye, T. & Turtle, A. J., 1993, in New aspects of Magellanic Clouds Research, ed. B. Baschek, G. Klare, & J. Lequex, (Berlin: Springer-Verlag), 167–168

Ye, T., 1995, Description of mosaicing program, Molonglo Technical Report 95.005, School of Physics, University of Sydney

Ye, T., 1996, Description of FITSMSYN program, Molonglo Technical Report 96.002, School of Physics, University of Sydney

Yoshikoshi, T., Kifune, T., Dazeley, S. A., Edwards, P. G., Hara, T., Hayami, Y., Kakimoto, F., Konishi, T., Masaike, A., Matsubara, Y., Matsuoka, T., Mizumoto, Y., Mori, M., Muraishi, H., Muraki, Y., Naito, T., Nishijima, K., Oda, S., Ogio, S., Ohsaki, T., Patterson, J. R., Roberts, M. D., Rowell, G. P., Sako, T., Sakurazawa, K., Susukita, R., Suzuki, A., Tamura, T., Tanimori, T., Thornton, G. J., Yanagita, S., & Yoshida, T., 1997, Ap. J., 487, L65–L68